NUREG/CR-6708

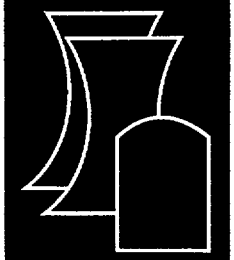

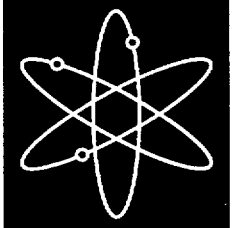

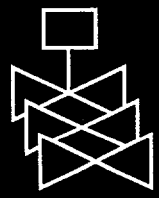

Surface Complexation Modeling of Uranium (VI) Adsorption on Natural Mineral Assemblages

U.S. Geological Survey

Office of Nuclear Regulatory Research
U.S. Nuclear Regulatory Commission
Washington, DC 20555-0001

AVAILABILITY OF REFERENCE MATERIALS IN NRC PUBLICATIONS

NRC Reference Material

As of November 1999, you may electronically access NUREG-series publications and other NRC records at NRC's Public Electronic Reading Room at www.nrc.gov/NRC/ADAMS/index.html. Publicly released records include, to name a few, NUREG-series publications; *Federal Register* notices; applicant, licensee, and vendor documents and correspondence; NRC correspondence and internal memoranda; bulletins and information notices; inspection and investigative reports; licensee event reports; and Commission papers and their attachments.

NRC publications in the NUREG series, NRC regulations, and *Title 10, Energy*, in the Code of *Federal Regulations* may also be purchased from one of these two sources.

1. The Superintendent of Documents
   U.S. Government Printing Office
   Mail Stop SSOP
   Washington, DC 20402–0001
   Internet: bookstore.gpo.gov
   Telephone: 202-512-1800
   Fax: 202-512-2250
2. The National Technical Information Service
   Springfield, VA 22161–0002
   www.ntis.gov
   1–800–553–6847 or, locally, 703–605–6000

A single copy of each NRC draft report for comment is available free, to the extent of supply, upon written request as follows:

Address: Office of the Chief Information Officer,
Reproduction and Distribution
Services Section
U.S. Nuclear Regulatory Commission
Washington, DC 20555-0001
E-mail: DISTRIBUTION@nrc.gov
Facsimile: 301–415–2289

Some publications in the NUREG series that are posted at NRC's Web site address www.nrc.gov/NRC/NUREGS/indexnum.html are updated periodically and may differ from the last printed version. Although references to material found on a Web site bear the date the material was accessed, the material available on the date cited may subsequently be removed from the site.

Non-NRC Reference Material

Documents available from public and special technical libraries include all open literature items, such as books, journal articles, and transactions, *Federal Register* notices, Federal and State legislation, and congressional reports. Such documents as theses, dissertations, foreign reports and translations, and non-NRC conference proceedings may be purchased from their sponsoring organization.

Copies of industry codes and standards used in a substantive manner in the NRC regulatory process are maintained at—

The NRC Technical Library
Two White Flint North
11545 Rockville Pike
Rockville, MD 20852–2738

These standards are available in the library for reference use by the public. Codes and standards are usually copyrighted and may be purchased from the originating organization or, if they are American National Standards, from—

American National Standards Institute
11 West 42nd Street
New York, NY 10036–8002
www.ansi.org
212–642–4900

Legally binding regulatory requirements are stated only in laws; NRC regulations; licenses, including technical specifications; or orders, not in NUREG-series publications. The views expressed in contractor-prepared publications in this series are not necessarily those of the NRC.

The NUREG series comprises (1) technical and administrative reports and books prepared by the staff (NUREG–XXXX) or agency contractors (NUREG/CR–XXXX), (2) proceedings of conferences (NUREG/CP–XXXX), (3) reports resulting from international agreements (NUREG/IA–XXXX), (4) brochures (NUREG/BR–XXXX), and (5) compilations of legal decisions and orders of the Commission and Atomic and Safety Licensing Boards and of Directors' decisions under Section 2.206 of NRC's regulations (NUREG–0750).

NUREG/CR-6708

Surface Complexation Modeling of Uranium (VI) Adsorption on Natural Mineral Assemblages

Manuscript Completed: January 2001
Date Published: March 2001

Prepared by
J.A. Davis

U.S. Geological Survey
Menlo Park, CA 94025

J.D. Randall
NRC Project Manager

Division of Risk Analysis and Applications
Office of Nuclear Regulatory Research
U.S. Nuclear Regulatory Commission
Washington, DC 20555-0001
NRC Job Code W6054

ABSTRACT

The value of surface complexation modeling of radionuclide adsorption in supporting the selection of K_d values should be given wider recognition within the performance assessment modeling process. Studies of uranium(VI) adsorption by a weathered schist and specimen mineral phases that comprise the schist were conducted as a function of aqueous chemical conditions in laboratory experiments. The schist was collected from weathered, subsurface soil in the vicinity of the Koongarra uranium deposit (Northern Territory, Australia). The variable aqueous chemical conditions in the experiments caused significant variations in the speciation of dissolved uranium(VI) and the distribution coefficient, K_d, that describes the partitioning of uranium(VI) between the aqueous and solid phases. K_d values determined in the laboratory experiments compared favorably with *in-situ* partitioning constants derived from analyses of dissolved uranium(VI) in groundwater and in the subsurface soils. Mineral coatings were more important than bulk mineralogy in controlling U(VI) adsorption by the schist. Various surface complexation modeling approaches were developed to describe adsorption of uranium(VI) on the schist and its reference mineral phases. One of the modeling approaches, the Generalized Composite approach, can reduce the uncertainty in K_d values chosen for performance assessment modeling. Surface complexation modeling offers a scientifically defensible means of linking the selection of K_d values for performance assessment modeling to existing knowledge of thermodynamic data for radionuclides and radionuclide speciation in aqueous systems.

CONTENTS

FIGURES

TABLES

1 APPLICATION OF SURFACE COMPLEXATION MODELING TO NATURAL MINERAL ASSEMBLAGES: SCIENTIFIC BACKGROUND AND OBJECTIVES

1.1 Introduction

Numerous sites throughout the United States are contaminated by radionuclides, especially uranium (U) and thorium (Th) and their by-products, due to mining, milling and other industrial processes (Morrison and Cahn, 1991). The United States Nuclear Regulatory Commission (USNRC) is responsible for licensing site remediation and clean up, or releasing the site for public or restricted use. Licensing decisions are made based on performance assessment (PA) calculations that utilize numerical models to estimate the increase in radioactivity exposure to the biosphere at selected locations. Contamination is often limited to the soils, subsurface sediments, and shallow aquifers at these sites. The calculated increase in biosphere exposure may involve above-ground exposure near the source of radionuclide contamination or ingestion at some location that radionuclides have been transported to via surface water, groundwater, or aeolian processes.

In addition to radionuclide contamination from various industrial and military uses, the United States and many other nations are faced with the problem of disposal of wastes from the nuclear power industry. These wastes contain high levels of radionuclides with long half-lives, and in most cases, the wastes will be disposed of in engineered facilities constructed underground in specific types of geologic formations. The most likely pathway for radionuclides to reach the biosphere from these repositories is by transport of dissolved radionuclides in groundwater (or transport of colloidal particles with adsorbed radionuclides).

To make the calculation of increased exposure to radioactivity in PA, it is necessary to calculate the total amount of each radionuclide that will be present at the selected locations as a function of time. A solute transport model is typically used to describe the physical processes of advection and dispersion that may transport radionuclides in groundwater from the source location to the site of ingestion. In current practice, chemical information is typically used in two ways in the groundwater transport modeling of PA studies: 1) radionuclide solubility limitations may be included to estimate when transport is affected by precipitation controls, especially near the source location, and 2) a distribution coefficient, K_d, for each radionuclide may be used to quantify retardation caused by adsorption processes. Although adsorption is only a part of the overall PA calculations, credit for retardation of radionuclide transport in the far-field geosphere zone may be extremely important in reducing the risk of biosphere exposure of certain radionuclides to levels that are in compliance with regulations.

The transport of actinide elements and other radionuclides in porous media can be strongly influenced by the competitive effects of the formation of mobile solution complexes and immobile adsorbed species. These elements can form many species in natural waters as a result of hydrolysis and complexation reactions. The distribution of these species can be highly dependent on chemical conditions, especially pH and the concentrations of complexing ligands, such as carbonate ions (Clark et al., 1995; Waite et al., 1994b). In natural waters, important complexing ligands for U(VI) include hydroxide, carbonate and dissolved organic carbon; such ligands may compete with adsorption sites for coordination of UO_2^{2+} (and other actinyl ions) and decrease the extent of adsorption via the formation of nonadsorbing aqueous complexes. The influence of some ligand interactions can be very complex, as demonstrated by the observed increased adsorption of metals in the presence of certain ligands (Davis and Leckie, 1978). However, in some cases, the effects of complexing ligands can be modeled in a straightforward way by

assuming that the aqueous complexes formed do not adsorb. For example, Kohler et al. (1996) showed that the adsorption of U(VI) on quartz in the presence of fluoride (F) ligands could be modeled as a competition between the quartz surface and aqueous F for coordination of U(VI).

The quality of thermodynamic data for radionuclide solubilities and aqueous speciation has been steadily increasing in recent years and is now available in critically reviewed compilations (Grenthe et al., 1992; Silva et al., 1995). In contrast, the choice of K_d values in PA modeling is generally made based on expert judgement of the available experimental data for individual radionuclides and various rock materials. The expert judgement may include an evaluation of laboratory measurements of K_d values from batch or column experiments with site-specific materials in contact with solutions of varying chemical composition. In addition to measurements with site-specific materials, databases of K_d values have been assembled for the adsorption of many radionuclides on a variety of single mineral phases (Turner, 1995), natural materials, including soils and rock powders (EPA, 1996; McKinley and Scholtis, 1995; Sheppard and Thibault, 1990; Looney et al., 1987; Baes and Sharp, 1983; Isherwood, 1981), and engineered barrier materials pertinent to nuclear waste disposal (Berry, 1992; Krupka and Serne, 1996).

One of the potentially large uncertainties in PA model calculations arises from the choice of K_d values for individual radionuclides. Depending on the type and purpose of the PA modeling study, either a single K_d value may be chosen for each radionuclide or a probability distribution function (PDF) may be derived that encompasses a range of K_d values. The uncertainty in the choice of K_d values or in the PDF arises from several sources, e.g. 1) experimental error, 2) extrapolation or interpolation of values to chemical conditions or rock types other than those used in actual experimental measurements of K_d, and 3) the scaling of K_d values measured for rock powders to the values expected for intact rocks in the site-specific, geologic setting.

Constant K_d models for adsorption do not adequately account for spatial changes in the composition of adsorbing phases or variable chemical conditions, such as pH, ionic strength, or concentrations of complexing ligands that may be encountered along a groundwater flow path (Davis et al., 1998; Kohler et al., 1996; Davis and Kent, 1990). For a variety of reasons, the range of K_d values that may need to be considered for each radionuclide/rock combination can be quite large. Spatial and temporal variability in chemical conditions can be considered in PA modeling with K_d values by separating the calculations into separate blocks of time or hydrologic units in space. Although the effects of changes in chemical conditions on the solubilities of radionuclides can usually be calculated in a straightforward manner, the effects of variable chemical conditions on adsorption and the choice of K_d values is more complex (Kohler et al., 1996). In order to be "conservative", large ranges of K_d values may need to be estimated by expert judgement in order to account for possible changes in chemical conditions and for other sources of error. The uncertainties in these ranges are difficult to assess quantitatively without doing large numbers of experiments.

1.2 Surface Complexation Modeling

Fortunately, the uncertainty in K_d values that arises from variations in the chemical composition of groundwater or mineralogical composition of the adsorbent phases along a flow path can be reduced with the use of surface complexation modeling (SCM) to describe adsorption (Kohler et al., 1996; Waite et al., 1994b). In addition, certain large sources of uncertainty (e.g., scaling from K_d values measured for rock powders to the surfaces of a fractured rock system) can be more easily addressed with SCM, because SCM is based on defining radionuclide adsorption per unit surface area rather than per unit mass.

Since publication of the surface complexation concept by Professors Stumm and Schindler (Schindler and Kamber, 1968; Hohl and Stumm,

1976), a voluminous literature on ion adsorption and SCM has appeared. Although a number of variations in the modeling approach have been developed, there are four tenets in all SCM (Davis and Kent, 1990):

- Mineral surfaces are composed of specific functional groups that react with dissolved solutes to form surface species (coordinative complexes or ion pairs), in a manner analogous to complexation reactions in homogeneous solution.

- The equilibria of adsorption reactions can be described by mass action equations. If desired, correction factors to these equations may be applied to account for variable electrostatic energy, using electrical double layer theory.

- The apparent binding constants determined for the mass action equations are empirical parameters related to thermodynamic constants by the rational activity coefficients of the surface species.

- The electrical charge at the surface is determined by the chemical reactions of the mineral functional groups, including acid-base reactions and the formation of ion pairs and coordinative complexes.

SCM could be of significant value to PA if it was used to determine the range of K_d values that need to be considered and provide a scientific basis for the range of values chosen. The uncertainties in SCM parameters are less than the uncertainties in K_d values (when considered over a range of chemical conditions), and the uncertainties are more easily quantified. For example, a recent report on batch studies of U(VI) adsorption on montmorillonite presented K_d values that ranged by more than 4 orders of magnitude over the pH range of 6.5 to 8.5 (Pabalan and Turner, 1996). Similar results were reported for U(VI) adsorption by ferrihydrite when adsorption was quantified in terms of K_d (Waite et al., 1994b). Davis et al. (1998) showed that the K_d values for Zn^{2+} in a sand and gravel aquifer varied by about two orders of magnitude because of variable chemical conditions in the groundwater. In each of these cases the datasets could be described by an SCM with a small number of independent parameters that remained constant and had comparatively little uncertainty in their values.

Using a range of 4 orders of magnitude in the uncertainty of K_d values (Pabalan and Turner, 1996) in PA calculations could lead to increased costs for waste cleanup at an industrial site or to rejection of an alternative waste disposal scenario. If used properly, SCM for radionuclide adsorption has the potential to increase the confidence and scientific credibility of PA transport modeling, by reducing the uncertainty in quantifying adsorption and providing a means of quantifying that uncertainty. In addition, SCM has the potential to lower the estimated remediation costs of sites contaminated with radionuclides (or the feasibility of a disposal scenario) by decreasing the uncertainty of K_d values (and the associated safety factor applied in PA modeling).

The use of equilibrium geochemical models to calculate radionuclide solubilities and aqueous speciation is well established in the PA field. Surface complexation modeling is simply an extension of this thermodynamic modeling approach to include the reactions between dissolved species and the functional groups (ligands) present on mineral surfaces. The adsorption reactions are included as part of the network of chemical reactions that require equilibration, rather than as a condition-dependent partitioning coefficient, like K_d. Once the model is calibrated, it allows predictive calculations for a range of geochemical conditions without changing the values of the stability constants for radionuclide adsorption. The adsorption equations can be included efficiently in transport simulations in which there are chemical gradients in the subsurface environment rather than constant chemical conditions (Kohler et al., 1996).

1.3 SCM with Natural Mineral Assemblages

The literature on SCM largely describes the results of well controlled laboratory investigations of the adsorption of ions by a variety of mineral phases (Davis and Kent, 1990). Most of these studies have been undertaken by aquatic scientists interested in developing a thermodynamic understanding of the coordinative properties of mineral surface functional groups. Such studies can benefit PA modeling because the chemical and physical principles that have been developed for individual mineral phases can guide K_d studies of natural materials (Davis et al., 1998; Dzombak and Morel, 1990).

In order to develop an SCM, the following steps must be taken:

- the total number of surface sites (functional groups) must be determined experimentally or a value must be assigned from other studies,

- an approach must be developed to describe surface site heterogeneity or the number of specific types of surface sites,

- the mass action and mass balance equations that describe the equilibria of surface reactions must be formulated and the apparent stability constants for surface species must be determined,

- an approach must be developed or assumed to quantify coulombic correction factors or rational activity coefficients to correct the equilibrium constants of surface acidity and complexation reactions.

There are two major approaches for applying the SCM concept to model metal ion and radionuclide adsorption to soils and sediments (Davis et al., 1998): 1) the ***component additivity*** approach, and 2) the ***generalized composite*** approach (Table 1-1). In the component additivity (CA) approach, the modeler attempts to *predict* adsorption on a complex mineral assemblage, using the results of a surface characterization of the assemblage and collected data for adsorption by pure, reference minerals or organic phases (Honeyman, 1984; Altmann, 1984). Strictly speaking, no fitting of data is required to develop the model for the mixed mineral assemblage in the CA approach, although comparisons of model simulations and experimental adsorption data for the assemblage are needed to build confidence in the model. It is assumed in this approach that the wetted surface of the complex mineral assemblage is composed of a mixture of one or more mineral (or organic) phases, whose surface properties are known from independent studies of the individual phases. From the studies of individual phases, a database of internally consistent SCM equilibria and stability constants can be developed that describe the adsorption reactions of solutes to each phase. For example, the compilation of Dzombak and Morel (1990) for hydrous ferric oxide represents such a database for an important adsorbing phase, and other databases are currently being developed (Turner, 1995). Once the relative abundance and identity of the major adsorptive phases have been determined and the appropriate databases for reference mineral phases have been assembled, a system of mass law equations can be written to describe the SCM equilibria for each phase of the mixture.

In the *generalized composite* (GC) approach, it is assumed that the surface composition of the mineral assemblage is inherently too complex to be quantified in terms of the contributions of individual phases to adsorption. Instead, it is assumed that the adsorptive reactivity of the surface can be described by SCM equilibria written with "generic" surface functional groups, with the stoichiometry and formation constants for each SCM equilibria determined by fitting experimental data (Davis et al., 1998; Koss, 1988; Westall et al., 1995). This approach can also be simplified by fitting the pH dependence of adsorption without explicit representation of electrostatic energies (Davis et al., 1998). Both types of modeling approaches will be tested in the results presented in this report.

Table 1-1. Characteristics of SC Modeling Approaches for Environmental Sorbents

Component Additivity	Generalized Composite
Predict adsorption	Simulate adsorption
Surface sites are unique for each specific sorbent	Generic surface sites
Surface site densities quantified by characterization of the surface of environmental sorbent mixture	Surface site densities quantified by measurement of surface area and fitting of experimental data for environmental sorbent mixture
Apparent stability constants and reaction stoichiometries obtained from studies of adsorption by specific sorbents	Apparent stability constants and reaction stoichiometries fit to experimental data for the environmental sorbent mixture
Overall adsorption predicted by the sum of adsorption by each specific sorbent	Numbers of site types and chemical reactions increased as necessary to achieve good model simulations and to meet modeling objectives

1.4 Project Goals

The overall objective of the project described in this report was to advance the state-of-the-art in the application of surface complexation modeling (SCM) to describe adsorption processes on the surfaces of geologic materials. The research was focused in several specific areas:

1. Experimental studies and SCM modeling were conducted of U(VI) adsorption by a weathered schist at the Koongarra field site (Northern Territory, Australia). The SCM modeling compared both the component additivity and generalized composite strategies for modeling U(VI) adsorption by the Koongarra subsurface material.

2. SCM models were developed for U(VI) adsorption by several single mineral phases that are present in the Koongarra subsurface material.

3. SCM models were developed for pure materials representative of secondary mineral coatings present in the Koongarra subsurface material and the importance of coatings in U(VI) adsorption was assessed.

4. EXAFS and FTIR spectroscopy were used to study the molecular structure of adsorbed U(VI) surface complexes on iron oxides. The goal of this work was to test for the existence of ternary surface-uranyl-carbonate complexes as was hypothesized in the SCM developed for U(VI) adsorption by ferrihydrite (Waite et al., 1994b).

5. The use of SCM rather than K_d was demonstrated in transport modeling of laboratory studies of U(VI) transport in columns under variable chemical conditions.

1.5 The Koongarra Field Site

The Koongarra uranium deposit lies 225 km east of the city of Darwin and 25 km south of the town of Jabiru in the Northern Territory of Australia (Fig. 1-1). The geographical and geological area is known as the Alligators River Region due to its being geographically dominated by the South Alligator and East Alligator Rivers. Koongarra is one of four major uranium deposits discovered in the region. The Koongarra deposit, which has not been mined, lies in the valley between the main Arnhem Land Plateau and the Mt. Brockman Massif outlier adjacent to the escarpment (Fig. 1-1).

Within the unweathered zone of the primary ore body, the ore consists of lenses containing coalescing veins of uraninite within the steeply dipping host Cahill quartz-chlorite schists. Secondary mineralization is present in the weathered schists, from below the surficial sand cover to the base of weathering at depths varying from 25 to 30 m below land surface. This mineralization has been derived from decomposition and leaching of the primary mineralized zone and forms a tongue-shaped fan of ore grade material dispersed downslope for about 80 m to the southeast (Fig. 1-2). Oxidation and alteration of uraninite within the primary ore zone have produced a variety of secondary minerals, particularly the uranyl silicates kasolite, sklodowskite, and uranophane (Snelling, 1990). Above the ore body the secondary mineralization in the weathered schists is characterized by uranyl phosphates, particularly saleeite, metatorbernite, and renardite. This phosphate-bearing zone constitutes weathered and leached primary ore, and is the former upward extension of the primary ore lenses. Further away from the primary ore zone, uranium is dispersed in the weathered schists (Fig. 1-2) and adsorbed onto clays and iron oxides (Waite and Payne, 1993).

For the study of U(VI) adsorption by the Koongarra weathered schist, cores were obtained from a number of locations (W1, W2, and W7) using a cable-tool rig (Waite et al., 1992). The samples were then prepared for adsorption studies as described in Section 9 of this report.

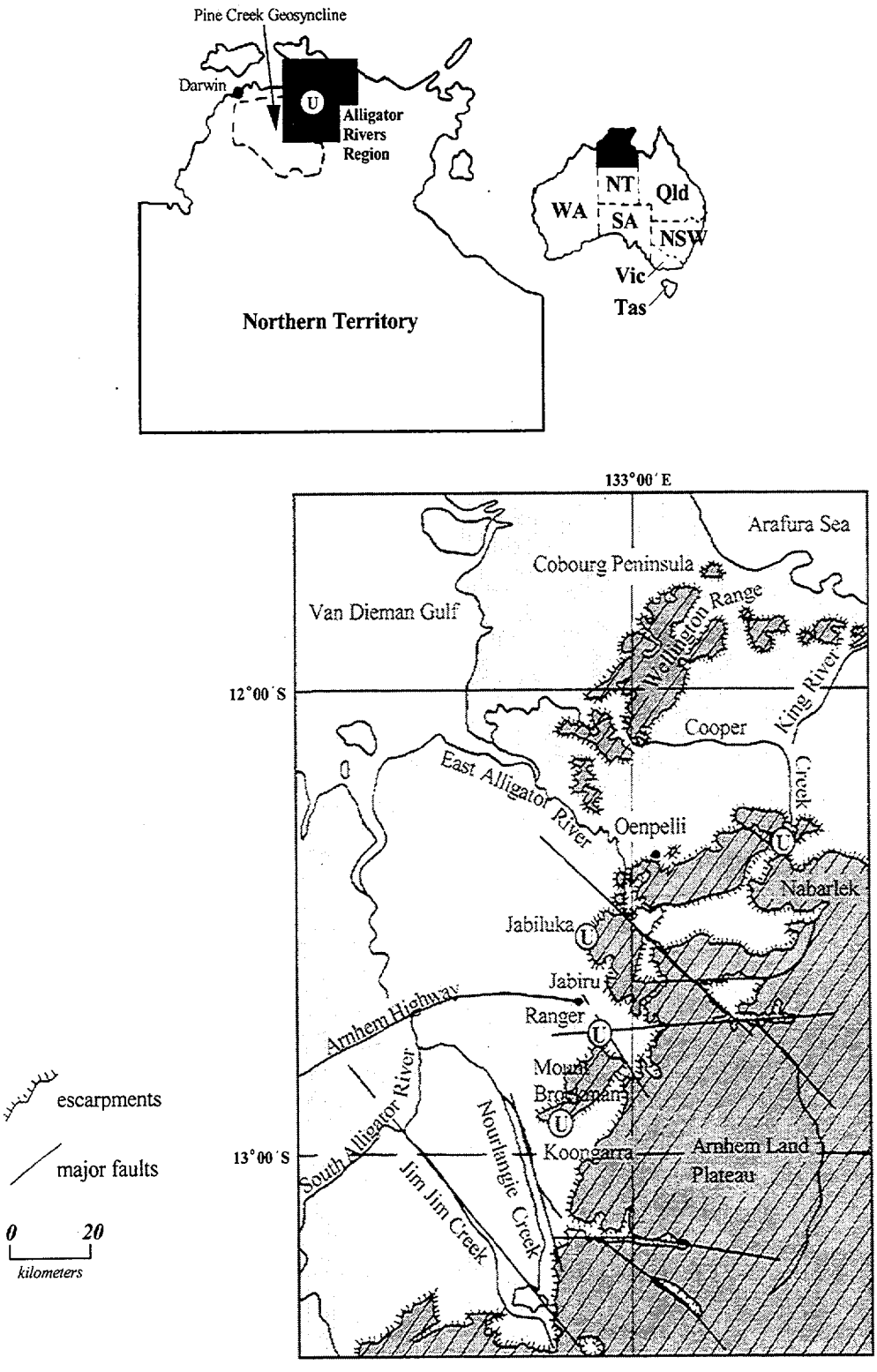

Figure 1-1. Location map showing the four uranium deposits of the Alligator Rivers Region, the sandstone escarpments and major faults (Snelling, 1992).

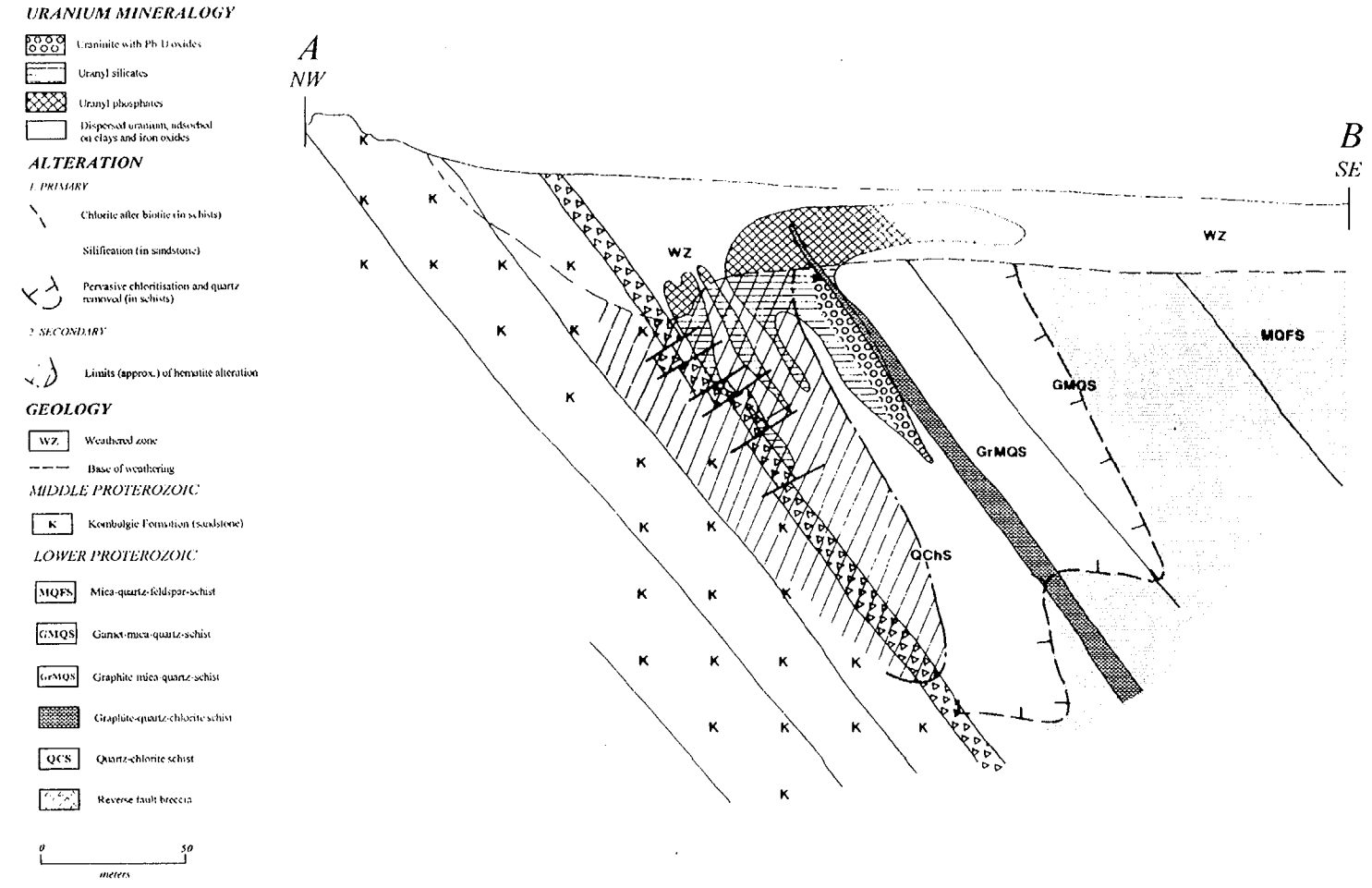

Figure 1-2. Simplified cross-section through the Koongarra No. 1 ore body. Geology, distribution of uranium minerals, hematite alteration zones, and groundwater flow are shown (after Snelling, 1990).

1.6 Overview of Report

Studies have been designed within this project to enable development of Component Additivity and Generalized Composite modeling approaches for description of U(VI) adsorption by the Koongarra weathered subsurface materials. The studies were completed under conditions of variable aqueous chemistry, which causes significant variation in the speciation of U(VI), as described in Section 2. Extensive investigations into the surface properties of single mineral phases and adsorption of U(VI) by these phases has been studied (Sections 3 to 8), and SCM have been developed (Sections 12 to 15) to describe adsorption as a function of solution conditions (pH, U(VI) concentration, ionic strength). Detailed characterization of the weathered schists collected in the vicinity of the Koongarra uranium deposit was completed using wet chemical and instrumental techniques (Section 10), and the extent of uranium partitioning to this material was studied as a function of aqueous chemical conditions (Section 9). A comparison of the extent of partitioning of uranium to natural Koongarra weathered material in laboratory batch experiments with "in situ" partitioning information derived from analyses of uranium in groundwater and solids from the Koongarra region is presented in Section 11. SCM models using the Component Additivity and Generalized Composite modeling approaches were developed to describe U(VI) adsorption by the Koongarra weathered subsurface materials, and these model results are given in Section 16.

The results of laboratory studies of U(VI) transport through quartz-packed columns are given in Section 17. These studies were conducted under conditions of variable pH, U(VI) concentration, and fluoride concentration, a U(VI) complexing ligand. The experimental results are modeled in Section 18 with the use of a solute transport model coupled with an SCM and U(VI) aqueous chemical reactions.

Section 19 summarizes the significance of the project results to PA modeling. The project impacts the evaluation of appropriate methods to determine K_d values for radionuclides and effects of their uncertainties on PA modeling. In addition, the study has application to the remediation of groundwater contamination and evaluation of environmental risk at licensed sites contaminated with uranium.

2 URANIUM(VI) AQUEOUS SPECIATION AND EQUILIBRIUM CHEMISTRY

2.1 U(VI) Solubility and Aqueous Speciation

The mobility of U(VI) in water-rock systems is dependent both upon its ability to form insoluble precipitates and upon its tendency to adsorb to solid substrates, particularly at relatively low total uranium concentrations. The geochemical conditions that lead to significant mobility are those under which strong aqueous complexes are formed that are weakly adsorbed. For example, under alkaline conditions, uranyl-carbonato complexes are formed that are weakly adsorbed (Waite et al., 1994b). Considerable advances have been made recently in developing a coherent set of thermodynamic data for describing the solution and mineral equilibrium chemistry of uranium (Grenthe et al., 1992; Silva et al., 1995). These advances allow better comparison of models for U(VI) adsorption, because consistent thermodynamic data can be used for the aqueous reactions in experimental systems.

Figures 2-1 and 2-2 show the complex distribution of U(VI) aqueous species as a function of pH in equilibrium with the partial pressure of CO_2 present in air. The calculations were made with the equilibrium speciation computer code, HYDRAQL (Papelis et al., 1988), using the thermodynamic data given in Table 2-1. The solubility of well-crystallized β-$UO_2(OH)_2$, in equilibrium with air, is illustrated in Figure 2-1. The aqueous speciation is dominated by mononuclear U(VI) species at low and high pH values in this system, but several multinuclear species, e.g., $(UO_2)_2(OH)_2^{2+}$ and $(UO_2)_3(OH)_5^{+}$, are important, and the mixed hydroxy carbonate complex, $(UO_2)_2CO_3(OH)_3^{-}$, is predicted to predominate in the pH range 6-8. However, considerable uncertainty in the thermodynamic data exists in the pH range 6-8, especially in the formation constant for the aqueous species, $UO_2(OH)_2$. We have chosen the value of −11.5 (Table 2-1) for the formation of this species (Silva, 1992); larger values for this constant may be possible (Grenthe et al.,1992), and this may affect the predicted dominant aqueous species in the circumneutral pH range.

There have been numerous studies of the thermodynamic properties of uranium oxides and hydroxides (Grenthe et al., 1992). Many of these are not highly relevant to the experimental studies presented in this report, because they focused on the solubility of well-defined crystalline minerals. In studies of crystalline solids, the presence of amorphous phases (such as newly formed precipitates) tends to invalidate the results.

Waite et al. (1994b] assumed that the formation of well crystallised β-$UO_2(OH)_2$ was kinetically hindered in their experiments, and therefore, this phase would not control the solubility of U(VI) in adsorption experiments. These authors suggested that an amorphous phase was more likely to form under the experimental conditions. Tripathi (1983) carried out a very thorough review of solubility data, including that of poorly crystalline phases. Tripathi assembled a range of log K_{S0} values, most of which were between -20.87 and -23.4, and after recalculation of original data, he proposed a value of log K_{S0} of -22.43 for the solubility of amorphous uranyl hydroxide. This was similar to values obtained by other workers (e.g., -22.4 proposed by Jensen (1982), although the data selection in this case was not as well documented). Another review of U(VI) solubility was carried out by Allard et al., (1984), who selected -22.4 for the log of the solubility product of amorphous uranyl hydroxide.

Various solubility constants for uranyl hydroxide were used to calculate the solubility of uranyl hydroxide in air-equilibrated systems (Figure 2-3). A representative curve for a system equilibrated with N_2 is also shown. The minimum solubility in air-equilibrated systems occurs between pH 6.5 and 7.0, and is about 2 x 10^{-6} M for β-$UO_2(OH)_2$, and close to 4 x 10^{-5} M

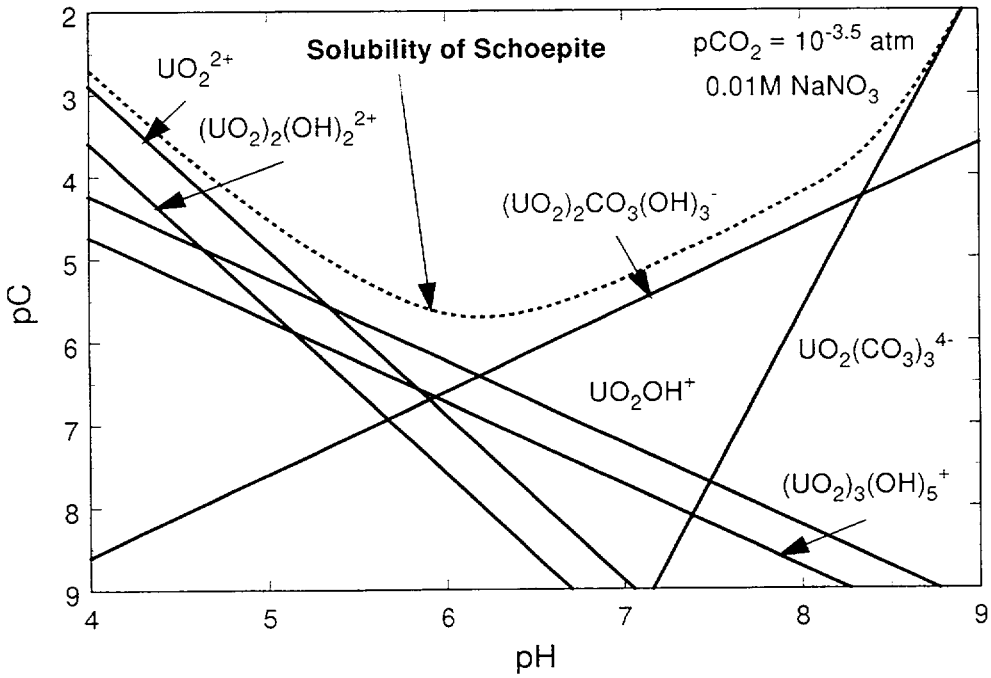

Figure 2-1. Solubility of β-$UO_2(OH)_2$, showing the pC (-log concentration) of predominant aqueous species as a function of pH in a 0.01M $NaNO_3$ solution.

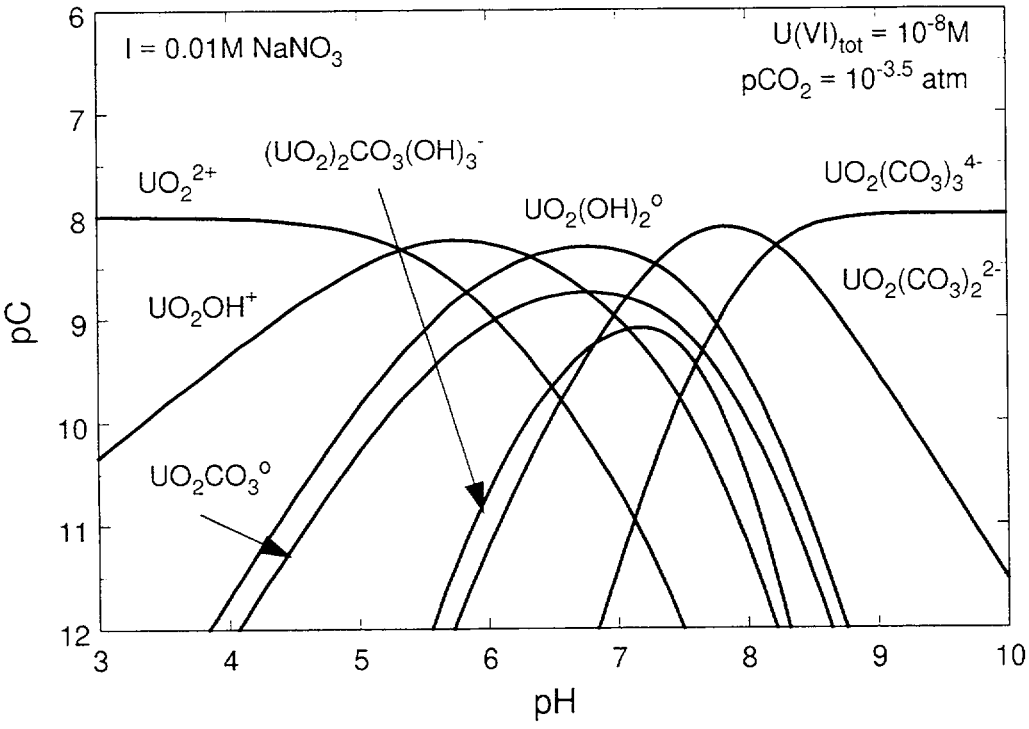

Figure 2-2A. Dissolved speciation of U(VI) as a function of total U(VI) concentration in an open atmosphere equilibrated with a partial pressure of CO_2 of $10^{-3.5}$ atm. Total dissolved U(VI) = 10^{-8}M.

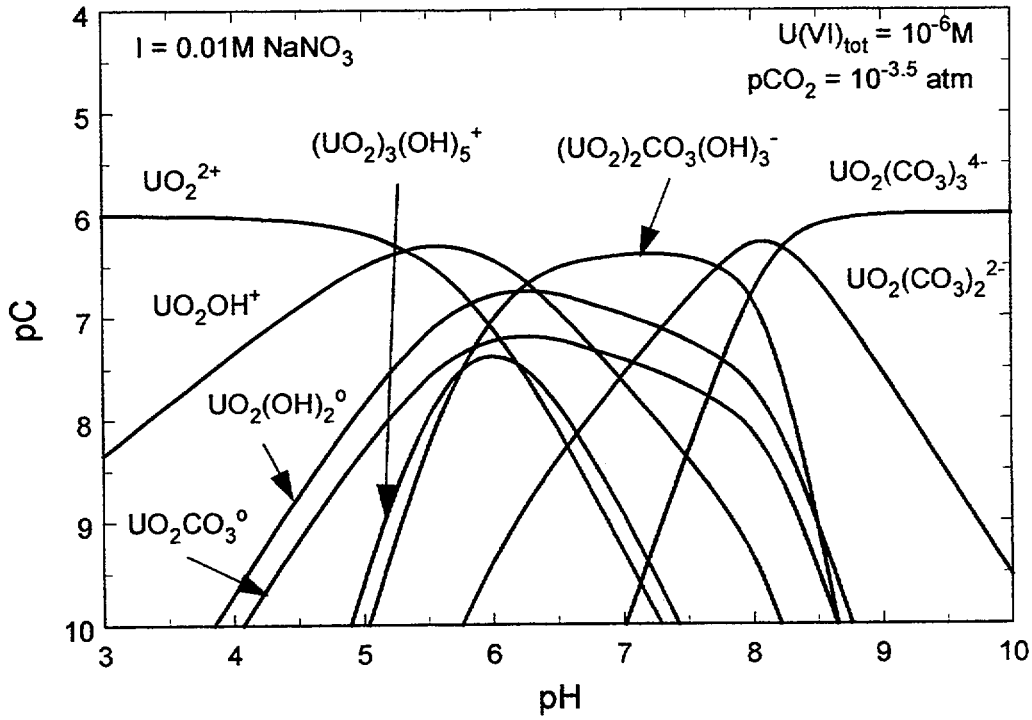

Figure 2-2B. Dissolved speciation of U(VI) as a function of total U(VI) concentration in an open atmosphere equilibrated with a partial pressure of CO_2 of $10^{-3.5}$ atm. Total dissolved U(VI) = 10^{-6}M.

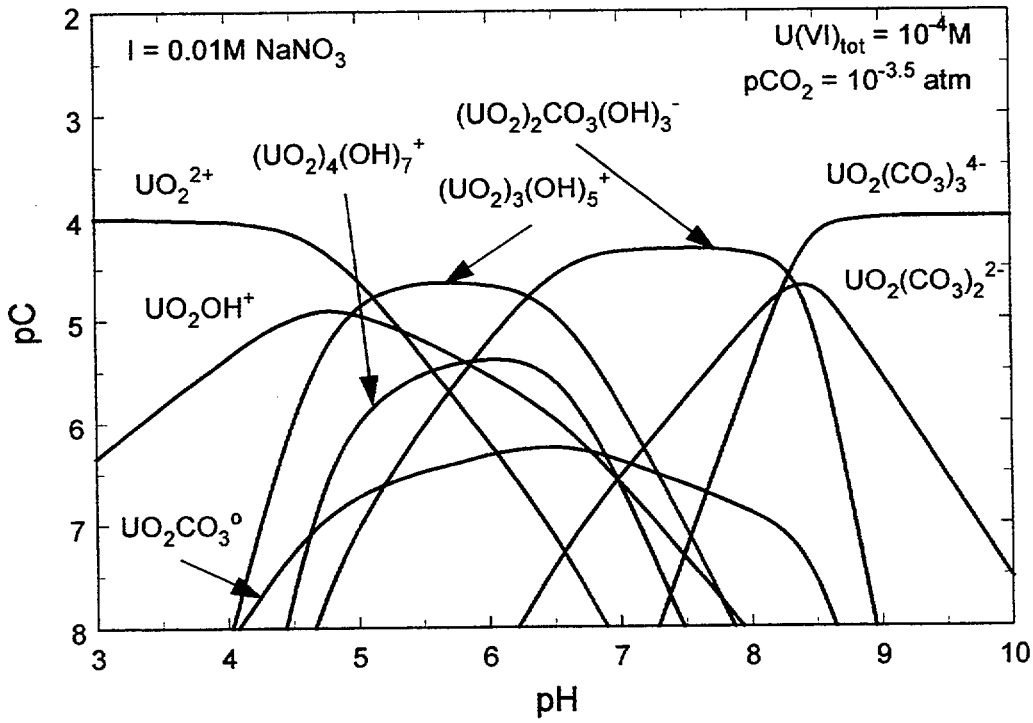

Figure 2-2C. Dissolved speciation of U(VI) as a function of total U(VI) concentration in an open atmosphere equilibrated with a partial pressure of CO_2 of $10^{-3.5}$ atm. Total dissolved U(VI) = 10^{-4}M; precipitation of crystalline U(VI)-hydroxides and -oxides prohibited in the calculation.

Table 2-1. Formation Constants for U(VI) Solution Complexes

Reaction	log ß* (I = 0)[a]
$UO_2^{2+} + H_2O \Leftrightarrow UO_2OH^+ + H^+$	-5.20
$UO_2^{2+} + 2H_2O \Leftrightarrow UO_2(OH)_{2.aq} + 2H^+$	-11.50[b]
$UO_2^{2+} + 3H_2O \Leftrightarrow UO_2(OH)_3^- + 3H^+$	-20.00[c]
$UO_2^{2+} + 4H_2O \Leftrightarrow UO_2(OH)_4^{2-} + 4H^+$	-33.0
$2UO_2^{2+} + H_2O \Leftrightarrow (UO_2)_2OH^{3+} + H^+$	-2.70
$2UO_2^{2+} + 2H_2O \Leftrightarrow (UO_2)_2(OH)_2^{2+} + 2H^+$	-5.62
$3UO_2^{2+} + 4H_2O \Leftrightarrow (UO_2)_3(OH)_4^{2+} + 4H^+$	-11.90
$3UO_2^{2+} + 5H_2O \Leftrightarrow (UO_2)_3(OH)_5^+ + 5H^+$	-15.55
$3UO_2^{2+} + 7H_2O \Leftrightarrow (UO_2)_3(OH)_7^- + 7H^+$	-31.00
$4UO_2^{2+} + 7H_2O \Leftrightarrow (UO_2)_4(OH)_7^+ + 7H^+$	-21.9
$UO_2^{2+} + CO_3^{2-} \Leftrightarrow UO_2CO_{3.aq}$	9.67 [d]
$UO_2^{2+} + 2CO_3^{2-} \Leftrightarrow UO_2(CO_3)_2^{2-}$	16.94
$UO_2^{2+} + 3CO_3^{2-} \Leftrightarrow UO_2(CO_3)_3^{4-}$	21.60
$3UO_2^{2+} + 6CO_3^{2-} \Leftrightarrow (UO_2)_3(CO_3)_6^{6-}$	54.0
$2UO_2^{2+} + CO_3^{2-} + 3H_2O \Leftrightarrow (UO_2)_2CO_3(OH)_3^- + 3H^+$	-0.86
$3UO_2^{2+} + CO_3^{2-} + 3H_2O \Leftrightarrow (UO_2)_3CO_3(OH)_3^+ + 3H^+$	0.66
$11UO_2^{2+} + 6CO_3^{2-} + 12H_2O \Leftrightarrow (UO_2)_{11}(CO_3)_6(OH)_{12}^{2-} + 12H^+$	36.43
$H^+ + CO_3^{2-} \Leftrightarrow HCO_3^-$	10.329
$2H^+ + CO_3^{2-} \Leftrightarrow H_2CO_3^*$	16.683
$CO_{2(g)} + H_2O \Leftrightarrow H_2CO_3^*$	-1.472
$UO_2^{2+} + NO_3^- \Leftrightarrow UO_2NO_3^+$	0.3
$UO_2^{2+} + Cl^- \Leftrightarrow UO_2Cl^+$	0.17
$UO_2^{2+} + 2Cl^- \Leftrightarrow UO_2Cl_{2.aq}$	-1.1
$UO_2^{2+} + SO_4^{2-} \Leftrightarrow UO_2SO_{4.aq}$	3.15
$UO_2^{2+} + 2SO_4^{2-} \Leftrightarrow UO_2(SO_4)_2^{2-}$	4.14
$SO_4^{2-} + H^+ \Leftrightarrow HSO_4^-$	1.98 [d]

$UO_2^{2+} + F^- \Leftrightarrow UO_2F^+$	5.09
$UO_2^{2+} + 2F^- \Leftrightarrow UO_2F_{2,aq}$	8.62
$UO_2^{2+} + 3F^- \Leftrightarrow UO_2F_3^-$	10.90
$UO_2^{2+} + 4F^- \Leftrightarrow UO_2F_4^{2-}$	11.70
$H^+ + F^- \Leftrightarrow HF_{aq}$	3.18 [d]
$H^+ + 2F^- \Leftrightarrow HF_2^-$	3.62 [d]
$UO_2^{2+} + Ac^- \Leftrightarrow UO_2Ac^+$	3.04[e]
$UO_2^{2+} + 2Ac^- \Leftrightarrow UO_2Ac_{2,aq}$	5.54[e]
$UO_2^{2+} + 3Ac^- \Leftrightarrow UO_2Ac_3^-$	6.94[e]
$H^+ + Ac^- \Leftrightarrow HAc$	4.757[e]
$UO_2^{2+} + PO_4^{3-} \Leftrightarrow UO_2PO_4^-$	13.23
$UO_2^{2+} + PO_4^{3-} + H^+ \Leftrightarrow UO_2HPO_{4,aq}$	19.59
$UO_2^{2+} + PO_4^{3-} + 2H^+ \Leftrightarrow UO_2H_2PO_4^+$	22.82
$UO_2^{2+} + PO_4^{3-} + 3H^+ \Leftrightarrow UO_2H_3PO_4^{2+}$	22.46
$UO_2^{2+} + 2PO_4^{3-} + 4H^+ \Leftrightarrow UO_2(H_2PO_4)_{2,aq}$	44.04
$UO_2^{2+} + 2PO_4^{3-} + 5H^+ \Leftrightarrow UO_2(H_2PO_4)(H_3PO_4)^+$	45.05
$PO_4^{3-} + H^+ \Leftrightarrow HPO_4^{2-}$	12.35 [d]
$PO_4^{3-} + 2H^+ \Leftrightarrow H_2PO_4^-$	19.562 [d]
$PO_4^{3-} + 3H^+ \Leftrightarrow H_3PO_{4,ag}$	21.702 [d]
$UO_2^{2+} + SiO_2(OH)_2^{2-} + H^+ \Leftrightarrow UO_2SiO(OH)_3^+$	21.54 [f]
$SiO_2(OH)_2^{2-} + 2H^+ \Leftrightarrow Si(OH)_{4,aq}$	23.14 [d]
$SiO_2(OH)_2^{2-} + H^+ \Leftrightarrow SiO(OH)_3^-$	13.33 [d]
$2SiO_2(OH)_2^{2-} + 2H^+ \Leftrightarrow Si_2O_3(OH)_4^{2-} + H_2O$	27.28 [d]
$2SiO_2(OH)_2^{2-} + 3H^+ \Leftrightarrow Si_2O_2(OH)_5^- + H_2O$	38.18 [d]

a) Values from Grenthe et al. (1992), unless otherwise indicated.
b) Silva (1992)
c) Sandino and Bruno (1992)
d) Silva et al. (1995)
e) Smith and Martell (1989), corrected to I=0 using the Davies equation if necessary.
f) Moll (1997)

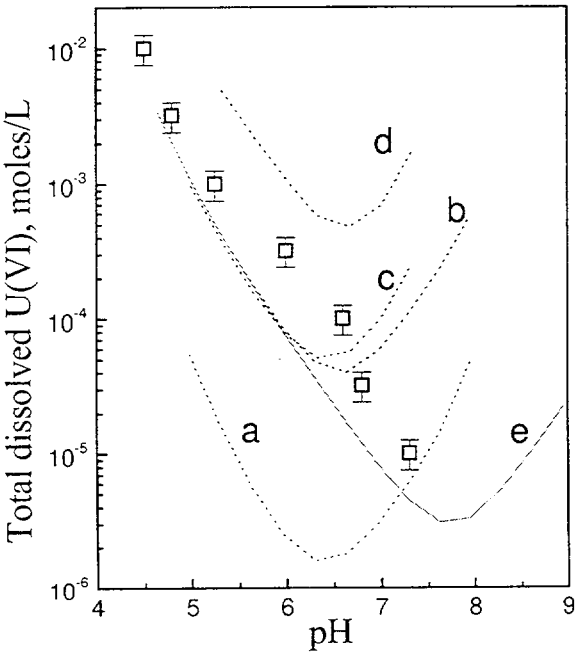

Figure 2-3. Calculations of the solubility of uranyl hydroxide, $UO_2(OH)_2$, at selected values of the solubility constant. For internal consistency, curves c) and d) calculated with the thermodynamic data of Allard et al. (1984), which differs slightly from that of Grenthe et al., (1992). a) log K_{SO} = -23.07, crystalline β-$UO_2(OH)_2$, from Grenthe et al. (1992) and used by Waite et al. (1994b), under air, b) log K_{SO} = -22.43, amorphous uranyl hydroxide, from Tripathi (1983), under air, c) log K_{SO} = -22.4, amorphous uranyl hydroxide, from Allard et al. (1984), under air, d) log K_{SO} = -22.0, amorphous uranyl hydroxide, highest values from Allard et al. (1984), under air, e) log K_{SO} = -22.43, amorphous uranyl hydroxide, from Tripathi (1983), under nitrogen gas.

using the log K_{S0} values of Tripathi (1983) or Allard et al. (1984). The calculated solubility is extremely sensitive to the value of log K_{S0}. While the selected log K_{S0} values appear very similar, even the slightly higher "maximum" value of Allard et al. (1984] raises the solubility by a factor of five (Figure 2-3). Figure 2-3 also shows the solubility of U(VI) in the absence of CO_2, and demonstrates the dramatic effect of carbonate, particularly at high pH values.

The calculated curves in Figure 2-3 can also be compared with experimental studies of the precipitation of uranyl hydroxide. Such studies are rare compared to studies of the solubility of crystalline U(VI) minerals. Brusilovskii (1958) studied the precipitation process by a primitive but direct method in which tubes with various amounts of U(VI) were shaken, periodically tested for pH and precipitation was 'watched for'. The experiments were carried out under nitrogen. While the experimental technique would appear to be fraught with potential errors, the data suggest a much greater U(VI) solubility in precipitation experiments than with a crystalline solid. The data appear consistent with the solubility proposed by Tripathi (1983), with a log K close to –22.43. The results of similar experiments are presented in Section 3.

At low total dissolved U(VI) concentrations ($<10^{-8}$M), aqueous multinuclear species do not comprise a significant fraction of total dissolved U(VI) (Fig. 2-2A). Aqueous speciation of U(VI) in the neutral to alkaline pH range is strongly influenced by the formation of strong carbonate complexes. At 10^{-6}M total dissolved U(VI), the $(UO_2)_2CO_3(OH)_3^-$ species becomes a predominant species in the pH range 6-8, but other multinuclear aqueous species are relatively unimportant (Fig. 2-2B). If it is assumed that the precipitation of β-$UO_2(OH)_2$ is kinetically hindered and the solubility of U(VI) is controlled by an amorphous phase, then other multinuclear species can predominate at higher total dissolved U(VI) concentrations (Fig. 2-2C). Different species predominate at different partial pressures of CO_2 (Waite et al., 1994b).

2.2 Review of U(VI) Adsorption Studies

Qualitative observations of U(VI) adsorption have been reported for a large range of single and complex substrates. For example, Starik et al. (1958) studied the adsorption of trace concentrations of U(VI) to iron oxyhydroxides and found adsorption to be greatest at approximately pH 5. U(VI) adsorption

decreased in the presence of carbonate. Tripathi (1983) and Hsi and Langmuir (1985) found that carbonate played a critical role in the distribution of U(VI) between the surfaces of iron oxide phases and solution. They observed that at higher carbonate concentrations, when the $UO_2(CO_3)_2^{2-}$ and $UO_2(CO_3)_3^{4-}$ species dominate in solution (Fig. 2-2), there was a sharp decrease in the extent of U(VI) adsorption with a resultant high-pH or "desorption" edge. Tripathi (1983) found that very high U(VI) adsorption was observed under conditions where $(UO_2)_2CO_3(OH)_3^-$ was the predominant U(VI) aqueous species.

Similar results were found by Ho and coworkers for U(VI) adsorption on hematite (Ho and Doern, 1985; Ho and Miller, 1985) and magnetite (Sagert el al., 1989). These authors were interested in the identity of the adsorbed uranyl species, particularly in the presence of carbonate. Based on the electrophoretic mobility of particles with adsorbed U(VI), Ho and coauthors concluded, as did Tripathi (1983), that $(UO_2)_2CO_3(OH)_3^-$ was an important adsorbing species when carbonate is present. Ho and Doern (1985) suggested that $(UO_2)_3(OH)_5^+$ was the major U(VI) adsorbing species in the absence of carbonate.

A number of authors have applied the surface complexation approach to modelling the partitioning of U(VI) between solid and solution phases over the last ten years. The basic modelling approach has been similar in each case with minor differences in the mode of description of the electrical double layer and, more importantly, differences in the proposed surface complexes. For example, Hsi and Langmuir (1985) and Turner et al. (1996) used the triple layer model of Davis et al. (1978) to describe their experimental results as a function of pH. In each case, it was assumed that the dominant aqueous phase species, UO_2OH^+ and $(UO_2)_3(OH)_5^+$, were adsorbed in the absence of carbonate. Good agreement between the experimental results and model simulations were achieved using the following surface complexation reactions:

$$\equiv FeOH + UO_2^{2+} + H_2O \Leftrightarrow \equiv FeO^-\text{--}UO_2OH^+ + 2H^+ \quad (2\text{-}1)$$

$$\equiv FeOH + 3UO_2^{2+} + 5H_2O \Leftrightarrow \equiv FeO^-\text{--}(UO_2)_3(OH)_5^+ + 6H^+ \quad (2\text{-}2)$$

where $\equiv FeOH$ represents a hydroxyl functional group on the surface and $\equiv FeO^-\text{--}UO_2OH^+$ represents a surface complex with electrical charge separation, consistent with the model of Davis et al. (1978). The left-hand side of Eqs. 2-1 and 2-2 are written in terms of system components rather than the predominant aqueous species (Dzombak and Morel, 1990).

In the presence of carbonate, Hsi and Langmuir (1985) found it necessary to assume the formation of strong ternary uranyl-carbonato complexes at the surface in order to fit their adsorption data. These authors assumed that the dominant solution phase species was the dominant adsorbing species and they included two new surface reactions in their model (writing the left-hand side of the equations in terms of components again):

$$\equiv FeOH + UO_2^{2+} + 2CO_3^{2-} + H^+ \Leftrightarrow \equiv FeOH_2^+\text{--}UO_2(CO_3)_2^{2-} \quad (2\text{-}3)$$

$$\equiv FeOH + UO_2^{2+} + 3CO_3^{2-} + H^+ \Leftrightarrow \equiv FeOH_2^+\text{--}UO_2(CO_3)_3^{4-} \quad (2\text{-}4)$$

By considering these additional surface species, Hsi and Langmuir (1985) were able to obtain excellent agreement between model simulations and U(VI) adsorption data on goethite for a single total inorganic carbon content ($C_T = 10^{-2}$M). However, the model simulations were less successful in describing adsorption data for a second data set with $C_T = 10^{-3}$M.

Payne and Waite (1991) applied the model of Hsi and Langmuir (1985), including the same reaction set and stability constants, to describe U(VI) adsorption on the amorphous iron oxide component of a weathered schist. These authors found poor agreement between model simulations and their experimental data. At the total carbonate concentrations used in their study

($C_T = 2 \times 10^{-3}$M), the $UO_2CO_3^0$ aqueous species was important in the pH range 4.8-6.4, and the fit of the model simulations to the data were greatly improved if it was assumed that a $\equiv FeO^-$-$UO_2CO_3^0$ surface complex formed.

As summarized above, many investigators have assumed that the predominant aqueous species are involved in surface complex formation of U(VI) (e.g., Hsi and Langmuir, 1985; Turner et al., 1996). Because U(VI) aqueous speciation is complex, this has led to a wide range of proposed surface species, and a unified approach to surface complexation modeling of U(VI) has been lacking. Major differences among the modeling approaches included: 1) the most appropriate choice of surface species at low pH, where complexation by carbonate is unimportant and 2) the number, type, and presumed importance of U(VI)-carbonate-surface ternary complexes.

The model of Waite et al. (1994b), however, was far simpler and was based on the coordination environment of U(VI) at the surface of iron oxides rather than the predominant aqueous species. Based on the results of uranium Extended X-ray Absorption Fine Structure (EXAFS) spectroscopy, these authors concluded that the uranyl cation formed bidentate complexes with the iron oxide surface in the weakly acidic pH range by the following reaction:

$$(\equiv Fe(OH)_2) + UO_2^{2+} + H_2O \Leftrightarrow (\equiv FeO_2)UO_2^{\circ} + 2H^+ \qquad (2\text{-}5)$$

The EXAFS results suggested that multinuclear uranium species were not present at the surface at pH<5.5, whereas both Hsi and Langmuir (1985) and Turner et al. (1996) assumed these species formed at the surface. Unfortunately, these authors did not test their model by systematic variation of the total U(VI) concentration in experiments, because Waite et al. (1994b) demonstrated that this approach is quite conclusive. This can be best understood by analogy with aqueous speciation as a function of total U(VI) concentration. As the total U(VI) concentration increases, multinuclear aqueous species become more significant for a given pH value (compare Fig. 2-2A with 2-2C). This occurs because the exponent of UO_2^{2+} in the mass law for species formation is greater than one. The situation is mathematically analogous if multinuclear species form at the surface (Eq. 2-2). In this case, the fractional uptake of U(VI) (or % adsorbed) should increase for a given pH value as the total U(VI) concentration increases. However, the results of Waite et al. (1994b) clearly showed the opposite trend, that the fractional uptake of U(VI) decreases at a given pH as the total U(VI) concentration increases. Similar results for U(VI) adsorption on quartz and imogolite are given in Sections 5 and 6 of this report. Had Turner et al. (1996) collected data as a function of U(VI) concentration, it is likely that they would have discovered that their model with a multinuclear surface species would not have described their data well.

In addition, Waite et al. (1994b) showed that U(VI) adsorption data for a wide range of chemical conditions could be modeled with only the bidentate surface species and one ternary uranyl-carbonato complex. The complex proposed was not the predominant aqueous species but rather a species with a single carbonate ligand. With these two species, the model could describe U(VI) adsorption on ferrihydrite as a function of pH, U(VI) concentration, and the partial pressure of carbon dioxide. Spectroscopic evidence for the existence of this species is presented in Section 3 of this report.

3 SPECTROSCOPIC CHARACTERIZATION OF U(VI)-CARBONATO SURFACE COMPLEXES ON HEMATITE AND FERRIHYDRITE

3.1 Background and Objectives

Waite et al. (1994b) postulated the existence of U(VI)-carbonato ternary complexes having composition $Fe<^{O}_{O}>UO_2CO_3^{2-}$ in order to model U(VI) adsorption on ferrihydrite. In the absence of such a species, *i.e.*, using a model that included only binary U(VI)-ferrihydrite surface complexes, U(VI) uptake on ferrihydrite was underpredicted between pH 7 and 9. Furthermore, the degree of underprediction of U(VI) adsorption in this pH range increased with P_{CO2}. Inclusion of the ternary complex in the surface complexation model made it possible to describe U(VI) adsorption at high pH (Waite et al., 1994b).

The existence of U(VI)-carbonato-Fe-oxide ternary complexes and their roles in controlling U(VI) adsorption and reactive transport in groundwaters are of considerable importance. Groundwaters can vary widely in the concentration of dissolved carbonate, which can profoundly affect the formation of U(VI)-carbonato ternary complexes. It will be shown in this section that such ternary surface complexes do occur and are important surface species on hematite and ferrihydrite surfaces in carbonate-bearing waters. Adsorption and reactive transport models which do not account for the existence of U(VI)-carbonato ternary complexes, or which use incorrect surface complexation reaction stoichiometries, may give inaccurate predictions of U(VI) mobility. Clearly, definition of the compositions and adsorption reaction stoichiometries for U(VI)-carbonato ternary complexes is important to accurate predictive modeling of U(VI) fate and transport in natural waters.

Indirect evidence for the existence of U(VI)-carbonato-Fe-oxide ternary complexes has been described by other investigators. Hsi and Langmuir (1985) were able to describe U(VI) adsorption on amorphous and crystalline Fe-(oxyhydr-)oxides in carbonate-bearing solutions using ternary U(VI)-carbonate complexes and a site-binding surface complexation model. Ho and Miller (1986) observed that hematite particles, which were positively charged in near-(and sub-)neutral pH carbonate-bearing solutions (*i.e.*, at pH < 7.5), acquired net negative charges following adsorption of U(VI). They attributed this charge reversal to the presence of negatively charged U(VI)-carbonato complexes at the hematite surface. However, no direct evidence for the existence of U(VI)-carbonato-Fe-oxide ternary complexes has been presented, to our knowledge. Conclusive demonstration of such complexes requires their direct observation under *in-situ* conditions (*i.e.*, in the presence of water and at ambient pressures and temperatures) using spectroscopic techniques or other techniques capable of directly probing the surface species.

The objectives of this phase of the project were to use FT-IR (Fourier Transform infrared) and EXAFS (extended X-ray absorption fine structure) spectroscopies to probe the existence of U(VI)-carbonato-Fe-oxide ternary complexes and to define their structures and compositions (if they exist). FT-IR and EXAFS spectroscopies are complementary techniques that are ideal for this study. Both techniques directly probe molecular species and can be used to obtain qualitative and quantitative information on the structures and compositions of adion species on Fe oxides. FT-IR and EXAFS spectroscopic measurements of adsorbates on oxide surfaces can be made *in-situ* at metal ion concentrations relevant to those found in the field. FT-IR spectroscopy primarily probes molecular vibrations and thus provides information about organic species and oxoanions. In contrast, EXAFS spectroscopy provides element-specific short-range structural and chemical information for metal ion coordination environments, including bond distances, coordination numbers, and oxidation states.

For this study, U(VI) adion complexes were studied on hematite and ferrihydrite. Both minerals occur in natural surface waters and aquifers, have high sorptive capacities for U(VI), and are believed to be primary sources and sinks controlling U(VI) reactive transport (Hobart, 1990; Krauskopf, 1991, and references therein). U(VI) adsorption on ferrihydrite was studied previously (Waite et al., 1994b), and the current study was intended to provide further constraints on U(VI)-carbonato surface species for the sake of reactive transport modeling. However, ferrihydrite, an amorphous high-surface-area ferric oxide, is chemically unstable and slowly crystallizes as goethite or hematite over a time scale of weeks to months in the laboratory. The reactivity of ferrihydrite presents several practical difficulties for the IR spectroscopist. For example, as the solid ages, the intensities of goethite IR bands increase at significant rates (0.19% mass conversion/week). These goethite bands obscure some of the UO_2 and CO_3 adsorbate IR peaks of interest to this study. Furthermore, the goethite peaks are difficult to subtract out of sample spectra since their intensities dynamically evolve over time and from sample to sample. Another problem arises from the lack of crystallinity of ferrihydrite, which gives rise to a wide variety of surface sites and adsorbate species and can lead to appreciable broadening of the peaks of IR species. In order to avoid some of these difficulties, spectra of U(VI) adsorbed to hematite were also measured. Hematite has no sharp or intense IR absorptions in the energy range of the most important adsorbate species peaks (800 - 2000 cm^{-1}). In addition, hematite is a crystalline solid, and thus has a more limited range of surface binding sites. Hence, spectra of U(VI) adsorbed on hematite are less complex than spectra of U(VI)/ferrihydrite, and the hematite results can be used to constrain interpretations of the ferrihydrite spectra.

3.2 Materials and Methods

3.2.1 HEMATITE AND FERRIHYDRITE SYNTHESIS AND CHARACTERIZATION

Hematite powders used in these experiments were synthesized from $Fe(ClO_4)_3$ following the method of Matijevic and Scheiner (1978) as described in Bargar et al. (1997b). The surface area of the dried powder was 49 m^2/g. XPS analyses of the powders showed the surfaces to be clean, having only Fe, O, and adventitious carbon. Powder XRD showed it to be crystalline α-Fe_2O_3. Detailed XRD scans from 19.5° to 23° 2θ (60 sec/point, 0.1° steps) were collected in order to check for the goethite (110) reflection, which would indicate the presence of any goethite. No evidence of this peak was observed. Diffuse reflectance FT-IR spectra of the hematite surfaces were recorded, and they showed no evidence of any goethite-specific peaks.

Ferrihydrite was synthesized from $Fe(NO_3)_3$ solutions, according to the following procedure: 1 L HDPE bottles and Teflon magnetic stirrers were washed in a detergent bath, rinsed in deionized water, soaked in 0.1 N HCl for at least 8 hours, and rinsed six times in Milli-Q water. 5 mM $Fe(NO_3)_3$ solutions were made by dissolving Baker Analyzed $Fe(NO_3)_3 \cdot 9H_2O$ reagent in Milli-Q water, which resulted in a solution at approximately pH 2.2. The solutions then were adjusted to pH 7 over approximately three- to four-hour time periods by addition of 100 μL aliquots of 1.0, 0.1, or 0.01 N NaOH solutions. The onset of precipitation typically began at about pH 2.5, as judged by an increase in the turbidity of the solutions. Above pH 4, the buffering capacity of the solutions decreased sufficiently to require the use of 0.1 and 0.01 N NaOH solutions for pH adjustment. After adjustment to pH 7, ferrihydrite slurries were stirred for 3-4 hours. The resulting ferrihydrite was cleaned by the following procedure: the solid was allowed to settle, about 95% of the supernatant was aspirated off, Milli-Q water was added to the bottle, and the bottle was shaken by hand to resuspend the ferrihydrite. This process was repeated 7-10 times to remove NO_3^{3-} from the ferrihydrite surface. After the final cleaning iteration, bottles were refilled with Milli-Q water to obtain solid:liquid ratios of approximately 5 g/L. Ferrihydrite stock suspensions were stored for less than 2 weeks before use in experiments.

FT-IR spectra of the cleaned ferrihydrite showed no evidence of the intense NO_3^{3-} ν_3 peak, which occurs at 1384 cm^{-1} and has a detection limit of approximately $1x10^{-7}$ moles/m^2. Each 1 L synthesis yielded 0.42 g of ferrihydrite (with a nominal composition of $Fe_2O_3 \cdot 3.37\ H_2O$; FW 220.26 g/mol (Waychunas et al., 1996)). For the sake of comparing the U(VI) adsorption densities on ferrihydrite to hematite samples, we assume that the ferrihydrite surface area is 600 m^2/g.

3.2.2 PREPARATION OF SAMPLES

Within this section $[U]_T$ is defined as the total concentration (molarity) of all U(VI) species, dissolved and adsorbed, in the system, and $[U]_{eq}$ is defined as the sum of all dissolved U(VI) species (molarity) in solution at the final pH of the sample equilibration and excludes adsorbed U(VI) species. All solutions were prepared from Milli-Q water. Stock suspensions of hematite in Milli-Q water were prepared in polycarbonate centrifuge tubes and were washed to remove trace ClO_4^- by suspending the sediment using ultrasound for 15 - 30 minutes and then centrifuging the slurry to separate the solid and liquid fractions. The supernatants were decanted and the tubes refilled with Milli-Q water. Five or fewer iterations of this procedure were required to remove ClO_4^-, as judged by the disappearance of the ClO_4^- ν_3 peak from FT-IR spectra, for which the detection limit is approximately $1x10^{-7}$ moles/m^2. The sediment was resuspended using ultrasound following the final cleaning step.

For hematite adsorption samples, aliquots of hematite stock suspensions were added to 500 mL HDPE bottles. Milli-Q water was added to bring the volume to approximately 500 mL. Solid NaCl was weighed into a few samples in which ionic strength control was desired. For ferrihydrite samples, 10 mL aliquots of 5 g/L ferrihydrite stock suspensions were added to 1 L HDPE bottles, followed by the addition 1 L of Milli-Q water to each bottle. For samples with ionic strength control, NaCl was added to the bottles at this stage. Samples for which only CO_3 adsorption was to be studied (hereafter referred to as CO_3/hematite or CO_3/ferrihydrite samples) were then adjusted to their final pH values by addition of 0.1-0.01 N HCl and/or 0.1 M $NaHCO_3$. At all times, the samples were stirred vigorously with Teflon-coated magnetic stir bars, and water-saturated air was bubbled through the samples in order to maintain equilibrium with atmospheric CO_2. U(VI) uptake was achieved by the following procedure, which were designed to avoid precipitation of U(VI) solids: Prior to addition of U(VI), samples were adjusted to pH values where U(VI) solubility is greater than 10^{-4} M, *i.e.*, pH < 4 or > pH 9 (depending on which of these values was closest to the desired final pH desired for the sample), and were maintained at this pH until they had reached equilibrium with respect to atmospheric CO_2, as judged by the pH stability of the suspensions. Sample bottles were then wrapped with Al foil to prevent photolytically catalyzed redox reactions at hematite and ferrihydrite surfaces. U(VI) was added dropwise as aliquots of an acidic 10 mM $UO_2(NO_3)_2$ solution while the samples were vigorously stirred. For all hematite samples, the maximum concentration of U(VI) in the system $[U]_T \leq 8.2$ μM. For U(VI)/ferrihydrite FT-IR samples, $[U]_T \leq 12.5$ μM, and for U(VI)/ferrihydrite EXAFS samples, $[U]_T \leq 91.6$ μM. After addition of U(VI), the samples were adjusted to their final pHs and thus maintained by addition of 20 - 50 μL aliquots 0.1 - 0.01 N HCl and/or 0.1 M $NaHCO_3$ until no drifts in pH were observed over several-hour time intervals in the absence of acid/base additions. Samples were stirred and bubbled with water-saturated air at all times to maintain equilibrium with atmospheric CO_2. Following these steps, samples were gently agitated in a shaker bath for 15 - 24 hrs to ensure that fast reactions and other short-term kinetic effects had gone to completion. No significant drifts in pH occurred during this step.

Samples were centrifuged at approximately 40,000 x g centrifugal force for 20 minutes (hematite samples) and approximately 43,100 x g centrifugal force for 11 to 15 minutes (ferrihydrite samples). After centrifugation, 10 mL aliquots of supernatants were taken from the

samples for ICP-MS analysis of $[U]_{eq}$. Results are given in Table 3-1. Typically, ≥ 99.5 % of the supernatant was removed (determined by change in mass). Since adsorption of U(VI) varied between 33% and 99% of U_T, (Table 3-1), the amount of surface-bound U(VI) was in excess of dissolved U(VI) in the remnant interparticle solution in the centrifuged-and-decanted samples by a factor of ≥ 100. Thus, the IR signal from nonadsorbed species can be neglected. The same statement applies to EXAFS samples.

The solubility of U(VI) precipitates was measured under conditions similar to those of the adsorption samples (including aging time), but in the absence of any Fe oxide powders, in order to help ascertain if precipitation of U(VI) solids could have occurred in the adsorption samples. 500 mL of Milli-Q water were added to a beaker, equilibrated with air by bubbling with water-saturated air, and then adjusted to the same starting pH values as the adsorption samples (pH < 4 or > 9). 0.5 mM U(VI) was added dropwise to the pH-adjusted solutions, which were vigorously stirred. The solutions were then adjusted to the final pH and stirred for an additional 24 hours. Following this period, the samples were filtered through a 0.05 μm cellulose nitrate filter; a sample was taken from the filtrate to measure $[U]_T$, and in the case of the pH 6.5 sample, the filter paper was saved for EXAFS analysis. The filtrates of all three solubility samples (pH 5.5, pH 6.5, and pH 7.5) were counted with a scintillation counter. Results are presented in Figure 3-1, where they are compared to adsorption samples.

3.2.3 FT-IR MEASUREMENTS AND ANALYSIS

In this section, we present results of DRIFT (diffuse-reflectance infrared FT) spectroscopic measurements of adsorption samples. The DRIFT technique has several key advantages over other FT-IR methods. It permits measurement of adsorption samples having substantially lower adsorbate and solute metal ion concentrations than any other IR measurement technique, such as the ATR (attenuated total reflection) method, which can be used to measure IR spectra of samples in contact with bulk water. All DRIFT sample measurements reported in this study are comprised of identical ratios of Fe oxide diluted into KBr matrix (detailed below). Hence, all samples have the same optical densities and IR path lengths. When plotted in Kubekla-Munk (K-M) units (as opposed to absorption or transmission units), the intensities of weak peaks, such as those of adsorbate species, are directly proportional to the absorber concentration (infinitely dilute approximation) (Coleman, 1993). Thus, DRIFT measurements can be used to measure adsorption density and facilitate direct comparison of spectra from different samples. In contrast, the intensities of ATR peaks from wet samples are not proportional to adsorption density because the interparticle distances in Fe oxide colloidal suspensions, and hence the optical densities and path lengths of IR light in the samples, are significantly affected by pH and ionic strength. Thus, Beer's law does not apply to ATR absorption peak intensities. Furthermore, changes in the interparticle distances in colloidal suspensions can affect the shapes of spectral baselines and the positions and shapes of H-O-H bending vibrations of interparticle water, making it difficult to accurately define ATR peak shapes at low adsorbate densities. These problems generally do not occur with DRIFT samples because bulk water is not present.

DRIFT samples are prepared in the following manner: A small amount (approximately 10 to 20 mg of Fe oxide) of the wet pastes that remained following centrifugation and decanting of adsorption samples were thinly spread onto filter membranes (Sartorius 0.05 μm cellulose nitrate membrane filter), which were placed in a dry-air-filled dessicator for approximately 25 min. Thus, a large fraction of the water remaining in the samples was removed by capillary action of the filter. Evaporative desiccation of the samples would be undesirable, since it could result in substantial pH and ionic strength changes and precipitation of salts in the samples. To test if our water removal procedure was causing such evaporative desiccation,

Table 3-1. Solution conditions of U(VI)-carbonato-Fe-oxide FT-IR and EXAFS samples. $[U]_T$ is defined as the sum of all aqueous and adsorbed species (molarity). $[U]_{eq}$ is the sum of all aqueous U(VI) species remaining in solution after equilibration at the final pH (molarity). N/A indicates that data are not available. Typical error on $[U]_{eq}$ is 2%.

Final pH	Electrolyte	Adsorption Density (μmoles/m^2)	$[U]_T$ (μM)	$[U]_{eq}$ (μM)	Solid: Liquid (g/L)	Ionic Strength	$[U]_T$:$[Fe\text{-}OH_{sfc}]_T$	$[U]_T$:$[CO3]_T$	Method
U(VI)/Hematite samples									
4.51	none	0.27	4.0	2.670	0.10	40 μM	0.21	0.33	DRIFT
5.00	none	0.46	4.0	1.710	0.10	53 μM	0.21	0.33	DRIFT
5.79	none	0.72	4.0	0.440	0.10	52 μM	0.21	0.304	DRIFT
7.99	none	0.63	4.0	0.910	0.10	1.2 mM	0.21	0.008	DRIFT
8.49	none	0.42	4.0	1.910	0.10	1.7 mM	0.21	0.003	DRIFT
5.00	20 mM NaCl	0.28	4.0	2.610	0.10	0.02 M	0.21	0.381	DRIFT
4.99	0.1 M NaCl	0.30	4.0	2.500	0.10	0.1 M	0.21	0.381	DRIFT
8.00	0.1 M NaCl	N/A	4.0	N/A	0.10	0.1 M	0.21	0.008	DRIFT
5.75	0.1 M $NaNO_3$	0.56	5.6	0.047	0.20	0.1 M	0.15	0.38	EXAFS
6.50	0.1 M $NaNO_3$	0.57	5.6	0.001	0.20	0.1 M	0.15	0.20	EXAFS
7.61	0.1 M $NaNO_3$	0.57	5.5	0.001	0.20	0.1 M	0.15	0.033	EXAFS
U(VI)/Ferrihydrite samples									
4.53	none	0.42	12.5	0.002	0.05	130 μM	0.11	1.04	DRIFT
5.00	none	0.12	12.5	8.90	0.05	110 μM	0.11	1.04	DRIFT
8.00	none	0.38	12.5	1.15	0.05	1.2 mM	0.11	0.02	DRIFT
8.49	none	0.22	12.3	5.83	0.05	4.9 mM	0.11	0.008	DRIFT
4.50	0.1 M NaCl	0.05	12.5	10.91	0.05	0.1 M	0.11	1.04	DRIFT
5.00	0.1 M NaCl	0.14	12.4	8.14	0.05	0.1 M	0.11	1.04	DRIFT
7.99	0.1 M NaCl	0.29	12.3	3.67	0.05	0.1 M	0.11	0.02	DRIFT
8.50	0.1 M NaCl	0.10	12.3	9.44	0.05	0.1 M	0.11	0.008	DRIFT
6.02	0.1 M $NaNO_3$	0.45	29.6	2.78	0.1	0.1 M	0.13	1.74	EXAFS
6.57	0.1 M $NaNO_3$	1.49	89.7	2.16	0.1	0.1 M	0.39	3.20	EXAFS
6.74	0.1 M $NaNO_3$	0.50	31.2	1.45	0.1	0.1 M	0.14	0.79	EXAFS
7.63	0.1 M $NaNO_3$	0.52	32.8	1.83	0.1	0.1 M	0.14	0.15	EXAFS

several samples were prepared in nitrate-bearing solutions. Below pH 5, nitrate is adsorbed, as indicated by the presence of the strong N-O stretching frequency at 1384 cm^{-1}. Above pH 5, carbonate competitively displaces nitrate from the oxide surfaces, as indicated by the absence of the nitrate absorption peak. The latter result also indicates that evaporative desiccation of the samples did not occur to a significant extent, since otherwise, strong nitrate peaks from precipitated salts should have been observed (such nitrate salt-containing samples can be easily prepared by using an oven to dry the samples instead of a membrane filter). 10 mg of the resulting sample were gently mixed with 0.5 g KBr in an agate mortar and loaded into sample holders for FT-IR analysis. Although the water content of the samples was low enough to allow mixing with KBr, a substantial amount of water remained on the oxide surfaces, as indicated by the presence of water IR bands in the sample spectra.

DRIFT spectra were collected using a Nicolet Magna-IR 750 Series II spectrometer equipped with a diffuse reflectance sample holder from Harrick Scientific Corporation. The sample compartment was continuously purged with dried air which had been scrubbed of CO_2 gas at ambient temperature and pressure, and intensity data were collected using a DTGS detector at an

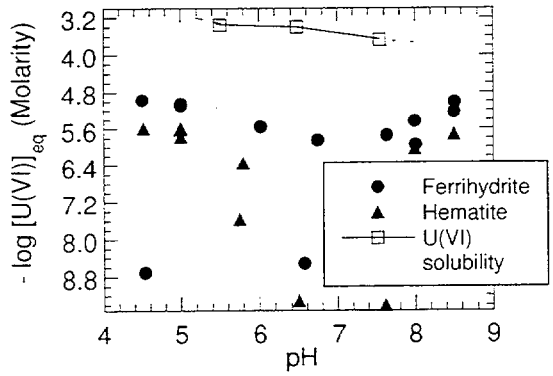

Figure 3-1. Comparison of adsorption sample data points to the solubility of U(VI) precipitates that occur in homogeneous solution over the time scale of adsorption sample preparation (see section 3.2.2). Filled circles and triangles give the concentration of U(VI) in solution after adsorption on ferrihydrite and hematite. The lines connecting the precipitate solubility data points are provided to help the reader define the general shape of the solubility curve.

energy resolution of 4 cm^{-1}. Typically, 4000 scans were collected and averaged for each sample. Spectra were converted to K-M units for analysis. In order to isolate the spectral features corresponding to adsorbed carbonate and uranyl complexes, the spectra of clean hematite or ferrihydrite stock suspensions were subtracted from the sample spectra in K-M units. To clean the ferrihydrite and hematite suspensions, they were adjusted to pH 3.5 and sparged with humidified N_2 for several hours. The final preparation steps for these samples (dessicating and mixing with KBr) were performed in an N_2-purged glove bag to avoid CO_2 adsorption. They were then quickly transferred (<30 sec) through air into the spectrometer. The low pH (3.5) of the sample preparation dramatically reduces readsorption of CO_3 species during transfer through air. Spectra of the cleaned solids exhibit only weak pH dependence over the spectral range of interest to this study (1100 - 1800 cm^{-1}). Any significant pH dependent changes in the Fe oxide spectra that did occur were taken into account when fitting the spectra of the CO_3-only/Fe-oxide samples, which were collected in tandem with each U(VI)-bearing Fe-oxide sample (described below). The subtraction factor was typically in the range 0.90 - 1.1.

As described below, some experiments required spectral measurement using the ATR technique. ATR spectra were collected using a Spectra Tech AMTIR ARK trough plate. Prior to analysis, each ATR sample (hematite or ferrihydrite reacted with carbonate- and /or U(VI)-bearing solutions following the procedures described above) was centrifuged, and the spectrum of its supernatant (about 5 mL) was recorded. During this period, the centrifuged paste was maintained in contact with the remainder of its supernatant. The ATR cell was then cleaned, and the centrifuged wet paste was spread evenly over the ATR cell to a depth of about 1 mm. Several mL of supernatant were placed over top of the paste to ensure it remained wet during data acquisition, and a volatile liquid cover was set in place to prevent evaporation of the supernatant. A DTGS detector (4 cm^{-1} resolution) was used to record 4000 scans per sample. Supernatant spectra were subtracted from the spectra of pastes to remove bulk water peaks and any detectable solution species peaks (typically, solute species are so dilute they cannot be detected in the supernatant spectrum) from the latter spectra. Spectra of clean hematite or ferrihydrite stock suspensions were also subtracted from the samples.

3.2.4 EXAFS DATA COLLECTION AND ANALYSIS

EXAFS samples were prepared in the following manner: Following reaction with uranyl solutions identical to that described above, samples were centrifuged and supernatants were decanted. The remaining wet pastes were loaded into Teflon sample holders with Mylar windows for EXAFS analysis. These were wrapped with moistened tissues to prevent their desiccation, and were placed in zip-lock bags for transport to the Stanford Synchrotron Radiation Laboratory (SSRL). Spectra were collected within 3 days of sample preparation. Fluorescence-yield U L_{III}-edge EXAFS data were collected at room temperature at SSRL at beamline 6-2. A silicon (111) double-crystal

monochromator crystal was used to tune the incident x-ray beam to the desired energies. Energy resolution was approximately 10 eV (HWHM). The X-rays were reflected off a Pt-coated silica mirror located upstream of the monochromator in order to reject high-energy X-rays that could be transmitted through the monochromator crystal at harmonic diffraction conditions. A set of Ta slits located in the experimental hutch was used to define a 2 mm vertical beam dimension. 2 mm vertical x 20 mm horizontal slits were used before the monochromator. A Sr 6-μx filter was used to reject elastic scattering off the samples, and four to five thicknesses of Reynolds aluminum foil were used to reject Fe-K_{ay} flourescence from the samples.

EXAFS spectra from samples were quantitatively analyzed using the EXAFSPAK software (George, 1993) following the procedure described in Bargar et al. (1997a). In all cases presented here, only one shell of backscattering atoms was fit to the raw data for each characteristic frequency present in the Fourier transforms. In no cases did the number of parameters that were varied during fitting exceed the total number allowed to vary, according to $N_{free} = 2\Delta k \Delta R/\pi$, where N_{free} is the number of degrees of freedom, Δk is the range of k-space being fit, and ΔR is the width of the characteristic frequency in the FT (Teo, 1986).

Backscattering phase and amplitude functions required for fitting of spectra were obtained from FEFF 6 calculations (Rehr and Albers, 1990; Rehr et al., 1991; Rehr et al., 1992) following the procedures of Thompson et al. (1997). They showed that use of FEFF-calculated parameters in fits of EXAFS data provide 1st shell U-O and 2nd shell U-U bond lengths accurate to ± .03 Å. U-C distances were accurate to about .08 Å. To assess the accuracies of EXAFS-determined coordination numbers (CNs), we fit EXAFS spectra for andersonite, schoepite, rutherfordine, and uranyl nitrate and compared them to their XRD structures. Accordingly, the accuracies for CNs are U-O: ± 30% (assuming that σ^2 is allowed to vary), U-U: ± 30% (σ^2 fixed at 0.01 to reduce degrees of freedom).

3.3 Results

Adsorption experiments were designed so that $[U]_T$ would be less than the solubility of schoepite, which should be the most insoluble U(VI) solid phase in these systems, at the final pH values of the samples. The minimum solubility of schoepite occurs at approximately pH 6.2, where $[U]_T > 2$ μM, based upon the thermodynamic constants used in this report (cf. Table 2-1 and Fig. 2-1). In addition, it was necessary to achieve adsorption densities of at least 0.25 to 0.5 μmoles/m^2 in order to obtain usable FT-IR and EXAFS spectra. Accordingly, the molecular speciation of U(VI) adsorbed on hematite and ferrihydrite was studied at pH 4.5 - 8.5 at U_T concentrations of 4 - 89.7 μM and at solid:liquid ratios of approximately 0.05 to 0.2 g/L (Table 3-1). DRIFT samples were studied with no added background electrolyte and in 0.1 M NaCl in order to investigate the effects of ionic strength. Nitrate and perchlorate were not used in FT-IR measurements because these anions have strong IR absorption peaks, which would obscure part of the data range of interest in the present study. $NaNO_3$ (0.1M) was used for EXAFS measurements in order to have results as directly comparable to those of Waite et al. (1994b) as possible.

3.3.1 UPTAKE AND SOLUBILITY OF U(VI)

Solubility data points for U(VI) in the absence of hematite and ferrihydrite under the pH and P_{CO2} conditions of adsorption experiments are compared with adsorption sample data points in Figure 3-1. All adsorption samples had final concentrations of total dissolved uranium, $[U]_{eq}$, below the solubility of the U(VI) precipitates, which implies that such U(VI) solid precipitates did not occur in the adsorption samples. This conclusion is reinforced by EXAFS spectra from the adsorption samples, which contain no evidence for the presence of U(VI) precipitates.

3.3.2 EFFECT OF FT-IR DRIFT TECHNIQUE ON ADSORBATE SPECIATION

The main peaks of interest are the ν_3 asymmetric ($\geq$ 1475 cm^{-1}) and symmetric ($\leq$ 1360 cm^{-1}) C-O stretching vibrations of the carbonate group (Nakamoto, 1986). We refer to both frequencies, which occur at different energies in the adsorption sample spectra, as ν_3 vibrations because they arise from splitting of the doubly-degenerate ν_3 vibration of the free CO_3^{2-}(aq) anion (D_{3h} point symmetry). This doubly-degenerate frequency can split into two peaks when the symmetry of the carbonate group drops to C_2, C_s or C_1 due to the formation of inner-sphere bonds to metal ions and/or protons. The CO_3 ν_3 peaks occur at different locations in DRIFT and ATR sample spectra. For example, in hematite and ferrihydrite DRIFT samples, the asymmetric CO_3 ν_3 occurs at 1545 to 1515 cm^{-1}, whereas in ATR measurements this peak lies between 1515 and 1502 cm^{-1}. In order to determine the source of these shifts, we measured ATR spectra of CO_3 adsorbate species on hematite as a function of KBr electrolyte concentration (0 to 4.4 M) and water content. The results are shown in Figure 3-2. As shown in Figure 3.2a, the spectrum measured from a adsorption sample prepared in saturated (approximately 4.4 M) KBr electrolyte was similar to that prepared with no KBr (or any other ionic strength control). Based on this comparison, we conclude that the presence of KBr (matrix) in the DRIFT samples cannot account for the DRIFT CO_3 peak shifts.

Ferrihydrite contains structural water and has an open, water-containing skeletal structure that yields a large surface area (600 m^2/g) (Waychunas et al., 1996; Waychunas et al., 1993). Hematite has one-tenth this surface area and is anhydrous. Hence, there should be more structural and interparticle water remaining in the ferrihydrite DRIFT samples than in the hematite samples. This conclusion is confirmed by the H-O-H water bending vibration at about 1660 cm^{-1}, which is substantially larger in the ferrihydrite DRIFT samples than the hematite DRIFT samples (cf., Fig. 3-3).

Figure 3-2b shows that the positions of the CO_3 ν_3 peaks change; the asymmetric - symmetric energy splitting increases as the amount of water in the samples decreases. Similar behavior has been observed previously for phosphate adsorbed on Fe oxides by Pohle et al. (1990) and Persson et al. (1996), who attributed the peak shifts to changes in the hydrogen bonding of interfacial water as a function of the humidity of the samples. An alternative explanation is that the peak shifts are related to changes in the coordination state of the adsorbed carbonate species (e.g., a change from monodentate to bidentate) as a function of water content of the sample. The peak shapes can be used to eliminate this latter hypothesis. Consider the asymmetric CO_3 ν_3 frequencies of the spectra in Figure 3-2b. If a major change in adsorbate speciation were to occur as the water content of the samples decreased, it should be manifested by the disappearance of the 1502 cm^{-1} asymmetric CO_3 ν_3 peak in the wet sample accompanied by growth of a distinct peak at the 1547 cm^{-1} position of the hematite DRIFT sample. That is, according to the latter hypothesis, the "ATR Dried" (AD) and "Ferrihydrite DRIFT" (FD) spectra should be linear combinations of the "ATR Wet" (AW) and "Hematite DRIFT" (HD) spectra. To illustrate this point, the AD and FD spectra in Figure 3-2b have been fit as linear combinations of AW and HD. The fits are poor; the AD and FD spectra are not well described by a linear combination of the peaks in AW and HD (similar poor fit results are obtained if one uses an ATR spectrum of wet ferrihydrite as a fitting component in place of AW). Hence, from a peak fitting perspective, the peak shifts observed in the spectra should not be attributed to a major change in carbonate speciation.

It has been documented previously that carbonate groups bonded to metal ions in a bidentate fashion have significantly wider splittings between the asymmetric and symmetric ν_3 peaks (typically $\geq$ 250 cm^{-1}) than for monodentate carbonate ligands (which are typically $\leq$ 200 cm^{-1}) (Nakamoto, 1986; Ross, 1972). For example, the bidentate ν_3 peak

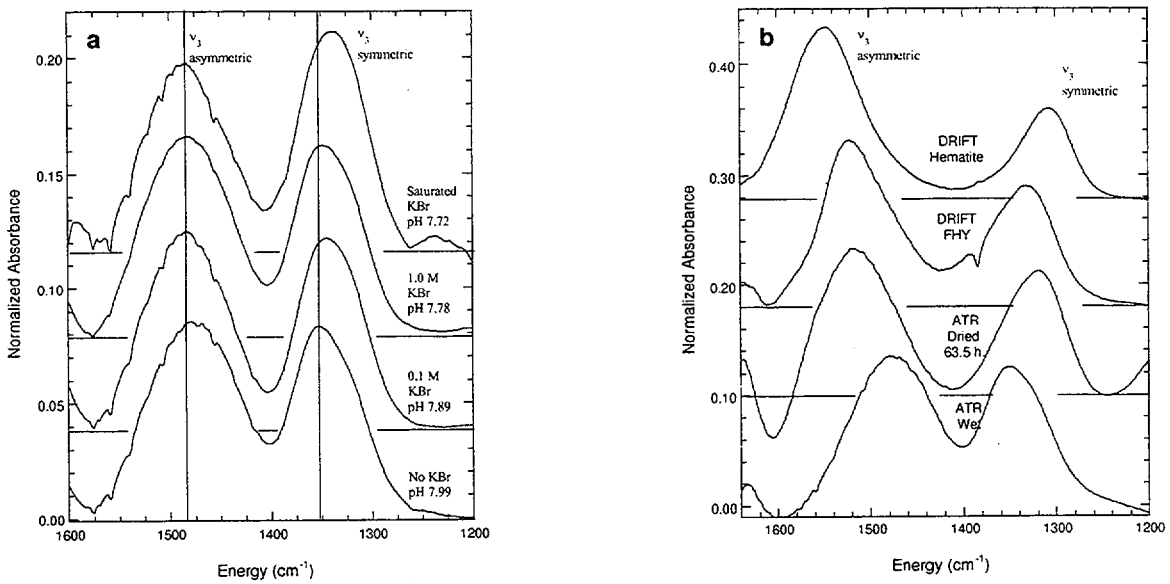

Figure 3-2. (a) Effects of KBr on sample spectra, measured using the ATR technique. All samples were in equilibrium with atmospheric CO_2. Saturated KBr electrolyte was approximately 4.4 M. The "No KBr" sample was prepared without added electrolyte. (b) Effects of sample water content on spectra (in equilibrium with atmospheric CO_2). The bottom spectrum ("ATR wet") is an ATR measurement of a hematite in contact with air-equilibrated water at pH 6.92. After recording this spectrum, the ATR hematite sample was uncovered and allowed to dessicate in the sample chamber for 63.5 h, and the spectrum was re-recorded. No electrolyte was added to this sample to prevent precipitation of salts during dessication. DRIFT measurements are at pH 8 and in 0.1M NaCl solution. The "ATR Dried" (AD) and "Ferrihydrite DRIFT" (FD) spectra were fit (least squares minimization) with linear combinations of the "ATR Wet" (AW) and "Hematite DRIFT" (HD) spectra. The fit results were: AD = 0.77*AW + 0.13*HD and FD = 0.81*AW + 0.19*HD. As described in the text, the peak position changes should not be attributed to changes in adsorbate speciation.

splitting for Fe(III)-carbonate complexes should be > 300 cm^{-1}, based on comparison to the Co(III)-carbonate system (for which the bidentate ν_3 peak splitting is as high as 610 cm^{-1}) (Nakomoto, 1986, and references therein). By analogy, the CO_3 ν_3 peak splitting in the AW spectrum in Figure 3-2b (about 163 cm^{-1}) suggests that carbonate anions are adsorbed in a monodentate conformation to surface Fe atoms. If the carbonate groups were to shift to bidentate configurations as a result of decreasing sample water content, the splitting of the ν_3 peaks should shift to ≥ 300 cm^{-1}. No such ν_3 peaks are observed. Furthermore, the asymmetric and symmetric ν_3 peaks of the hypothetical bidentate species should be observable at low and intermediate stages of desiccation and should increase in amplitude as sample water content decreases. This phenomenon is also not observed. Rather, the CO_3 ν_3 splittings increase smoothly with decreasing sample water content.

Based on these observations, we conclude that the CO_3 ν_3 peak shifts should be attributed to changes in the hydrogen bonding of interfacial water as a function of the humidity of the samples. The positions of CO_3 ν_3 peaks are primarily controlled by the polarization of the CO_3 group (Hester and Grossman, 1966). Therefore, the smoothly varying shifts in CO_3 ν_3 peak positions suggest the existence of gradual changes in the polarization of adsorbed carbonate groups. It is plausible that these changes could arise from changes in hydrogen

bonding and/or increasing polarization of the electrified interface as the interparticle water is increasingly removed from the samples.

In the discussion above, we have excluded the possibility that the adsorbate spectra are attributable to outer-sphere (*i.e.*, adsorbed only through electrostatic attraction and/or hydrogen bonding) carbonate or bicarbonate anions, and inner-sphere (*i.e.*, bonded directly to surface Fe atoms) bicarbonate ions. Outer-sphere carbonate ions should have D_{3h} (or quasi-D_{3h}) point symmetry. Thus, they should have only one ν_3 peak, which occurs at 1393 cm^{-1} in bulk solution (not shown). Such a peak is not observed in the wet ATR spectrum or any of the other spectra. Hence, it can be said that outer-sphere carbonate species do not occur in the samples in significant concentrations. Bicarbonate also has a single, very narrow (14 cm^{-1} half-width-half-max) CO_3 ν_3 peak (the splitting between the asymmetric and symmetric lines is very small, effectively unsplit, consistent with monodentate coordination), which occurs at about 1361 cm^{-1} (Fig. 3-3a). Since this feature is unsplit and much narrower than any adsorption sample peaks, outer-sphere bonding of bicarbonate cannot account for the CO_3 ν_3 peak position changes in Figure 3-2b. Inner-sphere bonding of bicarbonate to surface Fe(III) cannot be ruled out on the basis of the spectra alone, since we have no model compounds containing Fe(III)-HCO_3 bonding. However, such bonding configurations are very rare in inorganic systems. Furthermore, even if an inner-sphere bicarbonate species were to exist in the samples, it should have peaks at discrete positions that additively increase the apparent widths of peaks in the intermediate desiccation samples, as described above. Since no such broadening is observed, such a species cannot account for the observed smoothly varying changes in CO_3 ν_3 peak positions.

In summary, based on the observations and arguments presented above, we conclude that the DRIFT technique can be relied upon to provide useful measurements of carbonate adsorbate complexes in (dilute) concentration ranges where ATR spectra cannot be collected. As far as we can determine, the DRIFT sample preparation procedure does not induce speciation changes (as compared to wet samples) that adversely affect our interpretations of the spectra.

3.3.3 FT-IR SPECTRA OF U(VI) ADSORBED ON HEMATITE AND FERRIHYDRITE

In order to distinguish surface species that were unique to the pH-dependent U(VI)-bearing samples, it was necessary to collect spectra from samples having only adsorbed carbonato species over a corresponding range of pH values. Diffuse reflectance FT-IR spectra of carbonato species adsorbed on hematite and ferrihydrite in the absence of U(VI) are displayed in Figure 3-3. Peaks due to interparticle water bending vibrations, and hematite and ferrihydrite Fe-O-H bending and Fe-O stretching vibrations have been subtracted out of the raw spectra in order to isolate peaks arising from adsorbed species. No additional C-O stretching frequencies were observed in the absence of U(VI) in the region between 1300 cm^{-1} to 1650 cm^{-1} and between pH 3.5 and 8.5 on hematite or ferrihydrite samples. The ν_3 peaks in Figure 3-3a (hematite) have been fit with Gaussian lineshapes (Lorentzian character is < 1%), displayed as the dashed curves, in order to illustrate that the ν_3 peaks for carbonato species on hematite are symmetric, which indicates that no other C-O stretching frequencies are present. The ν_3 peaks in Figure 3-3b (ferrihydrite) have also been fit with Gaussians. Inspection of Figure 3-3b shows that the ν_3 peaks for carbonato species on ferrihydrite occur at slightly different energies than those for hematite carbonato adions. In addition, the ferrihydrite carbonato ν_3 peaks are broader, more asymmetric, and may contain more Lorentzian character than the hematite carbonato ν_3 peaks. The broadening and asymmetry of the carbonato ν_3 peaks suggests the existence of a larger distribution of coordination environments for carbonate species adsorbed on ferrihydrite than on hematite. This observation is consistent with the structural chemistry of hematite and ferrihydrite. Hematite is crystalline and the diameters of hematite

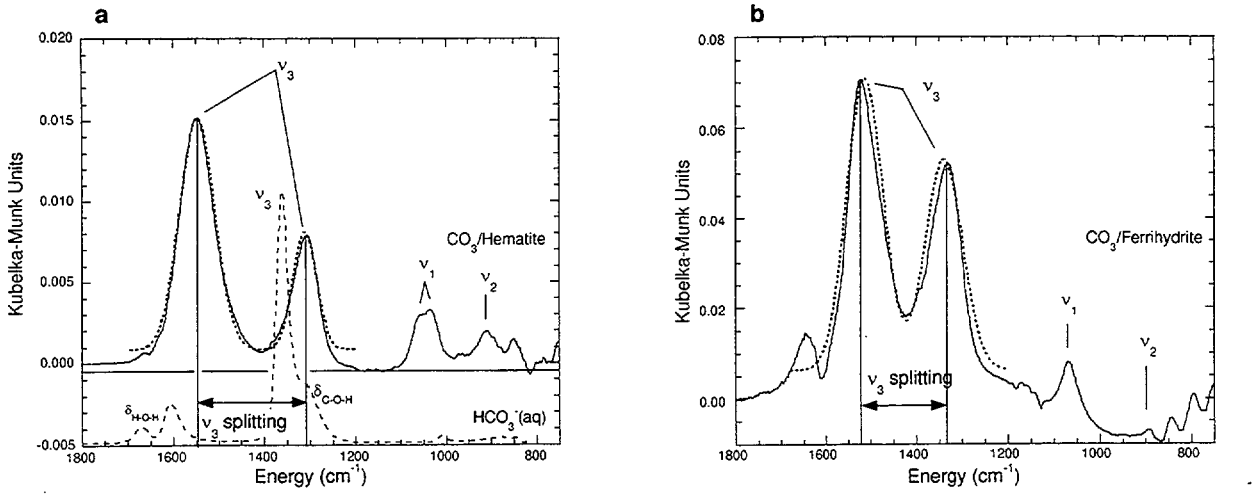

Figure 3-3. Spectra of carbonato surface species on (a) hematite and (b) ferrihydrite at pH 8, in 0.1M NaCl solution, and in equilibrium with atmospheric CO_2. Gaussian fits to the spectra are shown in thin dashed lines. The dashed spectrum in (a) is that of aqueous (0.1 M) HCO_3^-. The large peak at about 1360 cm^{-1} in this spectrum is the (essentially unsplit) CO_3 ν_3 vibration. The low-energy shoulder at about 1300 cm^{-1} is the $\delta_{C\text{-}O\text{-}H}$ (bending) vibration. When measured in D_2O, CO_3 ν_3 is unaffected, but the low energy shoulder shifts to < 1000 cm^{-1}, confirming its identity as $\delta_{C\text{-}O\text{-}D}$. The small peaks at about 1600 cm^{-1} are subtraction remnants from the bulk water $\delta_{H\text{-}O\text{-}H}$ vibration.

particles used in these experiments were larger than 100 nm. The hematite structure has only one O site and one Fe site (i.e., all oxygens are symmetrically equivalent as are all Fe atoms). Each Fe(III) cation has three Fe-O bonds of length 1.95 Å and three of length 2.12 Å (Blake et al., 1966). In comparison, ferrihydrite is poorly crystalline and has a large range of O and Fe coordination environments. Fe-O bond lengths in ferrihydrite range between 1.95 to 2.22 Å (Drits et al., 1993; Waychunas et al., 1996). Furthermore, given the high surface area of ferrihydrite (600 m^2/g), almost all of its O and Fe ions are at or near ferrihydrite-water interfaces (Rea et al., 1994; Waychunas et al., 1993). Thus, it is likely that ferrihydrite surfaces are more structurally and compositionally heterogeneous than hematite surfaces. For example, ferrihydrite surfaces should have a greater number of types of surface functional groups, each type having a relatively broad distribution of structural characteristics and acidities in comparison to hematite. Therefore, it is reasonable to conclude that a larger distribution of carbonato species exists on ferrihydrite than on hematite.

Other carbonate vibrational modes are visible in Figure 3-3. The carbonate ν_1 frequency occurs at 1050 - 1100 cm^{-1}. This peak is not IR active if the carbonate group is present as the free carbonate anion, which has D_{3h} symmetry. The presence of the ν_1 peak indicates that the adsorbed carbonato surface species have symmetry lower than C_{3v}, consistent with the splitting of the ν_3 frequency into two peaks. On hematite, the carbonate out-of-plane deformation vibration, labeled ν_2, is also discernible (*ca.* 920 cm^{-1}). The carbonate ν_2 peak cannot be distinguished on the ferrihydrite samples due to the presence of goethite Fe-O stretching frequencies between 750 and 950 cm^{-1}, which arise from the slow conversion of ferrihydrite to goethite. The goethite Fe-O stretching frequencies are very strong and can be detected at about 0.16% by mass. Goethite Fe-O stretching peaks were not detected until after the sixth day following ferrihydrite synthesis. After two weeks following synthesis, the height of the Fe-O goethite peaks indicate that about 0.37% of the ferrihydrite had crystallized as goethite (the ferrihydrite was stored as unstirred suspensions) at pH 6 - 8. This small amount of goethite is insufficient to complicate U(VI)/ferrihydrite

spectra interpretation. For example, the presence of goethite would have the greatest impact on our results if it were present exclusively as surfaces, i.e., as 1-unit-cell-thick (3 Å-thick) coatings on ferrihydrite. If this mechanism were to occur, after two weeks of aging, goethite should cover less than 0.21% of the ferrihydrite surface area in our samples, based on 0.37% mass conversion and 600 m^2/g surface area for ferrihydrite. However, it is likely that goethite occurs as particles instead of (or in addition to) monolayer-thick coatings, which would further reduce the amount of goethite surface area present, since goethite typically has much lower surface area than ferrihydrite. Furthermore, most U(VI)/ferrihydrite samples were prepared using ferrihydrite stored less than two weeks. Thus, the presence of trace goethite in the U(VI)/ferrihydrite samples should not affect our conclusions. No samples were prepared from ferrihydrite allowed to age for greater than two weeks in order to be consistent with the procedures of Waite et al. (1994b) and to avoid complications arising from the presence of significant quantities of goethite.

Figure 3-4 shows the spectrum for U(VI) adsorbed on hematite at pH 8 displayed over the C-O stretching frequency range. In the presence of U(VI), the CO_3 ν_3 peaks are noticeably asymmetric and substantially broader than those in the absence of U(VI). In particular, there is substantially more amplitude present between 1350 and 1500 cm^{-1} in the U(VI) adsorption sample spectrum than occurs when no U(VI) is present. These changes in the ν_3 lineshapes are attributable to the presence of a second set of ν_3 peaks that are split by a smaller amount than those in the absence of U(VI). The centroids, widths, and asymmetry peak intensity ratio of the ν_3 peaks observed in the CO_3/hematite pH 8 sample spectrum (Fig. 3-3a, and Table 3-2) were used as constraints when fitting the U(VI)/hematite pH 8 spectrum. The fit results indicate the presence of a second set of ν_3 peaks, centered at 1369 cm^{-1} and 1491 cm^{-1} (Table 3-2), having a ν_3 peak splitting (122.0 cm^{-1}) which is substantially less than the CO_3 ν_3 splitting of the CO_3-only peaks (228.5 cm^{-1}). Since the peaks

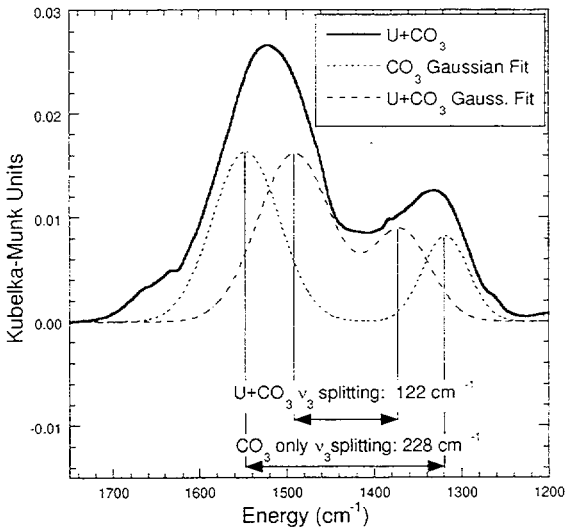

Figure 3-4. C-O stretching region of carbonate for U(VI)/hematite adsorption sample at pH 8, in 0.1M NaCl solution, and in equilibrium with atmospheric CO_2. Gaussian fits to the spectrum are plotted in dashed lines (see section 3.3.3 for details). The doublet with the 122 cm^{-1} splitting occurs only in the presence of U(VI) and is attributed to U(VI)-carbonate-hematite ternary complexes.

with the narrow ν_3 splitting appear only in the presence of adsorbed U(VI), while pH and ionic strength remain unchanged, we conclude they indicate the presence of U(VI)-carbonato-surface ternary complexes.

The effects of pH on the C-O stretching frequency region of U(VI)/hematite adsorption sample spectra are illustrated in Figure 3-5. For each U(VI) adsorption sample pH value, a spectrum was measured from a sample at the same pH but containing no U(VI). The characteristics of the ν_3 peaks in the U(VI)-free spectra were used as constraints to fit the ν_3 regions of the U(VI)/hematite spectra, as described above for the pH 8 sample. In general, the U(VI)/hematite C-O stretching frequency regions are similar to one another, regardless of pH. This uniformity suggests that U(VI)-carbonato-surface ternary complexes exist at all pH values measured.

The C-O stretching frequency regions of U(VI)/ferrihydrite adsorption sample spectra are shown in Figs. 3-6 and 3-7. The presence of

Table 3-2. Fit results for CO_3-only and U+CO_3 adsorbate species on hematite and ferrihydrite. Δ is defined as the difference in energy between the asymm and symm ν_3 peaks. All energies are given in cm^{-1}.

Substrate	pH	Electrolyte	CO_3 only			U+CO_3 complex		
			ν_3, asymm	ν_3, symm	Δ	ν_3, asymm	ν_3, symm	Δ
Hematite	4.5	none added	1543.9	1315.1	228.8	1481.3	1380.4	100.9
Hematite	5.0	none added	1544.1	1315.1	229.0	1487.4	1380.2	107.2
Hematite	5.8	none added	1543.4	1311.9	231.5	1486.9	1380.4	106.5
Hematite	8.0	none added	1541.9	1307.0	234.9	1484.1	1380.7	103.4
Hematite	8.0	0.1M NaCl	1547.1	1318.6	228.5	1491.0	1369.0	122.0
Hematite	8.5	none added	1544.1	1310.6	233.5	1483.8	1378.9	104.9
Ferrihydrite	4.5	none added	1517	1329	188	1466	1375	91
Ferrihydrite	5.0	none added	1524	1325	199	1466	1370	96
Ferrihydrite	8.0	none added	1523	1322	201	1467	1370	97
Ferrihydrite	8.0	0.1M NaCl	1522	1330	192	1465	1393	72
Ferrihydrite	8.5	none added	1530	1328	202	1475	1371	104
Ferrihydtite	8.5	0.1M NaCl	1522	1330	192	1482	1360	122

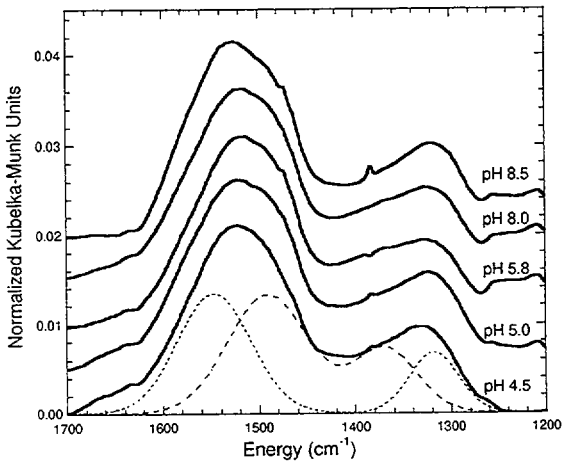

Figure 3-5. pH dependence of the C-O stretching region for U(VI)/hematite adsorption samples in equilibrium with atmospheric CO_2, no ionic strength control. Gaussian fits to the pH 4.5 spectrum are plotted in dashed lines to illustrate that at least two types of carbonate species are present on the hematite surfaces, one of which is a U(VI)-carbonate-hematite surface ternary species.

U(VI) has a similar effect on the CO_3 ν_3 stretching region as on hematite; in the presence of U(VI), the CO_3/ferrihydrite ν_3 peaks are noticeably asymmetric and broader than those in the absence of U(VI) (Fig. 3-6). In particular, there is substantially more amplitude present between about 1350 and 1500 cm^{-1} in the presence of U(VI), indicating the presence of additional CO_3 species, which we attribute to U(VI)-carbonato-ferrihydrite surface ternary complexes for the same reasons as discussed above for hematite. Fit results for these spectra are presented in Table 3-2. For each pH value, spectra from CO_3-only samples were used to constrain fits of the ν_3 regions of the U(VI)/ferrihydrite spectra, as described for the U(VI)/hematite samples. The adsorption densities obtained on the ferrihydrite samples (0.09 - 0.42 μmoles/m^2) were approximately half of those obtained on hematite (0.26 - 0.72 μmoles/m^2), and the heights of the ternary complex/ferrihydrite CO_3 ν_3 peaks are correspondingly smaller.

The effects of pH on the C-O stretching frequency region of U(VI)/ferrihydrite spectra are illustrated in Figure 3-7. All U(VI)/ferrihydrite samples contain contributions from U(VI)-carbonato ternary complex CO_3 ν_3 peaks between about 1350 and 1500 cm^{-1}. Thus, we conclude that U(VI)-carbonato ternary complexes exist at all pH values measured (4.5 - 8.5), as was observed on hematite.

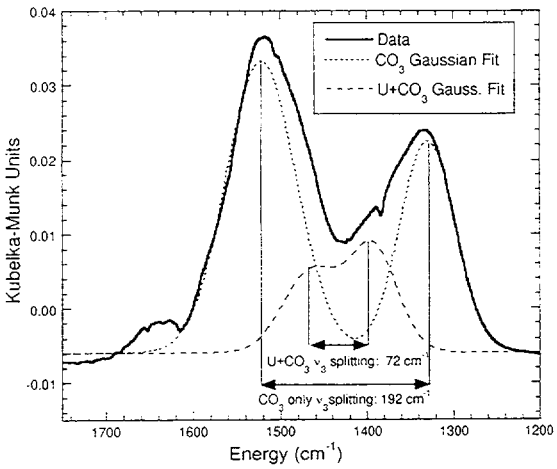

Figure 3-6. C-O stretching region of carbonate for pH 8 U(VI)/ferrihydrite adsorption sample (0.1M NaCl). Gaussian fits to the spectrum are plotted in dashed lines (see section 3.3.3 for details).

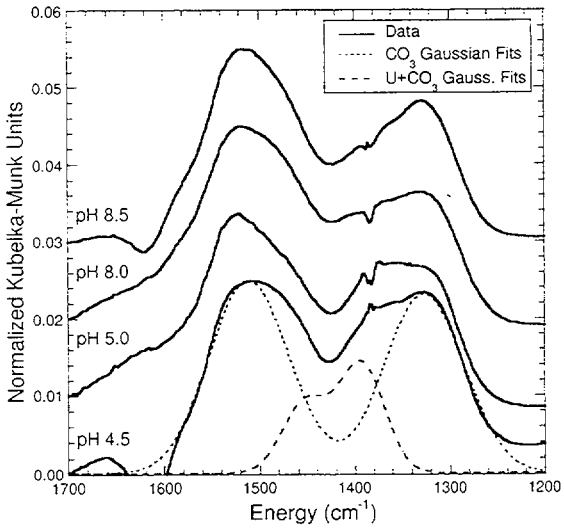

Figure 3-7. pH dependence of the C-O stretching region for U(VI)/ferrihydrite adsorption samples in equilibrium with atmospheric CO_2, no ionic strength control. Gaussian fits to the pH 4.5 spectrum are plotted in dashed lines. The sharp peaks at 1384 cm^{-1} are due to trace nitrate impurities in the samples originating from the filter membranes.

3.3.4 EXAFS SPECTRA OF HEMATITE SAMPLES

EXAFS spectra for U(VI) adsorbed on hematite at pH 5.75 and 7.61 are shown in Figure 3-8, and the results from fitting the spectra are displayed in Table 3-3. The EXAFS indicate that U(VI) adions in the samples have typical UO_2^{2+} first-shell coordination environments: two axial oxygens at 1.82 Å, and an equatorial shell of about five oxygens at 2.36 - 2.50 Å. Both spectra also contain contributions from Fe backscattering, and fits to the spectra indicate the U-Fe distance is 3.40-3.45 Å in both samples. The spectra contain no detectable backscattering from U neighbors, which indicates that U(VI) surface complexes are monomeric, since multimeric U(VI) complexes should have significant U-U contributions. EXAFS of the U(VI) precipitates (not shown), prepared as described in section 3.2.2, have strong U-U FT peaks at 3.8 Å (uncorrected for phase shift). Thus, the absence of U-U peaks in the U(VI)/hematite spectra also suggests that precipitation of U(VI) solids did not occur in the samples to a detectable extent. This conclusion is in agreement with the solubility data presented in section 3.3.1.

The *circa* 3.4 Å U-Fe distance observed in the U(VI)/hematite adsorption sample spectra can be used to deduce the attachment geometry of U(VI) to hematite surfaces, providing that basic geometric constraints regarding the stereochemistry of the oxide surface and the adsorbates are known, such as Fe-O and U-O bond lengths. The average Fe-O bond length in hematite is 2.02 Å, and the Fe coordination geometry is octahedral; each Fe(III) ion has six oxygen neighbors located at the corners of FeO_6 octahedra, in which the O-O separations (octahedron edge lengths) range from 2.59 Å to 3.04 Å. Since the axial oxygens of the UO_2^{2+} unit generally do not participate in bonding outside of the unit, it can be assumed that the 2.36 Å equatorial oxygens are responsible for adsorption of the U(VI) to the hematite surfaces, i.e., the equatorial oxygens at 2.36 Å are shared between the U(VI) adions and Fe(III) ions in the oxide surface.

Two basic attachment geometries to FeO_6 octahedra are possible for U(VI). UO_2^{2+} units can bond only to one corner (oxygen) of an

Table 3-3. Results of EXAFS analyses. CN = coordination number (± 20%), R = interatomic distance (± 0.03 Å), and σ^2 = Debye-Waller factor. Γ (adsorption density) is in units of μmoles/m^2.

Sample	U-Oax			U-Oeq			U-Fe		
	CN	R(Å)	σ^2	CN	R(Å)	σ^2	CN	R(Å)	σ^2
pH 5.75	2.1	1.76	0.003	3.4	2.20	0.01	0.4	3.40	0.005
Γ = 0.56				3.2	2.35	0.01			
pH 7.61	2.0	1.82	0.002	2.8	2.37	0.01	0.6	3.45	0.005
Γ = 0.55				2.4	2.53	0.01			

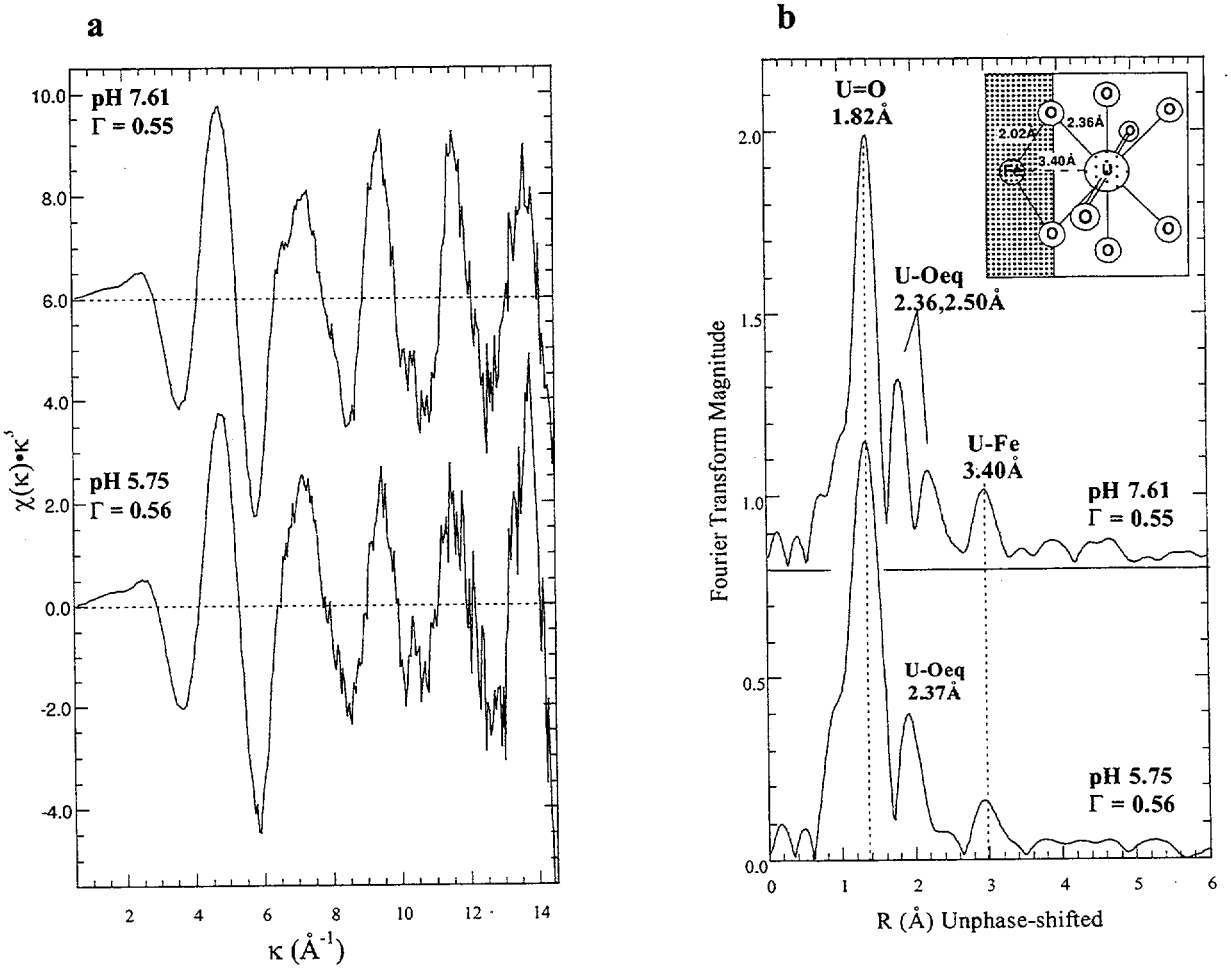

Figure 3-8. (a) U L_{III}-edge EXAFS spectra and (b) Fourier Transforms (uncorrected for phase shifts) of U(VI) adsorbed on hematite in 0.1 M $NaNO_3$ solutions at equilibrium with atmospheric CO_2. Adsorption densities (Γ) are in units of μmoles/m^2. U-O and U-Fe distances in (b) are from Table 3-3. The inset in (b) depicts the edge-sharing coordination geometry of U(VI) adions bonded to edges of FeO_6 octahedra at the hematite surfaces, which is deduced from the EXAFS-derived U-Fe distance (see text).

octahedron (corner-sharing) or to two corners of an FeO_6 octahedron (edge-sharing). UO_2^{2+} units are not free to bond to three corners of a single FeO_6 octahedron because the axial oxygens do not participate in bonding outside of the UO_2^{2+} group. Using the basic geometric constraints discussed above, it can be said that corner-sharing arrangements should have U-Fe distances > 4.05 Å, based on Fe-O-U bond angles > 135°. In contrast, edge-sharing configurations should give rise to U-Fe separations of 3.14 – 3.52 Å. Therefore, the 3.40 - 3.45 Å U-Fe distances observed in the U(VI)/hematite adsorption sample spectra imply that U(VI) is bonded to hematite in an edge-sharing fashion. Since these U-Fe distances are in the upper range of those expected for edge-sharing adsorption, we conclude that the Fe, U and their shared O atoms are approximately coplanar. Furthermore, since short O-O octahedron edge distances produce long U-Fe distances, the EXAFS-derived U-Fe distances suggest that U(VI) preferentially bonds to short octahedron edges (i.e., O-O about 2.60Å). Similar EXAFS results were reported by Waite et al. (1994b) for U(VI) adsorption on ferrihydrite.

If the U(VI) groups were to have no axial oxygens, then it would be possible for a single U(VI) adion to bond to multiple FeO_6 octahedra (edges) simultaneously. The axial oxygens place substantial steric limitations on such arrangements. Therefore, the EXAFS results imply that U(VI) adions bond to hematite and ferrihydrite surfaces in a bidentate, monomeric fashion. This U(VI)-Fe-oxide adsorption geometry is illustrated schematically in Figure 3-8b.

3.4 Discussion

3.4.1 STRUCTURE AND COMPOSITION OF U(VI)-CARBONATE TERNARY COMPLEXES

The molecular structures and compositions of U(VI)-carbonato surface complexes on hematite observed in this study can be deduced by inspection of the splitting of the ternary complex CO_3 ν_3 peaks. Bidentate coordination of U(VI) by carbonate groups gives rise to ν_3 peak splittings of about 87 cm^{-1} (rutherfordine) to 233 cm^{-1} ($K_4UO_2(CO_3)_3$) (Urbanec and Cejka, 1979a; Urbanec and Cejka, 1979b; Wilkins, 1971). In comparison, the splittings of the ν_3 peaks for carbonato adions bonded to U(VI) on hematite and ferrihydrite are mostly in the range 91 - 107 cm^{-1}. This similarity suggests that the adsorbed U(VI)-bonded carbonato groups are carbonate anions, bonded to U(VI) in a bidentate fashion. This conclusion is consistent with the prevalence of carbonate (as opposed to bicarbonate) as a ligand for U(VI) in alkaline aqueous solutions and solid U(VI) carbonates, and the prevalence of bidentate coordination of carbonate to U(VI) (Clark et al., 1995, and references therein). Hence, we conclude that the composition of the adsorbed U(VI) carbonato complexes should be $UO_2(CO_3)_x$.

From a purely structural standpoint, there are three possible geometries for the proposed U(VI)-carbonate complexes to attach to the Fe oxide surfaces: (1) U(VI) bonds directly to Fe oxide surface (hydr)oxo sites, and the carbonate ligands point away from the oxide surface (*i.e.*, $Fe\text{-}O_{sfc}\text{-}U(VI)\text{-}(CO_3)_x$-solution linkages), (2) U(VI) and its carbonate ligands bond to the Fe oxide surfaces simultaneously (*i.e.*, $Fe\text{-}O_{sfc}\text{-}U(VI)\text{-}(CO_3)\text{-}Fe_{sfc}$ linkages), and (3) the carbonate groups act as bridges between U(VI) and the Fe oxide surfaces (*i.e.*, $Fe_{sfc}\text{-}(CO_3)\text{-}U(VI)$-solution linkages). The EXAFS and macroscopic uptake results can be used to distinguish between these models. The first configuration (Figure 3-9) is consistent with the EXAFS results (bidentate coordination of U(VI) to Fe oxide surfaces) and has the fewest steric requirements since, in this scenario, the carbonate ligand(s) do not bond to any rigid surface structures (other than adsorbed U(VI)). Furthermore, the position of the low-pH U(VI) adsorption edge on ferrihydrite (uptake increases from about 10% at pH 4 to about 80% at pH 5, cf., section 4) is not much different in the absence of dissolved carbonate than it is in air-equilibrated water, even though FT-IR spectra indicate the presence of U(VI)-carbonate ternary complexes. The EXAFS observations suggest that U(VI)–Fe oxide (surface) bonding is

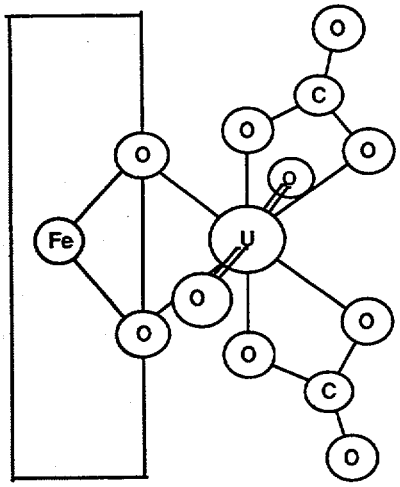

Figure 3-9. Ball-and-stick representation of postulated Fe<$^{O}_{O}$>$UO_2(CO_3)_x$ (x=2) ternary complex.

unaffected by the presence of carbonate ligands. It follows that ternary complexes having structural configuration (1) account for U(VI) uptake behavior better than complexes having configurations (2) or (3).

The second structure is consistent with the EXAFS results, but has substantially greater steric requirements for the carbonate groups, which would be completely bonded to relatively rigid structures. Thus, the O-O edge distances of the carbonate ligands would have to match both the edge lengths of the U(VI) equatorial belt and the Fe-Fe separation on the surfaces. The concentration of surface sites commensurate with such adsorption configurations is likely to be a small fraction of the total sites available for bidentate U(VI) binding. Furthermore, the decrease in the entropy of adsorption is larger for configuration (2) than for Fe-O_{sfc}-U(VI)-$(CO_3)_x$ complexes. Hence, we conclude that ternary complexes having configuration (2) should be present at much lower concentrations than Fe-O_{sfc}-U(VI)-$(CO_3)_x$ complexes.

Configuration (3) is inconsistent with the EXAFS results, since it implies that Fe-U separations should be much larger than the bidentate edge-sharing distance observed by EXAFS (3.40 - 3.45 Å). In addition, since Fe_{sfc}-(CO_3)-U(VI) ternary complexes are anchored to the Fe oxide surfaces at Fe_{sfc} ions, they should compete with aqueous OH- for these sites. Thus, they should show ligand-like adsorption behavior (*i.e.*, adsorption is maximal in the low-pH range and decreases with increasing pH). The observed U(VI) adsorption in the pH range 4-6 is exactly the opposite of this prediction (cf., Section 4). Hence, we conclude that such complexes do not occur or are present at insignificant concentrations.

Based on these arguments, we conclude that the predominant structure for U(VI)-carbonate ternary complexes is Fe-O_{sfc}-U-$(CO_3)_x$. Since the EXAFS results suggest that U(VI) adions are bidentately bonded to edges of surface FeO_6 octahedra (*i.e.*, a Fe<$^{O}_{O}$>U(VI) configuration), the surface complexes should have the structure and composition Fe<$^{O}_{O}$>$UO_2(CO_3)_x$ (Fig. 3-9).

The maximum possible value of the numeric subscript x should be 2, based on the EXAFS-derived U(VI) equatorial CN of about 6, and assuming that equatorial oxygens cannot be shared between carbonate groups and U(VI) axial oxygens, other carbonate groups (consistent with U(VI)-carbonate coordination chemistry (Clark et al., 1995)), or surface sites (consistent with the preceding discussion). We have not designated a charge for this species, since it will be determined by the partial charges on the surface oxygens and the possible presence of protons bonded to the surface oxygens.

3.4.2 pH DEPENDENT SPECIATION OF U(VI)-CARBONATE TERNARY COMPLEXES

The average value of the numeric subscript, x_{ave}, in the ternary complexes can be measured as a function of pH from the FT-IR spectra. This is possible because the intensities and areas of adsorption sample CO_3 ν_3 and UO_2 ν_{asymm} DRIFT peaks are linearly related to their respective adsorption densities (Beer's Law), providing the peaks are expressed in K-M units (for DRIFT measurements) and the

concentrations of absorbers (adsorbates) are dilute, which is the case for the adsorption samples. The molar absorptivity coefficients (in K-M units), which relate peak intensities to absorber concentrations, for the CO_3 ν_3 and UO_2 ν_{asymm} peaks were extracted from adsorption sample data, the spectrum of aqueous 0.1 M $UO_2(CO_3)_3^{4-}$(aq) (pH 10.4), and by comparison with the macroscopically measured U(VI) adsorption density. From these coefficients it is possible to calculate the adsorption density of adsorbed U(VI)-bonded carbonate ions (*i.e.*, carbonate ligands to adsorbed U(VI) ions). The pH dependence of x_{ave}, defined as the adsorption density of U(VI)-bonded adsorbed carbonate ÷ the macroscopically measured U(VI) adsorption density, is illustrated in Figure 3-10. This ratio contains no contributions from adsorbed CO_3 not bonded to U(VI), nor any solution species.

Figure 3-10 shows that the minimum value of x_{ave}, approximately 1, occurs between pH 5.8 and 8.0. At lower and higher pH values, x_{ave} increases, with a maximum value of about 2 at pH 4.5. At pH 8.5, $x_{ave} = 1.7$. Two conclusions follow from this result: (1) Ternary complexes having composition $Fe<^{O}_{O}>UO_2(CO_3)_2$ occur at pH 4.5, 5, 8, and 8.5. (2) In the vicinity of pH 5.8, U(VI) occurs as $Fe<^{O}_{O}>UO_2(CO_3)_1$ ternary complexes and/or as a 50/50 mixture of binary U(VI) and $Fe<^{O}_{O}>$ $UO_2(CO_3)_2$ complexes.

The existence of ternary surface complexes having net negative charges (*i.e.*, $Fe<^{O}_{O}>UO_2(CO_3)_2$, and possibly $Fe<^{O}_{O}>UO_2(CO_3)$), is not surprising. Ho and Miller (1986) demonstrated that adsorption of U(VI) on hematite (in 1 mM $NaHCO_3$ aqueous solution) caused the hematite surface charges to reverse and become overall negative at pH ≥ 7 and adsorption densities as low as about 0.7 μmoles/m^2 (they reported the isoelectric point for U(VI)-free hematite occurred at pH 7.6 in 1 mM $NaHCO_3$). In comparison, U(VI)/hematite adsorption densities reported in this manuscript are 0.27 - 0.72 μmoles/m^2. Ho and Miller did not report U(VI)/hematite surface charge

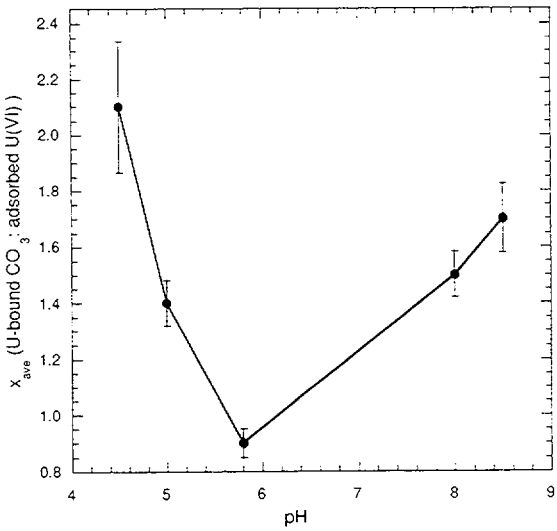

Figure 3-10 pH dependence of x_{ave}, defined as the adsorption density of U(VI)-bonded adsorbed carbonate ÷ macroscopically measured U(VI) adsorption density. Estimated errors do not include systematic errors in hematite surface area determinations and molar absorptivity coefficients, which affect all data in the same manner.

measurements at pH values lower than 7.

In the pH range where U(VI)-bearing hematite surfaces retain their positive charges (*i.e.*, at low U(VI) adsorption densities and low pH, *e.g.*, pH < 6), the presence of (negatively charged) carbonate ligands should lower the total free energy of adsorption of ternary complexes. Positive surface charge accumulates on the oxide surfaces as the pH and U(VI) adsorption density decreases, such as occurs on hematite between pH 5.8 and 4.5. In particular, since the U(VI) adsorption density drops rapidly between pH 5 to 4, the surface charge may rise quickly in this pH range. In opposition to the anion-adsorbate-stabilizing effect of increasing surface charge is the decrease in the concentration of aqueous carbonato reactants (HCO_3^- and/or CO_3^{2-}) with decreasing pH. According to the law of mass balance, the decrease in alkalinity (mostly HCO_3^-) acts to decrease the adsorption density of U(VI)-carbonato ternary complexes as pH decreases. The balance of these forces (surface charge and alkalinity; other involved

forces include the competition between protons and U(VI) for surface sites) will determine the pH dependence of x_{ave}. Therefore, the increase in x_{ave} as pH decreases from 5.8 to 4.5 in Figure 3-10 suggests that increasing positive surface charge stabilizes U(VI)-carbonato ternary complexes in spite of the low concentrations of aqueous HCO_3^- and CO_3^{2-}.

3.5 Summary and Conclusions

FT-IR measurements of U(VI) adsorption complexes on hematite and ferrihydrite indicate that U(VI)-carbonate-Fe-oxide ternary complexes are important surface species at all pH values of high U(VI) uptake (pH 4.5 - 8.5). The positions of the CO_3 symmetric and asymmetric stretching frequencies indicate that, within the ternary complexes, carbonate groups are bonded to U(VI) as bidentate ligands. In contrast, in the absence of U(VI), the predominant surface-bound carbonato species is monodentate inner-sphere carbonate. This conclusion is consistent with the results of Van Geen et al. (1994). Preliminary EXAFS analyses of U(VI)/hematite and U(VI)/ferrihydrite adsorption samples indicate that U(VI) is bonded to the Fe oxide surfaces in an edge-sharing bidentate fashion, in agreement with the results of Waite et al. (1994b). Integration of the FT-IR and EXAFS results suggests the predominant surface complexes at pH 4.5 and 8.5 are $Fe<^{O}_{O}>UO_2(CO_3)_2$. Between pH 5.8 and 8, the ternary complexes may have the composition $Fe<^{O}_{O}>UO_2(CO_3)_{0-2}$. The fraction of adsorbed U(VI) comprised by U(VI)-carbonato ternary complexes increases at pH < 5.8 and pH > 8 due to increasing surface charge at low pH and increasing aqueous carbonate concentrations at high pH. U(VI)-carbonato ternary surface complexes are of major importance to U(VI) adsorption on Fe oxides in carbonate-bearing waters.

4 URANIUM(VI) ADSORPTION ON FERRIHYDRITE IN SIMPLE $NaNO_3/HCO_3$ SYSTEMS, AND IN SYSTEMS CONTAINING ADDITIONAL COMPLEXING LIGANDS

In this section, we discuss U(VI) adsorption on ferrihydrite in systems containing $NaNO_3$ as the background electrolyte. These systems were equilibrated with air, or with an atmosphere containing an elevated partial pressure of CO_2. We studied the effects of pH, ionic strength, partial pressure of CO_2 (pCO_2) solid/liquid ratio, and U_T (the total concentration of U(VI) involved in adsorption equilibria) on U(VI) adsorption by ferrihydrite. In terms of surface complexation studies, this means varying the following aqueous components: H^+, U(VI), Na^+, NO_3^- and HCO_3^-; and the quantity of adsorbing minerals. In this section we also consider the effect of complexing and competing ligands including phosphate, citrate, sulfate and humic acid.

Much of the data for U(VI) adsorption on ferrihydrite in simple $NaNO_3/HCO_3$ systems was presented in a final report of the Alligator Rivers Analogue Project (ARAP) project (Waite et al., 1994a). In this section we consider all data for equilibrium systems, including the previous datasets presented in the ARAP report. The previous report included accounts of kinetic adsorption experiments and iron-mineral transformation experiments, which are not presented in this section.

4.1 Materials and Methods

4.1.1 FERRIHYDRITE

Ferrihydrite is an amorphous iron oxide with a high specific surface area which is thought to be an important U(VI) adsorbent phase in the near-surface environment. The ferrihydrite used for adsorption experiments was precipitated by raising the pH of a Fe(III)/HNO_3 solution to 6.0 and then aged for 65 h at 25°C in a stirred jacketed vessel. The resulting precipitate has a stoichiometry near $Fe_2O_3 \cdot H_2O$ and a surface area of 600 m^2/g (Waite et al., 1994b). The adsorption properties of ferrihydrite may change with time as it transforms to more crystalline phases such as goethite and hematite (Payne et al., 1994a). For this reason, fresh ferrihydrite was prepared for each experiment.

4.1.2 PROCEDURE FOR ADSORPTION EXPERIMENTS

Batch experiments were carried out in polypropylene centrifuge tubes which had holes drilled in their lids in order to ensure equilibration with the atmosphere. An aliquot of the ferrihydrite slurry was suspended in $NaNO_3$ (usually 0.1 M). For most experiments, the amount of solid corresponded to a total Fe content (Fe_T) of 1 mM (89 mg/L as $Fe_2O_3.H_2O$). For studies at pH > 7.0, sufficient $NaHCO_3$ was added to the system to achieve equilibrium with air at the desired pH. This ensured pH stability and fixed the carbonate content of the system. For experiments with added ligands, phosphate (as NaH_2PO_4), humic acid (a filtered solution of Aldrich sodium humate), sodium citrate or sodium sulfate was added at this stage.

The U(VI) was added after 24 h of pre-equilibration, during which time the system was allowed to come to equilibrium under the appropriate chemical conditions (pH, ionic strength, complexing ligands, etc.). The contact time for U(VI) was 48 h, with the pH being checked and adjusted if necessary after 24 h. The equilibration time was selected after carrying out preliminary experiments in which the uptake of U(VI) was studied as a function of time (Waite et al., 1994a). These experiments showed that uptake of U(VI) was rapid during the first 24 h, and was followed by a slower process, which probably involves diffusion into aggregates of particles.

The experimental tubes were gently shaken in a waterbath at 25°C. Immediately prior to sampling, the pH was again determined and the aqueous phase was then separated by high speed centrifugation (RCF > 6500g) for 30 minutes.

Uranium concentrations in the supernate were determined using the Kinetic Phosphorescence Analyser (model KPA-10) or by alpha spectrometry. Experiments at high pCO_2 were carried out in a glove box with a gas mixture of CO_2 (1%), N_2 (89%) and O_2 (10%). Further details of the techniques are available elsewhere (Waite et al. 1994a, 1994b).

4.1.3 REPRODUCIBILITY

The reproducibility of the techniques used in deriving U(VI) adsorption data was tested by repeating a U(VI) adsorption experiment carried out during the previous ARAP study (Waite et al., 1994a). The results of the two sets of experiments (Figure 4-1) show that good reproducibility can be obtained using the experimental techniques employed in this project.

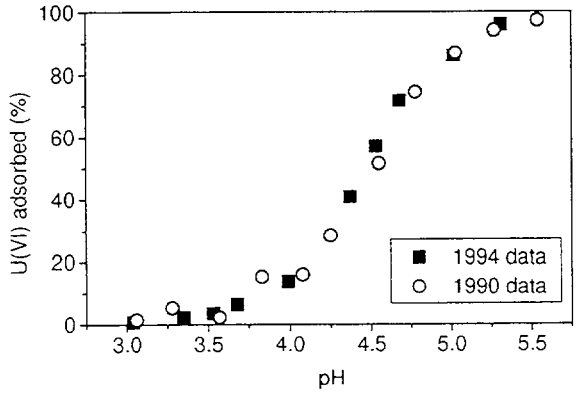

Figure 4-1. Reproducibility of U(VI) adsorption data. Comparison of data obtained in November 1994 with a previous dataset from March 1990. Data obtained after centrifugation. (U_T = 1 μM, Fe_T = 1 mM, 0.1M $NaNO_3$).

4.1.4 ADSORPTION ON VESSEL WALLS

Trace metals and radionuclides tend to adsorb onto any available surface. As a result, blank experiments carried out without a mineral sorbing phase present often indicate substantial uptake of metal onto the container walls. Recent work with several plastic materials (polypropylene, teflon and polycarbonate) has shown that these materials can remove 50% or more of U(VI) from solution, particularly at low total U(VI) concentrations (Pabalan et al., 1994). Teflon vessels were not used for our work, because fluoride has been detected in experimental solutions contained in Teflon, even in non-irradiated Teflon at low temperatures (Solomah, 1983; Crine, 1987). This presumably results from leaching of F from the Teflon. If this occurred, complexation of U(VI) with F would influence experimental results. Polypropylene centrifuge tubes were used for the adsorption experiments.

Blank experiments with polypropylene tubes in the absence of a sorbing solid showed that uptake on the vessel walls reached almost 25% at pH values between approximately 5 and 7 (Figure 4-2). In comparison, U(VI) adsorption on ferrihydrite (Fe_T of 10^{-3} M) was close to 100% across this pH range. In order to determine the quantity of U(VI) adsorbed by the vessel when ferrihydrite was present, we carried out some experiments in which the tube contents were vigorously shaken and then decanted, removing both the solid and liquid. The vessel walls were then leached with HNO_3 and the U(VI) content was determined. Iron was also measured in order to quantify the amount of U(VI) bound to ferrihydrite particles which were themselves attached to the vessel walls. It was concluded that direct uptake of U(VI) on the vessel walls was greatly reduced by the presence of ferrihydrite, and was probably less than 5% under the conditions of these experiments (Figure 4-2).

4.1.5 SEPARATION TECHNIQUE

As noted above, high speed centrifugation was used for solid/liquid phase separation in the U(VI) adsorption experiments. Compared to the alternative method of filtration, the main advantages of centrifugation are its greater simplicity, the lower probability of sample contamination, and the reduced opportunity for adsorption on the surfaces of filters and containers. These benefits arise because there is no transfer of sample into filtration equipment. The main drawbacks of centrifugation include the loss of information relating to the particle size distribution of adsorbed U(VI), and the

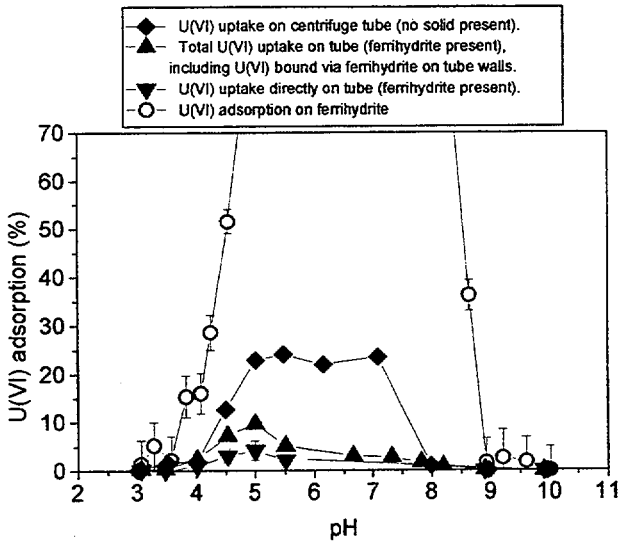

Figure 4-2. U(VI) uptake on polypropylene centrifuge tubes in presence and absence of ferrihydrite (U_T = 1 μM). Adsorption curve of U(VI) on ferrihydrite is also shown. (Fe_T = 1 mM, 0.1M $NaNO_3$).

possibility of inadequate separation of solid and liquid. Hsi and Langmuir (1985), in their study of U(VI) adsorption on iron oxides, noted that the inadvertent inclusion of particles in the supernatant could cause a significant overestimation of total dissolved U(VI) concentrations (referred to hereafter as, U_{eq}) when adsorption is close to 100%. In order to compare the results obtained by filtration and centrifugation, we carried out some experiments in which the position of the low-pH U(VI) adsorption edge (i.e., where adsorption increases from negligible amounts to >90% adsorption) was determined after separation using both procedures. The filtrations were carried out using various pore-sizes of 10,000 MW, 100,000 MW and 0.45 μm.

During the course of this work it was found that the U(VI) contents in filtrates obtained using new filters were lower than those obtained when the filters had been pre-conditioned with the sample solution. This indicated that adsorption of U(VI) occurred on unconditioned filter membranes, and is consistent with results obtained for other ions by Salbu et al. (1985). We concluded that pre-conditioning with the

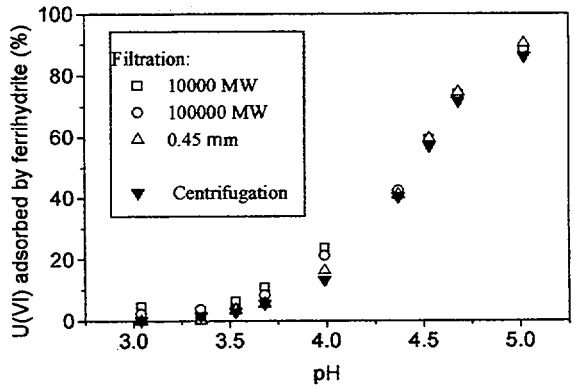

Figure 4-3. U(VI) adsorbed by ferrihydrite as determined by centrifugation or by membrane filtration using pre-conditioned membranes. (U_T = 1 μM, Fe_T = 1 mM, 0.1M $NaNO_3$).

sample solution is necessary when filtration is used for solid/liquid phase separation.

The results obtained by filtration with pre-conditioned filters of various pore-sizes were not significantly different to those obtained using centrifugation (Figure 4-3). It appears that during the course of the preparation and aging of the ferrihydrite, some agglomeration of particles must occur. The particle sizes are such that no effects of filter pore-size and no differences between centrifugation and filtration were observed at this ionic strength.

We concluded that the use of centrifugation rather than filtration does not significantly affect data obtained in these adsorption studies, where attention is primarily focused on the position of the adsorption edges in systems with ionic strength ≥ 0.01. Centrifugation is less susceptible to problems of cross-contamination and is much simpler, particularly when the necessity of pre-conditioning filters is considered. Therefore, we continued to use centrifugation for obtaining adsorption data.

4.2 Results of U(VI) Adsorption Experiments with Ferrihydrite

4.2.1 EFFECT OF pH AND SOLID/LIQUID RATIO

Below pH 7, the adsorption of U(VI) in air-equilibrated systems typically increases with increasing pH (the 'low pH adsorption edge'), with a sharp decrease in adsorption occurring above pH about 8 (the 'high pH edge'). The percentage of U(VI) adsorbed by ferrihydrite as a function of pH is shown in Figure 4-4. The data for the air-equilibrated system containing a total of 1.0 μM of U(VI) and 1.0 mM of Fe in a background electrolyte of 0.1M $NaNO_3$ (shown in Fig. 4-4 as squares) comprise a standard data set with which much of the data obtained for U(VI) adsorption on ferrihydrite will be compared.

The data shown in Figure 4-4 confirm that the uptake of U(VI) in air-equilibrated systems is greatest at near-neutral pH values. The strong complexation of U(VI) with carbonate in the solution phase (Section 2) is responsible for the decrease in adsorption of U(VI) at pH values above 8. Tripathi (1983) showed that there is no decrease in the extent of U(VI) adsorption at high pH values in systems which are free of CO_2.

As might be expected, the uptake of U(VI) on ferrihydrite is a function of the solid/liquid ratio of the solid in the system (Figure 4-4). This is due to the greater number of surface sites available for U(VI) uptake.

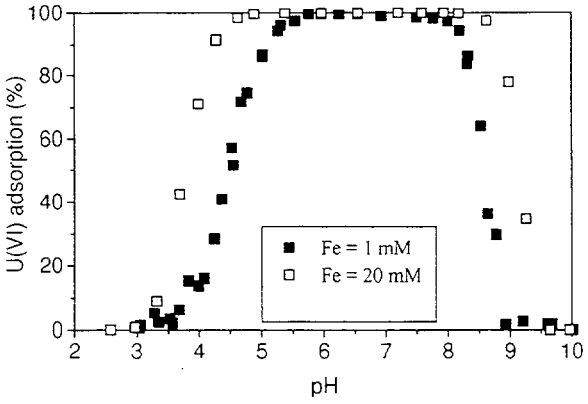

Figure 4-4. U(VI) sorption on ferrihydrite – effect of pH and solid/liquid ratio of ferrihydrite. (U_T = 1 μM, 0.1M $NaNO_3$).

4.2.2 EFFECT OF TOTAL U CONCENTRATION

Figure 4-5 shows adsorption curves for U(VI) on ferrihydrite with U_T ranging from 10^{-8} to 10^{-4} M. The positions of the adsorption edges in Figure 4-5 are dependent on U_T. For a given pH, the percentage of U(VI) adsorbed decreases with increasing U_T. This can be explained on the basis of the existence of a relatively small number of 'strong' surface sites, and a larger number of 'weak' sites (Waite et al., 1994b). Such two-site models have been found to be applicable to the adsorption of a range of metals on ferrihydrite (Dzombak and Morel, 1990).

The adsorption of U(VI) on ferrihydrite (expressed as mole U(VI) adsorbed per mole of Fe in ferrihydrite) can be plotted against the total concentration of U(VI) in solution to yield a plot known as an adsorption isotherm. The shape and slope (if linear) of the resulting curve may then be examined to determine if it conforms to one of various expressions including the Langmuir and Freundlich isotherms. In cases when adsorption is strongly dependent on pH, the construction of such curves is only of value when the pH is held constant. In Figure 4-6, a series of isotherms for U(VI) adsorption on ferrihydrite (at various pH values) clearly shows that U(VI) adsorption on ferrihydrite is non-linear. This indicates that sites of differing affinity for U(VI) adsorption are present on the surface of the solid. It should be noted in interpreting Figure 4-6 that U(VI) aqueous

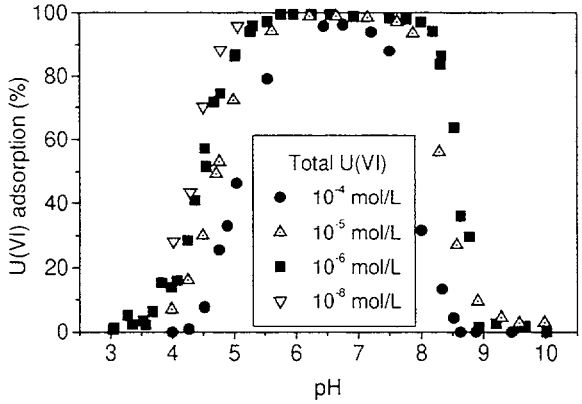

Figure 4-5. U(VI) adsorption on ferrihydrite for a range of U_T. (Fe_T = 1 mM, 0.1 M$NaNO_3$).

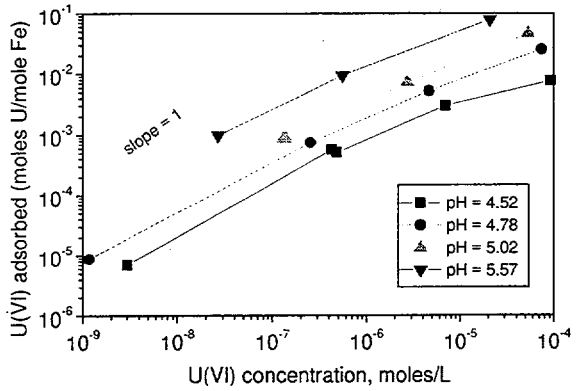

Figure 4-6. U(VI) adsorption data on ferrihydrite presented as isotherms. Each of the curves was obtained at a fixed pH value, with an uncertainty in pH of approximately 0.05 units. A hypothetical isotherm with a slope of unity is shown for comparison.

speciation is a function of U(VI) concentration as well as pH (see Section 2).

4.2.3 EFFECTS OF THE PARTIAL PRESSURE OF CO_2 AND IONIC STRENGTH

As noted above, carbonate is important in U(VI) aqueous speciation, so additional experiments were carried out in a glove-box with an elevated pCO_2 of 10^{-2} atm. The adsorption of U(VI) on ferrihydrite in the high pH range was significantly reduced at the higher partial pressure of CO_2, due to the dominance of weakly sorbing anionic uranyl carbonate species (Figure 4-7). The low pH adsorption edge was not significantly affected by pCO_2 although there may be a slight increase in adsorption at higher pCO_2.

Another parameter which was considered likely to affect U(VI) adsorption was ionic strength, which in natural systems may vary over a wide range. Varying ionic strength has little or no measurable effect on the low pH edge, but at high pH values increasing ionic strength reduces U(VI) adsorption on ferrihydrite (Figure 4-8).

The dependence of metal uptake on ionic strength may indicate whether inner sphere or outer sphere surface complexes are present

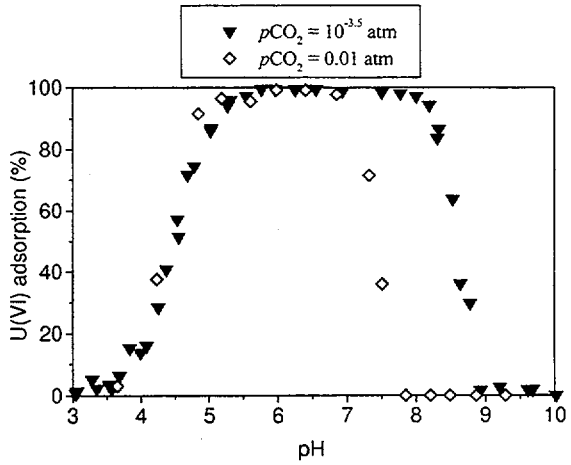

Figure 4-7. Effect of pCO_2 on U(VI) adsorption by ferrihydrite. (U_T = 1 μM, Fe_T = 1 mM, 0.1M $NaNO_3$).

(Stumm, 1992). However, the ionic strength dependence of U(VI) adsorption in the pH range of 8 to 9.5 has been attributed to a change in the activity of aqueous species of U(VI) when the ionic strength is varied (Waite et al., 1994b). In this pH range, the dominant aqueous U(VI) species are highly charged carbonate complexes, such as $UO_2(CO_3)_3^{4-}$. The activity of this species is significantly affected by ionic strength, and this influences the distribution of aqueous U(VI), and thus its adsorption.

4.3 Effect of Complexing Ligands

The experimental work described above shows that the adsorption of U(VI) in simple laboratory systems is influenced by a number of experimental parameters, including pH, ionic strength, U_T, solid/liquid ratio and pCO_2. Considering the complexity of natural systems, it would be expected that U(VI) adsorption in the environment would be influenced by additional factors, including the presence of inorganic and organic ligands in the aqueous phase.

In our initial studies of the importance of complexing ligands, we investigated the effect of phosphate and humic acid (HA) on U(VI) uptake by ferrihydrite. These ligands were chosen because they may be important in the migration of U(VI) at the Koongarra uranium

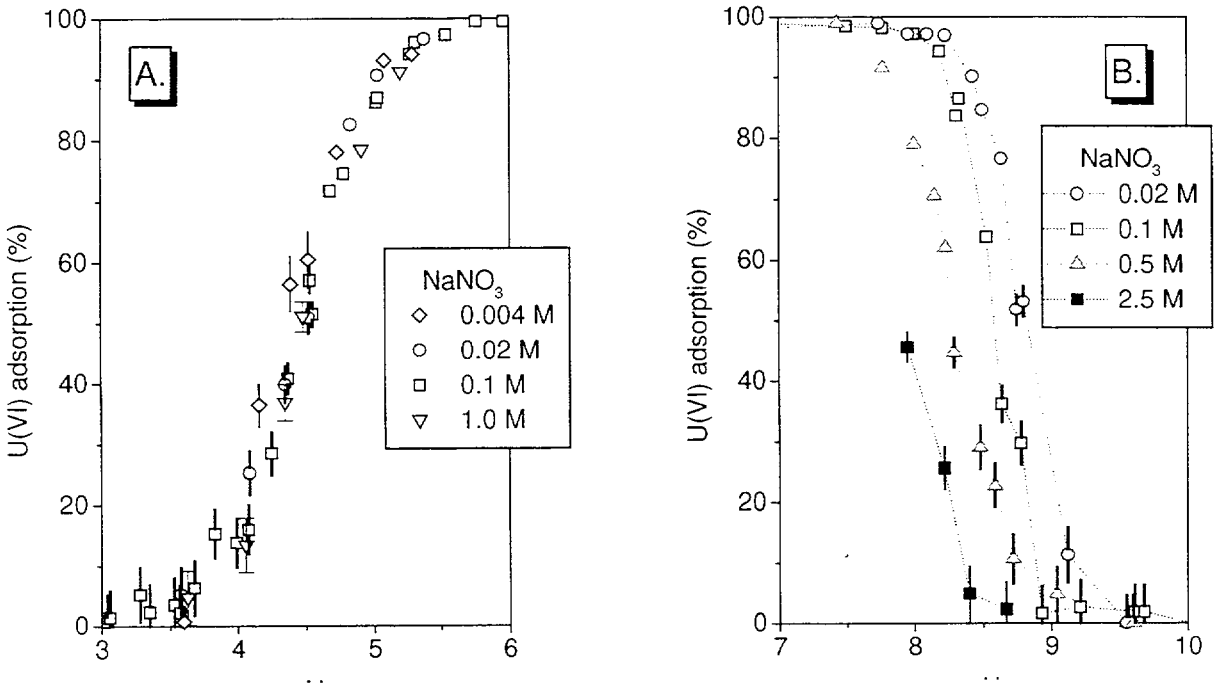

Figure 4-8. Effect of ionic strength on U(VI) adsorption edges. A) Low pH adsorption edge B) High pH adsorption edge. (U_T = 1 μM, Fe_T = 1 mM).

deposit (Yanase et al., 1995). Both ferrihydrite and uranyl phosphate minerals (e.g. saleeite - $Mg(UO_2)_2(PO_4)_2 \cdot 8H_2O$) are found at Koongarra, and significant levels of phosphate (up to 700 μg/L) have been measured in contacting groundwaters (Payne et al., 1994b). The

presence of natural organic matter has also been reported in Koongarra groundwaters, however the behavior and distribution of humic materials in this system has not been studied in detail. Nonetheless, the reported levels of natural organic matter at Koongarra may well be sufficient to influence the migration of uranium (Yanase et al., 1995).

The study of complexing ligands also included the effects of sulfate (SO_4^{2-}) and citrate. These ligands may be significant in affecting U(VI) speciation in anthropogenically affected surface and subsurface environments. For example, SO_4^{2-} may be found in the wastewater from uranium milling operations or in acid mine drainage, and citrate is a component of some mixed wastes of the nuclear industry.

4.3.1 EFFECT OF PHOSPHATE ON U(VI) ADSORPTION

The addition of phosphate to the U(VI)/ ferrihydrite system might be expected to have several potential effects.

- competition with phosphate for surface sites could decrease U(VI) adsorption.

- phosphate might compete with the surface for coordination of UO_2^{2+} by forming aqueous U(VI)-phosphato complexes, thus reducing U(VI) uptake. As shown by the speciation diagram for U(VI) in the presence of phosphate (Figure 4-9), the $UO_2HPO_4^0$ and $UO_2PO_4^-$ complexes are predicted to have an important role in U(VI) speciation under certain conditions.

- precipitation could decrease the amount of U(VI) in solution.

- U(VI) adsorption could be enhanced by the formation of ternary surface complexes involving both UO_2^{2+} and PO_4^{3-}. The formation

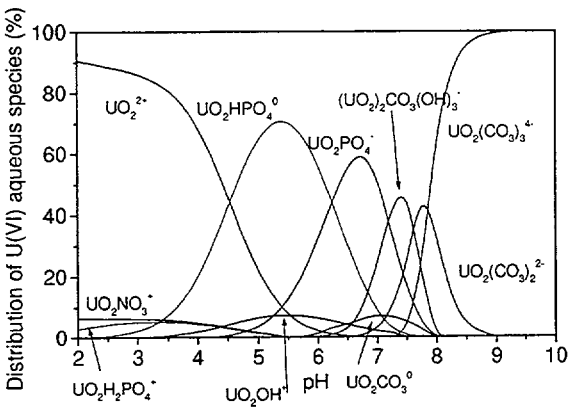

Figure 4-9. U(VI) speciation in the presence of phosphate (precipitation excluded). (U_T = 1 μM, total phosphate = 100 μM).

of ternary surface complexes has been considered in modeling trace metal adsorption (Davis and Kent, 1990) and was described in Section 3 for uranyl-carbonato complexes. For the experiments involving phosphate, we studied systems with U_T of 10^{-4} and 10^{-6} M, and added phosphate of 10^{-4} M (as NaH_2PO_4). The results were compared with corresponding data for phosphate-free systems (Figure 4-10). As in phosphate-free systems, there was a trend of lower adsorption with higher U_T (Figure 4-10), suggesting the existence of surface sites with differing reactivities. This trend suggests that precipitation is not important. If precipitation was occurring, increasing U_T by a factor of 100 would greatly increase the proportion of U(VI) removed from aqueous solution, in which case the "sorption" edges would move to lower pH

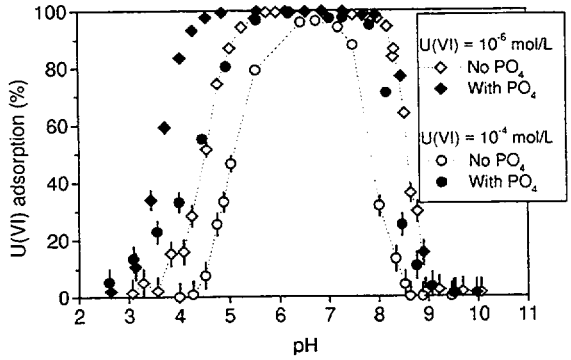

Figure 4-10. Effect of phosphate on U(VI) adsorption by ferrihydrite. (total phosphate = 100 μM, Fe_T = 1 mM, U_T = 1 or 100 μM).

values. A reasonable explanation of the shifts in the edges to higher pH values with increasing U_T is that uptake at low U_T occurs on energetically favorable sites, and on less favored sites with increasing U_T, both in the presence and absence of phosphate.

At both U(VI) concentrations studied (U_T of 10^{-6} and 10^{-4} M), the low pH adsorption edge was moved to the left by about 0.8 pH units by the addition of phosphate. The uptake of phosphate by ferrihydrite was almost complete in this pH range (discussed below), which suggests that the increased adsorption of U(VI) is due to the formation of a ternary complex, rather than a change in aqueous speciation. Increasing U_T from 10^{-6} to 10^{-4} M moved the high pH edge to lower pH values (decreased the proportion of U(VI) adsorbed at a given pH, see Fig. 4-10), both in the presence and absence of phosphate.

For experiments with U_T of 10^{-4} M, the addition of phosphate moved the high pH edge for U(VI) adsorption to the right (increased uptake), whereas phosphate had little or no effect on the high pH edge for U_T of 10^{-6} M (Fig. 4-10). It may at first seem surprising that the effect of phosphate is much smaller in the latter case, where it is present in a large excess relative to U(VI). However, it has been suggested that phosphate is more important than carbonate in U(VI) speciation when the ratio of total phosphate to total dissolved carbonate exceeds 0.1 (Sandino and Bruno, 1992). In our experiments, total phosphate was fixed (10^{-4} M), and total phosphate/total dissolved carbonate decreased from about 0.15 at pH 8 to 0.015 at pH 9 (due to the increase of dissolved carbonate with increasing pH). Therefore, the value of this ratio suggests that phosphate may have a greater effect on the high pH edge for U_T of 10^{-4} M (which, in the absence of phosphate, occurs in the pH range 7 to 8) than on the edge for U_T of 10^{-6} M.

4.3.2 IONIC STRENGTH EFFECTS WITH PHOSPHATE PRESENT

Figure 4-11 shows that the presence of phosphate had a very large effect on the low pH edge, and no discernible effect on the high pH

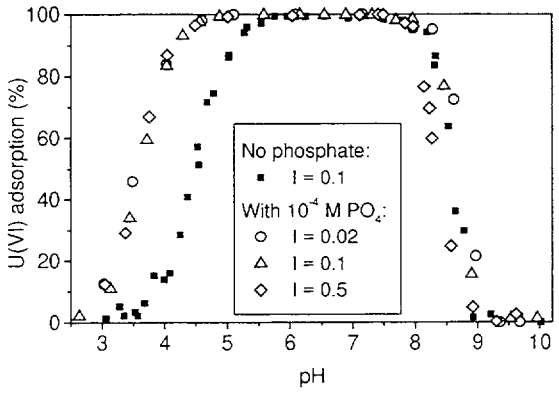

Figure 4-11. Effect of phosphate and ionic strength on U(VI) adsorption by ferrihydrite. Data with added phosphate obtained in 0.02M, 0.1M and 0.5 M $NaNO_3$. (Fe_T = 1 mM, U_T = 1 μM).

edge at I = 0.1. As in the phosphate-free systems, total ionic strength did not affect the low pH U(VI) adsorption edge (Fig. 4-11), but had a significant effect on the high pH adsorption edge. The high pH region is shown in expanded form in Figure 4-12, with data obtained both in the presence and absence of phosphate at various ionic strengths. The presence of phosphate had no effect on U(VI) adsorption above pH 8.0, although the ionic strength had a significant effect. There appeared to be an increase in U(VI) adsorption when phosphate was present at pH < 8.25 with I = 0.5M.

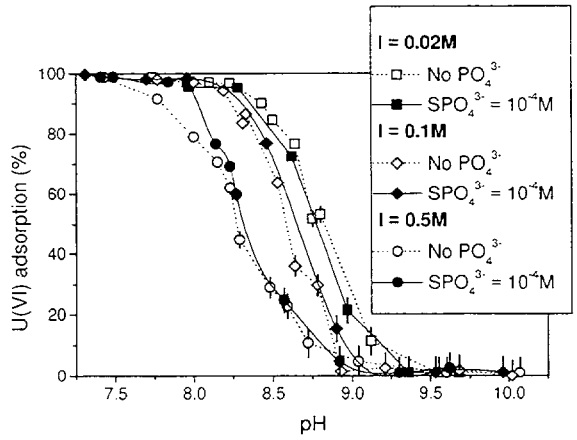

Figure 4-12. U(VI) adsorption by ferrihydrite: effect of ionic strength on the high pH edge in the presence and absence of phosphate. (U_T = 1 μM, Fe_T = 1 mM).

4.3.3 ADSORPTION OF PHOSPHATE ON FERRIHYDRITE IN PRESENCE AND ABSENCE OF U(VI)

The amount of phosphate adsorbed was routinely measured in U(VI) adsorption experiments, and a significant amount of data regarding the adsorption of phosphate in the presence of U(VI) was obtained. Phosphate in solution was measured using the ascorbic acid spectrophotometric method (APHA, 1985). For comparative purposes a set of phosphate adsorption data was obtained in U(VI)-free systems (Fig. 4-13).

Adsorption of phosphate was almost 100% for pH < 6, with a gradual decrease above this pH (Fig. 4-13). The trend of decreasing phosphate adsorption with increasing pH was also found in a previous study (Hawke *et al.*, 1989). Adsorption of phosphate did not seem to be affected by the presence of U_T at 10^{-6} M, which is not surprising because phosphate was present at 100 times greater concentration. Although the data are somewhat scattered, particularly above pH 8, Figure 4-13 suggests that the presence of U_T of 10^{-4} M increased phosphate adsorption in the pH range between 6 and 8. The uptake of U(VI) was strong at these pH values (Fig. 4-10) and this again suggests the formation of a

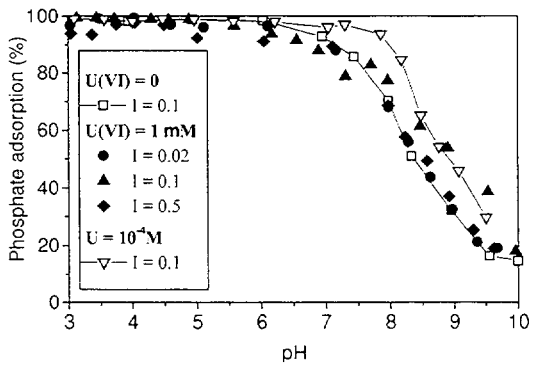

Figure 4-13. Adsorption of phosphate (100 μM) on ferrihydrite in the presence of various U_T. The experiments with 1 μM U(VI) were carried out at 3 ionic strengths and are the same experiments for which U(VI) adsorption data are shown in Fig. 4-11.

ternary surface complex involving PO_4^{3-} and UO_2^{2+}.

Similar results have been found in studies of zinc and phosphate adsorption on goethite (Bolland *et al.*, 1977). These authors reported that "the presence of phosphate or zinc on the goethite surface was found to increase slightly the adsorption of zinc and phosphate respectively", and suggested the formation of a surface complex involving both Zn^{2+} and phosphate ions.

There was not a discernible effect of ionic strength on phosphate adsorption, although as mentioned previously, the high pH adsorption edge for U(VI) in both the presence and absence of phosphate was affected by ionic strength (compare Figs. 4-12 and 4-13). It may be tentatively concluded that the ternary surface complex involves direct binding via the uranyl cation at the surface, rather than phosphate being a bridging ligand.

4.3.4 DISCUSSION OF THE EFFECTS OF PHOSPHATE ON U(VI) ADSORPTION

The formation of a ternary surface complex involving UO_2^{2+} and PO_4^{3-} on the ferrihydrite surface provides a possible explanation for the experimental results with ferrihydrite. However, the possibility that precipitation might be occurring in the experiments was also considered.

Calculations with MINTEQA2, using the thermodynamic data for uranyl/phosphate aqueous complexes and solid phases from the NEA data base (Grenthe *et al.*, 1992), showed that precipitation of $(UO_2)_3(PO_4)_2 \cdot 4H_2O$ was possible between pH values of approximately 4.75 and 7.25 for systems with a U_T of 10^{-6} M, total phosphate of 10^{-4} M, and no adsorbents. When ferrihydrite was present (and the equilibrium concentrations of U(VI) and phosphate were greatly reduced by sorption), no supersaturation was predicted. Figure 4-10 shows that the presence of phosphate increased U(VI) adsorption at pH < 4.5, at which no precipitation was expected even in the absence of ferrihydrite. Further evidence that precipitation of U(VI)-phosphate phases was not responsible for removing U(VI) from solution in the adsorption experiments comes from analogous experiments with kaolinite (see Section 7), in which much higher equilibrium concentrations of U(VI) and phosphate were measured at pH < 6. This would not be expected if precipitation was occurring in the experiments with ferrihydrite.

A ternary surface complex involving both U(VI) and phosphate on the ferrihydrite surface is therefore a reasonable explanation of our experimental results. However, another possible mechanism has been suggested by Benjamin and Bloom (1981), who studied adsorption of Zn(II) on ferrihydrite in the presence of phosphate. Their experimental system contained equal amounts of phosphate and Fe (10^{-3} M), and it was proposed that a secondary surface phase formed in the presence of strongly sorbing anions (such as phosphate). It was further suggested that this surface phase adsorbed trace metals more strongly than the original ferrihydrite. Benjamin and Bloom (1981) hypothesized that adsorption was the dominant mechanism at low adsorption density, but there existed a certain adsorption density at which an iron-anion surface precipitate would form. The systems presented here contain an order of magnitude more Fe(III) than phosphate, and it appears that the uptake of phosphate could be explained by adsorption alone. Nonetheless, surface precipitation of another solid phase (such as ferric phosphate) could influence the experimental results, particularly if it bound U(VI) very strongly.

4.3.5 EFFECTS OF HUMIC ACID

The effect of natural organic materials on the mobility of various pollutants has been studied by several workers. It has been suggested that the adsorption behavior of oxide surfaces is modified when adsorption sites for trace metal ions become dominated by the functional groups of adsorbed humic compounds (Davis, 1984).

There have been several studies of the importance of humic substances in actinide

speciation (e.g. Tipping, 1993), and some previous work has focused on the impact of these substances on actinide adsorption (Ho and Miller, 1985; Moulin and Ouzounian, 1992). U(VI) adsorption on hematite was increased by the presence of humic acids (HA) (Ho and Miller, 1985), whereas the presence of model organic materials did not alter the adsorption of Np on Fe- or Al- oxides, or tuff material (Kung and Triay, 1994).

For our experiments with HA, a stock solution of HA was prepared by dissolving 50 mg of Aldrich sodium humate in 500 mL of MilliQ water, and filtered through a glass fibre filter. The proportion of solid retained by the filter was determined (by weighing) to be 10±2%. The amount of HA in the adsorption experiments was a 1:10 dilution of the filtered stock solution, corresponding to a HA content of approximately 9 mg/L. The amount of HA adsorbed was determined using spectrophotometry at 350 nm (Nomizu *et al.*, 1989). Shorter wavelengths could not be used due to absorption by the background electrolyte ($NaNO_3$). Although the absorbance at 350 nm followed a Beer's law relationship, the technique is non-specific and gave only a semi-quantitative indication of HA uptake by the solid.

The addition of HA (9 mg/L) moved the low pH adsorption edge on ferrihydrite to lower pH values (increasing adsorption), but had little effect on the high pH edge (Fig. 4-14). The uptake of HA by the ferrihydrite was generally strong, but decreased at high pH values, which is a similar trend to that previously reported for adsorption of HA on Al_2O_3 (Stumm, 1992; Davis, 1982) and hematite (Ho and Miller, 1985).

Moulin and Ouzounian (1992) reported that the formation of an organic coating increased the uptake of americium (Am) at low pH values, whereas at higher pH values, humic substances were predominantly in solution and prevented Am adsorption through aqueous complex formation. The present results for U(VI) adsorption are consistent with the reported behaviour of Am. In our experiments, HA was strongly adsorbed across a wide pH range, and

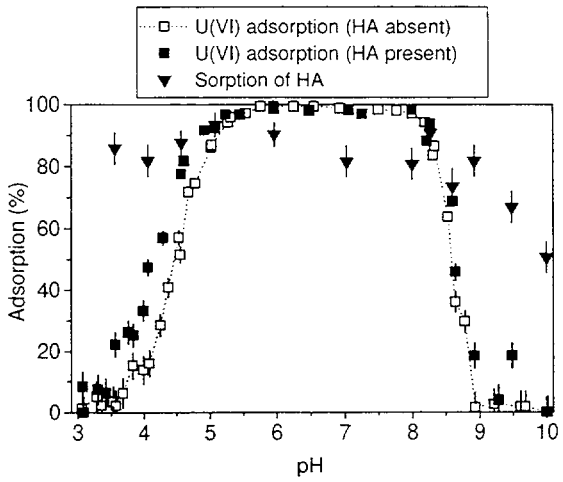

Figure 4-14. Adsorption of U(VI) by ferrihydrite in the presence and absence of humic acid (HA). Sorption of HA by ferrihydrite is also shown. (U_T = 1 μM, HA = 9 mg/L, Fe_T = 1 mM, 0.1M $NaNO_3$ in equilibrium with air).

there were no conditions under which U(VI) adsorption was prevented by the formation of aqueous complexes involving HA. However, as was observed for Am, the presence of HA increased U(VI) uptake in the low pH range, thereby moving the low pH adsorption edge to lower pH values.

During the adsorption experiments, over 80% of the HA was adsorbed to the ferrihydrite, and the final concentrations of HA in solution (1 - 2 mg/L) were comparable to the amount of total organic carbon (TOC) reported for Koongarra groundwaters by Yanase *et al.* (1995). Consequently, it seems probable that organic matter has a significant affect on U(VI) adsorption at the Koongarra field site, even though it is only present at low concentrations in the groundwater. However, natural humic materials are dissimilar in many respects to commercial humic substances, such as the Aldrich humic acid used in this work (Malcolm and MacCarthy, 1986), and the natural organic materials present in Koongarra groundwaters have not been characterized in detail. Consequently, the effect of natural organic matter on U(VI) adsorption in the Koongarra system is yet to be fully understood.

4.3.6 EFFECTS OF SULFATE

We have shown that adsorption of U(VI) on ferrihydrite is greatly increased by the presence of phosphate. It has been reported that some other anions have an effect on U(VI) adsorption on various oxides, with both increases and decreases in U(VI) adsorption being observed when SO_4^{2-} was present (Venkataramani and Gupta, 1991). Sulfate is present in many groundwaters, but is of particular importance in the vicinity of some uranium milling operations, where sulfuric acid may be used in the leaching process. Sulfate is also a component of acid mine drainage. Consequently the effect of sulfate on U(VI) adsorption is of both theoretical and practical interest.

The presence of SO_4^{2-} has a significant influence on U(VI) speciation at pH < 6. The speciation of U(VI) (U_T = 1 μM) in the presence of 0.01M SO_4^{2-} is shown in Figure 4-15. The thermodynamic data for aqueous U(VI)-sulfato complexes was taken from Grenthe *et al.* (1992).

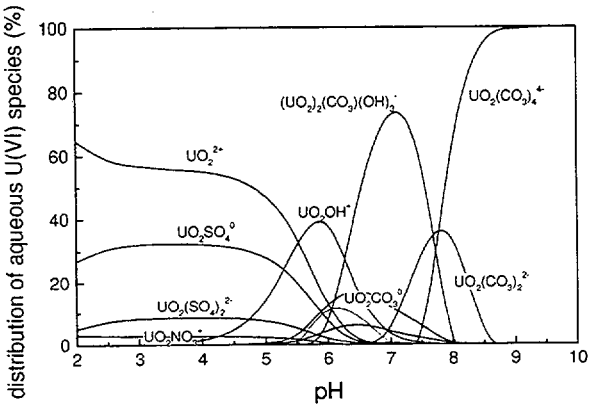

Figure 4-15. Speciation of U(VI) in the presence of 0.01M SO_4. (Background electrolyte $NaNO_3$, I = 0.1M, system in equilibrium with air, U_T = 1 μM).

Experimental data for U(VI) adsorption on ferrihydrite in the presence and absence of SO_4^{2-} (0.01M) are illustrated in Figure 4-16. Sulfate had a small effect on the low pH edge, generally causing a slight decrease in U(VI) adsorption at pH < 6 at both U_T concentrations. The decrease in U(VI) adsorption is attributed to the formation of the U(VI)-sulfato complexes (Fig. 4-15). The data are a marked contrast to phosphate, which dramatically increased U(VI) adsorption on ferrihydrite even at low phosphate concentrations.

4.3.7 EFFECTS OF CITRATE

The citrate anion is another ligand that is of relevance to migration studies, and which is present at low levels in natural soil solutions (Sposito, 1989). It is among the organic anions that are expected to be present in the radioactive wastes which will be emplaced in repositories such as the WIPP site (Choppin *et al.*, 1996).

The presence of citrate of 0.01M had a major effect on the adsorption of U(VI) by ferrihydrite (Fig. 4-17). At U_T concentrations of 10^{-5} and 10^{-6} M, the adsorption of U(VI) was reduced to zero across the entire experimental pH range from 3 to 10. In the ligand-free system, U(VI) uptake was close to 100% at pH values between 5 and 8. It was noted, however, that the ferrihydrite apparently dissolved in the presence of the citrate, particularly in the low pH range.

To further investigate this phenomena, both the solid residual phase and supernatant phases were analyzed for Fe (after centrifugation). The results are shown in Figure 4-17, together with corresponding data for systems in which no citrate was present. When citrate was absent, the ferrihydrite was stable across a wide pH range, with significant amounts dissolved only at pH < 3.5. However, when citrate was present, the ferrihydrite was entirely dissolved at pH < 6.5. Thus, the reduced uptake of U(VI) can be attributed to both complexation of U(VI) in the aqueous phase by citrate and to dissolution of the adsorbent.

The dissolution of ferrihydrite in the presence of citrate was calculated with MINTEQA2, using the thermodynamic data for the solubility of ferrihydrite and Fe(III)-citrate complexes supplied with the code. The computational results are shown in Figure 4-18, which predict a large increase in the solubility of ferrihydrite in the presence of citrate. This is consistent with the experimental data. Although the calculated

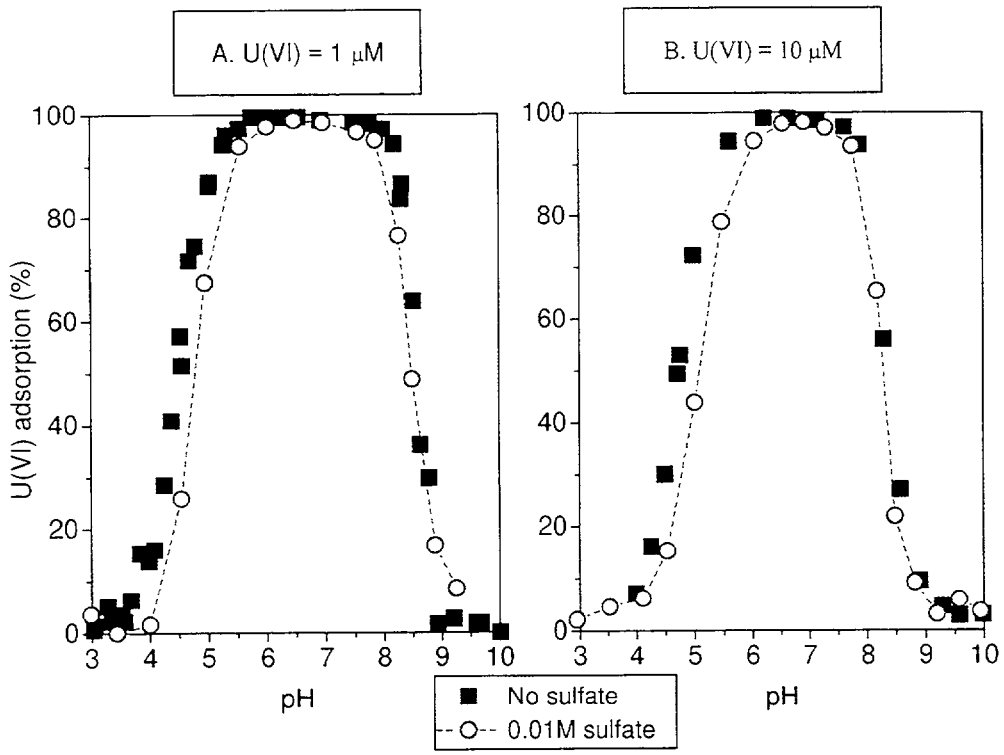

Figure 4-16. Effect of sulfate on U(VI) adsorption by ferrihydrite. (Fe_T = 1 mM, I=0.1, system in equilibrium with air, SO_4 = 0 and 0.01M). A) U_T = 1 μM, B) U_T = 10 μM.

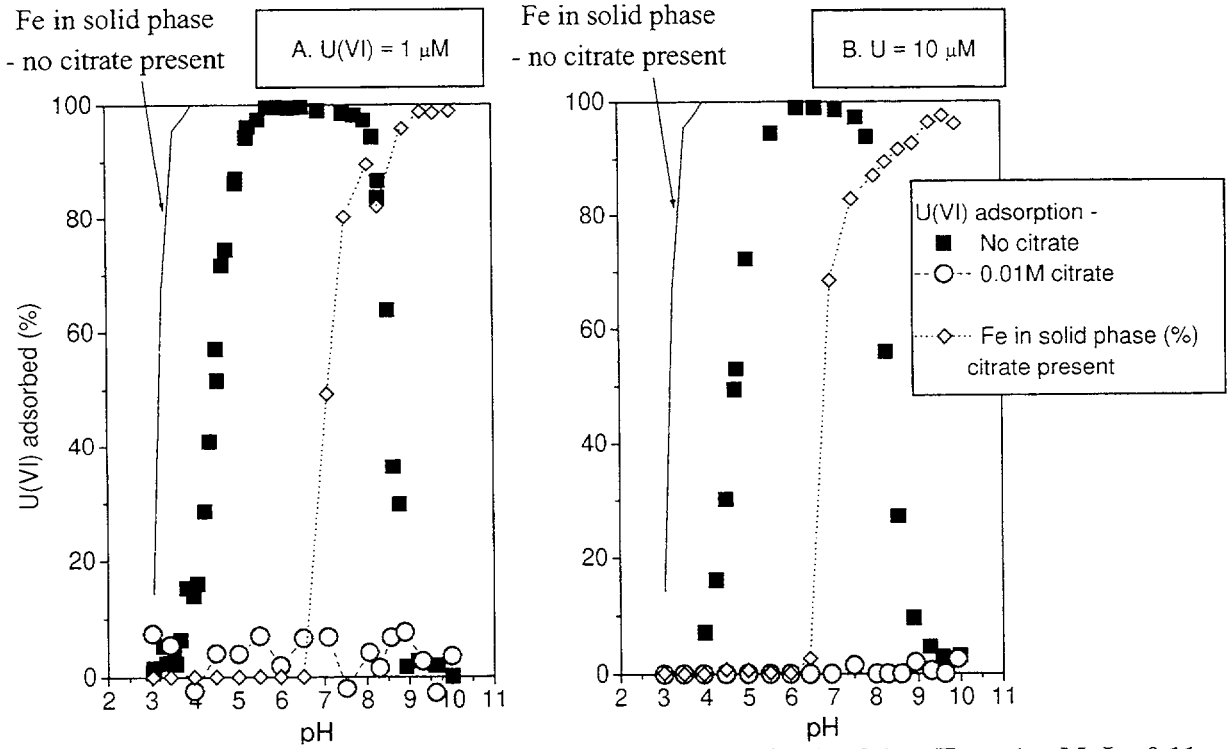

Figure 4-17. Effect of 0.01M citrate on U(VI) adsorption by ferrihydrite. (Fe_T = 1 mM, I = 0.11, system in equilibrium with air). A) U_T = 1 μM, B) U_T = 10 μM.

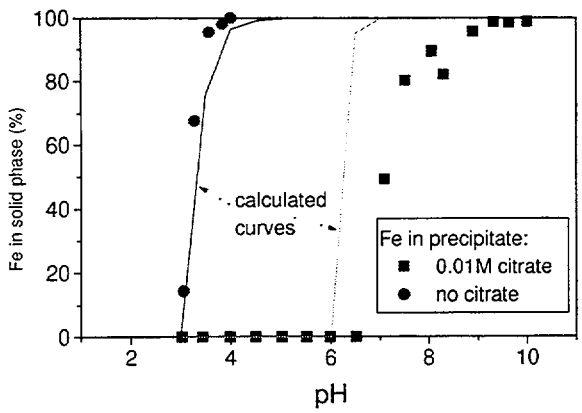

Figure 4-18. Experimental data and MINTEQA2 simulations of the amount of Fe in the ferrihydrite phase in the presence and absence of 0.01M citrate. (Fe_T = 1 mM).

curve is somewhat displaced from the experimental data, this may be explained by differences in experimental conditions, such as the aging of ferrihydrite.

It has recently been reported that U(VI) adsorption on goethite, gibbsite and phyllosilicate minerals is unaffected, or dramatically *increased* by the presence of citrate (Redden *et al.*, 1996), with a stable bridging structure between uranyl and citrate at the surface being suggested. This observation is in marked contrast with the results for ferrihydrite because of the facile dissolution of the solid phase.

4.3.8 IMPLICATIONS FOR MODELING U(VI) ADSORPTION

The results show that phosphate, sulfate, citrate and dissolved humic material may influence U(VI) migration in natural environments. They have a diverse range of effects. Phosphate appeared to generally increase U(VI) adsorption via formation of a ternary surface complex and may also affect U(VI) solubility. Sulfate decreased U(VI) adsorption by forming an aqueous complex. Citrate decreased U(VI) adsorption by dissolving ferrihydrite. Humic acid adsorbed strongly at low pH and increased adsorption of U(VI) by forming a surface complex. At higher pH values, humic material may be predominantly dissolved and possibly decreased adsorption by forming aqueous U(VI)-HA complexes.

Some of the factors which influence U(VI) adsorption on ferrihydrite are summarised in Table 4-1. Whilst a large number of factors play a role, it appears that an SCM model can be developed to take into account this diverse range of interactions, provided an adequate database is accumulated.

4.4 Conclusions

U(VI) adsorption on ferrihydrite is influenced by a large number of factors, including pH, ionic strength, partial pressure of CO_2, solid/water ratio, and U_T. The isotherm for U(VI) adsorption is not linear and the constant K_d approach to modeling adsorption is not applicable. A large database suitable for modeling U(VI) adsorption using the surface complexation model has been accumulated.

The effects of various ligands on U(VI) adsorption by ferrihydrite have been studied. Phosphate and humic acid generally enhanced U(VI) adsorption, which was attributed to strong surface binding of both phosphate and humic substances, and the formation of ternary surface complexes. Adsorbed phosphate and humic materials could play an important role in U(VI) migration in acidic environments, even when only small concentrations of these substances are present in the aqueous phase.

Existing thermodynamic data appear to provide a reasonable qualitative explanation of the effects of SO_4^{2-} and citrate on U(VI) adsorption. Development of an SCM to describe U(VI) interactions with adsorbed phosphate and HA requires that the aqueous speciation of U(VI) in the presence of these ligands be well understood. However, the values of complexation constants for species involving dissolved UO_2^{2+} and PO_4^{3-} are still uncertain, and the identity of the principal species has been the subject of debate (Sandino and Bruno, 1992). In the case of humic materials, the situation is complicated by the fact

that these materials comprise a diverse range of natural substances.

This study highlights the complexity of modeling U(VI) adsorption and the importance of understanding the adsorptive behavior of complexing ligands, as well as any radionuclide of interest. A large number of parameters affect U(VI) adsorption, and large multidimensional datasets will be required to apply an SCM to natural systems.

Table 4-1. Factors that influenced U(VI) adsorption on ferrihydrite

Factor	Range studied	Effect
Ionic strength [$NaNO_3$]	0.02 - 2.5M	An increase in ionic strength reduced U(VI) adsorption at high pH values, but did not significantly affect adsorption at pH < 7.0.
pCO_2	$10^{-3.5}$ atm and 10^{-2} atm	Increasing pCO_2 decreased U(VI) adsorption at high pH values.
U_T	10^{-8}, 10^{-6}, 10^{-5} and 10^{-4} M	The proportion of U(VI) adsorbed decreased with increasing U_T. That is, the low pH edge moves to higher pH values and the high pH edge to the lower pH values.
Amount of ferrihydrite	$Fe_T = 10^{-3}$, $2x10^{-2}$ M	Increasing total Fe increased U(VI) adsorption.
Humic acid	HA = 9 mg/L	HA increased U(VI) adsorption at pH < about 7, and had little effect at high pH values
Phosphate	$(PO_4)_T = 10^{-4}$ M	The presence of PO_4 appeared to increase U(VI) adsorption at pH values up to about 8, but had little effect on the high pH 'desorption' edge. When phosphate was present, the low pH edge for U(VI) adsorption was unaffected by ionic strength, and the high pH edge for U(VI) adsorption was sensitive to ionic strength.
Sulfate	0.01M	Sulfate slightly decreased U(VI) adsorption at pH values below about 7.0. This appears to be due to formation of aqueous $UO_2SO_4^0$ and $UO_2(SO_4)_2^{2-}$. The effect was much weaker than that of phosphate.
Citrate	0.01M	0.01M citrate completely suppressed U(VI) adsorption on ferrihydrite and (at pH values up to about 6.5) dissolved the ferrihydrite.

5 URANIUM(VI) ADSORPTION ON CRUSHED QUARTZ IN $NaNO_3/HCO_3$ SYSTEMS

This section presents the results of batch studies of U(VI) adsorption by suspensions of cleaned quartz powder in $NaNO_3$ solutions. In a subsequent section, these data are used to develop and calibrate a surface complexation model to describe U(VI) adsorption on the quartz surface. Other studies of U(VI) adsorption on silica phases include those of Lieser et al. (1992) and Turner et al. (1996).

5.1 Methods and Materials

5.1.1 CHARACTERIZATION OF QUARTZ

Quartz was obtained under the brand name Min-U-Sil 30 (Pennsylvania Glass & Sand Company) and was treated to remove surface contaminants and to obtain a narrow distribution in particle diameter. After heating to 550°C for 48 to 60 hours to destroy organic material, batches of quartz were refluxed in 4M HNO_3 to dissolve and remove traces of aluminum and iron oxides (MacNaughton, 1973; Vuceta, 1976). After repeating the acid reflux, Min-U-Sil 30 was washed in deionized water several times, followed by suspension in deionized water adjusted to a pH between 9 and 10. The dilute alkaline solution leaches readily soluble silica, which dissolves more rapidly at high pH values (Wirth and Gieskes, 1979). After several additional acidic washes, the quartz was washed and decanted at least 8 times with deionized water. BET surface analysis (Kr and N_2 adsorption) yielded a specific surface area of 0.33 m^2/g (± 0.03). Figure 5-1 shows a typical Kr adsorption isotherm and the corresponding BET plot; the slope and intercept of the plot were used to determine the specific surface area. Scanning electron microscope (SEM) photographs show that the grain size ranged from 8 to 30 μm. Figure 5-2 shows two SEM photographs at two different enlargements of the cleaned quartz. The mineralogy was greater than 99% quartz by X-ray diffraction.

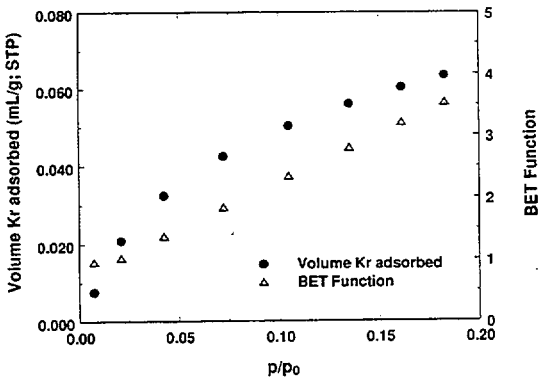

Figure 5-1. Adsorption isotherm and BET function for krypton gas on the crushed, cleaned quartz surface.

5.1.2 SOLUTIONS

Solutions were made from reagent grade chemicals following standard laboratory procedures. A combination glass electrode (Ross pH Combination Electrode, Orion No 8102) was used for pH measurements after two point pH calibrations. pH was measured in quiescent suspensions after thorough mixing. Background electrolytes were $NaNO_3$ or KNO_3, and in some cases the solutions contained the ligands fluoride, phosphate, carbonate or acetate. Acetic acid buffer solutions were made up from glacial acetic acid and sodium acetate trihydrate.

U(VI) solutions contained depleted natural uranium (except for the lowest total U(VI) concentrations) and ^{233}U tracer. ^{233}U tracer was obtained in 1N HCl solution with a specific activity of approximately 2 μCi/mL (UO_2Cl_2 precipitates were dissolved in HCl). Aliquots of a 1000 ppm $UO_2(NO_3)_2$ atomic absorption standard (Anderson Laboratories) were added to make stock solutions of 10^{-4} M or $5 \cdot 10^{-3}$ M U(VI), both with a ^{233}U activity of approximately 10,000 dpm/mL. Stock solutions of U(VI) were diluted 1:100 with electrolyte for the batch experiments.

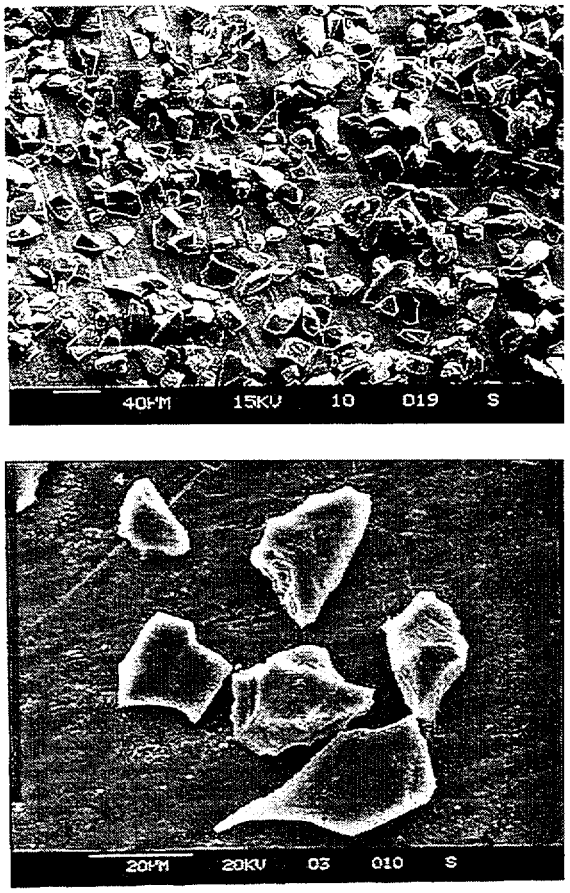

Figure 5-2. Scanning electron micrographs of typical particles of the crushed, cleaned quartz sample used in the batch adsorption experiments. Pictures courtesy of D. B. Kent (USGS, Menlo Park, CA).

5.1.3 URANIUM ANALYSIS

^{233}U was determined by liquid scintillation counting (LSC) on a Beckman LS 6000 counter. Alpha peaks were integrated after background subtraction. The efficiency for the α particles was 100%. Analytical uncertainties in ^{233}U α-counting lead to an overall uncertainty in the relative concentration for U(VI) of 3% or less. In some cases U(VI) concentrations were determined with a kinetic phosphorescence analyzer (Chemchek Instruments, model KPA-11). Results reported by this method agreed very well with the ones obtained with the radiometric method using ^{233}U described above.

5.1.4 METHODS FOR BATCH EXPERIMENTS

Two grams or 200 mg of quartz were weighed into polycarbonate centrifuge tubes (Oak Ridge type, Nalgene #3118-0050) and 20 mL of electrolyte (0.01M $NaNO_3$ or KNO_3) were added. The pH was adjusted with 0.01N NaOH or HNO_3 to the desired initial value, and samples were preequilibrated at that pH for approximately 20 hours. After preequilibration, a small aliquot of a concentrated uranium spike solution (typically 200 µL) containing ^{233}U and depleted natural U(VI) was added, and the pH was readjusted to the initial desired value. Samples were then equilibrated on a rotor for typically 16 hours. At the end of this equilibration time the final pH was measured. The quartz was allowed to settle and 4 mL of supernatant was withdrawn and mixed with liquid scintillation cocktail (Ecolite+) for analysis by LSC. Occasionally, activity balance checks were conducted by transferring an entire suspension from one centrifuge tube (CT) into another CT that was not previously exposed to any U(VI). The contents of both CT's were then acidified with HNO_3 and the activity of aliquots was measured after 10 hours. With this method it could be tested whether significant fractions of U(VI) were adsorbed to the CT's, and from the mass balance calculations, a value for the reference activity was obtained.

5.2 Results

5.2.1 KINETICS OF U(VI) ADSORPTION AND DESORPTION

Results from U(VI) adsorption kinetic experiments with quartz are shown in Figure 5-3. Experiments were carried out at a total U(VI) concentration of 10^{-6}M, 100 g quartz/L, and an ionic strength of 0.01M $NaNO_3$. Since U(VI) uptake was very pH sensitive, the solutions were buffered to pH = 4.80 (±0.05) with an acetate buffer of 10^{-4} M total acetate concentration. HYDRAQL (Papelis et al., 1988) calculations of the solution speciation have shown that only a small fraction (3%) of U(VI) is complexed with the acetate ion under these conditions. U(VI) uptake was on the order of minutes as can be

seen in Figure 5-3. In fact constant dissolved U(VI) concentrations were obtained before phase separation and final pH measurements could be completed. Data for the desorption kinetics were obtained by replacing the supernatant at the end of a batch experiment with an aliquot of solution with the same pH and volume as the supernatant. In this experiment, the total U(VI) concentration in the system was approximately $6 \cdot 10^{-7}$M, because of the U(VI) withdrawn with the supernatant solution. Acetate buffer was not present in the desorption solution and the pH drifted from 4.8 to 4.9. As a consequence of the decrease in total U(VI) in the experiment and the slight pH change, the fractional uptake (expressed in percent of total U(VI) in the system) increased from 55% in the adsorption experiment to 65% in the desorption experiment. However, as can be seen in Figure 5-4, equilibrium was achieved in the desorption experiment within minutes. The fast kinetics for the U(VI) adsorption reactions were advantageous in the transport experiments conducted in this study, which are described in Section 17 of this report.

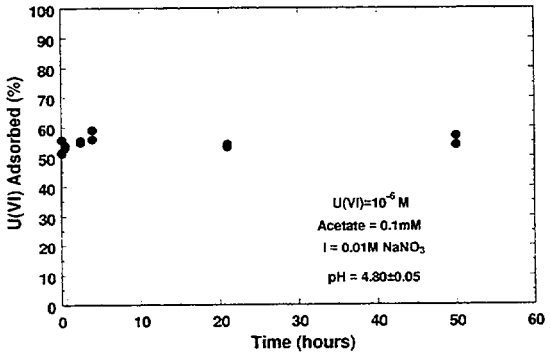

Figure 5-3. Adsorption of 10^{-6}M U(VI) on a 100 g quartz/L suspension in 0.01M $NaNO_3$ solution at pH 4.8 as a function of time. The pH was buffered with 10^{-4}M acetate buffer.

5.2.2 U(VI) ADSORPTION AS A FUNCTION OF IONIC STRENGTH

Adsorption edges of 10^{-6}M total U(VI) at ionic strengths (I) of 0.1M, 0.01M and 0.005M KNO_3 are shown in Figure 5-5 for suspensions of 100 g quartz/L. No clear trend in U(VI) adsorption was

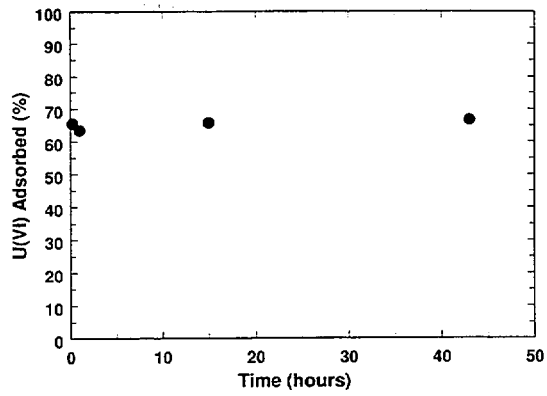

Figure 5-4. Desorption of U(VI) as a function of time after resuspension of quartz particles with adsorbed U(VI) in $NaNO_3$ solution without U(VI). The data are expressed as fractional adsorption of 6 x 10^{-7}M U(VI) on a 100 g quartz/L suspension in $NaNO_3$ solution at pH 4.9. At time = 0, 100% of the U(VI) was adsorbed (after a 20 hour adsorption experiment).

found over this range of ionic strengths; data points for different ionic strengths at any given pH were within experimental error. Similar results were observed for U(VI) adsorption on ferrihydrite for the pH range 4 to 7 (Waite et al., 1994b). The lack of adsorption dependence on ionic strength is commonly observed to be consistent with "inner-sphere" surface complexation (Davis and Kent, 1990) as determined by surface spectroscopy. In this case, the observation is consistent with the

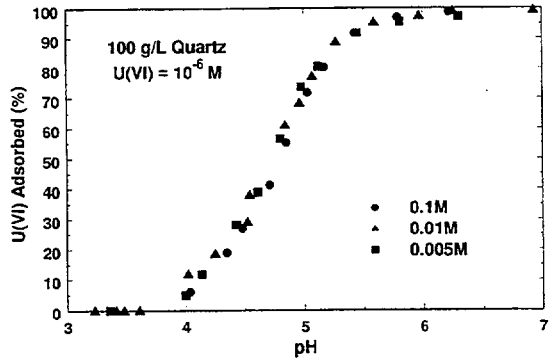

Figure 5-5. Adsorption of 10^{-6}M U(VI) on 100 g quartz/L as a function of pH and ionic strength. System open to the atmosphere.

bidentate uranyl bonding with surface functional groups determined from EXAFS spectroscopy for iron oxides (see Section 3). Specific adsorption by the formation of coordinative bonds at the surface, as opposed to an ion exchange mechanism, is indicated from the lack of dependence on ionic strength. The same result would be expected if Na^+ rather than K^+ was used as the electrolyte cation.

5.2.3 EFFECT OF FLUORIDE, CARBONATE, AND PHOSPHATE ON U(VI) ADSORPTION

U(VI), as uranyl (UO_2^{2+}), is a "hard" cation which readily forms solution complexes with a number of "hard" ligands (mostly O-donor ligands, such as carboxylic acids). Such complexes can enhance the mobility of U(VI) and other metals in the groundwater environment (Kohler et al., 1996; Lienert et al., 1994; Doner, 1978; Jardine et al., 1993; Killey et al., 1984; Cleveland and Rees, 1981; Kent et al., in preparation). An important ligand is the carbonate ion because many groundwaters in the pH range from 7 to 10 contain significant concentrations of U(VI)-carbonate species, such as $UO_2CO_3^0{}_{aq}$, $UO_2(CO_3)_2^{2-}$, $UO_2(CO_3)_3^{4-}$, and $(UO_2)_2CO_3(OH)_3$ (see Section 2). Another "hard" ligand, fluoride, was chosen for study because its complexation effects can be studied without the possible experimental complexity required to control the partial pressure of carbon dioxide (pCO_2).

Figure 5-6a shows the pH dependence of U(VI) adsorption over a wide pH range. At pH values greater than 7, a steep decrease in U(VI) adsorption was observed due to the formation of aqueous uranyl-carbonato complexes (Lieser et al., 1992). Waite et al. (1994b) showed that the pH range at which this sharp decrease in U(VI) adsorption occurs depends on pCO_2, and although this was not tested, it is likely true for the quartz system as well. In many aquifers, pCO_2 increases along groundwater flow paths due to microbiological or carbonate weathering processes. As this occurs, the mobility of U(VI) will increase due to the formation of aqueous uranyl-carbonato complexes. Transport modeling of this type of system can best be

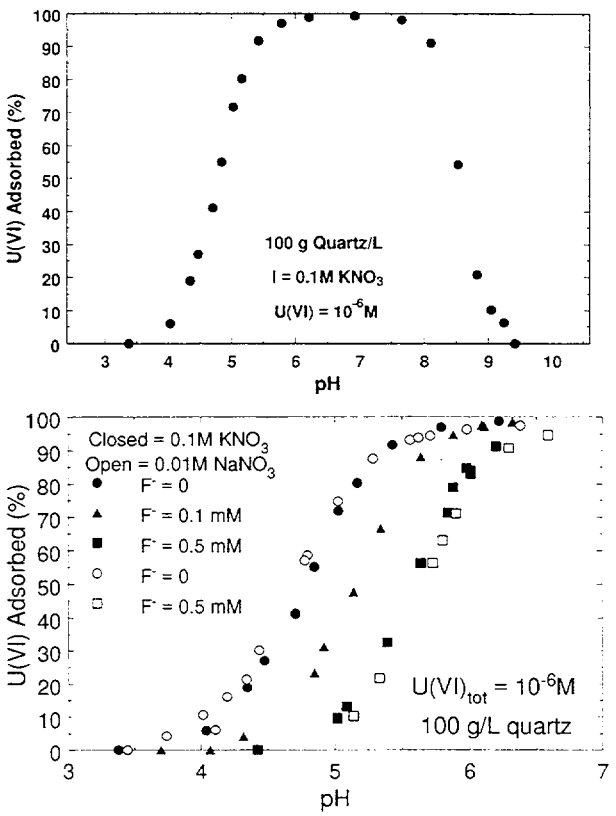

Figure 5-6. Adsorption of 10^{-6}M U(VI) on 100 g quartz/L as a function of pH and the concentration of complexing ligands. (Part A, top) System equilibrated with ambient atmosphere in 0.01M KNO_3 solution, illustrating effect of aqueous complexation with carbonate in alkaline pH range, and (Part B, bottom) Effect of fluoride concentration at two different ionic strengths.

accomplished by including the surface complexation concept to describe adsorption (Kohler et al., 1996).

Figure 5-6b shows the effects of fluoride complexation on the adsorption of U(VI) onto 100 g quartz/L. Fluoride (F) shifted the U(VI) adsorption edge one half pH unit higher at a total F concentration of 100 μM and approximately one entire pH unit higher at 500 μM F. Thus, enhanced U(VI) mobility in the presence of fluoride during transport through quartz porous media can be expected, and this effect has now been observed and modeled (Kohler et al., 1996; Chaps. 17 and 18 of this report). The data shown

in Figure 5-6 were obtained by two different investigators in our laboratory, each using different techniques for U(VI) analysis and different batches of cleaned quartz. These two datasets show very close agreement, well within experimental error.

Phosphate at a low concentration ($2 \cdot 10^{-6}$M) had a negligible effect on U(VI) adsorption (Figure 5-7). This experiment was performed because surface complexation model results had shown that calculated U(VI) adsorption on quartz in the presence of phosphate was sensitive to the value of the thermodynamic formation constant chosen for the aqueous uranyl-phosphate complex. Understanding the importance of phosphate to U(VI) mobility is of interest in the Koongarra field setting (Payne et al., 1996; Yanase et al., 1995; Sandino and Bruno, 1992). At the experimental conditions given in Figure 5-7, model simulations predicted a very large decrease in U(VI) adsorption using the constant of Dongarra and Langmuir (1980) for the aqueous uranyl-phosphate complex. In contrast, the value of the constant chosen by Grenthe et al. (1992) (Table 2-1) predicts negligible effect on U(VI) adsorption, which was the result observed (Fig. 5-7).

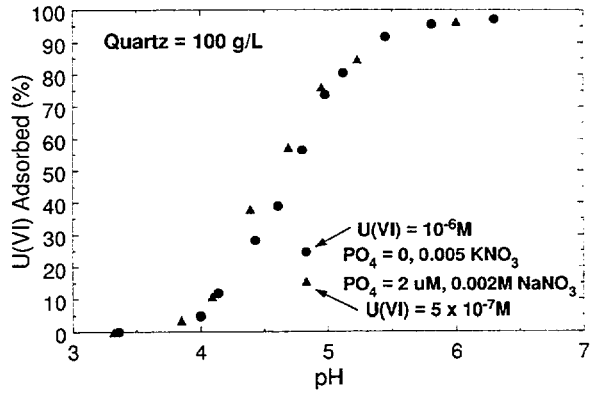

Figure 5-7. Comparison of U(VI) adsorption on 100 g quartz/L as a function of pH in the presence and absence of phosphate. Circles: 10^{-6}M U(VI) in 0.005M KNO_3 solution without phosphate. Triangles: 5 x 10^{-7}M U(VI) in 0.002M $NaNO_3$ solution with 2 x 10^{-6}M phosphate added.

5.2.4 BATCH ADSORPTION ISOTHERMS

A series of batch adsorption experiments was conducted with quartz suspensions with I = 0.01M $NaNO_3$ and variable total U(VI) concentrations ranging from 10^{-8} M to 10^{-4} M. The results of these experiments are shown in Figure 5-8a (for 10g/L) and Figure 5-8b (for 100g/L) as a series of pH-adsorption edges. The error for each point is of the order of 3% U(VI) adsorbed, and thus the relative error for points below 10% U(VI) adsorbed is relatively high. With increasing total U(VI) concentration the edges become flatter, until at 10^{-4}M (for 100g/L) and 10^{-5}M (for 10g/L), saturation of the quartz surface occurs. The fact that the same surface coverage is obtained for two different quartz/solution ratios and two different total U(VI) concentrations confirms that the surface is saturating and suggests that precipitation of uranium hydroxide is not controlling the aqueous U(VI) concentration. The equilibrium solution concentration of U(VI) is ten times greater for the 100 g/L experiments than for the 10 g/L experiments, yet the surface adsorption densities are approximately the same. Isotherms can be constructed from the adsorption edges by interpolating data between experimental points at constant pH. The isotherms are shown in Figure 5-9. The slopes of the isotherms (in log-log form) are less than one, and they become flatter at U(VI) concentrations greater than 10^{-5}M. The fact that the slopes are less than one indicates that the isotherms are non-linear, even at the lowest U(VI) concentrations. The consequences of the non-linear isotherm will be discussed further in Sections 13, 17 and 18.

5.3 Summary

U(VI) adsorption by quartz had a similar pH dependence to that observed for U(VI) adsorption on ferrihydrite (see Section 4). Fluoride complexation of U(VI) in the acidic pH range decreases U(VI) adsorption, while carbonate complexation decreases adsorption in the alkaline pH range. Similar to U(VI) adsorption on ferrihydrite, the low pH adsorption edge shows little ionic strength dependence.

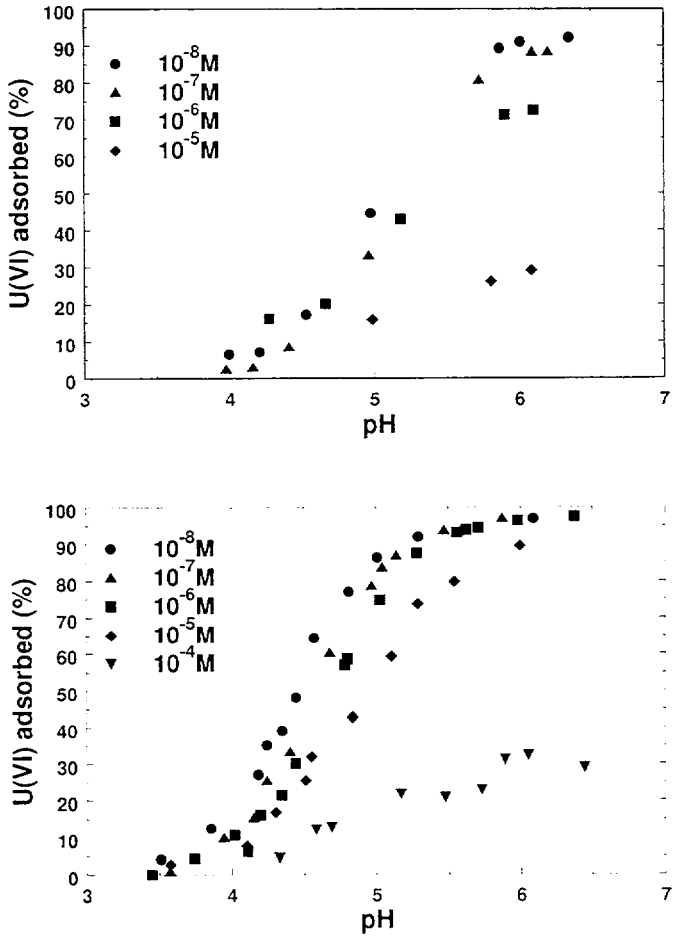

Figure 5-8. Adsorption of U(VI) on quartz as a function of pH and the total U(VI) concentration in 0.01M $NaNO_3$ solution in systems open to the atmosphere. (Part A, top) 10 g quartz/L, and (Part B, bottom) 100 g quartz/L.

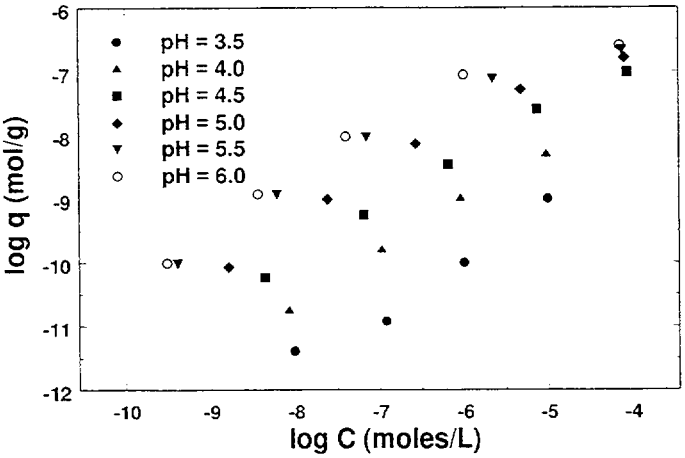

Figure 5-9. Adsorption isotherms for U(VI) on quartz at various pH values.

6 URANIUM(VI) ADSORPTION ON IMOGOLITE

Imogolite ($(OH)_3Al_2O_3SiOH$) is a tubular aluminosilicate mineral analogous to natural, poorly-crystallized aluminosilicates present in weathered soil environments. In this section, results are presented for U(VI) adsorption by natural and synthetic imogolite over a range of pH, ionic strength, and U(VI) concentrations.

6.1 Background

The mineralogy of the Koongarra (Australia) locality consists of a chloritized quartz-mica schist, with secondary mineralizations in the weathered schist such as clays, ferrihydrite, and other materials (Edis et al., 1992). Adsorbed U(VI) species are found in the weathered zone, with the predominant adsorptive minerals being ferrihydrite and secondary aluminum minerals. Selective extractions on core material demonstrated a significant relationship between bound U and surficial Al and Fe secondary mineralizations present in the system (Fenton and Waite, 1996).

Previous adsorption research has focused on the importance of Fe oxides and clay minerals, such as smectite, for U(VI) adsorption (Waite et al., 1994b; Turner et al. 1996). However, in some studies (e.g. Coston et al., 1995), aluminum-bearing phases in mineral coatings have been identified as important adsorbents. Imogolite is a paracrystalline aluminosilicate that is found in volcanic soils as an amorphous coating or cement around primary particles (Jongmans, et al.,1995; Violante and Tait, 1979). It has also been identified in the Bs and C horizons of spodosols (Dahlgren and Ugolini, 1993) and podzols (McKeague and Kodama, 1981; Farmer, 1982; Violante and Tait, 1979). Imogolite has been described as a curved gibbsite structure (Cradwick, et al. 1972) with AlOH groups on the outer surface of the tube, and SiOH groups on the inner surface, bridged by oxygens. Imogolite was chosen in this study as an analogue for amorphous aluminosilicate gels in aquifers, for its consistency and ease of synthesis, and its high surface area.

6.2 Materials and Methods

6.2.1 SOLUTIONS

Solutions were made using standard laboratory procedure from reagent-grade chemicals and deionized water.

^{233}U tracer was obtained in 1 N HCl solution with a specific activity of approximately 2 μCi/mL. Aliquots of a 1000 ppm $UO_2(NO_3)_2$ atomic absorption standard (Anderson Laboratories) were added to make stock solutions of 10^{-4} M or 10^{-6} M U(VI), both with a ^{233}U activity of approximately 10,000 dpm/ml. Natural U(VI) isotopes solutions were made for the adsorption isotherm, high pH kinetics, and the high U(VI) concentration adsorption edge ($3 \cdot 10^{-5}$ M U) by dissolving $UO_2(NO_3)_2 \cdot 6H_2O$ (s) (Johnson-Matthey) in deionized water. All stock solutions of U(VI) were diluted 1:100 with electrolyte for the batch experiments.

6.2.2 ANALYTICAL TECHNIQUES

pH measurements were made with a Ross pH combination electrode (±0.02 pH units) calibrated with NBS-certified buffers and corrected for temperature. pH was measured in stirred suspensions. No electrode drift was evident during the approximately 2 hour measurement periods.

^{233}U was determined by liquid scintillation counting on a Beckman LS 6000 counter. Peaks were integrated after background subtraction. The efficiency for the α particles was 100%. Analytical uncertainties in ^{233}U lead to uncertainties in the relative concentration of <3%. Natural isotope solutions were analyzed for total uranium on a Perkin-Elmer inductively coupled plasma mass spectrometer (ICP-MS) using 5 external calibration standards with a relative analytical uncertainty of <2%.

Al and Si were measured by inductively coupled plasma atomic emission spectrophotometry (ICP-AES) using single-point external

calibration standards with a relative analytical uncertainty of <3%. In addition, Si concentrations for the imogolite precipitation solutions were measured using the molybdate blue colorimetric method (Strickland and Parsons, 1968).

6.2.3 IMOGOLITE PREPARATION AND VERIFICATION

Synthetic imogolite was precipitated using the method described by Su et al. (1992). A solution of 0.10 M $Al(ClO_4)$ was added to 2.0 mM H_4SiO_4 and titrated with 1.0 M NaOH to pH 5. The solution was acidified using 0.40 M acetic acid/0.20 M nitric acid solution, and the suspension heated under reflux at approximately 98°C for 5 days. NaCl(s) was added to flocculate the suspension at a total concentration of 0.1 M NaCl. The suspension was centrifuged to concentrate the solid, which was then freeze-dried to reduce volume and protect structural integrity. After freeze-drying, the solid was cleaned under ultrafiltration until the conductivity of the filtrate reached that of deionized water (<20 μS/cm). The cleaned imogolite was freeze-dried again for storage. Total yield of cleaned, dried imogolite was approximately 0.9 g per precipitation.

Nine batches of imogolite were synthesized and combined into a single composite after verification of the individual batches as imogolite. The average ratio of Al to Si in the synthetic solids was 2.10 ± 0.14 based on Tamm's acid oxalate (TAO) digestions of the precipitated solid. The solids were verified structurally as imogolite by transmission electron microscopy (TEM) and Fourier transform infrared absorption spectra (FTIR) analysis. TEM (JEOL 1200EX) microscopy was done by air-drying a suspension of 0.01% imogolite in deionized water onto a copper grid. Infrared spectra were obtained using 5% (w/w) imogolite in a spectral grade KBr powder matrix on a Nicolet Magna 750.

A natural imogolite from Japan (Kitakama pumice bed, courtesy of R. Dahlgren, U.C. Davis) was cleaned using the method of Su et al. (1992). The solid was treated first with H_2O_2 to oxidize organic material, followed by a dithionite citrate leach to remove any amorphous iron. Next, the imogolite was rinsed thoroughly in deionized water. The remaining solid was freeze-dried and stored dry. The solid had an Al:Si ratio of 1.94 (+/- 0.07) and a FTIR spectrum similar to that published in Wada et al. (1979).

6.2.4 CHARACTERIZATION OF THE SURFACE PROPERTIES AND REACTIVITY OF IMOGOLITE

The cleaned and dried imogolite was rehydrated for each adsorption experiment using the same pre-treatment protocol. An imogolite - $NaNO_3$ suspension was made by mixing the dry imogolite into $NaNO_3$ solution of the desired ionic strength (generally 0.10 M). The suspension was sonicated for 1 hour to disperse the imogolite particles and stirred for 24 hours. The desired suspension volume was added to polycarbonate centrifuge tubes with a tilting repeater dispenser and the pH of each tube adjusted with dropwise additions of dilute HNO_3 and NaOH solutions.

6.2.4.1 Point of zero charge

The point of zero charge (PZC) of imogolite was estimated using the salt titration method of Davis (1977). This method actually measures the point of zero salt effect (PZSE) which is theoretically equivalent to the PZC in the absence of any specific interactions between dissolved solutes and the surface (Davis and Kent, 1990). In this method, the pH change of an aqueous suspension of the solid is measured under a nitrogen atmosphere after addition of electrolyte. At the PZSE, the pH remains constant with additions of salt. A suspension of 400 mg/L imogolite in 0.001 M $NaNO_3$ solution was pre-equilibrated for 24 hours. The suspension was then split into several aliquots and the pH of the aliquots was adjusted to a new value within the range 6.7-10 and re-equilibrated. After another 24 hours, the pH was measured, and enough $NaNO_3$ (s) was added to increase the concentration to 0.01M, and then to 0.1M $NaNO_3$. The pH was measured at each new electrolyte concentration; a constant pH

was reached within 7 minutes of each salt addition.

6.2.4.2 Site density and surface area

Specific surface area was measured by outgassing at 100°C and under 100% N_2 at atmospheric pressure on a Micromeritics FlowSorbII (Model 2300). Determinations were made on samples of the synthetic imogolite with the single-point BET method (e.g., Gregg and Sing, 1982) at a N_2(g) relative partial pressure of 0.3.

The number of hydroxyl surface sites was estimated using the tritium-exchange technique described by Bérubé et al. (1967) and Yates and Healy (1976). The imogolite sample was labeled with tritium by mixing the solid in tritiated water for 24 hours on a rotator. Following the labeling, the sample was centrifuged and the excess liquid decanted. The sample was then placed on a vacuum line for approximately 6 days to remove all physically adsorbed water. After returning the sample to atmospheric pressure using $N_{2(g)}$, the solid was dispersed in deionized water and centrifuged at 47,800 g for 30 minutes. Tritium activity in the supernatant was measured by liquid scintillation counting to determine the number of exchangeable hydrogen atoms on the surface. A mass balance for tritium showed that exchange with the centrifuge tube surface was <2.3% of the total exchange measured.

6.2.4.3 U(VI) adsorption experiments

The amount and rate of U(VI) adsorption onto imogolite was investigated over a range of pH, ionic strength, and U(VI) concentrations. All batch experiments were conducted open to the atmosphere. For studies at pH>7.0, sufficient $NaHCO_3$ or Na_2CO_3 was added to achieve equilibrium with the atmosphere at the desired pH value. The suspensions were mixed using end-over-end rotators spinning at 12 revolutions per minute for 24 hours to equilibrate the suspension at the desired pH value. After pH equilibration, the desired amount of U(VI) was introduced and the pH was adjusted immediately to compensate for any significant drift (>0.2 pH units) caused by the U(VI) addition. Typically drift was much less than 0.2 pH units. The centrifuge tubes were rotated for another 24 hours or the desired reaction time in kinetic experiments. At the end of the reaction period, the final pH of each tube was measured and the tubes were centrifuged. In experiments with added ^{233}U tracer, 3 ml of supernatant were added to 15 ml of scintillation cocktail (Ecolite), and the activity of ^{233}U tracer was measured with a liquid scintillation counter. In a comparison of experimental methods, no difference in U(VI) adsorption was detected between experiments using natural U(VI) isotopes (ICP-MS analysis) or added ^{233}U tracer. U(VI) adsorption was always measured in duplicate for each experiment; all data points are shown in the plots of results.

Mass balance calculations were performed on ten centrifuge tubes used in adsorption experiments to determine the amount of U(VI) that adsorbed to the tube walls. The total amount of U(VI) in the tube was determined by pouring out the original suspension into a clean centrifuge tube, rinsing out imogolite attached to the walls of the original tube with neutral pH, CO_2-free water, and then filling the original tube with 0.01 M HNO_3. The transferred suspension was acidified to pH<2 with concentrated HNO_3. The tubes were rotated overnight, and samples taken of the solution. The amount of uranium found in the original tube (in activity units) was then divided by the overall amount of uranium found in the original suspension plus the washes and the amount from the transfer tube. The average percentage of uranium associated with the tube walls was 3.1%, with a maximum of 7.2% and a standard deviation of ±2.5%.

6.2.4.4 Imogolite Solubility

Dissolution of imogolite was studied at pH values bracketing the pH range studied in U(VI) adsorption experiments. A high-pH solubility experiment (pH 9.96 ±0.01) was carried out by making standard suspensions following the procedures outlined above for the batch adsorption studies and adjusting the suspension to the desired pH. The suspension was then dispensed into centrifuge tubes and rotated end-over-end. At selected times, a tube was

removed from the rotator, the pH measured and the supernatant sampled after centrifugation.

The procedure for measuring solubility at low pH was altered because of the difficulty of attaining a constant pH in an unbuffered system. The low pH solubility was performed in a batch reactor, with a ratio of 400 mg/L synthetic imogolite in a solution of 0.1 M $NaNO_3$. After pre-equlibration, dilute nitric acid was added to adjust the pH of the suspension to 4.6 (±0.05) using a pH stat system. The desired pH was achieved in 15 minutes. 10 ml of suspension was withdrawn at appropriate time intervals, centrifuged, and the supernatant measured for dissolved Al and Si.

6.3 Results and Discussion

6.3.1 IMOGOLITE STRUCTURE

Figures 6-1 and 6-2 illustrate similarity in structural features between natural and synthetic imogolite. The electron micrograph shows bundles of random threads, considered typical of imogolite. No hollow spheres of allophane were observed. The FTIR spectra are very similar to published spectra of imogolite (Farmer and Fraser, 1979). There are small differences between the spectra of the natural and synthetic solids (Fig. 6-2), such as absorbance, and small

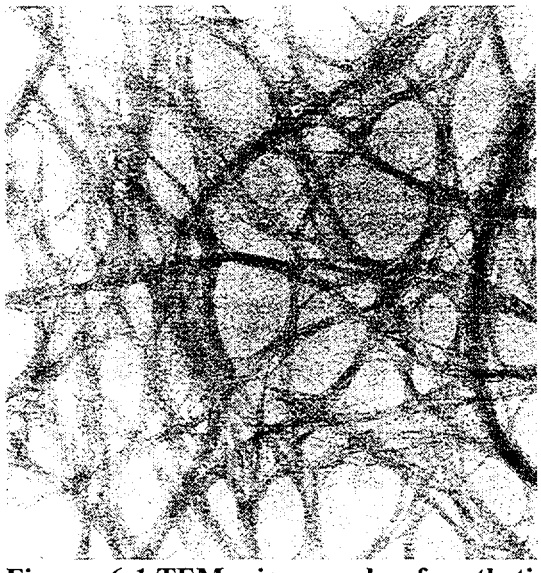

Figures 6-1 TEM micrographs of synthetic imogolite solid.

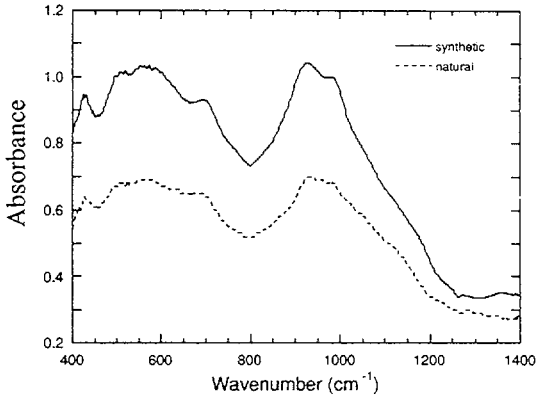

Figure 6-2. FTIR spectra of natural and synthetic imogolite.

peak shifts and morphological differences which indicate slight structural differences between the solids. Infrared spectra from Wada et al. (1979) show similar changes in peak morphology and location. These differences are attributed in part to heating of the solid during synthesis which may cause stretching of the Si-O bond (Pohl et al. 1996). Electron micrographs and differential thermal analysis (Farmer et al., 1977; Farmer et al., 1979) revealed differences between synthetic and natural imogolite. Synthetic imogolite had a wider-diameter tubular structure, less stable OH groups, and a less well-formed structure when compared to the natural material. Computer modeling of the structure suggests natural imogolite tubes have a mean inner diameter of 6.5Å compared to an internal diameter of 8-10Å for synthetic imogolite solids (Pohl et al., 1996).

6.3.2 IMOGOLITE SITE DENSITY, SURFACE AREA, AND POINT OF ZERO CHARGE

Surface area measurements by the BET-N_2 method gave a value of 166 m^2/g. This value is not considered representative of the true reactive surface area, although N_2-BET surface areas were used to model the diameter and number of gibbsite units in an imogolite tube (Pohl et al. 1996). Measurement by the ethylene glycol monoethyl ether (EGME) adsorption method yields surface areas between 800-1100 m^2/g for synthetic imogolite (Egashira and Aomine, 1974; Dahlgren et al., 1993; Wada, 1989). The large discrepancy between the two methods

suggests EGME has a specific interaction with the imogolite surface, similar to the cation solvation and bulk penetration effect observed with clays such as illite and montmorillonite (Chiou et al., 1993).

Polar substances, e.g., EGME, are believed to be more effective at measuring the available surface area of imogolite (Wada, 1989). The surface area value chosen for the final calculation of site density in this study was 800 m^2/g. Using this value for the surface area, the number of surface hydroxyls estimated by tritium exchange for two synthetic imogolite samples was 9.21 and 9.81 sites/nm^2, respectively. These values are in reasonable agreement with site densities reported for both α-$Al(OH)_3$ and amorphous SiO_2 surfaces (Davis and Kent, 1990).

Figure 6-3 shows the pH change measured upon addition of electrolyte to an imogolite suspension. For aqueous suspensions of pure hydrous metal oxide phases, the pH of the suspension will shift toward the PZC upon addition of electrolyte (Davis, 1977). For imogolite suspensions at pH values less than 7, the pH increased upon addition of electrolyte, suggesting that the PZC was at a pH greater than 7. However, for imogolite suspensions at pH values greater than 7.5, the change in pH was small and did not produce symmetrical curves with a clear PZSE. Since imogolite is believed to have an outer alumina surface and an inner

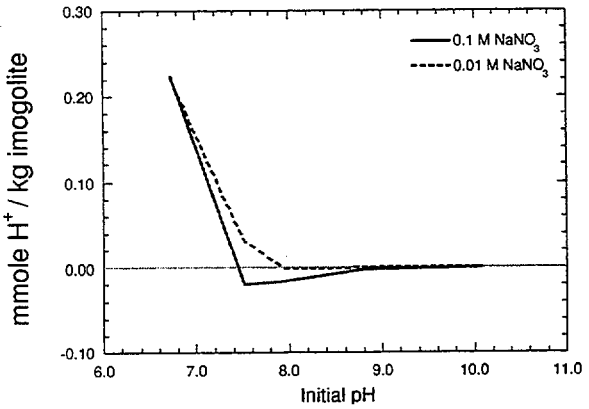

Figure 6-3. Amount of hydrogen ion uptake by synthetic imogolite as the solution pH approaches the PZC of the solid during salt titrations.

silica surface, it is possible each surface has its own distinct PZC, and the salt titration results indicate the net pH change of the two surfaces upon electrolyte addition. However, the results might also be compromised by adsorption of Al(III) species on the silica surface or silicate on the alumina surface, since these species are released by dissolution. Other investigations have reported PZC values between pH 8.5-9 using electrophoretic mobility measurements on cleaned natural imogolite (Horikawa, 1975; Karube et al., 1992). Karube et al., (1992) showed mobilities of zero occur at pH 7.4 for imogolite samples with a very low solid to solution ratio (< 0.01 g/L). Su and Harsh (1993) measured the electrophoretic mobility of synthetic imogolite in the presence of nitrate (among other anions) but were unable to determine a PZC value. Su and Harsh hypothesized that the difference in PZC findings between their study and that of Horikawa (1975) and Karube et al. (1992) was attributable to the use of natural imogolite in the latter studies, the results of which may have been affected by impurities, structural defects, and adsorbed ions left from the cleaning process.

6.3.3 IMOGOLITE SOLUBILITY

Dissolution of the composite synthetic imogolite was studied at pH 4.6 and pH 10.0 following the same procedures used in U(VI) adsorption experiments. At both pH values, the ratio of Al:Si dissolved reached nearly constant values within a few hours (Fig. 6-4). The dissolution at higher pH (closed symbols) exhibited some incongruent dissolution, with an average Al:Si ratio of 2.90:1 (±0.09). The ratio at pH 4.6 plateaued after about four hours at an Al:Si ratio of approximately 2. In both pH ranges, the total amount of aluminum and silica dissolved accounted for less than 2% of the total imogolite mass present in the system.

Su et al. (1995) and Dahlgren and Ugolini (1989) measured solubility of imogolite from soil solutions from the Bs, BC and C horizons of soils collected from the Cascade Range in Washington state in the pH range 4.4-5.5. Both of these studies showed imogolite in

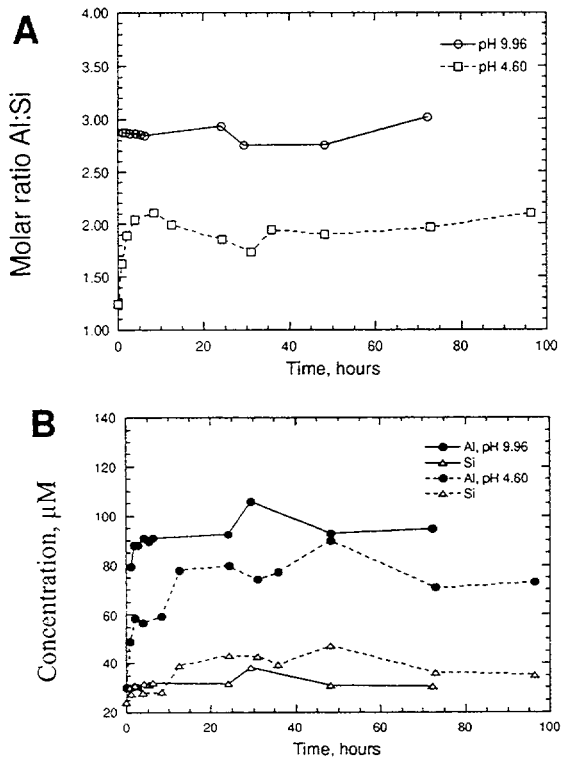

Figures 6-4. Solubility of synthetic imogolite in 0.1 M $NaNO_3$. A) the ratio of dissolved Al to Si measured over time in separate tubes at pH 4.6 and 9.96 and B) total concentration of dissolved Al and Si measured in the same experiment.

simultaneous equilibrium with a phase of $Al(OH)_3$ of varying crystallinity. Wieland and Stumm (1992) found the dissolution of another aluminosilicate mineral, kaolinite, to be incongruent at pH>4.3 due to precipitation of a gibbsite phase, and they suggested that measurements of Al in solution do not reflect 'true' rates of kaolinite dissolution. Thus, we cannot be certain that the measurements indicate a true rate of imogolite dissolution or that no other phase influenced the final solubility measurements, but the measurements do indicate the concentrations of dissolved Al and Si that were present in the U(VI) adsorption experiments at the extreme ends of the pH range studied.

6.3.4 ADSORPTION OF U(VI) BY IMOGOLITE

The time dependence of U(VI) uptake by imogolite at pH 4.9 and 9.3 is shown in Figure 6-5. Although there is considerable scatter in the data, we conclude that the concentration of U(VI) in the supernatant at both pH values reached a constant value within the first few hours of reaction.

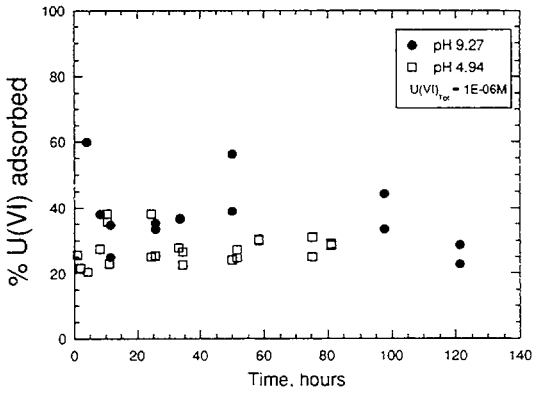

Figure 6-5. Rate of U(VI) adsorption on imogolite at pH 4.94 (±0.04) and pH 9.27 (±0.03).

At pH 4.9, a constant U(VI) concentration was reached before the first sample was taken, and at higher pH the concentration of U(VI) appeared to be constant within 12 hours. The adsorption rate found in this study appears to be considerably faster than that observed by Prikryl et al. (1994) in studies of U(VI) adsorption by α-alumina powders of significantly lower surface area. These authors found no difference in adsorption rates on alumina powders with surface areas differing by three orders of magnitude and suggested that the surface functional group type is the most important factor in determining the rate of adsorption reactions. U(VI) adsorption onto synthetic imogolite at different ionic strengths is shown in Figure 6-6. Adsorption was strong near neutral pH, similar to U(VI) adsorption by other minerals such as α-alumina, ferrihydrite and kaolinite (Prikryl et al., 1994; Waite et al., 1994b; Waite et al., 1992, and see Section 7 of this report). Adsorption of U(VI) at pH 9 by

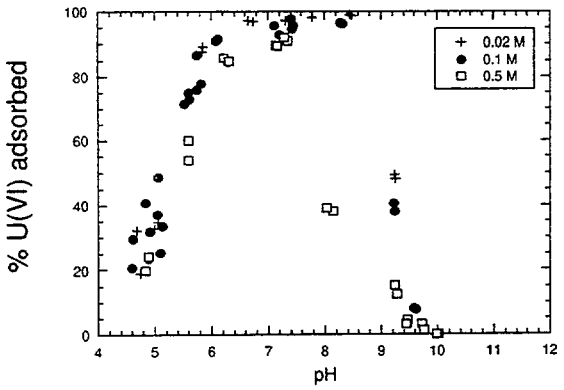

Figure 6-6. Adsorption of 10-6 M U(VI) onto synthetic imogolite at different ionic strengths.

imogolite was greater than that reported for ferrihydrite but shows some similarity with adsorption of U(VI) by kaolinite (Waite et al., 1992). U(VI) adsorption on imogolite was relatively independent of ionic strength in the pH range 5 to 7 (Fig. 6-6), but adsorption decreased at higher $NaNO_3$ concentrations in the pH range 7.5 to 9.5. Waite et al. (1994b) also observed that U(VI) adsorption was dependent on ionic strength in the alkaline pH range (on ferrihydrite). These authors showed that the ionic strength dependence could be explained by changes in the activity of the predominant aqueous species in this pH range, $UO_2(CO_3)_3^{4-}$. It is possible that the ionic strength dependence of U(VI) adsorption on imogolite also includes some surface effects. For example, at pH 9 the

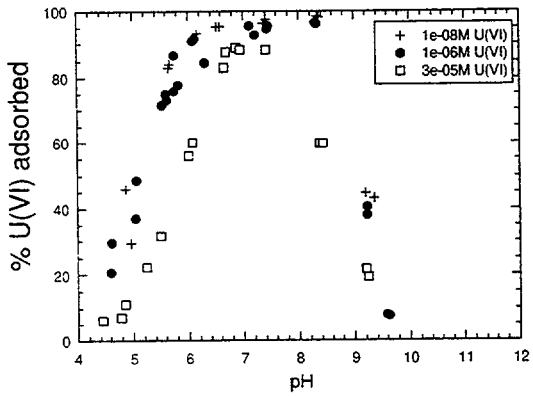

Figure 6-7. Adsorption onto synthetic imogolite of varying concentrations of U(VI) in 0.1 M $NaNO_3$ solution.

outer gibbsite-like surface may be only weakly charged, while the inner silica-like surface may be highly negatively charged. This could cause significant repulsion of large anions, such as $UO_2(CO_3)_3^{4-}$, and thus limit their diffusion into the imogolite tubes.

The effect of variation of U(VI) concentration on its adsorption by imogolite is shown in Figure 6-7. U(VI) adsorption at the highest concentration studied ($3 \bullet 10^{-5}$ M total U(VI)) showed a smaller fractional uptake at a given pH than at lower concentrations (10^{-6} and 10^{-8} M total U(VI)). As pointed out in Section 5, this effect suggests that mononuclear U(VI) complexes are the predominant species at the surface for the systems at 10^{-6} and 10^{-8} M total U(VI), because polynuclear complexes should cause increasing fractional (%) adsorption with increasing concentration, in accordance with the mass law (see arguments in Section 5 and by Waite et al., 1994b).

Results comparing adsorption of U(VI) on natural vs. synthetic are shown in Figure 6-8. The dependence of U(VI) adsorption on pH appears very similar, suggesting that the synthetic imogolite was a good analogue for the naturally formed mineral phase. U(VI) adsorption by the natural sample was slightly lower, perhaps reflecting a difference in surface areas. Unfortunately an error was made in the experiments with the natural imogolite sample; insufficient sodium bicarbonate carbonate was

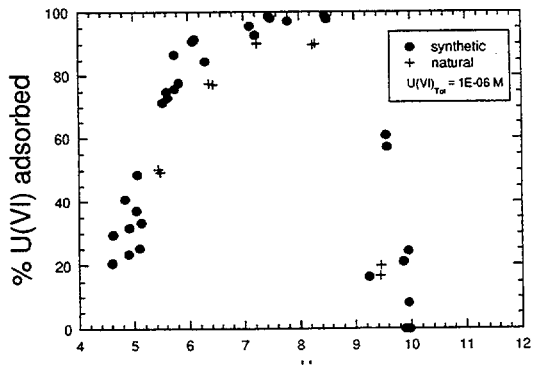

Figure 6-8. Comparison of U(VI) adsorption onto natural and synthetic imogolite.

added to centrifuge tubes to achieve equilibrium with the atmosphere at the selected pH values in the experiments (for pH>7). The experiments could not be repeated because the supply of natural imogolite was exhausted. In order to properly compare U(VI) adsorption data for the synthetic and natural imogolite samples, experiments were conducted with synthetic imogolite under identical non-equilibrium conditions for carbonate equilibration with the atmosphere (data shown in Fig. 6-8). Clark and McBride (1984a) compared phosphate adsorption isotherms for both natural and synthetic imogolite and found that the synthetic sample had significantly higher adsorption than either of two samples of natural imogolite. This is consistent with the structural model that suggests that natural imogolite has narrower tubes and therefore a decreased capacity for adsorption (Pohl et al., 1996).

Figure 6-9 shows an adsorption isotherm for U(VI) on imogolite at pH 9.2. The data are well described by a linear isotherm. Synthetic imogolite isotherms for phosphate adsorption show greater curvature (Clark and McBride, 1984a).

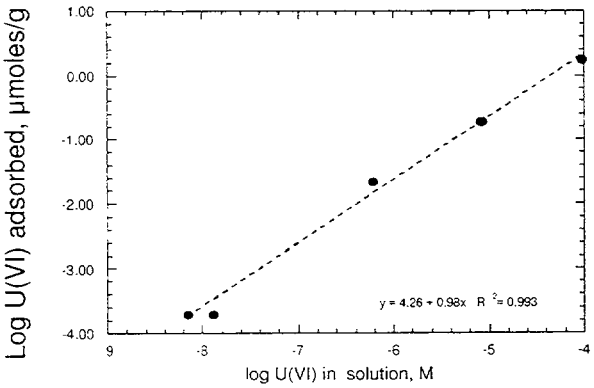

Figure 6-9. Adsorption isotherm of U(VI) adsorption on imogolite in 0.1 M $NaNO_3$ solution.

6.4 SUMMARY OF FINDINGS

1. The lack of an ionic strength dependence on U(VI) adsorption at pH values less than 7 suggests that an inner-sphere surface complex forms at low pH.

2. The shift in pH-adsorption edges with increasing total U(VI) concentration is consistent with adsorption of a mononuclear species.

3. Synthetic imogolite adsorbed more U(VI) per unit weight under identical conditions than a sample of natural imogolite.

4. Adsorption of uranium on imogolite appears to be similar at high pH (>7) to adsorption of uranium on kaolinite (Waite et al., 1992). Stronger U(VI) adsorption occurred on these aluminosilicate minerals at pH 9 than on oxide phases, such as ferrihydrite, quartz, and α-alumina.

6.5 ACKNOWLEDGMENTS

The authors wish to thank Dr. Randall Dahlgren for providing the natural imogolite sample as well as helpful discussion about the properties of imogolite, and Dr. Chunming Su for his assistance with procedures for precipitation of synthetic imogolite. We also thank Jennifer Joye and Matthias Kohler for their technical support. Bernard Thomas (R. J. Lee Group Inc., Berkeley, CA) provided TEM images and diffraction patterns.

7 URANIUM(VI) ADSORPTION ON KAOLINITE IN SIMPLE $NaNO_3/HCO_3$ SYSTEMS, AND IN SYSTEMS CONTAINING ADDITIONAL COMPLEXING LIGANDS

Iron oxides and clay minerals occur throughout the Koongarra weathered zone and are a product of the weathering of chlorite, a major component of the host chlorite schists (Murakami et al., 1994). During weathering, the iron-rich chlorite is converted to vermiculite, then kaolinite, in a sequence of reactions which also leads to the precipitation of iron minerals, including goethite, hematite and ferrihydrite. Ferrihydrite is believed to play a major role in adsorbing U(VI) in the weathered part of the Koongarra system, and a detailed study of the adsorption of U(VI) on ferrihydrite was presented in Section 4. However, the relative importance of various minerals in adsorbing U(VI) in the Koongarra system has not yet been conclusively demonstrated. Giblin (1980) considered that U(VI) adsorption on kaolinite was an important concentration mechanism for U in the Alligator Rivers Region deposits.

In this section, we discuss U(VI) adsorption on kaolinite in systems containing $NaNO_3$ as the background electrolyte. The effects of pH, U_T, ionic strength, and solid/liquid ratio on U(VI) adsorption were studied, as well as the effects of complexing and competing ligands including phosphate, citrate, sulfate and humic acid. This study was carried out in parallel to the study of the U(VI)/ferrihydrite systems. Section 4 contains further details of experimental procedures and the rationale behind the experiments.

7.1 Materials and Methods

7.1.1 KAOLINITE SAMPLES

Kaolinite standards KGa-1 and KGa-1B were obtained from the Clay Minerals Society (CMS) Source Clays Repository in Columbia. KGa-1 has been extensively characterised (Van Olphen and Fripiat, 1979), and KGa-1B is a mineralogically similar sample which was selected to replace the exhausted stock of KGa-1 (Pruett and Webb, 1993). KGa-1 and KGa-1B are well-crystallised kaolins from Washington County, Georgia, and both samples contain a trace abundance of anatase (TiO_2).

The BET surface areas of KGa-1 and KGa-1B are 8.4 m^2/g and 11.7 m^2/g, respectively. The solid/liquid ratio of kaolinite in the experiments was usually 4 g/L. Prior to adsorption experiments we established that leaching of natural U(VI) from these clay materials was insufficient to significantly increase the concentration of U(VI) in any of the experiments. For comparative purposes, a small number of experiments were also carried out with a standard material sourced from Japan, known as Kanpaku kaolinite. This material had been used in some experiments in the previous ARAP study (Waite et al., 1994a).

U(VI) adsorption on mixed substrates containing both kaolinite and ferrihydrite was also studied. These substrates were prepared by raising the pH of an acidic solution of Fe(III) in the presence of a weighed amount of kaolinite (KGa-1). After an aging time of 65 h, the mixed slurry was vigorously agitated and aliquots were transferred to centrifuge tubes for adsorption experiments. The amounts of ferrihydrite and kaolinite were chosen so that the final suspension had the same solid/liquid ratio of these minerals as were present in other experiments (89 mg/L and 4 g/L, respectively).

7.1.2 PROCEDURE FOR ADSORPTION EXPERIMENTS

The experimental procedures were similar to those used for U(VI) adsorption experiments on ferrihydrite (Section 4). Batch experiments were carried out in polypropylene centrifuge tubes and were equilibrated with air. A weighed amount of clay was suspended in $NaNO_3$ (usually 0.1M). For studies at pH > 7.0, sufficient $NaHCO_3$ was added to ensure pH stability and fix the carbonate content of the

system. For some experiments, phosphate (as NaH_2PO_4), humic acid (a filtered solution of Aldrich^R sodium humate), sodium citrate or sodium sulfate was added. The U(VI) was added after 24 h pre-equilibration, during which time the system was allowed to come to equilibrium under the appropriate chemical conditions (pH, ionic strength, complexing ligands, etc.). The contact time for U(VI) was 48 hr, with the pH being checked and adjusted if necessary after 24 hours. The experimental tubes were gently shaken in a waterbath at 25°C. Immediately prior to sampling the pH was again determined and the aqueous phase was then separated by high speed centrifugation (RCF > 6500g) for 30 min. U(VI) concentrations in the supernatant were determined using the Kinetic Phosphorescence Analyser (model KPA-10) or by alpha spectrometry.

As discussed in Section 4, uptake of U(VI) by tube walls may complicate adsorption experiments. Wall sorption is potentially a greater problem in experiments with kaolinite, which has a smaller specific surface area, and is a weaker U(VI) adsorber than ferrihydrite. Experiments to precisely quantify tube wall sorption with kaolinite present were unsuccessful, because the kaolinite particles tended to aggregate and adhere to the vessel walls. However, the results indicated that if sufficient solid was present, the mineral surfaces would dominate U(VI) adsorption in the system. As a result of these investigations, much higher solid/liquid ratios (4 g/L) were used for kaolinite adsorption experiments than were used with ferrihydrite (0.089 g/L).

7.1.3 ANALYTICAL ELECTRON MICROSCOPY

The association of adsorbed U(VI) with kaolinite surfaces was studied using Analytical Electron Microscopy (AEM). We used a JEOL 2000FX transmission electron microscope (TEM) equipped with a Tracor-Northern Si(Li) energy dispersive X-ray (EDX) spectrometer and a Link Isis analyser (Oxford Instruments). AEM was carried out with an operating voltage of 200 kV and a beam current of 110 μA. Analyses were acquired for 400 - 600 seconds live time and reduced to elemental weight percentages using the Link Isis software package TEMQuant. Experimental k-factors for the data reduction were obtained from a large suite of silicate mineral standards.

Samples of kaolinite were examined subsequent to adsorption experiments. These samples were prepared by evaporating a small droplet of clay suspension onto a holey carbon TEM grid. Samples which had been suspended in $NaNO_3$ were centrifuged and re-suspended in milli-Q water prior to the evaporation step, to reduce the amount of $NaNO_3$ on the grid.

7.2 Results of U(VI) Adsorption Experiments with Kaolinite

7.2.1 EFFECT OF pH AND SOLID/LIQUID RATIO

The main features of U(VI) adsorption on the KGa-1B kaolinite are shown in Figure 7-1. In qualitative terms, the data are similar to those of ferrihydrite. In particular, adsorption is greatest in the near-neutral pH range, with a 'low pH edge' of increasing uptake from pH of about 3.5 to 6.5, and a much steeper 'high pH edge' between pH 8 and 9. Compared to ferrihydrite, the amount of adsorption (expressed as amount of U(VI) adsorbed per gram of sorbing substrate) is much lower. This reflects the much higher surface area of ferrihydrite. The

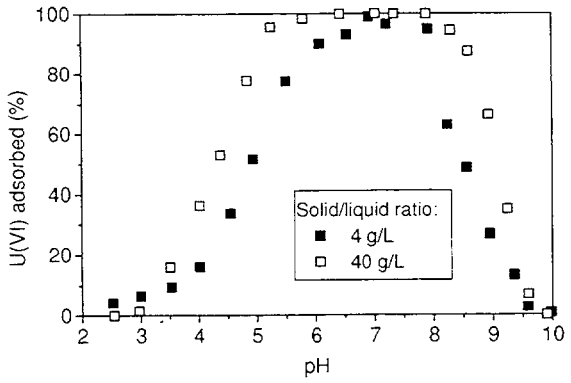

Figure 7-1. U(VI) adsorption on kaolinite (KGa-1B) – pH dependence and effect of solid/liquid ratio. (U_T = 1 μM, 0.1M $NaNO_3$, equilibrated with air).

comparison with ferrihydrite is discussed in further detail below. As was the case with ferrihydrite, the amount of U(VI) adsorbed on kaolinite increased at higher kaolinite solid/liquid ratios.

7.2.2 EFFECT OF U_T CONCENTRATION

As with ferrihydrite, there was a decreased percentage of U(VI) adsorbed with increased U_T in the system (Figure 7-2), which suggests that there are at least two types of binding sites with different affinities for U(VI) adsorption on the KGa-1B kaolinite.

Similar data for KGa-1 kaolinite across a wide range of U_T indicate a substantial shift in the position of the low pH-edge between U_T of 10^{-6} and 10^{-5} M (Fig. 7-3). U(VI) adsorption at U_T concentrations of 10^{-4} and 10^{-3} M had an entirely different pH dependence, with the pH edge being much steeper and moving to lower pH values with increasing U_T. These curves obtained at high U(VI) concentrations were entirely different to the data obtained in other experiments, and suggest that another process, such as precipitation, may have been occurring. A precipitating solid in this type of experiment is unlikely to be a crystalline phase such as β-$UO_2(OH)_2$ or schoepite, but is more likely to be an amorphous uranyl hydroxide (Tripathi, 1983). Tripathi defined a solubility product for this phase as $\{UO_2^{2+}\}\{OH^-\}^2$, with a value of log

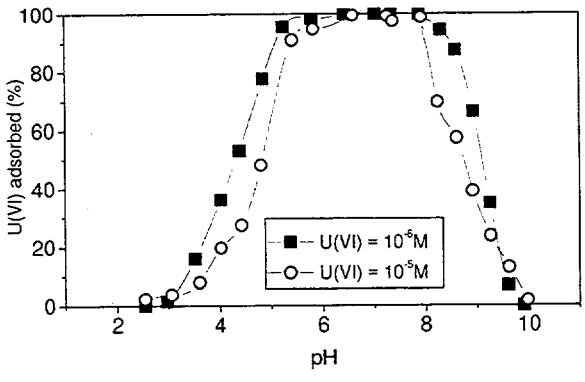

Figure 7-2. Effect of U_T on U(VI) adsorption by kaolinite sample KGa-1B. Solid/liquid ratio of 4 g /L.

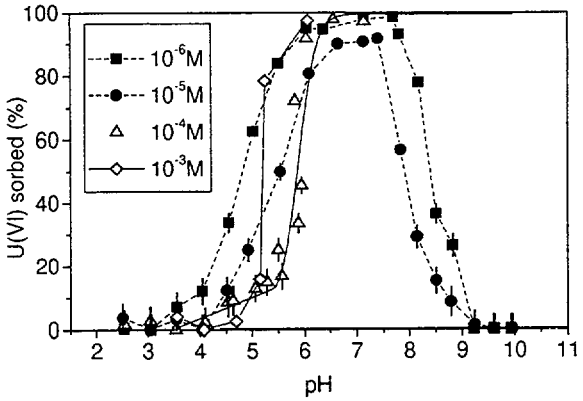

Figure 7-3. Effect of U_T on U(VI) adsorption by kaolinite sample KGa-1. Solid/liquid ratio of 40 g /L.

K_{SO} = -22.43 (see Section 2). When the experimental results are plotted as U(VI) in solution as a function of pH, it appears that the data are consistent with the solubility of this phase placing an upper limit on dissolved U(VI) (Fig. 7-4).

It is instructive to compare the set of experimental data obtained at the U_T

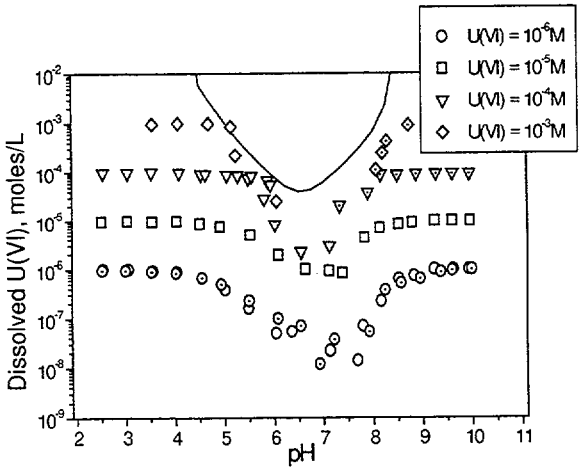

Figure 7-4. Dissolved U_{eq} in experiments with kaolinite for U_T ranging from 10^{-6} to 10^{-3}M. The solid curve was calculated from the solubility of uranyl hydroxide with log K_{SO} for $UO_2(OH)_2$ of -22.43 [Tripathi, 1983]. Data are for experiments with kaolinite KGa-1 (open symbols) and with KGa-1B (dot centre). Solid/liquid ratio of 4 g/L, 0.1M $NaNO_3$ solution.

concentration of 10^{-3}M with model predictions that include precipitation of the amorphous uranyl hydroxide phase. In this case, we plot the experimental data as 'U(VI) associated with the solid phase' rather than 'U(VI)-adsorbed' to emphasize that adsorption is not the major process involved.

The resulting data are presented in Figure 7-5. It can be seen that the agreement between the model predictions and experimental data is quite satisfactory. While the fit is not perfect, particularly at high pH values, it should be borne in mind that the published K_{SO} values for $UO_2(OH)_2$ cover a vast range of many orders of magnitude (see Section 2). This is largely due to errors introduced by inconsistent thermodynamic data and poor solid phase characterization (as discussed by Tripathi (1983)). Thus, the agreement between model and experiment can be considered to be surprisingly good. The experimental evidence therefore indicates that precipitation is occurring at high U_T in the 'sorption' experiments.

An important feature of the model curve shown in Figure 7-5 is the very steep (near vertical) slope of the 'edge' (both calculated and in the experimental data). This contrasts with the distinctive 'S-shaped' curve, which was observed in numerous experiments when adsorption appears to be the major process. The shapes of these uptake curves are compared in Figure 7-3. Based on our calculations, the datasets for U_T of 10^{-5} and 10^{-6}M (Fig. 7-3) are below the solubility limitations. It will be observed that whereas the adsorption curves for U_T of 10^{-5} and 10^{-6}M move to higher pH values with increasing U_T, the vertical edge for U_T of 10^{-3}M is at lower pH values than the edge U_T of 10^{-4} M (Fig. 7-3). Thus, constraints imposed by the solubility affect the experimental curves in a different way to those due to adsorption phenomena. This suggests that families of curves such as those in Figure 7-3 can be used to identify when precipitation is occurring (rather than adsorption), as well as providing information about binding sites of different affinity.

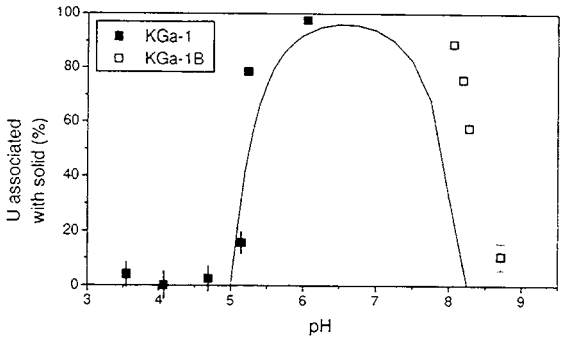

Figure 7- 5. U(VI) associated with solid phases in experiments with kaolinite (4g/L) and with U_T of 10^{-3}M. The line is calculated for precipitation of amorphous $UO_2(OH)_2$ with log K_{SO} = -22.43 [Tripathi, 1983]. The curve shows a good fit to the data, considering the range of published log K_{SO} values and the sensitivity of the calculations to a small change in this parameter.

7.2.3 COMPARISON WITH FERRIHYDRITE

The experimental data for ferrihydrite and kaolinite are compared directly in Figure 7-6. Here attention is restricted to U(VI) concentrations which are below the solubility limitations. The sets of curves are distinctive both in the steepness of the curves and in their spacing. Compared to the corresponding experimental data for ferrihydrite, the pH dependence (steepness of the edges) is not as great for kaolinite, possibly indicating a different proton stoichiometry of adsorption or a different distribution of site-binding energies. The displacement between the curves at different U_T in the case of kaolinite is much greater than for the closely spaced edges for ferrihydrite.

As might be expected, the data clearly indicate that, on a mass basis, ferrihydrite is a much stronger adsorber of U(VI) than kaolinite. For example, at pH of 4.5 and U_T of 10^{-6}M, the R_d values (defined in Section 11) for U(VI) adsorption by ferrihydrite and kaolinite are about 104 mL/g and 102 mL/g, respectively. To some extent, this reflects their surface areas of

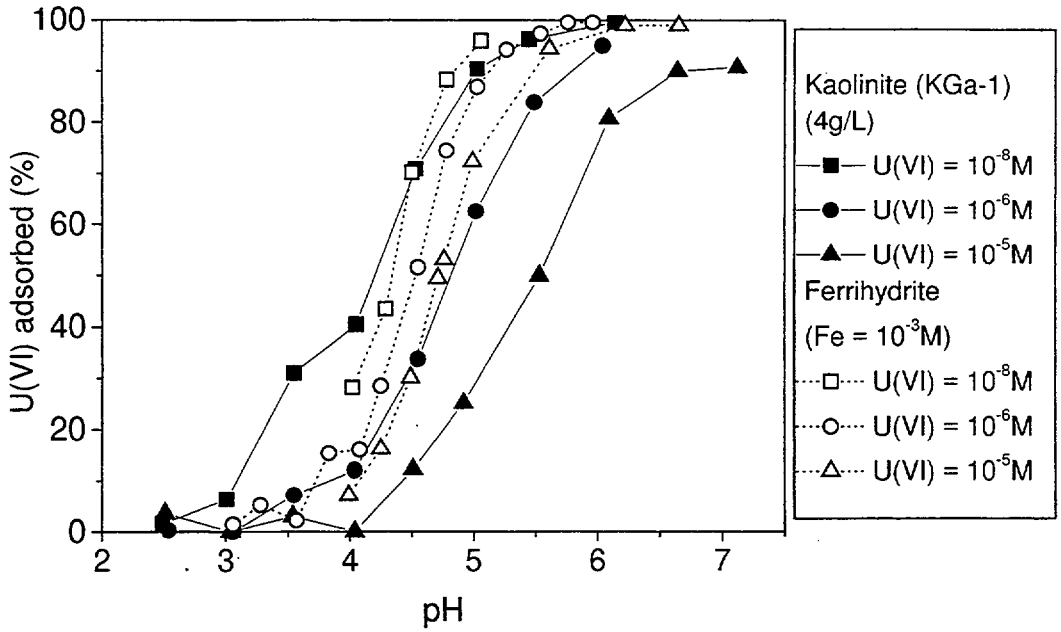

Figure 7-6. pH-edges for U(VI) adsorption on kaolinite and ferrihydrite for various U_T. Note that the curves for ferrihydrite are more closely spaced and have a steeper slope.

approximately 600 and 8.4 m^2/g, respectively. While the R_d for U(VI) adsorption by ferrihydrite is inevitably greater than kaolinite under similar conditions, the ratio between the two R_d values is variable and dependent on factors such as pH and U_T concentration.

7.2.4 EFFECT OF IONIC STRENGTH

A limited amount of data for the ionic strength dependence of U(VI) adsorption on kaolinite KGa-1B was obtained (Fig. 7-7). The data indicate that the high pH edge is displaced to the left (i.e. adsorption is reduced) with an increase in ionic strength. This would be consistent with the results for ferrihydrite. The effect of ionic strength at low to neutral pH values is less clear. Taken at face value, the data appear to indicate an increase in adsorption at higher ionic strength (Fig. 7-7). In contrast, the data obtained with KGa-1 in the previous ARAP study suggested an increase with lower ionic strength, although the data were again inconclusive (Waite et al., 1994a). After reviewing all the available data-sets, it appears that the differences between the two curves in Figure 7-7 (at pH values below 7) may be explained by experimental variation. Although greater than the analytical uncertainty

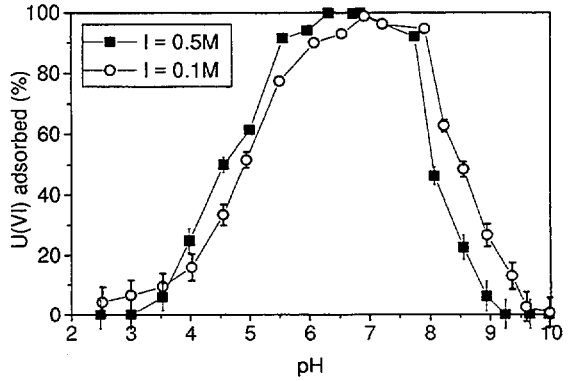

Figure 7-7. Effect of ionic strength on U(VI) adsorption by kaolinite sample KGa-1B (4g/L). U_T = 1 μM.

(shown by the error bars), there may be additional sources of experimental error, which could lead to slight differences in measured adsorption between experimental runs. The most important of these (in this case) may be differences in the solid/liquid phase separation, with the ionic strength affecting the aggregation and settling of the particles during centrifugation. This would particularly affect data obtained under conditions of high adsorption (pH 5.5-7.5). Another possibility may

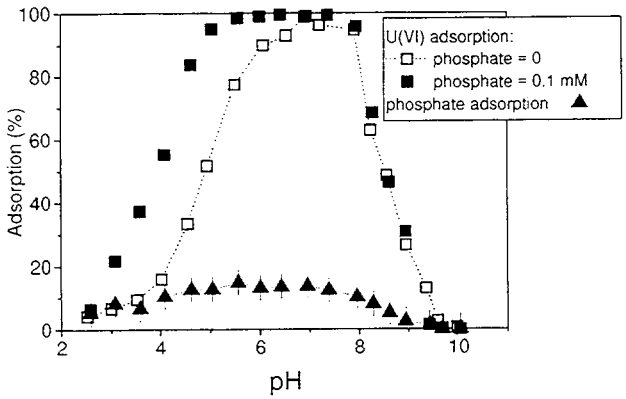

Figure 7-8. Effect of phosphate on U(VI) adsorption by kaolinite sample KGa-1B (4 g/L). U_T = 1 μM.

be sampling variation in the source clay materials.

7.3 Effect of Complexing Ligands

7.3.1 PHOSPHATE

Experiments with added phosphate (total concentration of 10^{-4}M) showed that the presence of phosphate substantially increased U(VI) uptake on kaolinite at low pH values (Fig. 7-8) and had little effect at higher pH values. In contrast to the data for ferrihydrite, adsorption of phosphate was minor, less than 20% at all pH values. However, because the total concentration of phosphate in the system was greater than U_T, the adsorption density of phosphate is greater than that of U(VI).

The low-pH U(VI) adsorption edge on kaolinite was displaced to more acidic pH values when phosphate was present, although only a relatively small proportion of phosphate was adsorbed (Fig. 7-8). The presence of phosphate increased U(VI) adsorption across a wide pH range from 3 to 7.5. The increase in U(VI) uptake occurred across a pH range in which aqueous U(VI)-phosphato complexes form (Fig. 4-9). Thus, the increased U(VI) adsorption may be attributable to the formation of a ternary surface complex.

The results of these experiments suggest that precipitation of U(VI)-phosphate phases was not responsible for removing U(VI) from solution in the experiments with ferrihydrite (see Section 4), because higher equilibrium concentrations of both U(VI) and phosphate were measured in the kaolinite experiments at pH < 6. This would not be expected if precipitation was occurring in the experiments with ferrihydrite.

In order to better understand the system, further experiments were carried out with a higher solid/liquid ratio of 40g kaolinite/ L (Fig. 7-9). Adsorption of both U(VI) and phosphate was greater in this experiment. As was the case at the lower solid/liquid ratio, the presence of phosphate increased U(VI) adsorption. The data suggest that adsorption rather than precipitation occurred, since the solid/liquid ratio should not affect U(VI) concentration limits imposed by the solubility of uranyl hydroxide.

To allow a better assessment of the effect of the higher solid/liquid ratio, the systems with phosphate and U(VI) are shown in Figure 7-10. Clearly adsorption of both phosphate and U(VI) are related to the solid/liquid ratio. In the case of U(VI), thr higher ratio leads to a shift in the low pH edge to lower pH values, and the high pH edge to higher pH values (i.e. increasing adsorption), while the uptake of phosphate was uniformly increased across the entire pH range.

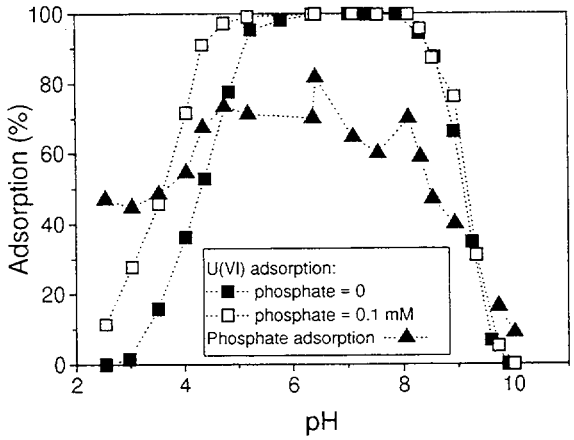

Figure 7-9. Effect of phosphate on U(VI) adsorption by kaolinite sample KGa-1B (40 g/L). U_T = 1 μM.

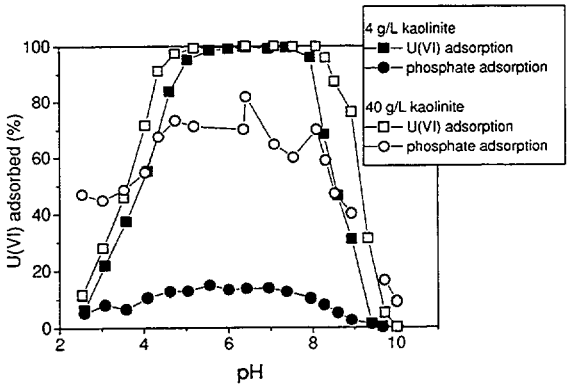

Figure 7-10. U(VI) and phosphate adsorption by kaolinite at solid/liquid ratios of 4 g/L and 40 g/L. U_T = 1 μM; phosphate = 10^{-4}M.

7.3.2 HUMIC ACID

The rationale for studying the effect of humic acid (HA) on actinide adsorption and some previous published results were discussed in Section 4. Adsorption data for the U(VI)/HA/ ferrihydrite system were presented in that section.

The addition of HA (9 mg/L) moved the low pH adsorption edge on kaolinite to lower pH values (increasing adsorption), and had little effect on the high pH edge (Fig. 7-11). These results were similar to the U(VI)/ferrihydrite/HA system.

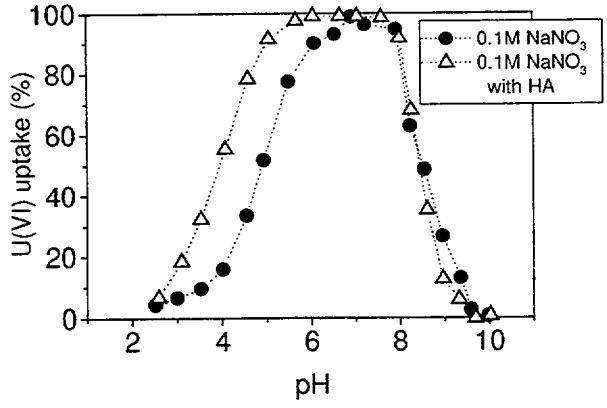

Figure 7-11. Effect of humic acid (HA) on U(VI) adsorption by kaolinite sample KGa-1B (4 g/L). U_T = 1 μM; HA = 9 mg/L.

7.3.3 SULFATE

Results of experiments exploring the effect of sulfate and citrate on U(VI) adsorption by kaolinite are presented in Figure 7-12. In all experiments the kaolinite was KGa-1B. The effect of 0.01M sulfate on U(VI) adsorption by kaolinite was relatively small. The data possibly suggest a small decrease in U(VI) uptake, however, the effect was minor compared to the effects of changes in other experimental conditions.

7.3.4 CITRATE

As was found with the ferrihydrite, the presence of citrate causes a dramatic decrease in U(VI) uptake on kaolinite across the entire pH range (Fig. 7-12). It is possible that some dissolution of kaolinite (particularly of any iron-rich impurity phases which may be present) may have occurred, and this may contribute to the reduced adsorption in the presence of citrate. However, it appears that the most likely explanation is that complexation of U(VI) by citrate in the aqueous phase greatly reduced U(VI) uptake.

7.4 Effect of Trace Impurities on U(VI) Adsorption by Kaolinite

7.4.1 U(VI) ADSORPTION IN MIXED FERRIHYDRITE / KAOLINITE SYSTEMS

U(VI) adsorption was studied on a mixture of solids containing kaolinite and ferrihydrite, with solid/liquid ratios of 4 g/L and 89 mg/L, respectively. Under the experimental conditions, the ferrihydrite probably coats the surface of kaolinite, as has been observed in nature. The resulting solid had a slight pink tinge, whereas pure kaolinite is off-white in color.

The results (Fig. 7-13) showed that the adsorption properties of the mixed system were very similar to ferrihydrite, although it was the minor phase on a mass basis (about 2.2 wt%). This supports the hypothesis that strongly adsorbing trace mineral phases may dominate metal adsorption in the natural environment (Coston et al., 1995).

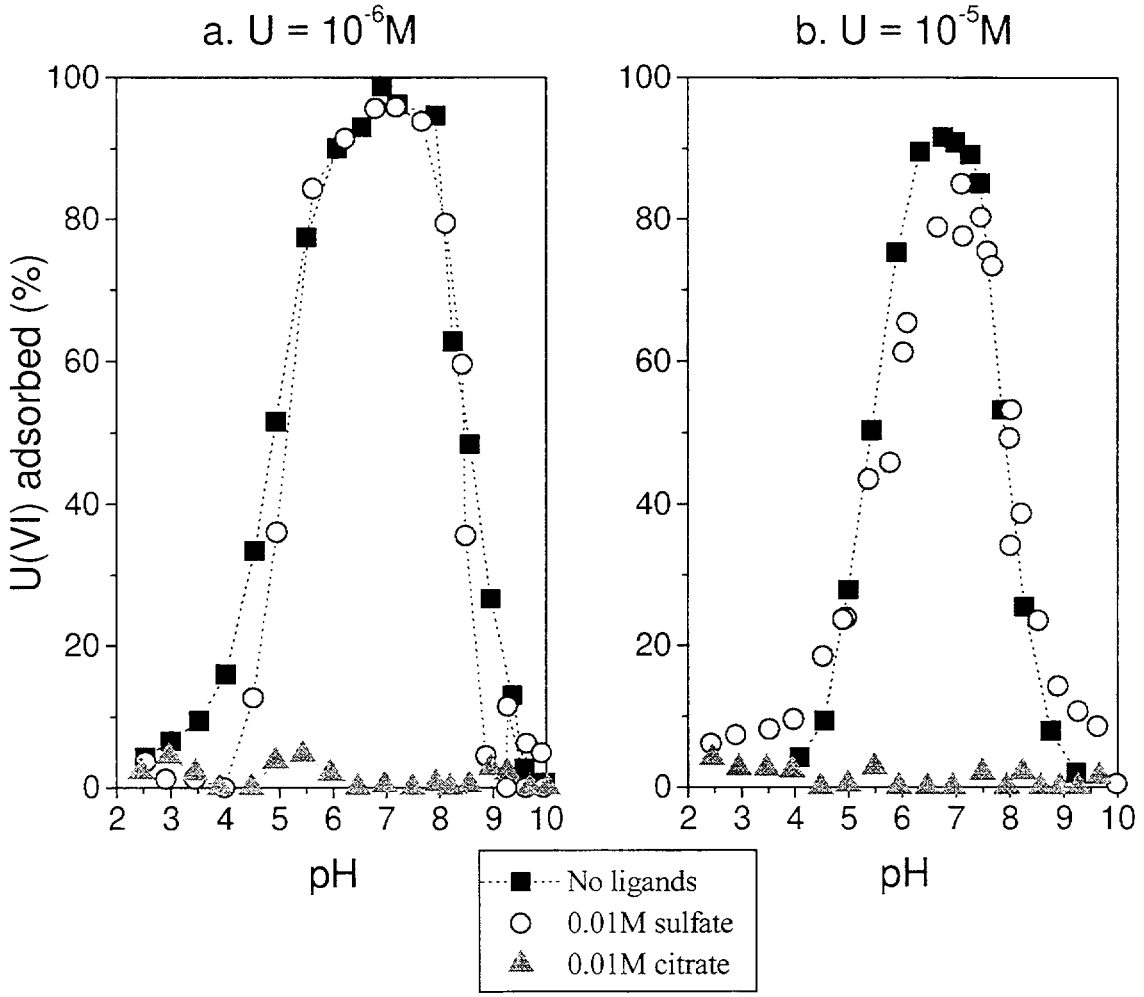

Figure 7-12. Effect of sulfate and citrate ligands on U(VI) adsorption by kaolinite sample KGa-1B (4 g/L). 0.1M $NaNO_3$ solution, equilibrated with air. a) U_T = 1 μM, b) U_T = 10 μM.

7.4.2 ANALYTICAL ELECTRON MICROSCOPY RESULTS

The association of adsorbed U(VI) with the various mineral surfaces was studied using AEM. A sample of kaolinite KGa-1, which had been used in an experiment with U_T of 10^{-4}M, was found to consist of abundant kaolinite particles and a smaller proportion of Ti-rich particles.

Electron microscope images and corresponding point analytical data for the kaolinite and Ti-rich particles are shown in Figure 7-14 and 7-15 respectively. The particles are entirely different both in their appearance and chemical composition.

The AEM data for 25 kaolinite grains in this sample are summarized in Table 7-1. The elemental results for Al and Si are similar to that expected for a pure kaolinite, and are close to reported values for the bulk composition of KGa-1. The average U content of the kaolinite particles examined was only 0.06%, which was much less than was expected on the basis of the amount of U(VI) taken up by the solid in this experiment. Therefore, the kaolinite particles in this sample were only responsible for a small proportion of the U(VI) uptake.

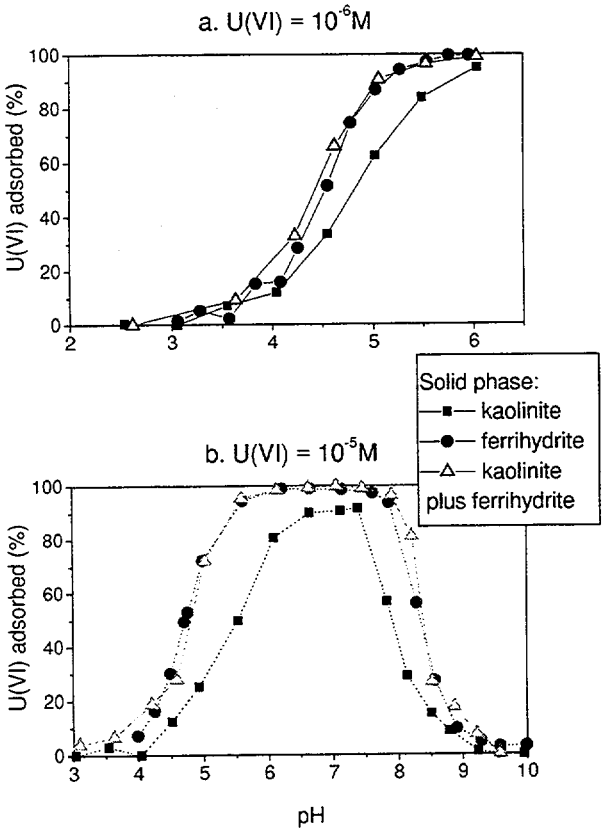

Figure 7-13. Adsorption of U(VI) on ferrihydrite (Fe_T = 1 mM), kaolinite (KGa-1, 4g/L) and a mixture comprising both minerals. a) U_T = 1 μM, b) U_T = 10 μM.

The separate Ti-rich particles were identified by electron diffraction as being anatase and rutile. Anatase is the more abundant TiO_2 polymorph, and occurs as clusters consisting of grains generally less than 0.2 - 0.3 μm in size, and also as single crystals up to 0.5 μm in size. Rutile is less common, but several single crystals up to approximately 1 μm in length were observed. The presence of these phases is consistent with previous work on Georgia kaolinite (Weaver, 1976). The amount of U associated with Ti-rich particles was about 0.7%, more than ten times higher than the kaolinite particles (Table 7-1). Therefore, the Ti-rich particles, despite being less abundant than the kaolinite particles, were responsible for a substantial proportion of the total U(VI) adsorbed by the KGa-1 sample. We observed a significant negative correlation between the amount of U present and the grain size of the Ti-rich particles, indicating that

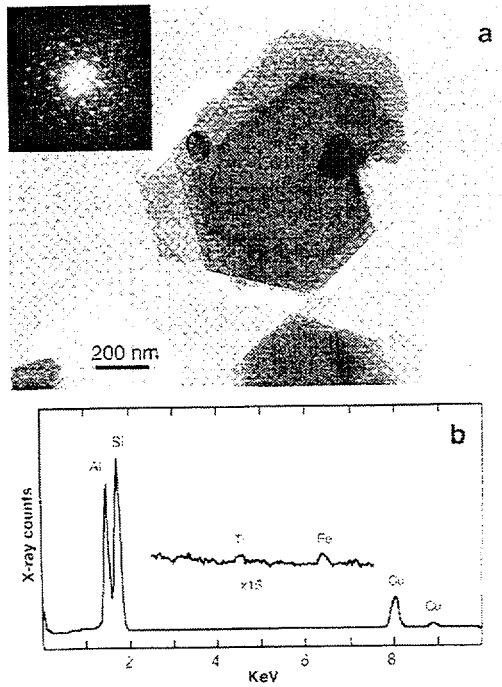

Figure 7-14. Electron microscopy results for U(VI) adsorption experiments with kaolinite sample KGa-1. Part A (top): TEM bright field image and electron diffraction pattern (inset). Note two small anatase single crystals on the kaolinite in the bright field image. Part B (bottom): EDS spectrum of kaolinite. The expanded scale shows little evidence of adsorbed U.

U(VI) is preferentially adsorbed by the fine-grained anatase clusters.

Mass balance calculations showed that the anatase and kaolinite particles could not be responsible for all the loss of U(VI) from solution. This discrepancy was resolved when agrain containing predominantly U in the EDX spectrum was observed in the sample (Fig. 7-16, Table 7-1). This indicated that some precipitation had occurred in experiments with high U_T on the KGa-1 sample, and was consistent with the solubility calculations described above. Based on the presence of diffuse rings in its diffraction pattern, the U-rich particle was predominantly amorphous. However, it had some crystallinity, which may have been acquired by evaporation during the sample preparation, or by electron beam heating

Table 7-1. Summary of AEM data for samples from U(VI) adsorption experiments[a]

	KGa-1 bulk compo-sition[b]	Kaolinite (KGa-1) with added U of 0.6 wt %			KGa-1 + ferrihydrite (Fe of 1.4 wt %, added U of 0.06 wt%)	
		Kaolinite grains (n = 25)	Ti-rich grains (n = 12)	U-rich grain (n = 1)	Kaolinite grains (n = 25)	Ti-rich grains (n = 6)
Al	21.0	20.7	1.23	1.35	20.6	0.85
Si	20.7	21.6	0.75	0.69	21.4	0.36
Ti	0.83	0.14	56.0	0.00	0.12	56.9
U	-	0.06	0.71	76.4	0.05	0.08
Fe	0.15	0.15	0.62	0.15	0.76	0.94

[a]all data expressed as weight %
[b]From Van Olphen and Fripiat (1979)

while under observation in the TEM. Crystalline spots in the diffraction pattern were consistent with a partially dehydrated form of schoepite.

We also studied mixed KGa-1/ferrihydrite samples with adsorbed U(VI). Kaolinite and anatase particles were both examined, and the results showed that Fe was fairly uniformly distributed over the clay and anatase particles (Table 7-1). The Fe content of the kaolinite grains averaged 0.76% compared to 0.15% in pure KGa-1. The Fe associated with the anatase increased slightly from 0.62% to 0.94%. Presumably the U(VI) was adsorbed on Fe oxide coatings, since separate particles rich in Fe or U (or both) were not observed.

7.4.3 IMPLICATIONS OF TRACE MINERAL PHASES TO SCM MODELING

Minor phases such as anatase or ferrihydrite may play a major role in systems where much greater

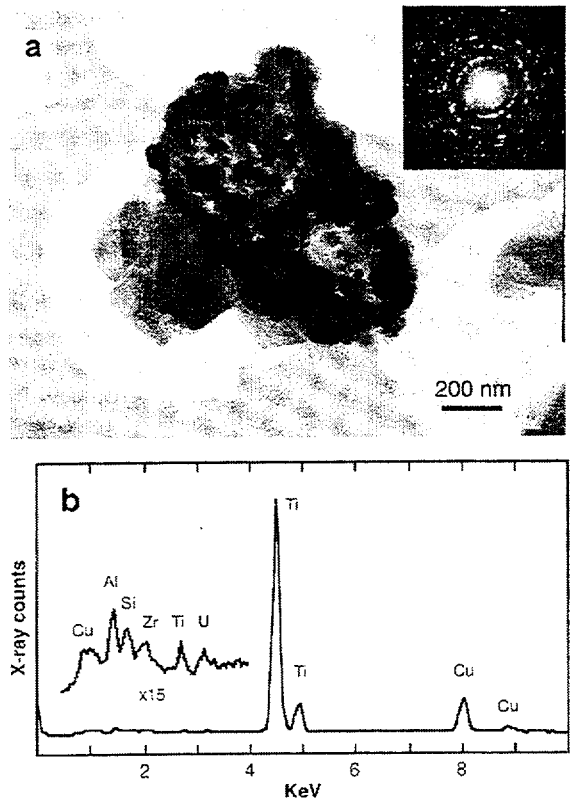

Figure 7-15. Electron microscopy results for anatase. Part A (top): TEM bright field image and electron diffraction pattern (inset). In this example, the anatase occurs as a cluster of many small crystals. Part B (bottom): EDS spectrum of anatase. Expanded scale shows positive evidence of adsorbed U.

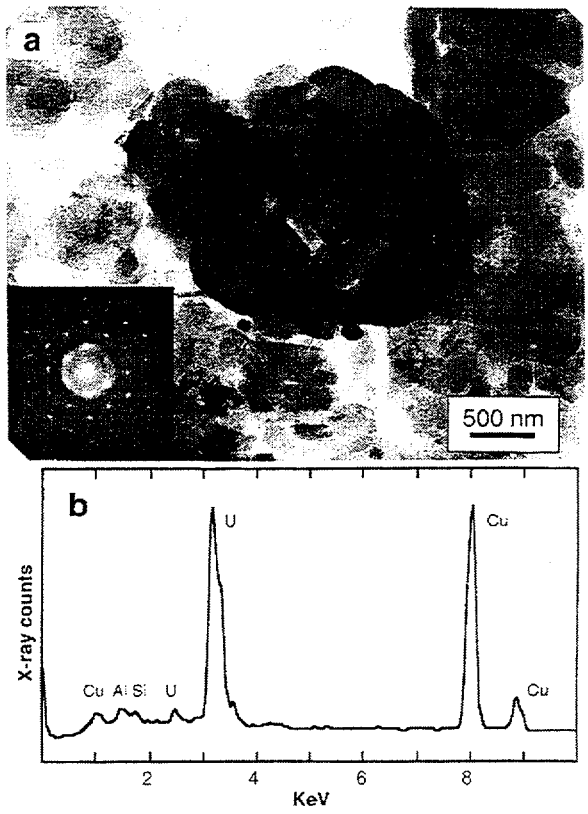

Figure 7-16. Electron microscopy results for U-rich precipitate. Part A (top): TEM bright field image and electron diffraction pattern (inset). Note diffuse rings in the diffraction pattern. Part B (bottom): EDS spectrum. Combined data indicate that the phase is a partially dehydrated form of schoepite.

amounts of kaolinite are present. The influence of Ti-rich particles on the U(VI) adsorption behavior of KGa-1 may be important in any study in which KGa-1 or a similar kaolinite is used. This suggests that the uptake of U(VI) (and possibly other species) by KGa-1 should not be modeled on the basis of surface coordination by Al or Si surface sites alone. The much stronger adsorption on anatase (i.e., Ti sites) should be taken into account. The greater Fe content of the anatase particles (relative to the kaolinite particles) may also contribute to U(VI) adsorption (Table 7-1). Although the AEM work in the present study was carried out at relatively high sorption densities of U(VI), it is likely that the proportion of U(VI) taken up by anatase will be even greater at lower U_T concentrations.

In previous work, extractions of weathered natural samples with the DCB (dithionite / citrate/ bicarbonate) reagent, which dissolves amorphous and crystalline iron minerals, removed less than 2% of the contained titanium (Payne et al., 1994). Therefore, extraction techniques which aim to dissolve trace iron impurities are likely ineffective in dissolving anatase. Indeed, it was previously shown that extraction with the DCB reagent had no effect on U(VI) uptake by the KGa-1 kaolinite (Waite et al., 1994a). For the present study, we did not carry out chemical treatments to remove amorphous or trace mineral phases. The presence of chemically resistant anatase in the

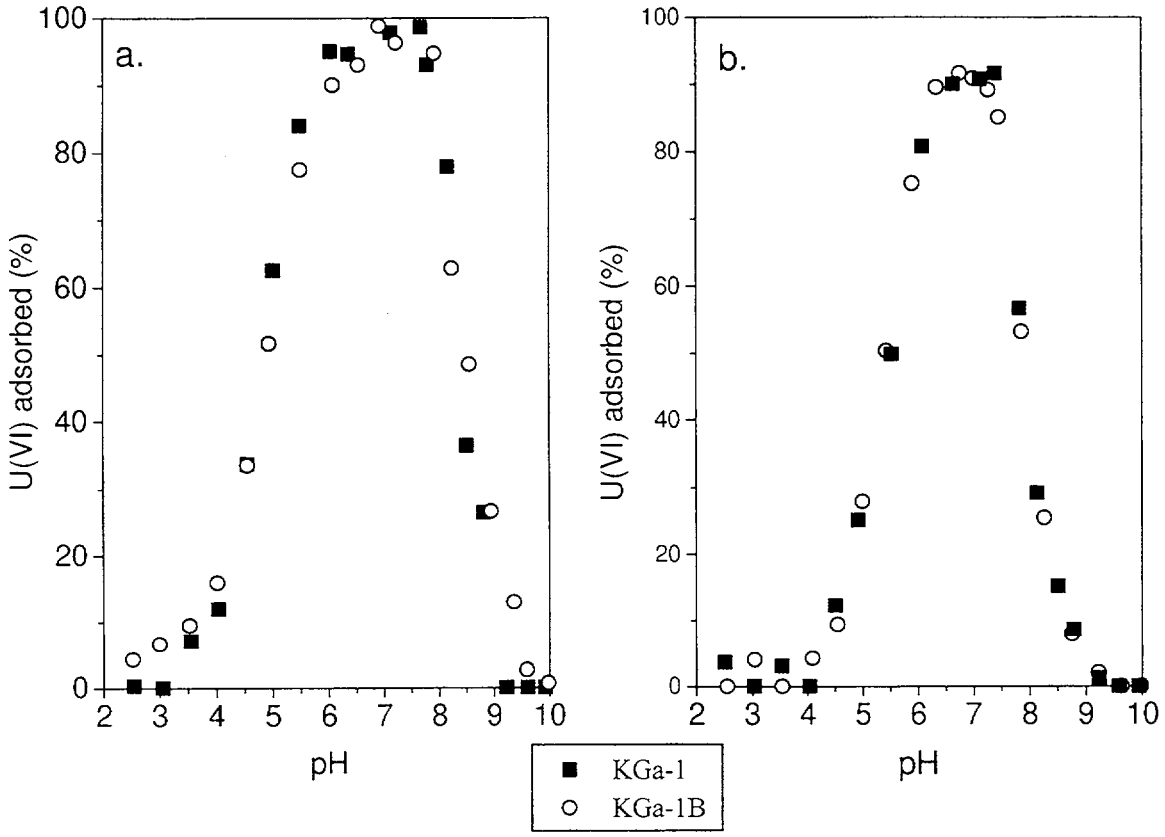

Figure 7-17. U(VI) adsorbed by kaolinite samples KGa-1 and KGa-1B (solid/liquid ratio of 4g/L). Part A (left) U_T = 1 μM; Part B (right) U_T = 10 μM.

KGa-1 sample (and possibly other kaolinites) may well influence the results of adsorption experiments, even after prior chemical extraction.

7.5 Comparison of U(VI) adsorption on KGa-1, KGa-1B and Kanpaku kaolinite

As noted above, supplies of the standard KGa-1 kaolinite, which was used in the early part of our experimental program, became exhausted, and the Clay Mineral Society substituted the similar material denoted KGa-1B. A description of thelatter material and a comparison with KGa-1 has been published (Pruett and Webb, 1993). The elemental compositions of the two kaolinites are given in Table 7-2. A comparison of U(VI) adsorption data on KGa-1 and KGa-1B is shown in Figure 7-17. In general the data are quite similar. At a U_T concentration of 10^{-5}M, both samples appeared to be near saturation with adsorbed U(VI) (Fig. 7-17b).

It was shown above that a titanium impurity phase, which is present in the Georgia kaolinites KGa-1 and KGa-1B (as well as many other kaolinites), is a preferential adsorbing surface for the uptake of U(VI). This leads to a greater density of adsorbed U(VI) on the surface of the Ti-rich phase, which consists mostly of anatase. Consequently we obtained another kaolinite (kindly provided by Professor Watanabe, Joetsu University of Education, Japan). The chemical composition of this kaolinite is summarised in Table 7-2. It contains a much lower level of Ti than the KGa-1 and KGa-1B samples previously studied, and lower amounts of impurities such as Fe.

The experimental data (Fig. 7-18) for U(VI) adsorption on the Kanpaku kaolinite are similar to the other kaolinites, with a slightly reduced

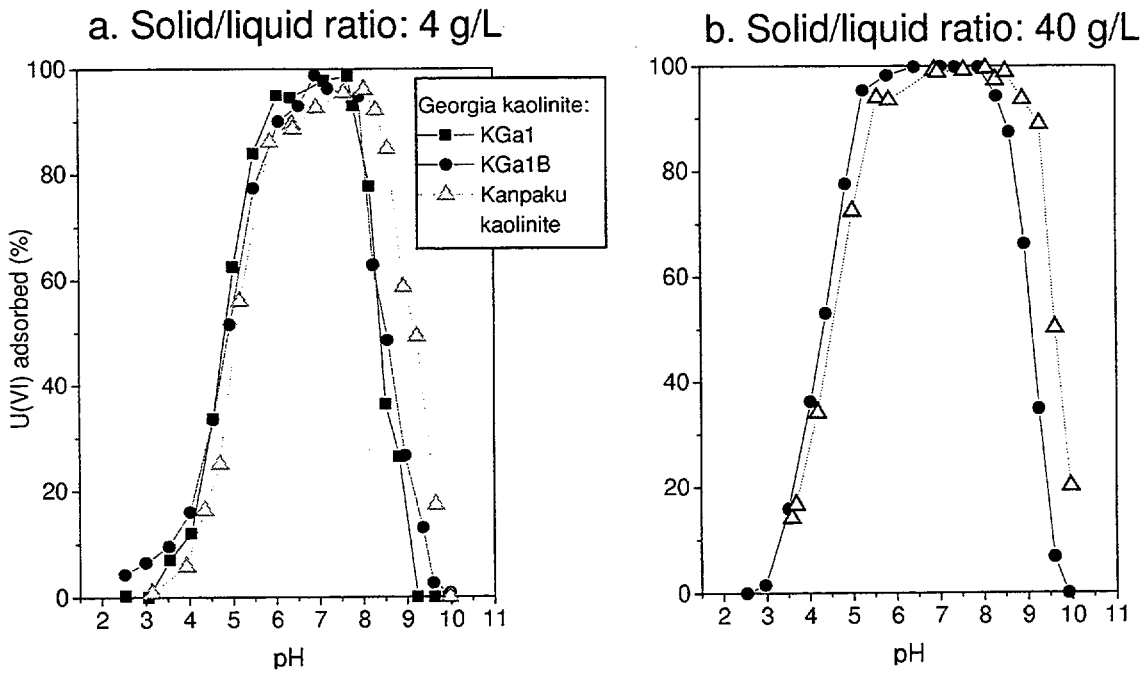

Figure 7-18. Comparison between U(VI) adsorption on Kanpaku kaolinite and Georgia kaolinite samples with U_T = 1 μM. Part A) 4g/L; Part B) 40g/L.

adsorption at low pH values. A much greater effect on the high pH edge was observed, with the high pH edge being displaced to higher pH values (i.e., significantly increased U(VI) adsorption. At this stage, we do not have an explanation for the experimental data, however the results provide a further indication that U(VI) uptake on 'kaolinite' samples is significantly affected by impurity phases and differences between samples. The interpretation of adsorption data on model kaolinites (at least in studies of U(VI) adsorption) may be difficult to generalize as these materials do not adsorb U(VI) in a uniform fashion. Clearly the nature and content of impurities and other heterogeneities between samples must be considered.

Although there are problems in interpreting the adsorption data for model kaolinites, it is clear that kaolinite is a comparatively weak U(VI) adsorber. The conclusion of Giblin (1980) that adsorption of U(VI) on kaolinite surfaces is an important pre-concentration mechanism for the genesis of U deposits at the Alligator Rivers uranium field (including Koongarra) appears unlikely on the basis of our experimental data.

7.6 Summary

For a given set of experimental conditions, U(VI) adsorption by kaolinite (expressed as U(VI) sorbed per gram of adsorbent) is much less than for ferrihydrite. However, the amount of U(VI) adsorbed by kaolinite is similarly dependent on experimental variables such as pH, U_T, solid/liquid ratio, and the presence of complexing ligands. The presence of phosphate increased U(VI) uptake in the low pH range, and this appears to be attributable to the formation of a ternary surface complex involving both U(VI) and phosphate. U(VI) adsorption on kaolinite samples is strongly influenced by the presence of Ti-rich impurity phases (predominantly anatase), which occur in many natural kaolinites. Due to weak U(VI) adsorption on kaolinite, precipitation of a U(VI)-rich phase occurred in some experiments. A small amount of a ferrihydrite phase added to the model kaolinite

completely modified its adsorptive reactivity, further demonstrating the importance of trace impurity phases in the natural environment.

Table 7-2. Chemical composition of KGa-1, KGa-1B and Kanpaku[a] Kaolinites

	Kanpaku	KGa-1 [b]	KGa-1B [c]
SiO_2	44.53	44.2	45.2
TiO_2	0.21	1.39	1.64
Al_2O_3	39.15	39.7	39.1
Fe_2O_3	0.03	0.13	0.21
FeO	0.01	0.08	-
MnO	n.d.	0.002	-
MgO	0.05	0.03	0.05
CaO	0.07	n.d	0.02
Na_2O	0.05	0.013	0.04
K_2O	0.03	0.05	0.02
P_2O_5	0.19	0.034	
$H_2O(+)$	14.37		
$H_2O(-)$	0.98		
CO_2	0.21		
Total	99.88		
C, H, N analysis:			
C	0.00058		
H	0.01719		
N	0.00018		
Minor elements	Ba Ce V La Zr		

[a]Kanpaku kaolinite sample and analysis provided by Professor Watanabe, Joetsu University of Education, Japan
[b]Van Olphen and Fripiat,1979
[c]Pruett and Webb, 1993

8 URANIUM(VI) ADSORPTION ON CRUSHED QUARTZ WITH SYNTHETIC IRON OXYHYDROXIDE COATINGS

8.1 Background

Reactions with mineral grain coatings that contain Fe- and Al-oxyhydroxides, silicate, and organic material are commonly believed to control metal-ion adsorption in natural systems (Davis and Kent, 1990). Many experimental studies have documented the role of Fe oxyhydroxides as an adsorbent of metal ions in soils and sediments (Payne and Waite, 1991; Bourg et al., 1989; Lienert et al., 1994; Fuller et al., 1996; Coston et al. 1995). In the soil profile near the Koongarra uranium ore body (Australia), iron minerals form in the weathered zone (25-30 m depth) primarily by alteration of chlorite (Edis et al., 1992). Ferrihydrite is known to occur as interstitial material between chlorite and vermiculite slabs and act as a scavenger for uranyl species by adsorption (Waite and Payne, 1993). Therefore, in order to predict mobility of uranium at Koongarra, it is important to understand the fundamental physical-chemical interaction of U(VI) with hydrous ferric oxides, both as pure phases and as coatings. The main objective of this study was to investigate whether coatings of ferrihydrite adsorb U(VI) in a quantitatively similar fashion as pure precipitates of ferrihydrite. If this could be proven, then the surface complexation model developed by Waite et al. (1994b) could be applied to describe U(VI) adsorption by coatings. Quantification of ferrihydrite in coatings in the soil profile can be accomplished by chemical extractions (Waite and Payne, 1993).

8.2 Materials and Methods

Min-U-Sil 30, a crushed quartz powder available commercially, was used as a pure quartz analog. Min-U-Sil 30 was cleaned in the manner described in Section 5. The resulting particle size ranged between 10 and 30 μm (Fig. 5-2), and the surface area measured by BET N_2 gas adsorption was 0.37 m^2/g.

Reagent grade ferric nitrate, $Fe(NO_3)_3 \cdot 9H_2O$, was used to make all Fe stock solutions. Iron oxyhydroxide precipitates were used fresh and therefore were assumed to be "two-line" ferrihydrite (Waychunas et al., 1993; Schwertmann and Fischer, 1973), except for the precipitate in Method VI (described below) that was aged. The ferrihydrite surface area was measured by BET N_2 gas adsorption as 177 m^2/g after freeze drying the solid. All water used in the study was Milli-Q water and all other chemicals used were reagent grade.

8.2.1 IRON OXYHYDROXIDE COATING METHODS

There were seven methods of synthesis used to prepare quartz samples with Fe(III) oxyhydroxide coatings for U(VI) adsorption experiments. In each of the methods, the final solid mixture contained 3 μmoles Fe(III) per gram of quartz. The methods are summarized in Table 8-1. Details of these methods are presented below.

Method I - Physical Mixture. The physical mixture method may provide the weakest association of iron oxide with the quartz surface because the Fe was polymerized by precipitation as ferrihydrite before contacting the quartz surface. The ferrihydrite was prepared in a 1 L HDPE bottle, open to the atmosphere, starting with a 1 mM ferric nitrate solution which was titrated from pH 3 to pH 7. The titration was completed over a 45 minute time period by dropwise addition of a combination of 0.1 M and 0.01 M NaOH; the suspension was allowed to equilibrate at pH 7 for 1 hour. Aliquots of the stirred ferrihydrite suspension were sampled with an autopipet and added to centrifuge tubes containing quartz suspensions in 0.01 M $NaNO_3$ solution. Each tube was adjusted to a pH within the range 3-6.5 and allowed to equilibrate for 18 hours before use in U(VI) adsorption experiments.

Table 8-1. Descriptions of Synthesis Methods Used to Prepare Iron Oxyhydroxide Coatings on the Quartz Surface

Method/Purpose	Brief Description
I. Physical mixture: "minimum possible" interaction of ferrihydrite with quartz particles	Physical mixing of quartz and ferrihydrite suspensions in electrolyte solutions, each prepared separately and then mixed together.
II. Physical mixture with 'poisoned' ferrihydrite: "minimum possible" interaction of silicate-poisoned ferrihydrite with quartz particles	Physical mixing of quartz and ferrihydrite that was precipitated separately in the presence of dissolved silicate.
III. Titration precipitation: allows for sorption of Fe(III) hydrolysis products prior to formation of ferrihydrite; Fe(III) present from lowest pH to pH 7	Addition of an acidified Fe(III) solution to an acidic quartz suspension, with subsequent addition of NaOH to adsorb or precipitate Fe(III).
IV. Slow Fe(III) precipitation at pH 7: Fe(III) hydrolyzes at pH 7 in the presence of the quartz surface	Addition of an acidic Fe(III) solution over 18 hours to a suspension of quartz in 0.01 M $NaNO_3$ solution held at pH 7.
V. Fe(III) precipitation at pH 7, aged: produce a coating of different crystallinity or structure	Product of Method IV aged for 1 month at 50 °C
VI. Slow Fe(III) precipitation at pH 7 in the presence of dissolved silicate: observe effects of greater concentration of silicate	Same as Method IV with dissolved silicate present.
VII. Oxidation of Fe(II) at pH 7: compare to precipitation of added Fe(III) to form coatings	Addition of Fe(II) solution to a suspension of quartz in 0.01 M $NaNO_3$ solution held at pH 7 and with dissolved silicate present.

Method II - Physical mixture of quartz with ferrihydrite precipitated in the presence of dissolved silicate. This method is identical to Method I, except for the synthesis of the ferrihydrite. An aliquot of a silicate standard solution was added to Milli-Q water, and the pH was decreased below 3. An aliquot of ferric nitrate solution was added to a concentration of 1 mM. This solution was titrated dropwise up to pH 7 to precipitate the iron oxyhydroxide. Aliquots of this suspension were then added to centrifuge tubes containing the quartz/electrolyte (0.01 M $NaNO_3$) suspension before use in U(VI) adsorption experiments.

Adsorption of silicate by ferrihydrite during co-precipitation was measured in a separate experiment. In this experiment, ferrihydrite was precipitated in the presence of 100 μM dissolved silicate, the precipitate was centrifuged, and the resulting supernatant was measured for Fe and Si by ICP-AES.

Method III - Titration precipitation. This method allows for the possibility of Fe(III) sorption and polymerization on the quartz surface by hydrolyzing the Fe(III) in the presence of quartz. An aliquot of 1 mM ferric nitrate solution at pH 2.6 was added to quartz suspensions in 0.01M HNO_3 solution at pH 2 in centrifuge tubes. Each tube was then titrated to pH 5 over a 45 minute period to sorb/precipitate the iron oxyhydroxide coating, and the contents were allowed to equilibrate for 1 hour. Each tube was then adjusted to a pH value in the range 3-6.5 and allowed to equilibrate for 18 hours before use in U(VI) adsorption experiments.

Method IV- Slow Fe(III) precipitation at pH 7. This method also allowed Fe(III) to sorb and polymerize on the quartz surface during precipitation. However, in this case, the system was pH-stated at 7, which could result in rapid Fe(III) polymerization in the aqueous phase prior to attachment to the quartz surface. In Methods I-III polymerization likely occurred at low pH. The intent of this method was to compare what happened when polymerization occurred at near-neutral pH, however, it is recognized that the pH at which polymerization occurred may have been influenced by the mixing rates. The pH stat system used for this method consisted of: (1) two motorized syringes, one for delivery of Fe(III) stock solution and a second syringe for delivery of base to neutralize the acid in the Fe(III) stock solution; (2) an HDPE plastic bottle, which the syringes fed, containing a pH 7 quartz/electrolyte (0.01 M $NaNO_3$) suspension; (3) a N_2 gas line for purging the solution at pH 4 (for 1 hr) before Fe(III) stock solution addition and to purge the headspace to exclude carbonate during precipitation. The acidified Fe(III) stock solution was added over 18 hours and the pH of the quartz suspension was held at pH 7±0.1. After the 18 hour precipitation period, the system was adjusted to pH 5 and allowed to equilibrate for 1 hour. The batch was then transferred into a calibrated tilt dispenser and 20 mL aliquots were added to centrifuge tubes to begin U(VI) adsorption experiments.

Method V- Fe(III) precipitation at pH 7 with aging. This method was identical to Method IV, except the resulting quartz/iron oxyhydroxide suspension was placed in a shaking water bath at 50±1 °C for 4 weeks. The pH of the suspension was checked daily during the first week and every other day afterwards and was kept at pH 7±0.1 by adjusting with 0.01 M NaOH solution. Volume loss due to evaporation was accounted for and replaced.

Method VI - Fe(III) precipitation at pH 7 with dissolved silicate. This method was used in order to observe if an increased concentration of dissolved silicate would affect the type of coating formed on the quartz surface. The same experimental setup was used as in Methods IV and V, except that an aliquot of silicate was added to the quartz suspension prior to N_2 sparging at pH 4 for removal of $CO_2(g)$.

Method VII – Oxidation of Fe(II) at pH 7 with dissolved silicate. Oxidation of Fe(II) may be a more common process by which Fe(III) oxyhydroxide coatings form in nature (Schneider and Schwyn, 1987) than sorption of pre-formed Fe(III) polymers or precipitates. This method was intended to mimic this process of coating formation in which Fe(II) is transported to a zone of oxidation, oxidized and sorbed/polymerized at circumneutral pH in the presence of dissolved silicate. The process could occur via: (1) reduction of Fe(III) by microorganisms, followed by transport of Fe(II); or (2) release of Fe(II) in the weathering process from a Fe(II)-bearing mineral phase. This method used the same pH-stat setup as in Methods IV, V, and VI, except in this method an acidic ferrous sulfate solution was added slowly via syringe pump to a quartz suspension in 0.01 M $NaNO_3$ solution with 100 µM dissolved silicate. The suspension was bubbled with CO_2-free air to oxidize the added Fe(II) solution in the presence of quartz. Samples were taken of the Fe(II) stock solution in the syringe to make sure the Fe(II) solution did not oxidize before exiting the syringe. Samples were also taken of the final supernatant to be certain that all dissolved Fe(II) was oxidized. Fe(II) analyses were done using the ferrozine method of Gibbs (1979), which has a linear range from 0 to 17.9 µM Fe(II). Absorbance was determined at a wavelength of 562 nm.

8.2.2 SOLID CHARACTERIZATION METHODS

Solid characterization techniques included: (1) naked eye observation of the solid color in the batch tubes; (2) scanning electron microscopy (SEM, including energy dispersive spectroscopy, SEM-EDS) to observe textures and identify iron oxide on the silica surface; (3) Tamms-acid oxalate (TAO) extraction of the aged precipitate of Method V to estimate the degree of crystallization of the iron oxydroxide coating; (4) Fe(III) sorption experiments, similar to Method III, to gain further insight into

the process of coating formation by Fe(III) oxyhydroxides; and (5) Si dissolution experiments with the Min-U-Sil solid.

Scanning Electron Microscopy. SEM was used to examine the texture of ferrihydrite and to observe its association with the quartz surface. SEM-EDS was used for elemental mapping of Fe on the surface. Samples were prepared by the methods described above, centrifuged, and freeze dried. Freeze-dried samples were placed on aluminum sample holders with glass cover slips. All samples were coated with gold palladium before analysis.

TAO Extraction. TAO extractions were performed on the precipitate prepared by Method IV only, following the method of Landa and Gast (1973).

Fe (III) Sorption Experiments. These experiments were performed to examine the partitioning of Fe(III) between the aqueous and solid phases as a function of pH in a system similar to that prepared by Method III. The Method III procedure was used to conduct these experiments, except for the final step at which the pH of the quartz suspension was raised to 5. Instead, the pH in individual centrifuge tubes was raised to a target pH value between 3 and 6, and the suspensions were equilibrated for 18 hours. At the end of the reaction period, the suspensions were centrifuged, the pH values of the supernatants were measured, and the concentrations of Fe(III) in the supernatants were determined by ICP-AES.

Si Dissolution from Min-U-Sil Solid. It was mentioned earlier that silicate can affect ferrihydrite particle formation and transformation to more crystalline phases. A few experiments were performed in order to observe the dissolved silicate concentrations that occurred due to dissolution of the Min-U-Sil quartz phase. First, a quartz dissolution rate experiment was carried out in which a series of centrfuge tubes containing 10 g/L quartz in 0.01M $NaNO_3$ solution were adjusted to a pH value of 5.35 and allowed to equilibrate for various time periods. The samples were centrifuged and the supernatants were analyzed for Si by ICP-AES. In addition, the same experiment was performed with an initial concentration of 100 μM Si to examine whether the rate of Si dissolution was changed by the addition of silicate.

8.2.3 METHODS OF U(VI) ADSORPTION BATCH EXPERIMENTS

8.2.3.1 Experiments with quartz particles.

All experiments were conducted with a solid/liquid ratio of 10 g/L quartz. In all experiments with quartz with Fe(III) oxyhydroxide coatings, the total Fe(III) concentration present as a precipitate or coating was 30 μM (3 μmoles Fe(III) per gram quartz). Total Fe concentrations were checked for consistency by acidifying selected samples to pH 2 and measuring dissolved Fe in the supernatant. ICP-AES was used for all dissolved Fe(III) and Si analyses.

For each method of preparing quartz with Fe(III) oxyhydroxide coating, aliquots of the precipitate mixtures were suspended (without washing or drying) in $NaNO_3$ solution of the desired concentration to yield a total volume of 20 mL in a centrifuge tube. Each suspension was pre-equilibrated for 18 hours at a chosen pH value within the range of 3 to 7, and then spiked with 200 μL of $1 \cdot 10^{-4}$ M U(VI) stock solution with ^{233}U tracer to yield a total concentration of $1 \cdot 10^{-6}$ M U(VI). (See Section 5 for more information on the ^{233}U tracer). The pH values of the suspensions were immediately readjusted to their original values to compensate for the addition of acid in the U(VI) stock solution, and the suspensions were equilibrated for an additional 18 hours.

At the end of the reaction period, pH measurements were made with an Orion Ross combination electrode in both stirring and quiescent modes, with readings taken at exactly 3 minutes after electrode immersion. The electrode was calibrated using a two point calibration with NBS-certified buffers. After final pH values were measured, the tubes were centrifuged and supernatant samples were measured for ^{233}U tracer activity by liquid

scintillation counting. Two samples of the initial solution without solid phases were prepared in each experiment and kept at low pH to provide a measurement of the total ^{233}U tracer activity in each experiment. U(VI) adsorption was determined by difference in ^{233}U tracer activities. A U(VI) mass balance was checked by adding 0.01 M HNO_3 to selected sample centrifuge tubes and equilibrating overnight. Mass balances were also checked by transferring samples equilibrated at various pH values to new tubes, rinsing the tube with deionized water, and then acidifying the empty, used centrifuge tubes to check for U(VI) adsorption by the tube walls.

8.2.3.2 Experiments with pure ferrihydrite.

U(VI) adsorption experiments with pure ferrihydrite were conducted by two different methods: (1) a modification of the method of Waite et al. (1994b); and (2) by precipitation at pH 7. Similar to the method of Waite et al. (1994b), ferrihydrite was precipitated by titration of a 1 mM ferric nitrate solution with NaOH from about pH 3 to pH 7 and aged for one hour at pH 7. However, to compare the data with the experiments with coated quartz particles, the ferrihydrite concentration in the adsorption experiments needed to be 30 μM (as Fe). Typically, much higher ferrihydrite concentrations are used in adsorption experiments (Waite et al., 1994b). To achieve the lower ferrihydrite concentrations, aliquots of the ferrihydrite suspension were taken (after the one hr of aging) and resuspended in 0.01 M $NaNO_3$ solution in centrifuge tubes at a concentration of 30 μM (as Fe). The pH in each tube was adjusted to a target pH value within the range 4 to 6 and aged for 18 hours. Then U(VI) was added to initiate the batch adsorption experiment following the same method described above for coated quartz samples.

In the second method, ferrihydrite (30 μM as Fe) was precipitated by slow addition of ferric nitrate solution to 0.01 M $NaNO_3$ solution held at pH 7 (identical to the titration method of Method IV above, except that no quartz particles were present). Aliquots of this suspension were transferred to centrifuge tubes and prepared for U(VI) adsorption experiments following the same procedure described in the previous paragraph.

8.2.3.3 Experiments with Ferrihydrite Co-precipitated with Silicate.

To assess the effect of adsorbed silicate on the adsorption of U(VI) by ferrihydrite, two sets of experiments were performed with ferrihydrite precipitated in the presence of dissolved silicate. In the first set, ferrihydrite (200 μM as Fe) was precipitated from ferric nitrate solution at about pH 3 containing 100 μM silicate by dropwise addition of NaOH until a pH of 7 was achieved. Aliquots of the suspension were taken (after one hr of aging) and resuspended in 0.01 M $NaNO_3$ solution in centrifuge tubes at a concentration of 30 μM (as Fe). The aliquots were then prepared for U(VI) adsorption experiments as above.

In the second set of experiments, ferrihydrite (30 μM as Fe) was precipitated in 0.01 M $NaNO_3$ solution containing 200 μM silicate. Aliquots of this suspension were transferred to centrifuge tubes and prepared for U(VI) adsorption experiments following the same procedure described above.

8.3 Results

8.3.1 CHARACTERIZATION OF THE SOLID PHASES

Of the seven methods of preparing coated quartz particles, only the physical mixture (Method I) and the titration precipitation (Method III) showed a separation of phases that could be distinguished by color separation with the naked eye. The physical mixture (Method I) appeared as two separately colored solids after settling and the distinction was even more clear after centrifugation. In Method III, solids of two to three types could be distinguished, with two end member colors and a colored solid in between. In all other methods, the solid phase appeared as a uniform color, slightly darker than the white quartz sample.

The solid phases from Methods I,III, IV and VI were observed with SEM. Observation of the

physical mixture (Method I) with SEM and SEM-EDS revealed patchy coatings of iron oxyhydroxide, with most of the quartz surface showing no visible coatings or detectable iron. These patchy coatings are shown in Figure 8-1 as ropy islands on the large center grain. In the other three methods, neither coatings nor detectable Fe were observed, possibly indicating that the Fe(III) was distributed on the quartz surface in much thinner coatings in which Fe was not detectable by EDS.

Tamms-acid oxalate (TAO) and warm 6 M HCl extractions were performed on the aged precipitate (Method V). Although the aging for one month at 50°C was intended to transform some of the ferrihydrite to more crystalline material, both extractions dissolved all of the 3 μmoles/g of Fe(III) present in the samples. According to the operational method, TAO extractions only dissolve negligible quantities of goethite and hematite (Chao and Zhou, 1983; and see Section 9). The results suggests that the iron oxyhydroxide coating produced by this method was not transformed significantly to either goethite or hematite. Goethite and hematite peaks were absent in an XRD analysis of the samples.

Figure 8-2 shows Fe(III) sorption on quartz as a function of pH. Fe(III) sorption increased with

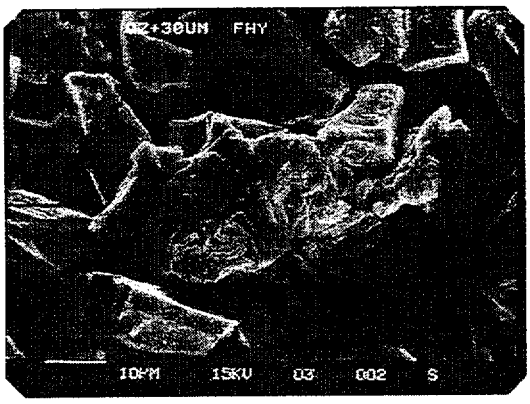

Figure 8-1. Scanning electron micrograph of quartz particles observed with patched iron oxyhydroxide coatings in a sample of the quartz/ferrihydrite mixture produced by Method I.

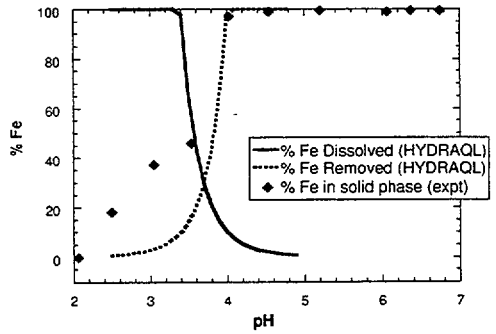

Figure 8-2. Experimental observations and model calculations of dissolved and precipitated Fe(III) as a function of pH in a system containing 10 g/L quartz and 30 μM Fe(III).

pH in the pH 2 to 3.5 range. The suspension contained 10 g/L quartz, which is equivalent to 3.7 m^2/L of surface area. Assuming a density of 3.84 μmoles surface sites per m^2 of surface area (Davis and Kent, 1990), the suspension had 14.2 μmoles surface sites/L of water. The total Fe(III) concentration in the experiment was 30 μM. If each site could bind one Fe(III) atom and no multilayers formed, then a monolayer of adsorbed Fe(III) in this experiment would occur at 47% Fe sorbed. Interestingly, the data exhibit asymptotic curvature toward this level of sorption, but then sorption abruptly increased between pH 3.6 and 4 (Fig. 8-2). Figure 8-2 also shows the results of solubility calculations for ferrihydrite (K_{so} = -38.15 at I=0) at a total Fe(III) concentration of 30 μM. The calculations predict that Fe(III) precipitates as ferrihydrite between pH 3.7 and 4.0, and this is the likely reason for the abrupt increase in Fe(III) sorption observed in this pH range (Fig. 8-2). However, the results suggest that during the pH titration of Method III a significant percentage of Fe(III) is first sorbed as monomers or multimers on the quartz surface before the precipitation of ferrihydrite occurred.

Dissolved Si as a function of time in 10 g/L quartz suspensions in 0.01 M $NaNO_3$ solution at pH 5.3 (25 °C) is shown in Figure 8-3. In the experiment without initial dissolved Si, the Si concentration increased from 6 μM after a few

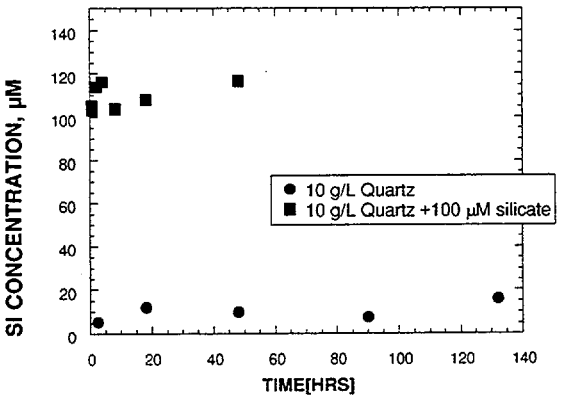

Figure 8-3. Dissolved Si as a function of time in batch experiments containing 10 g/L quartz with and without 100 µM added silicate.

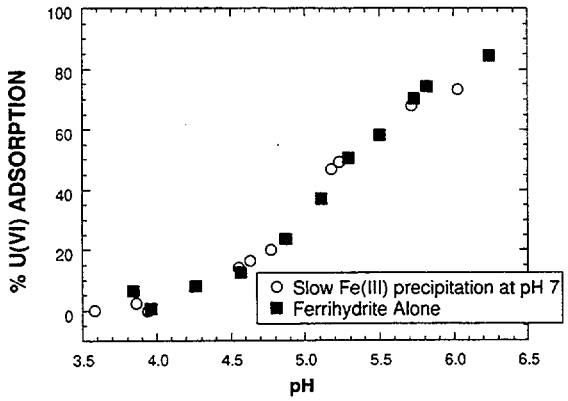

Figure 8-4. U(VI) adsorption on ferrihydrite as a function of pH (U_T = 1 µM; Fe_T = 30 µM as ferrihydrite). Comparison of two methods of ferrihydrite precipitation.

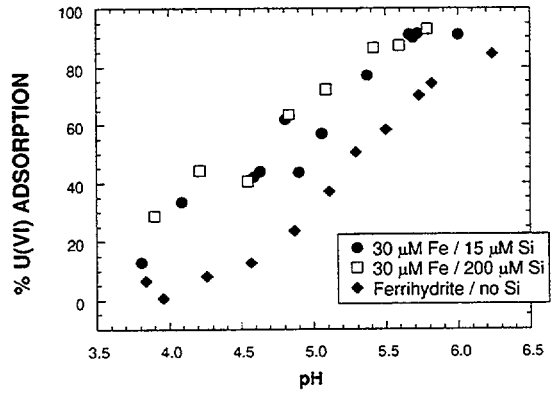

Figure 8-5. U(VI) adsorption on ferrihydrite with and without co-precipitated silicate as a function of pH (U_T = 1 µM; Fe_T = 30 µM as ferrihydrite).

hours of dissolution to 16 µM at 130 hours. In a similar experiment with 100 µM dissolved silicate present initially, the dissolved Si concentration increased to 115 µM after 48 hours. The results suggest that very little Si dissolved from the quartz during the U(VI) batch adsorption experiments. However, in the pH titration method (Method III), the pH of quartz suspensions was lowered to pH 2 before adding ferric nitrate solutions. Dissolved Si in these suspensions was 74 µM, suggesting that Si dissolution was acid-catalyzed.

8.3.2 URANIUM(VI) ADSORPTION

Figure 8-4 shows U(VI) adsorption by pure ferrihydrite suspensions (30 µM as Fe) in 0.01 M $NaNO_3$ solution as a function of pH. No difference in U(VI) adsorption was observed between ferrihydrite produced by titration from low pH values to that produced by slow ferric nitrate addition to 0.01 M $NaNO_3$ solution held at pH 7.

The presence of dissolved silicate during ferrihydrite precipitation caused a significant increase in U(VI) adsorption (Fig. 8-5). The U(VI) adsorption edge was shifted about 0.5 pH units toward more acidic pH values in both experiments in which silicate was present during ferrihydrite precipitation. Three hypotheses that might explain the increased U(VI) adsorption are: (1) an increase in surface area as a result of smaller particle formation (Fuller et al., 1993); (2) an increase in the U(VI) surface binding constant (Anderson and Benjamin, 1985); or (3) the formation of a U(VI)-silicate ternary complex. The observations in Figure 8-5 were made early in this study and provided motivation to examine quartz/ferrihydrite associations. The objective was to learn if ferrihydrite in surface coatings adsorbed U(VI) in a similar manner as pure ferrihydrite. Smaller ferrihydrite particle formation due to surface poisoning may occur in natural systems and affect the transformation of ferrihydrite to goethite or hematite, and the adsorption and release of other contaminants (Fuller et al., 1993; Schwertmann and Thalmann, 1976).

U(VI) adsorption as a function of pH on quartz with each of the iron oxyhydroxide coating methods is shown in Figures 8-6 to 8-12. Figure 8-6 shows U(VI) adsorption edges for the quartz/ferrihydrite physical mixture (Method I) and for quartz and ferrihydrite suspensions alone. At the selected concentrations of quartz and ferrihydrite for these experiments, there were about twice as many surface sites present for ferrihydrite as for quartz, and the U(VI) adsorption edge for the physical mixture seems to reflect a simple additive combination of the two adsorbents. However, modeling of the combination is required to test this hypothesis; modeling results for these experiments are presented in Section 15.

In general, the U(VI) adsorption edges on all the samples of quartz with iron oxyhydroxide coatings (Figs. 8-7 to 8-12) were similar to that of the physical mixture (Method I). Only the titration precipitation (Method III) had a U(VI) adsorption edge that can be considered significantly greater (Fig. 8-8). Average errors in U(VI) adsorption reported are 7% in the pH range 3 to 4.5, 5% in the range 4.5 to 5.5, and 2% in the range 5.5 to 6.5. The Fe(III) precipitation at pH 7 that was aged (Method V) exhibited U(VI) adsorption similar to ferrihydrite alone, and thus, less than the physical mixture (Fig. 8-10). The precipitates produced by Methods II and VI had similar U(VI) adsorption to the physical mixture (Figs. 8-7 and 8-11), even though the presence of dissolved silicate had significantly increased U(VI) adsorption by pure ferrihydrite (Fig. 8-5).

8.4 Discussion

The objective of the experiments was to precipitate a variety of types of iron oxyhydroxide coatings to see if they produced a range of U(VI) adsorptive properties. The range of U(VI) adsorptive properties observed was relatively small, in most cases smaller than experimental error. In a few cases, the adsorptive properties were significantly different. The results are encouraging in terms of the general applicability of surface complexation modeling, since they suggest that a model developed for pure ferrihydrite (Waite et al., 1994b) can likely be applied to describe U(VI) adsorption by ferrihydrite present as a mineral coating.

Greater U(VI) adsorption was observed for the titration precipitation method of coating preparation (Method III) in comparison to the physical mixture. The titration precipitation (Method III) may have produced a coating of relatively high surface area, since it is likely that at least half of the Fe(III) was adsorbed over a large portion of the quartz surface in the initial stage of the titration at low pH (Fig. 8-2). Schindler et. al. (1976) also observed an Fe(III) adsorption edge on silica near pH 2. In a 30 μM ferric nitrate solution acidified to pH 2.5, essentially all dissolved Fe(III) is present in monomeric species. Thus, it us unlikely that Fe(III) sorption occurred because of the onset of Fe(III) polymerization in aqueous solution. In hydrolysis-precipitation studies of Fe(III) solutions, Dousma and De Bruyn (1976) found that the hydrolysis of Fe(III) solutions can be divided into two parts: 1) the hydrolysis of monomers and formation of dimers, and 2) the formation of larger polymers. At an Fe(III) concentration of 30 μM, these authors suggested that polymer formation would begin at about pH 3 in aqueous solutions. In the presence of quartz, the polymer formation may occur as a multilayer coating distributed all over the quartz surface after Fe(III) monomeric species are adsorbed. In contrast, Fe(III) has already been hydrolyzed and precipitated in the physical mixture sample prior to contacting the quartz surface, and the association may be dominated by large islands of attached precipitate, as suggested by the SEM results. Thus, the greater distribution of Fe(III) on the quartz surface may explain the higher U(VI) adsorption measured (Fig. 8-8) by this type of coated quartz (Method III). In a surface complexation model, this difference would need to be accomodated by an increase in surface area or site density for the ferrihydrite.

Less U(VI) adsorption was observed for the coating produced by Fe(III) precipitation at pH 7 with aging (Method V) in comparison to the

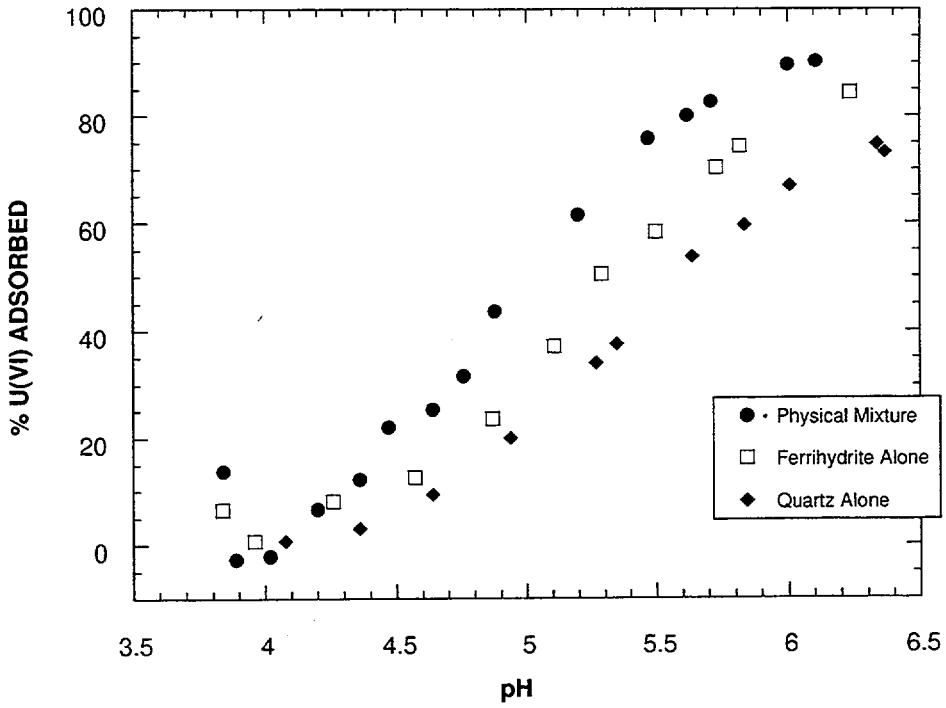

Figure 8.6. U(VI) adsorption as a function of pH in systems with 10 g/L quartz alone, with 30 μM Fe_T (as ferrihydrite) alone, and a physical mixture of the two phases (Method I). U_T = 1 μM.

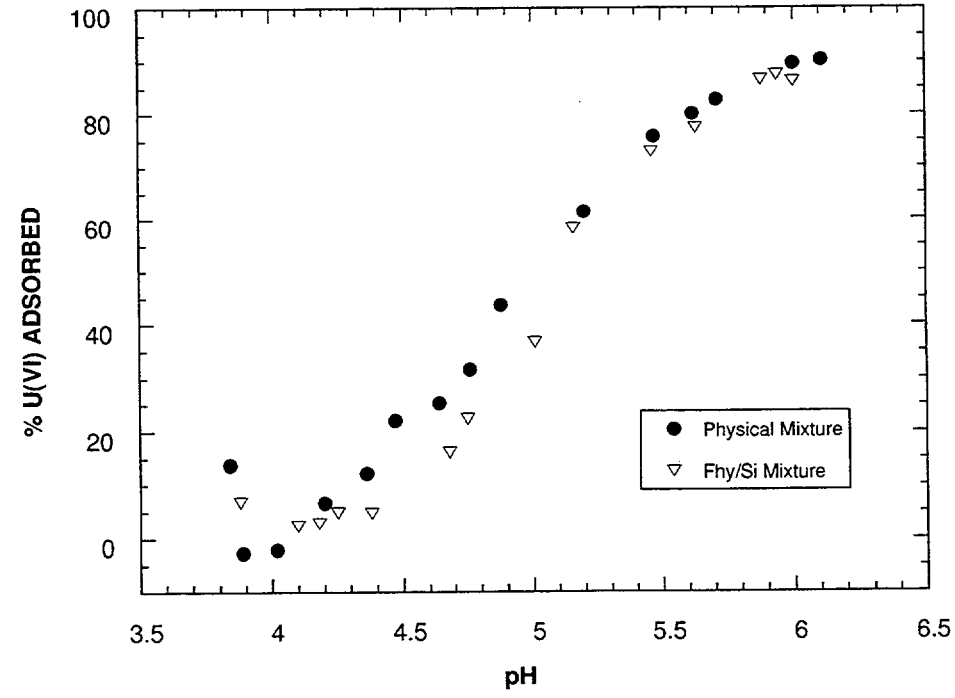

Figure 8.7. U(VI) adsorption as a function of pH in systems with 10 g/L quartz and 30 μM Fe_T (as ferrihydrite) as physical mixtures (Methods I and II). U_T = 1 μM.

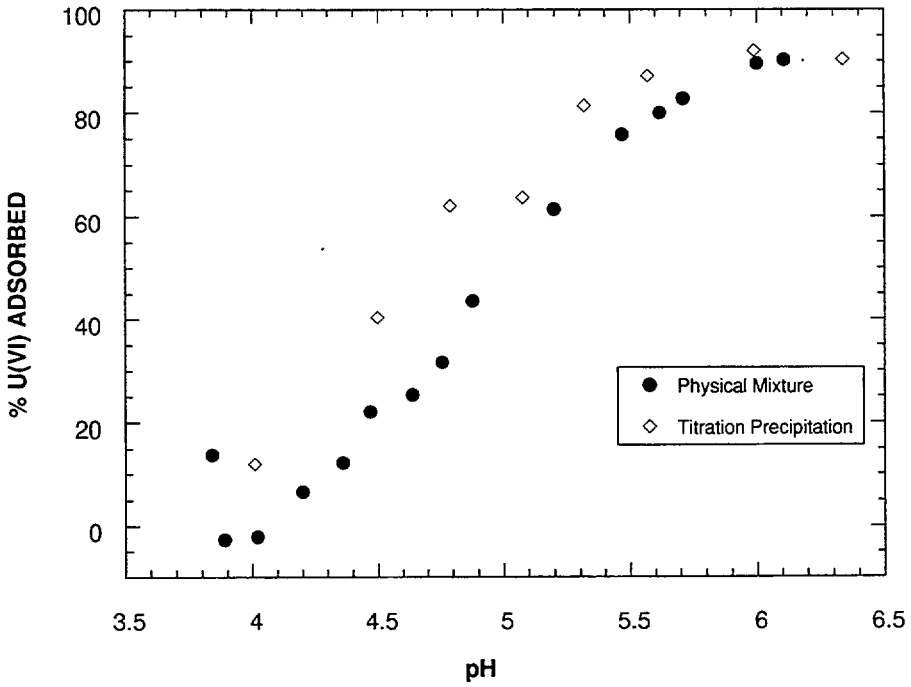

Figure 8.8. U(VI) adsorption as a function of pH in systems with 10 g/L quartz and 30 μM Fe_T (as ferrihydrite) as a physical mixture (Method I) and produced by titration precipitation of Fe(III) (Method III). U_T = 1 μM.

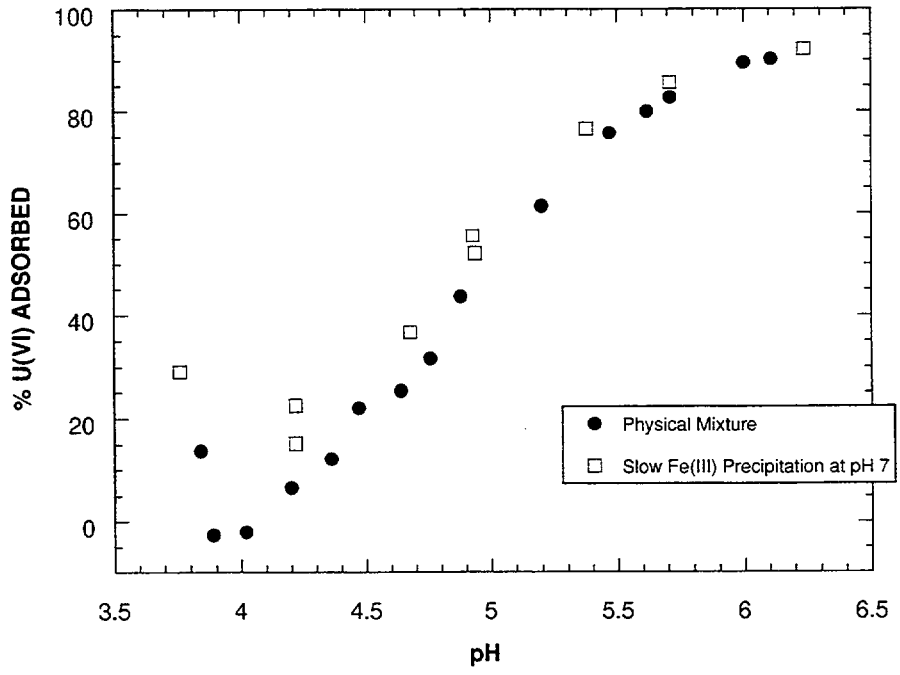

Figure 8.9. U(VI) adsorption as a function of pH in systems with 10 g/L quartz and 30 μM Fe_T (as ferrihydrite) as a physical mixture (Method I) and produced by slow precipitation of Fe(III) at neutral pH (Method IV). U_T = 1 μM.

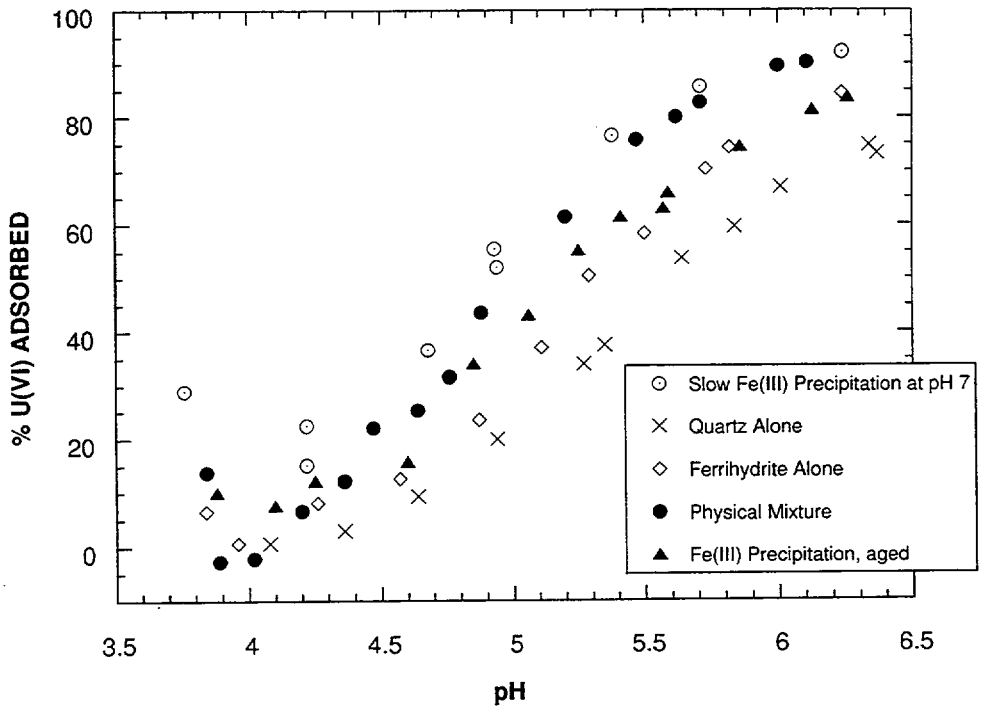

Figure 8.10. U(VI) adsorption as a function of pH in systems with 10 g/L quartz alone, with 30 μM Fe_T (as ferrihydrite) alone, as a physical mixture of the two phases (Method I), produced by slow precipitation of Fe(III) at neutral pH without (Method IV) and with aging (Method V). U_T = 1 μM.

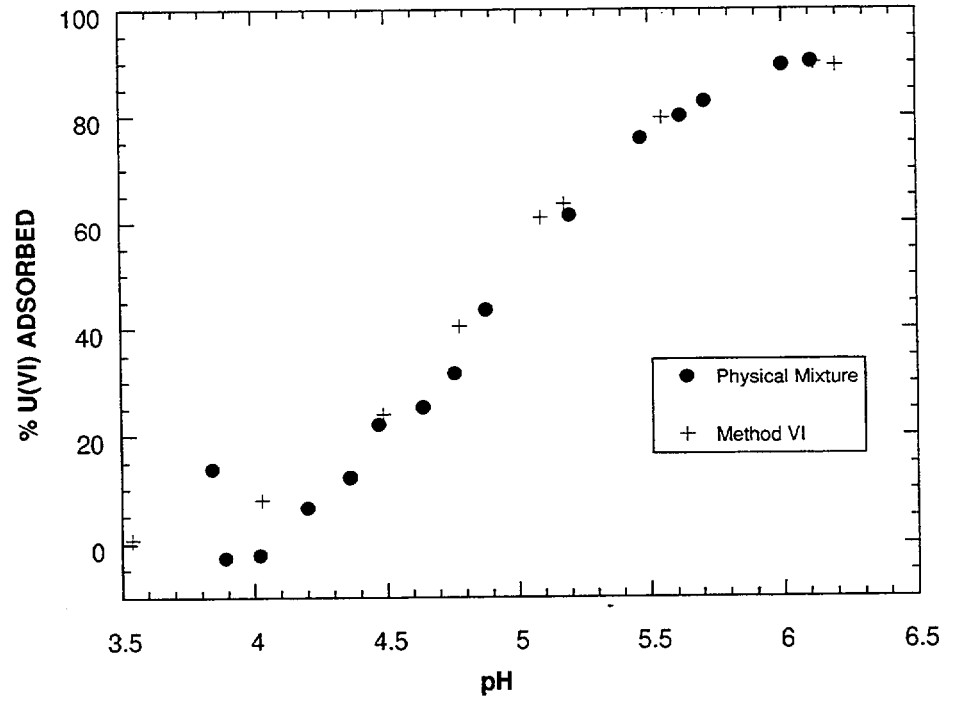

Figure 8.11. U(VI) adsorption as a function of pH in systems with 10 g/L quartz and 30 μM Fe_T (as ferrihydrite) as a physical mixture (Method I) and produced by slow precipitation of Fe(III) at neutral pH in the presence of silicate (Method VI). U_T = 1 μM.

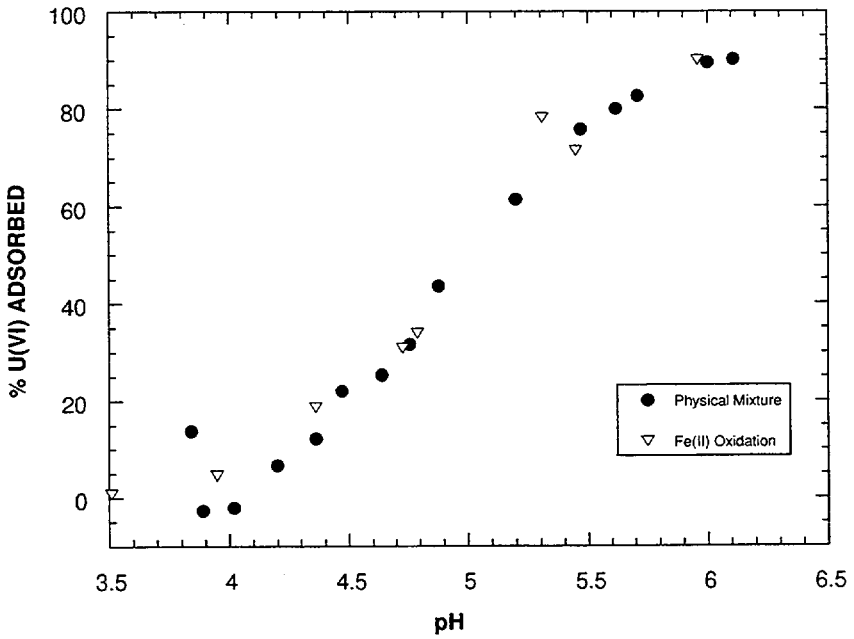

Figure 8.12. U(VI) adsorption as a function of pH in systems with 10 g/L quartz and 30 μM Fe_T (as ferrihydrite) as a physical mixture (Method I) and produced by slow oxidation of Fe(II) at neutral pH (Method VII). U_T = 1 μM.

physical mixture. The TAO extractions and XRD results suggest that Fe-O-Si bonds greatly slowed the transformation of the precipitated Fe(III) to goethite or hematite, as was expected given the time and temperature of the aging (Schwertmann and Thalmann, 1976; Anderson and Benjamin, 1985). The Fe-O-Si bonding may have included adsorption of silicate dissolved from the quartz sample by ferrihydrite or ferrihydrite-quartz surface associations (Waychunas et al., 1997). However, the aging process may have produced a coating precipitate of lower surface area than the pure ferrihydrite, thus decreasing U(VI) adsorption.

Increased U(VI) adsorption was also observed when dissolved silicate was co-precipitated with ferrihydrite (Fig. 8-5). Anderson and Benjamin (1985) demonstrated that binding constants for Cd were orders of magnitude greater for Si-rich, iron oxyhydroxides than for pure phases. Adsorbed silicate can prevent particle growth by poisoning growth sites. This can cause the preservation of smaller particles, and hence, more surface area and sites would be available for adsorption. However, it is puzzling that increases in U(VI) adsorption were not observed for the coatings produced by Method II and VI, which also involved precipitation of ferrihydrite in the presence of large concentrations of dissolved silicate.

8.5 Concluding Remarks

It is recognized that the synthetic coatings produced in this study may not be excellent analogues for natural coatings. However, the results are a step forward in our understanding of the role that iron oxyhydroxides play as a component of natural coatings and their adsorptive behavior. Different methods of synthesis were used to associate Fe(III) with the quartz surface, and most produced U(VI) adsorption edges similar to a physical mixture of ferrihydrite and quartz. Thus, modeling the adsorption of radionuclides by ferrihydrite present in mineral coatings may be similar to modeling the adsorption by pure ferrihydrite alone. Additional molecular scale studies are needed to determine what influence adsorbed silicate had on U(VI) binding to ferrihydrite.

9 URANIUM(VI) ADSORPTION ON SUBSURFACE MATERIAL FROM THE KOONGARRA WEATHERED ZONE

This section presents the results of an experimental study of U(VI) adsorption on weathered rock material from the Koongarra uranium ore deposit. The experimental systems contained $NaNO_3$ as a background electrolyte. This study was carried out in parallel with the experimental work on the U(VI)/ferrihydrite and U(VI)/kaolinite systems, described in Sections 4 and 7 of this report.

The experiments with the natural substrates involved separation of a fine particle fraction, and some sample characterizations are described in this section. These included measuring the total and 'accessible' U content, and carrying out a sequential extraction to study the association of U and other key elements with chemically separated phases. The sequential extraction also provided data on the $^{234}U/^{238}U$ ratios in chemically extracted phases, which are relevant to U(VI) migration in the Koongarra system.

As in the experiments with the reference mineral phases, we studied the effects of pH, U_T, pCO_2, ionic strength, and solid/liquid ratio on U(VI) adsorption by the Koongarra materials. Some additional adsorption investigations were carried out with the natural substrates. These included the effect on U(VI) adsorption of removing Fe-oxides with the CDB reagent, and isotope exchange studies of both the uptake of ^{236}U from the aqueous phase and the desorption of ^{238}U from the solid phase. In addition, we also studied some systems in which Mg^{2+} was added to the aqueous phase. These experiments were undertaken because Mg^{2+} is the dominant cation in Koongarra groundwaters (resulting from weathering of the host-rock chlorite).

The work described in the present report continued an experimental program which was initiated under the ARAP project (Waite et al., 1994a). The samples discussed here are from Koongarra boreholes W1, W2 (2 samples) and W7 (see Table 9-1). The U(VI) adsorption data on one of the samples of the W2 material were previously reported, together with some of the W1 data (Waite *et al.*, 1994a). To distinguish it from the previous W2 sample, the more recent composite sample will be referred to as sample W2c in this section (with the original sample continuing to be referred to as W2). It should be noted that the experimental measurements described in other sections of the present report were carried out with the new W2c substrate. This includes the detailed sample characterizations discussed in Section 10 (in which this material is referred to as the Koongarra 'natural' or 'composite' substrate). Elsewhere in this report, the earlier data on the W1 and W2 samples are discussed and modeled (for example, in Sections 11 and 16).

This section will survey the full adsorption data set for the four samples, including results previously reported by Waite *et al.* (1994a). However, the characterization of the W1 and W2 samples was previously reported in detail, and is only summarized here.

9.1 Sample Preparation and Characterization

9.1.1 PREPARATION OF KOONGARRA SUBSTRATES

Cores were obtained from a number of locations (W1, W2, and W7) in the Koongarra weathered zone using a cable-tool rig, which produces intact samples (rather than the pulverized samples obtained with a percussion rig). Sample depths are indicated in Table 9-1. The W1 core is a highly weathered schist from above the upstream edge of the orebody - a region considered to be the former upward extension of the primary ore. W2 is near the leading edge of the dispersion fan approximately 50 m downgradient from the primary ore zone. W7 is about 100 m further downgradient and the U content of the solid phase is only slightly elevated relative to background (Table 9-1). This sample allowed the study of systems containing much lower U_T concentrations. A detailed

Table 9-1. Summary of Koongarra samples used in Adsorption Experiments (data for separated fine fractions)

Sample name[a]	Depth (m)	Total U content (μg/g)	TAO extract-able U content (μg/g)[b]	BET surface area (m^2/g)	Comment
W1	13.0 – 13.2	356	42.6	24.6	Characterization and adsorption data partially reported in Waite *et al.* [1994a]
W2	14.0 – 14.2	426	225.0	52.3	Characterization and adsorption data reported in Waite *et al.* [1994a]
W2c	12.0 – 12.2	213.5	97.3	20.3	Not previously reported.
W7	13.0 – 13.2	10.4	1.0	51.9	Not previously reported.

[a] Sample name is the same as the borehole except for the second sample from W2 which is denoted W2c.
[b] See text.

description of the geology of the Koongarra deposit and location of boreholes is given by Snelling (1994).

A fine fraction for adsorption experiments (nominally < 10 μm) was obtained from each of these samples using sieving and sedimentation, following the procedure described in Waite *et al.* (1994a). The resulting slurry contained a homogeneous suspension of fine particles which could be reproducibly subsampled by vigorous agitation, followed by removal of an aliquot of known volume. Repeat samplings showed that the sample removal technique was reproducible to within 3%.

9.1.2 PHYSICAL/CHEMICAL PROPERTIES

The fine particles from samples W1, W2 and W7 were examined using SEM/EDS. The resulting data are reviewed in this section. (The characterization of the W2c material, which is similar to the W2 sample, is discussed in Section 10 of this volume). All EDS spectra exhibited peaks of Si and Al. Where only Si and Al were present, the particles were assumed to be kaolinite. Where K was observed in the EDS, it was attributed to the presence of mica. A peak of Mg was assumed to indicate chlorite, or more probably, altered chlorite (this may include vermiculite or smectite).

All samples were predominantly kaolinite, however the W1 sample had greater amounts of hematite as evidenced by its brick-red colour. In contrast, the W2 and W7 samples were yellow/ brown.

The main features of the samples can be generalized as follows:

- The mineralogy of all samples was dominated by kaolinite.

- Mica was a minor component of all samples.
- Altered chlorite was found in W2 and W7, but was almost absent from W1. This may be attributed to the greater depth of weathering (leading to alteration of chlorite) near to the Koongarra fault.
- Iron was found as coatings on clay particles and as abundant fine particles about 1 μm in size.
- The Fe-dominated particles appeared to consist of aggregates of smaller particles.
- The minor components P, Ti and Mn were only observed in particles rich in Fe, indicating a possible association of these elements.

The BET surface areas of the fine fractions of the W2 and W7 materials were significantly higher (per unit mass) than W1 (Table 9-1).

9.1.3 SEQUENTIAL EXTRACTION STUDY

A detailed characterization of the fine fractions used in the adsorption studies was undertaken using a selective extraction technique. This involved treating the sample with a sequence of chemical reagents, with the objective of partitioning the contained elements amongst a series of phases (adsorbed metals, carbonate minerals, iron oxides, clay minerals, residual phases). It is generally agreed that the resulting information is of greater use in environmental studies than merely determining total metal concentrations (Tessier *et al.*, 1979). Although considerable information about the extracted phases has been obtained in some cases, it should be remembered that these phases are operationally defined by the extractants used to remove them.

Tessier et al. (1979) used a five step chemical extraction procedure to separate exchangeable, carbonate, Fe/Mn oxide, organic and residual phases of river sediments. Similar techniques have been applied in studies of radionuclides. A sequential extraction procedure was used in a study of U and Th isotopic distributions in deep soil profiles from the Ranger No.1 ore body (Lowson *et al.*, 1986). In this case the extraction scheme separated the following phases:

1) soluble salts and exchangeable ions,
2) amorphous oxide minerals,
3) crystalline iron minerals,
4) amorphous alumina and silica compounds, and
5) resistate material.

Sequential extraction techniques were successfully applied to samples from the Koongarra deposit (Yanase *et al.*, 1991), and were extensively used within the ARAP project.

The samples used in the adsorption studies were subjected to a five-stage sequential extraction scheme (Table 9-2). This extraction scheme was developed from the one employed by Lowson *et al.* (1986). The selection of chemical reagents and extraction conditions has been previously discussed (Yanase *et al.*, 1991). Extraction solutions obtained from each extraction step were analysed for their radionuclide content using alpha spectrometry. The W2c sample was subjected to duplicate extractions and the data for the two extractions were compared.

9.1.4 ELEMENTAL DISTRIBUTIONS IN CHEMICALLY SEPARATED PHASES

The chemical extraction data (Table 9-3) indicated that Al, Ti and K were predominantly associated with residual phases, such as anatase and clay minerals. The Fe tended to be associated to a large extent with the fractions extracted by the CDB reagent or the 6M HCl extraction. About 1% of the Fe in the samples was in the amorphous phases extracted with the TAO reagent. Magnesium was associated with a readily extractable phase, presumably adsorbed or as carbonate (dissolved by the Morgan's reagent) and also with residual phases, possibly primary or altered chlorite. Mg was not associated with the Fe-minerals. The data in Table 9-3 are particularly useful for estimating the amount of sorbing mineral phases (such as ferrihydrite or crystalline Fe-oxides) in the samples.

Table 9-2. Extraction scheme used for Koongarra samples

Reagent	Main phases dissolved	Extraction conditions
1) Morgan's solution[a]	Carbonate minerals, adsorbed trace elements	40 mL/g sample, shaken for 4 hours
2) Tamms acid oxalate (TAO)[b]	Amorphous minerals of Fe, Al and Si, secondary U minerals	40 mL/g sample, shaken in dark for 4 hours
3) Citrate / dithionite / bicarbonate (CDB) reagent[c]	Crystalline iron oxides, hydroxides and oxyhydroxides	60 mL/g sample, stirred for 30 minutes at 85°C (repeated)
4) 6 M HCl	Clay minerals, uranium oxides	Stirred for 2 hours at 85°C
5) Digestion and fusion	Remaining resistant minerals (quartz, muscovite)	$HF/HClO_4$ digestion followed by Na_2CO_3/borax fusion

[a]Morgan's solution: 1M NaOAc adjusted to pH 5.0 with acetic acid
[b]TAO: 10.9 g/L oxalic acid + 16.1 g/L ammonium oxalate.
[c]CDB: 0.3M trisodium citrate, 0.2M $NaHCO_3$, 1 g/g sample sodium dithionite

We have extensively studied the reproducibility of the technique. Table 9-3 shows results obtained from repeated extractions of the W2c sample. Typically the extraction data for a particular sample were highly consistent. However, in common with many other types of geological analyses, sampling variability can lead to significant differences between samples, even those in close proximity to one another.

9.1.5 URANIUM-SERIES DATA

For these analyses, a known amount of ^{232}U was added to the solution obtained from the chemical extraction. Following standard radiochemical separation procedures (Waite *et al.*, 1994a), the uranium isotopes were counted in an ORTEC ALPHA-KING α-spectrometer, and the amounts of ^{234}U and ^{238}U were determined from their count rates relative to ^{232}U.

Data on the distribution of uranium amongst the chemically separated phases in the samples from the Koongarra weathered zone are shown in Table 9-4. Relatively large amounts of the uranium were removed by Morgan's reagent. This reagent appears to remove adsorbed U(VI), since there was only minor elemental release from other mineral phases (Table 9-3). When carried out after an extraction with Morgan's reagent, the TAO extraction only removed only a small increment of U(VI). This indicates that U(VI) is more likely to be bound to the surface of amorphous Fe-oxides, rather than incorporated within them.

The $^{234}U/^{238}U$ ratio for each phase is also indicated in Table 9-4. For all four samples, the readily leachable U(VI) in the Morgan's and TAO phases had a much lower $^{234}U/^{238}U$ isotope ratio than the chemically resistant phases. In samples from the Koongarra weathered zone the $^{234}U/^{238}U$ ratio in labile phases was generally significantly below 1.0. This was very similar to the $^{234}U/^{238}U$ isotope ratio in groundwater samples from the weathered zone (Payne *et al.*,

1994). Thus, it may be inferred that U(VI) present in the TAO and Morgan's fraction is accessible to the groundwater over relatively short geological timescales. These fractions are therefore of most interest in interpreting the results of adsorption experiments, which necessarily occur over limited timescales.

The $^{234}U/^{238}U$ ratios in the Koongarra samples tend to increase from the more readily extracted phases (Morgan's, TAO) through the more resistant phases (CDB, 6M HCl, and resistate fractions). This suggests that U in these latter phases does not rapidly exchange with the groundwater, and may therefore be regarded as immobile over short timescales.

The isotopic fractionation between ^{234}U and ^{238}U has been attributed to alpha-recoil emplacement of ^{234}U in resistate phases. These phases have a low U content and make up the majority of the sample mass. When the decay of a ^{238}U nucleus occurs in an adjacent U-rich mineral phase, the daughter ^{234}U may lodge in the U-poor resistate phase. Indeed, this is likely since the resistate phase comprises such a large proportion of the sample. This process causes an input of ^{234}U to the resistate, resulting in an excess of ^{234}U developing in this phase (see Edis *et al.*, 1994).

9.2 Procedure for adsorption experiments

The experimental procedures were similar to those used for U(VI) adsorption experiments on ferrihydrite (Section 4). Batch experiments were carried out in polypropylene centrifuge tubes and were equilibrated with air. The stock slurry of fine particles was vigorously agitated to fully suspend the solid, and aliquots containing known amounts of particles were transferred to 25 mL polypropylene centrifuge tubes, and suspended in $NaNO_3$ (usually 0.1M). Each tube had a 2 mm hole in the lid to permit air equilibration without loss of sample during agitation. For studies at pH > 7.0, sufficient $NaHCO_3$ was added to ensure pH stability and fix the carbonate content of the system. The U(VI) was added after 24 hour pre-equilibration, during which the system was allowed to come to equilibrium under the appropriate chemical conditions (pH, ionic strength, complexing ligands, etc.).

U(VI) was added to the systems either as ^{236}U or ^{238}U, depending on the required experimental U(VI) concentration range. The amount of ^{236}U spike added was sufficient to achieve a U(VI) concentration of either 10^{-8} or 10^{-7} M. Except for experiments with the W7 sample, the amount of ^{236}U added to the aqueous phase was much lower than the concentration of ^{238}U derived from the accessible U(VI) content of the solid phase (indicated in Tables 9-1 and 9-5). Therefore, the latter contribution must be estimated in order to determine the total amount of U_T in the experimental systems. Experiments at higher concentrations were carried out after addition of ^{238}U. In these experiments, the added U(VI) (typically 10^{-4}M) provided the major part of U_T in the system.

The contact time for U(VI) was 48 h, with the pH being checked and adjusted if necessary after 24 hr. The experimental tubes were gently shaken in a water-bath at 25°C. Immediately prior to sampling the pH was again determined and the aqueous phase was then separated by high speed centrifugation (RCF > 6500*g*) for 30 min. U(VI) concentrations in the supernatant were determined using the Kinetic Phosphorescence Analyser (model KPA-10) or by alpha spectrometry (see Waite *et al.* (1994a)). The latter technique provides isotopic measurements and was used for experiments where ^{236}U was added.

While most studies were undertaken under atmospheric conditions, some investigations were performed in a glove box at an elevated partial pressure of carbon dioxide (pCO_2). A special gas mixture of 2% CO_2 and 98% N_2 was obtained for these experiments. The gas composition used in the glove-box was a 50:50 mixture of this gas with ordinary air. The gas composition in the glove-box was thus approximately 1% CO_2 : 10% O_2 : 89% N_2. The presence of oxygen derived from the air ensured the stability of the solid phases against reductive dissolution, and provided a convenient means to

Table 9-3. Elemental distribution in Koongarra samples as determined by a sequential extraction

W1 (13-13.2 m) **Elemental distribution (mg extracted/g of solid)**

Extractant	Fe	Al	Mn	Mg	Ca	Ti	K
Morgans	0.12	0.18	0.00	0.52	0.08	0.00	0.22
TAO	0.88	0.58	0.00	0.06	0.01	0.00	0.25
CDB	35.10	1.08	0.00	0.03	0.07	0.05	0.60
HCl	35.30	6.37	0.00	0.28	0.01	0.16	1.42
Fusion	9.14	166.0	0.03	4.30	0.01	2.76	9.82
Sum(mg/g)	80.6	173.8	0.04	5.2	0.2	3.0	12.3

W2 (14-14.2 m) **Elemental distribution (mg extracted/g of solid)**

Extractant	Fe	Al	Mn	Mg	Ca	Ti	K
Morgans	0.52	0.61	0.01	3.93	0.20	0.00	0.37
TAO	1.17	1.21	0.15	0.25	0.01	0.01	0.04
CDB	6.77	0.89	0.03	0.13	0.11	0.00	0.54
HCl	79.20	35.00	0.13	9.67	0.01	0.05	0.28
Fusion	20.80	90.30	0.04	3.48	0.03	0.84	7.84
Sum(mg/g)	108.4	128.1	0.3	17.5	0.4	0.9	9.1

W2c (12-12.2 m) **Elemental distribution (mg extracted/g of solid)**
Data for duplicate extractions (1 and 2) are shown.

Extractant		Fe	Al	Mn	Mg	Ca	Ti	K
Morgans	1	0.00	0.00	0.00	4.72	0.12	0.0	0.0
	2	0.00	0.00	0.00	4.93	0.12	0.0	0.0
TAO	1	0.26	0.41	0.11	0.42	0.48	0.0	0.0
	2	0.27	0.42	0.12	0.46	0.50	0.0	0.0
CDB	1	0.33	0.49	0.00	0.08	0.37	0.0	0.27
	2	0.41	0.46	0.00	0.07	0.31	0.0	0.34
HCl	1	75.50	64.5	0.08	12.60	0.03	0.20	2.00
	2	78.50	53.0	0.08	12.45	0.06	0.16	1.25
Fusion	1	4.83	32.8	0.01	1.51	0.23	4.46	2.76
	2	8.40	54.0	0.02	2.66	0.20	5.3	3.88
Sum (mg/g)	1	80.9	98.2	0.20	19.3	1.23	4.66	5.03
	2	87.6	107.5	0.22	20.6	1.19	5.46	5.47

W7 (13-13.2 m) **Elemental distribution (mg extracted/g of solid)**

Extractant	Fe	Al	Mn	Mg	Ca	Ti	K
TAO[a]	0.41	0.41	0.18	2.04	<0.04	<0.06	0.07
CDB	6.83	1.01	0.02	0.46	<0.10	<0.01	0.27
HCl	38.20	23.60	0.10	3.51	<0.01	0.18	0.98
Fusion	7.68	60.9	0.04	1.27	<0.01	1.26	4.95
Sum(mg/g)	53.1	85.9	0.3	7.3	<0.15	1.50	6.30

[a]There was no extraction with Morgan's solution for the W7 sample.

Table 9-4. Uranium distribution and $^{234}U/^{238}U$ in Koongarra samples as determined by a sequential extraction

U content of extracted phases (μg/g)

	W1	W2	W2c	W7
Morgan's	30 ± 1	182 ± 8	69.3 ± 2.4 71.1 ± 1.5	-
TAO	12.6 ± .4	43 ± 2	26.0 ± 0.9 28.2 ± 0.9	1.00 ± 0.06
CDB	131 ± 4	65 ± 3	15.1 ± 0.7 16.1 ± 1.0	4.6 ± 0.6
HCl	177 ± 8	130 ± 3	98.1 ± 2.6 97.1 ± 2.6	3.9 ± 0.4
Fusion	5.2 ± .1	6.4 ± 0.2	5.0 ± 0.3 6.3 ± 0.4	0.9 ± 0.1
Total	356 ± 14	426 ± 16	213.5 ± 3.8 218.8 ± 3.4	10.4 ± 0.8

$^{234}U/^{238}U$ in extracted phases

	W1	W2	W2c	W7
Morgan's	0.82 ± 0.03	0.61 ± 0.03	0.64 ± 0.03 0.66 ± 0.02	-
TAO	0.85 ± 0.03	0.64 ± 0.05	0.66 ± 0.03 0.63 ± 0.03	0.97 ± 0.06
CDB	0.93 ± 0.03	0.9 ± 0.1	0.67 ± 0.04 0.75 ± 0.06	0.80 ± 0.10
HCl	1.02 ± 0.03	1.20 ± 0.04	1.16 ± 0.04 1.17 ± 0.03	1.00 ± 0.10
Fusion	1.71 ± 0.06	1.83 ± 0.07	1.85 ± 0.11 1.96 ± 0.14	1.60 ± 0.15

monitor the mixing ratio of the air and special gas. This was done by measuring the oxygen concentration in the glovebox and maintaining the measured value at close to 10%, i.e., half the value in normal air.

9.2.1 ALPHA SPECTROMETRY

As indicated above, particular use was made of α-spectrometry in studies with natural substrates, as it was possible to monitor both the uptake of ^{236}U and the desorption of a portion of the natural ^{238}U from the samples. The various U isotopes were simultaneously measured using α-spectrometry.

The uranium spectrum of the solution phase on completion of a typical adsorption experiment is shown in Figure 9-1. The ^{238}U peak results from the leaching of natural uranium into the aqueous phase, whereas the ^{236}U peak indicates the amount of the ^{236}U spike remaining in solution after adsorption. The amounts of ^{238}U and ^{236}U in the solution phase were calculated from their count rate relative to the ^{232}U peak after correction for the minor background count rates.

Table 9-5. Representative calculations of total U(VI) concentrations in experimental systems

Solid	TAO extractable U	Solid/ Liquid Ratio	Natural U(VI) in experiments*		Added U(VI)	Total U(VI) (U_T)
	(μg/g)	(g/L)	(μg/L)	(μM)	(μM)	(μM)
W1	42.6	20	852	3.6	0.1	3.7
W1	42.6	4	170.4	0.72	0.01	0.73
W2	225	4	900	3.8	0.1	3.9
W2	225	4	900	3.8	100 (as ^{238}U)	103.8
W2c	97.3	4	389	1.6	0.01	1.6
W7	1.0	4	4	0.017	0.01	0.03
W7	1.0	4	4	0.017	100 (as ^{238}U)	100.02

*Assumed to equal the U extracted by the TAO reagent.

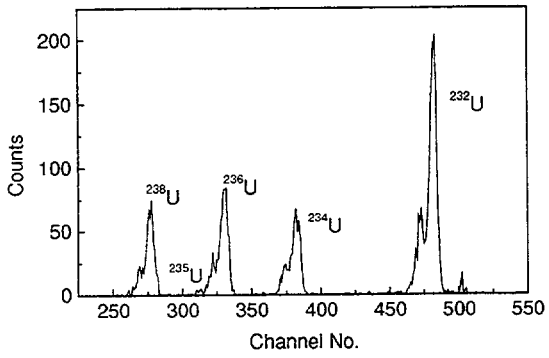

Figure 9-1. Uranium α-spectrum obtained after adsorption/desorption experiment.

9.2.2 TOTAL AND ADDED U(VI) IN EXPERIMENTAL SYSTEMS

It will be shown below that some of the natural U in the solid phase was 'inaccessible' or unavailable for leaching. The amount of the natural U(VI) in the samples which participates in adsorption reactions (accessible U) may be estimated by the TAO extraction (see Table 9-1). These amounts may then be combined with the added U(VI) (either ^{236}U or ^{238}U) to give the total U(VI) (or U_T concentration) in the experimental systems (Table 9-5).

The purpose of Table 9-5 is to demonstrate the method of estimating U_T in typical adsorption experiments with the natural substrate, and to emphasize that the different sources of U(VI) must be considered in order to understand and model the system. The exact amount of U(VI) participating in adsorption interactions and the method used to estimate 'accessible' U(VI) (in this case using the TAO extraction) are discussed further below. However, it will be demonstrated that there is a fair correspondence between the accessible U(VI) determined by the TAO extraction and the estimate obtained by isotope exchange.

9.3 Results of U(VI) adsorption experiments

9.3.1 EFFECT OF pH

The main features of U(VI) adsorption on the Koongarra natural materials (W1, W2, W2c and W7) are shown in Figure 9-2. These data are for experiments in which a trace of ^{236}U was added to the system as a spike, with a solid/liquid ratio of 4 g/L.

In qualitative terms, the data are similar to those of ferrihydrite. In particular, adsorption is greatest in the near-neutral pH range, with a 'low pH edge' of increasing uptake from pH of about 2.5 to 6.5, and a steeper 'high pH edge' (desorption edge) between pH 8 and 9. This is due to the effect of complexation between UO_2^{2+} and carbonate in the aqueous phase at high pH values (see Sections 2, 4, and 5).

The adsorption data for the W7 sample are significantly different from the other samples. This could reflect differences in mineralogy or surface area. However, the mineralogy of W7 is similar to the W2 sample, and its surface area is not much higher than the other samples (Table 9-1). The stronger adsorption on the W7 sample is more likely a result of the much lower U_T in the experiments with the W7 sample (see Table 9-5). This is because the U_T in the experiments is dominated by the U(VI) naturally present in the samples (rather than the U(VI) spike), and W7 has a low intrinsic U(VI) content. The stronger adsorption in experiments with lower U_T is attributed to the presence of a small number of strong binding sites on the surfaces of the natural substrates. These would dominate adsorption phenomena when U_T is small. Further experiments in which U_T was manipulated by adding larger increments of U(VI) (as ^{238}U) are discussed below.

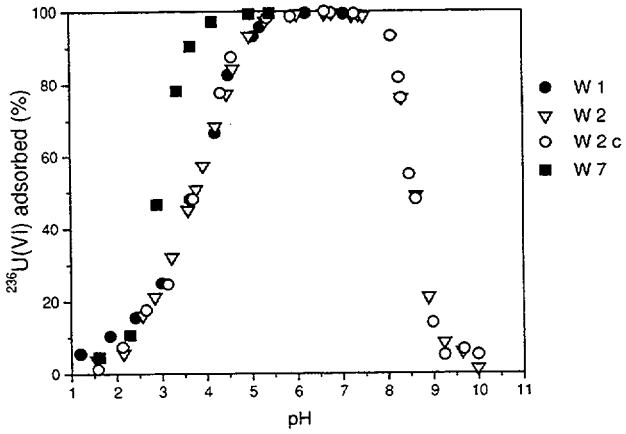

Figure 9-2. Uptake of $^{236}U(VI)$ spike as a function of pH in experiments with Koongarra sediment. Solid/liquid ratio of 4 g/L. U_T in each experiment was dominated by the natural U(VI) in the samples, and is much lower in the experiment with the W7 sample (see Table 9-5). Background electrolyte is 0.1 M $NaNO_3$ in equilibrium with air.

9.3.2 EFFECT OF SOLID/LIQUID RATIO

Results of experiments with different solid/liquid ratios are shown in Figure 9-3. This figure shows that adsorption was greater with a higher solid/liquid ratio, as is typically found in experimental systems.

In considering the data in Figure 9-3, the different U_T in the two experimental systems must be taken into account. In the experiments with the higher solid/liquid ratio, U_T is also greater, because most of the U(VI) in the system is derived from the natural U(VI) content of the solid phase. Thus, the experimental data obtained with these natural substrates may be less strongly dependent on solid/liquid ratio than is typically found with the reference mineral phases. In the latter case, U_T remains the same when the solid/liquid ratio is increased.

To summarize, there is usually much stronger adsorption when the solid/liquid ratio is increased in experiments with a reference mineral phase (e.g., kaolinite or ferrihydrite). This is because more unoccupied adsorption sites, including those with high affinity for U(VI) adsorption are added. However, a similar increase in the solid/liquid ratio with the U(VI)-containing natural substrates may have a lesser effect, because the adsorption sites on the added solid are already occupied, and U_T is increased when the solid/liquid ratio is increased.

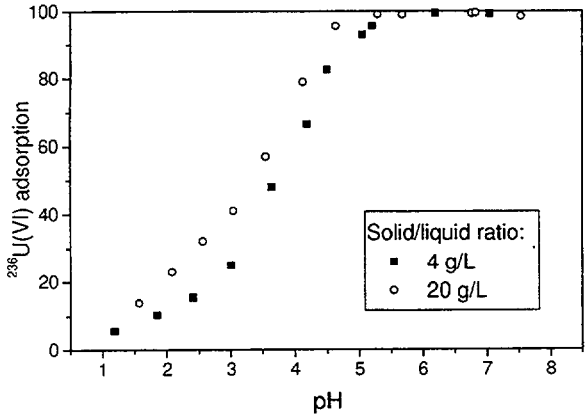

Figure 9-3. Uptake of ^{236}U(VI) on the W1 sample at two solid/liquid ratios. Note that as most of the U(VI) in the system comes from the solid, U_T differs between the 2 data sets (see Table 9-5).

9.3.3 EFFECT OF U_T CONCENTRATION

As with ferrihydrite, there was a decreasing percentage of U(VI) adsorbed with increased U_T in the system (Fig. 9-4). This suggests that there are at least two types of binding sites with different affinities for U(VI) adsorption, which is similar to the trends obtained with the reference mineral phases.

It is instructive to compare the W2 data-set, obtained with 100 μM of added U(VI) (solid/liquid ratio 4 g/L) with the data for the W7 sample with the same amount of U(VI) added. The adsorption curves are very similar, with the pH_{50} (the pH at which 50% of the added U(VI) is adsorbed) being close to 5.3 (Fig. 9-4). This contrasts with the data obtained when a trace amount of U(VI) was added as a spike (Fig. 9-2) where the W2 and W7 results were quite dissimilar. The reason for this is that when 100 μM of ^{238}U was added, the natural U(VI) content of the samples was greatly exceeded in both cases and the U_T was almost the same (as shown in Table 9-5). In contrast, when a spike amount of ^{236}U was added, U_T was 3.7 μM for the W2 and 0.03 μM for the W7 sample). This confirms the conclusion reached above, that the most reasonable explanation for the different results for the W2 and W7 samples in the experiments with the added ^{236}U spike (Fig. 9-2)

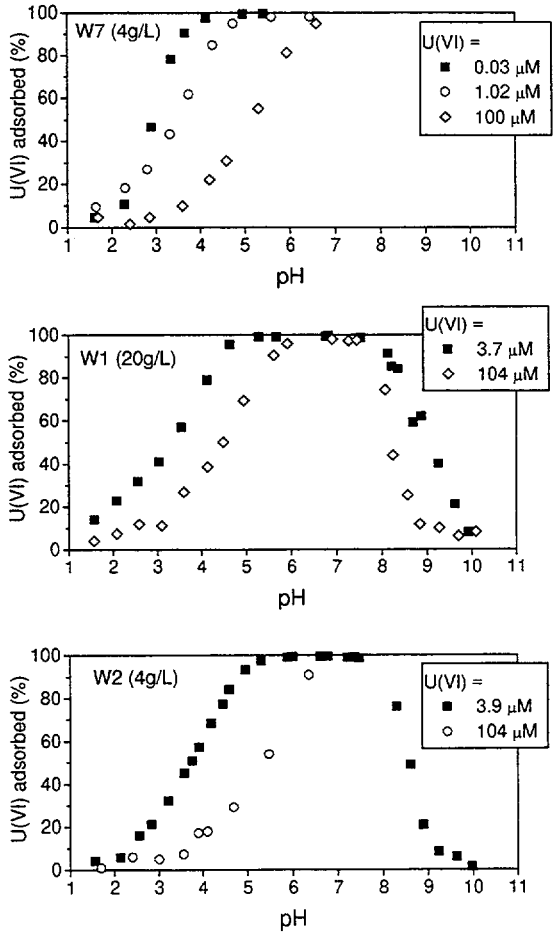

Figure 9-4. Effect of increased U_T on U(VI) adsorption on the Koongarra sediments. The data indicated with the closed symbols were obtained after addition of a ^{236}U spike. Data denoted with a diamond or circle were obtained by addition of ^{238}U. U(VI) in these experiments includes the TAO-extractable content of the sediments (Table 9-5).

was the lower U(VI) content of the W7 sample.

The data for the W7 sample were obtained across a wide range of U_T, because of its lower natural U(VI) content. These results indicate a substantial shift in the position of the low pH edge between U_T of 3×10^{-8} and 10^{-5} M. The stronger adsorption of U(VI) at lower U_T was also encountered in the experiments with ferrihydrite and clays. It is of significance that it also occurs in the experiments with the natural samples, and by implication, the Koongarra

system. This would imply that a linear K_d model is inapplicable in the natural environment.

9.3.4 EFFECT OF INCREASED pCO_2

The pCO_2 in Koongarra groundwaters is higher than that found in ordinary air. In experiments carried out with 1% CO_2, U(VI) adsorption was greatly reduced at pH > 6.0, relative to experiments carried out in air (Fig. 9-5). This is due to the greater dominance of aqueous U(VI)-carbonate complexes (Waite *et al.*, 1994b). The low pH adsorption edge was not significantly affected by the higher pCO_2.

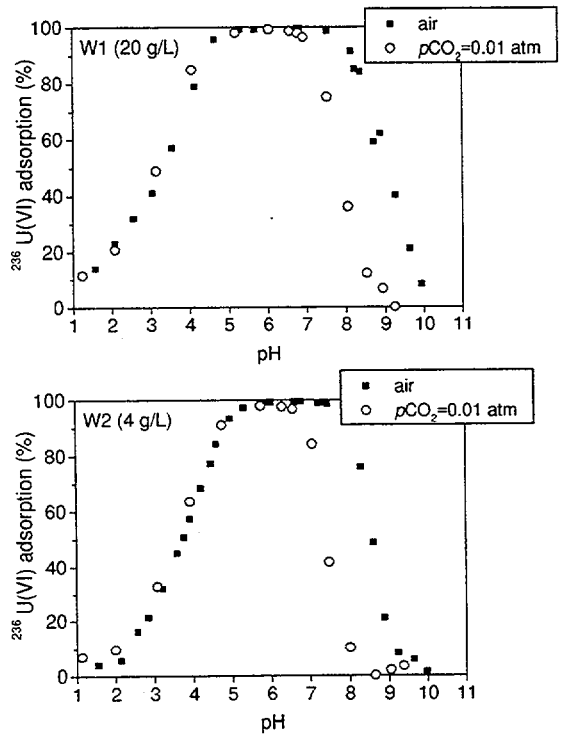

Figure 9-5. Effect of elevated pCO_2 on U(VI) adsorption by the Koongarra sediments.

9.3.5 EFFECT OF IONIC STRENGTH

A limited amount of data for the ionic strength dependence of U(VI) adsorption on natural substrates was obtained. The data indicate that the high pH edge occurs at lower pH values (i.e., adsorption is reduced) with an increase in ionic strength (Fig. 9-6). This would be consistent with the behavior of ferrihydrite. The effect of ionic strength at low to neutral pH values is less clear. However, it appears that there are no systematic trends in the data obtained in the region of the low pH edge.

Although an ionic strength dependence can be attributed to outer sphere surface complexes, the diffuse double layer model, which was used to model the ferrihydrite U(VI) adsorption data (Waite *et al.*, 1994b), does not accommodate outer sphere surface complex formation. However, even with only inner-sphere complexes included, the model correctly predicts a decrease in U(VI) adsorption on ferrihydrite with increasing ionic strength. This is because the activity of the highly charged aqueous U(VI)-carbonate complexes, which prevail in the high pH range, is significantly affected by ionic strength (see Section 4). This influences the distribution of aqueous U(VI) species and affects U(VI) adsorption.

9.3.6 EFFECT OF PRESENCE OF Mg^{2+}

The effect of elevated concentrations of Mg^{2+} on the adsorption of U(VI) by the W2c natural substrate was investigated. This is of interest because Mg^{2+} is present in Koongarra groundwaters as a result of weathering reactions involving chlorite (Payne *et al.*, 1994). Typical Mg^{2+} concentrations are about 1 mM. The presence of Mg^{2+} may possibly be expected to reduce U(VI) adsorption as a result of competition for surface sites, as has been reported in the case of montmorillonite (Borovec, 1981). The amount of Mg^{2+} added in these experiments was 243 mg/L (10 mM), which exceeds the amount of Mg^{2+} in Koongarra groundwaters. In addition, it is about an order of magnitude greater than the amount of readily leachable Mg^{2+} in these experiments (Table 9-3).

The addition of this relatively large amount of Mg^{2+} had no apparent effect on U(VI) adsorption (Fig. 9-7). In addition, there was no significant uptake of added Mg^{2+} from the aqueous phase. It would appear that Mg^{2+} plays very little role in affecting U(VI) adsorption in the Koongarra system.

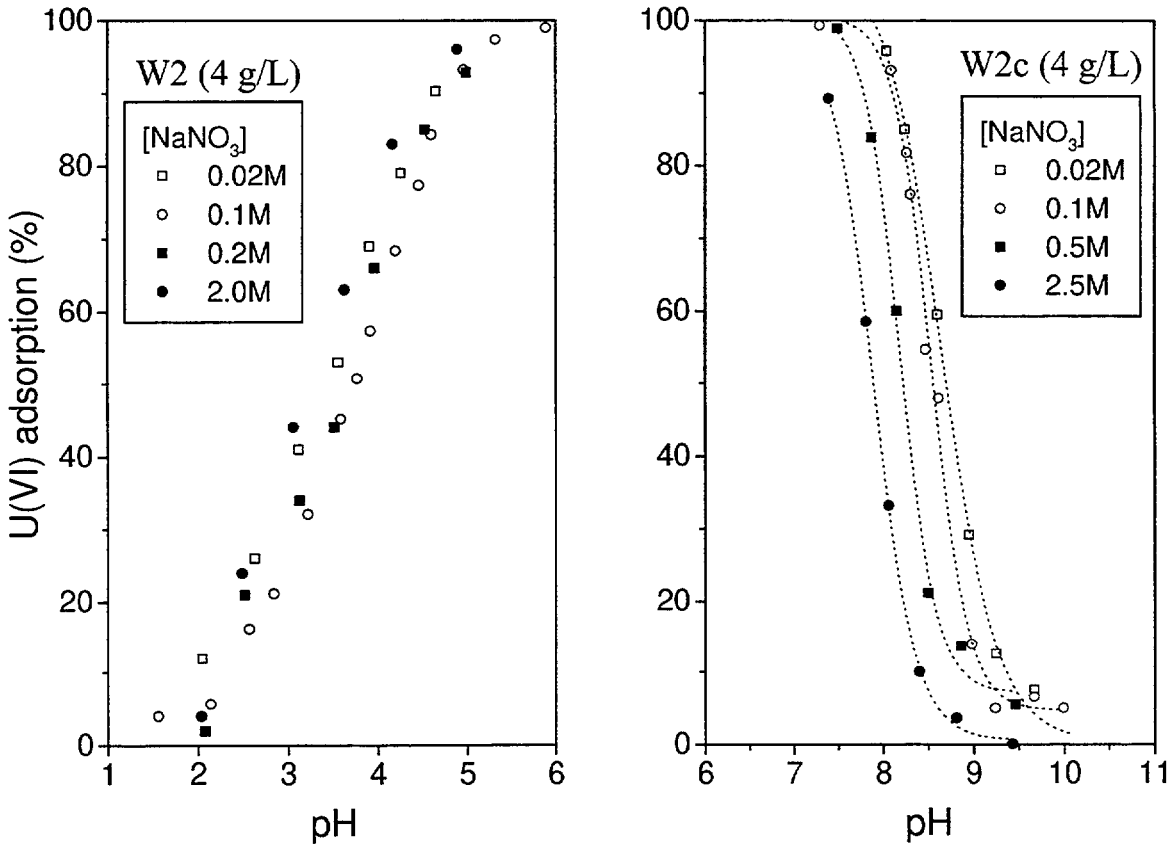

Figure 9-6. Effect of ionic strength on U(VI) adsorption by Koongarra sediments. At high pH values U(VI) adsorption is significantly reduced by higher ionic strength.

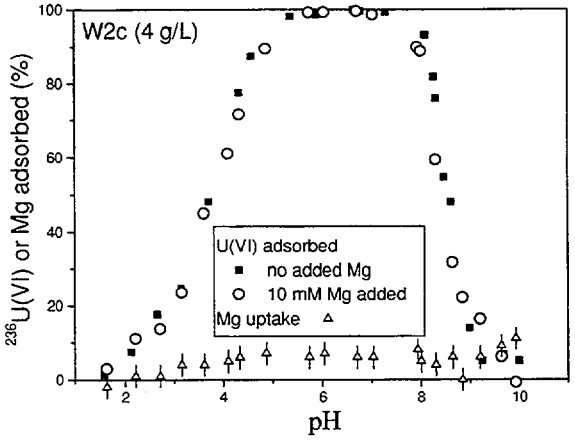

Figure 9-7. Results of U(VI) adsorption experiments with Koongarra sediments in systems with and without added Mg^{2+} (243 mg/L). Adsorption of Mg^{2+} is also shown.

9.3.7 EFFECT OF CDB EXTRACTION

Additional substrates for adsorption experiments were prepared by treating the W1 and W2 fine-particle slurries with the CDB reagent to remove iron oxides (see table 9-2). The samples were then repeatedly washed with deionized water until the conductivity of the aqueous phase was unchanged by contact with the solid. The solid residue was tested for the presence of organic material using the Walkley-Black method (Allison, 1965). This analysis was performed because of the potential impact of any trace of reagent on subsequent adsorption experiments. The amount of organic matter was below the detection limit, from which it was concluded that the CDB reagent had been eliminated from the samples.

The samples were analysed using X-ray diffraction (XRD). The main peaks observed in the XRD spectrum of the untreated W1 sample

corresponded to muscovite, kaolinite and quartz, with a small peak of goethite. The goethite reflection was absent after the CDB extraction, whilst all other peaks were unaffected. Chlorite, kaolinite, goethite and mica were present in the XRD pattern of the untreated W2 sample, and all of these peaks except for the goethite were present in the CDB-treated sample. These results confirmed that crystalline iron minerals were removed by the CDB reagent. Adsorption experiments were then carried out using a ^{236}U spike (10^{-7}M) with solid/liquid ratios of 4 g/L on CDB-treated W1 and W2 samples, and the data were compared with the results obtained with untreated samples (Fig. 9-8).

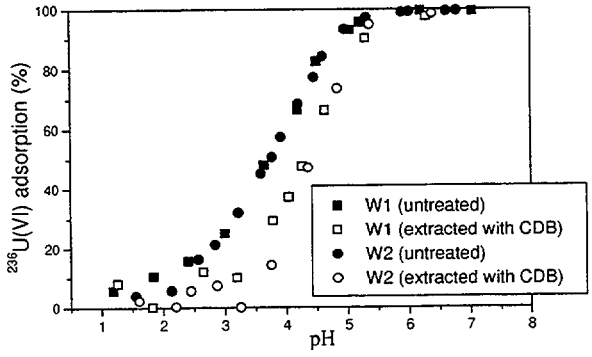

Figure 9-8. Effect of the CDB extraction on U(VI) adsorption by the Koongarra W1 and W2 sediment samples (solid/liquid ratio of 4 g/L).

The effect of the CDB extraction was to move the adsorption edges to higher pH values (i.e., reduce U(VI) adsorption) by approximately 0.5 pH units. Similar experiments with kaolinite samples of low Fe content showed that the CDB extraction had no effect on U(VI) adsorption in that case (Waite *et al,* 1994a). The lower adsorption on the CDB-treated Koongarra samples was attributed to the removal of Fe oxides, which generally make up a substantial proportion of the total surface area of a soil (Borgaard, 1982). Iron oxide removal does not always result in decreased adsorption of heavy metals, and may increase uptake by unblocking surface sites (Elliott *et al.,* 1986). However, the effect of the CDB treatment on U(VI) uptake by the W1 and W2 samples suggests that, in these samples, Fe oxides are important in U(VI) adsorption.

The surface areas of the samples used in these experiments were determined using the BET technique. The W1 sample had a surface area of 19.0 m^2/g, with this value reduced to 13.3 m^2/g by the CDB treatment. The corresponding figures for the W2 sample were 53.3 m^2/g (untreated) and 29.5m^2/g (treated). Therefore, the lower adsorption on the samples after the CDB treatment corresponded with a decrease in surface area of 30-40%. However, factors other than surface area must also play a role, because the curves for the untreated W1 and W2 samples were similar although the surface area of the W2 sample was much greater. The same is true of the CDB-treated samples.

It should be noted that an additional effect of the CDB treatment was to reduce U_T in the experimental systems (as well as removing crystalline iron minerals). This is because the U content of the samples was partially removed by the CDB reagent. In particular, U in accessible phases was removed. The remaining U (in residual phases) would play little or no role in adsorption interactions. The experiments with the CDB-extracted samples therefore involved a lower U_T than the corresponding experiments with the untreated samples. On the basis of the α-spectrometry data for the aqueous phases, this U_T was estimated as being below 0.2 μM, compared to about 3.7 – 3.9 μM in the experiments with the untreated samples (Table 9-5). Thus, the reduced adsorption found with the CDB treated samples occurred *despite* the fact that the U_T in the experimental systems was lower. As discussed above, the effect of decreasing U_T would normally be to increase the proportion of ^{236}U spike adsorbed, if all other parameters remained the same. Thus, in this case, the effect of Fe oxides on U(VI) adsorption appears to be substantial.

9.3.8 ISOTOPE EXCHANGE AND LEACHING RESULTS

As has been previously reported (Payne and Waite, 1991; Waite *et al.*, 1994a), the measurement of both ^{238}U and ^{236}U in the

aqueous phase by α-spectrometry enables the amount of natural ^{238}U in the samples which participates in adsorption/desorption reactions to be determined. This provides another means of estimating accessible ^{238}U, which can be compared with the data obtained from a chemical extraction (e.g. with the TAO reagent).

The basis of the isotope exchange method is to construct a plot of the amount of ^{238}U leached from the solid into the aqueous phase as a function of the percentage of ^{236}U in solution at equilibrium. In Figure 9-9, the results of adsorption experiments in air-equilibrated systems are shown in this form. The corresponding plots derived from the experiments in the elevated CO_2 experiments are shown in Figure 9-10.

The linear nature of these graphs suggests that isotope exchange occurs between ^{236}U in solution and accessible ^{238}U on the surface of the solid phase (Payne and Waite, 1991). The position of each data point depends on the experimental pH, which determines the amount of both ^{236}U and ^{238}U in the aqueous phase. The intercept on the y-axis (on the right hand-side) indicates how much of the ^{238}U participates in the adsorption reactions. This amount corresponds to the ^{238}U which would be in the aqueous phase when 100% of the ^{236}U is in solution (this occurs at very high and very low pH where little U(VI) is sorbed). The resulting estimates of the accessible ^{238}U in the samples may then be compared with estimates from the chemical extraction method (Table 9-6).

The correspondence between the data obtained by isotope exchange and by TAO extraction (Table 9-6) provides support for using both methods to estimate accessible U(VI) in the Koongarra samples. As noted above, this quantity is critical in modeling adsorption, where the U_T in experimental systems is required. It should be pointed out that a linear relationship between ^{236}U and ^{238}U in solution can only be expected when the solution conditions are mild; i.e. the amount of accessible uranium is constant. Under extreme leaching conditions, the amount of ^{238}U available to the solution phase would be increased by the

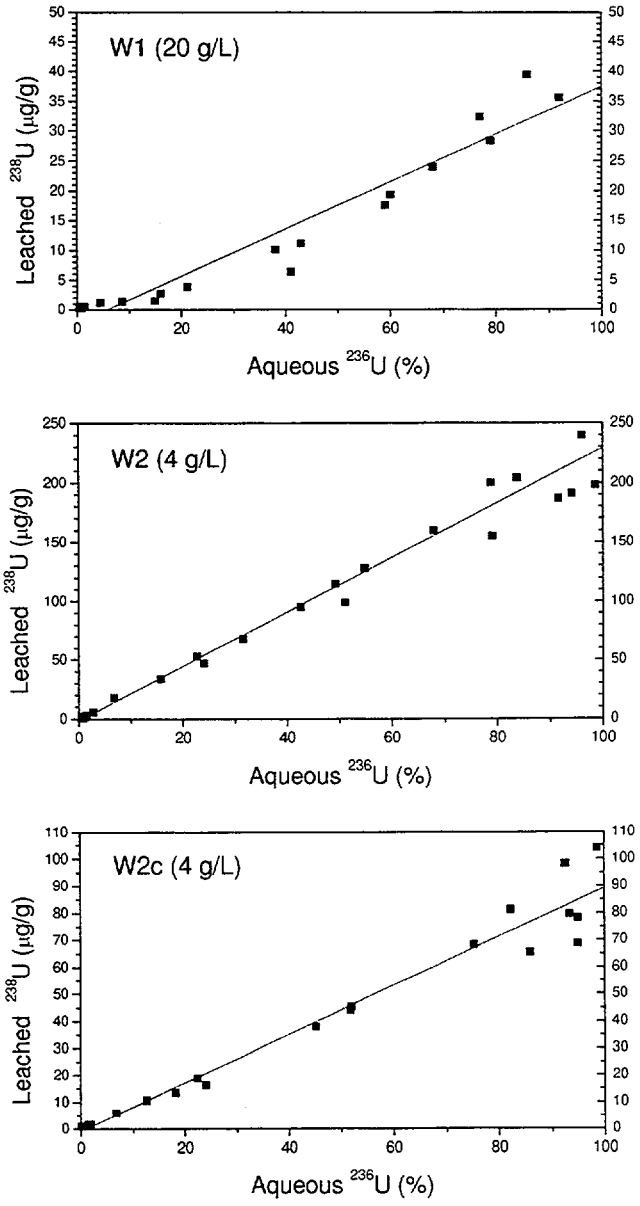

Figure 9-9. Summary isotope exchange plots for adsorption/desorption experiments with Koongarra sediments in air-equilibrated systems.

dissolution of stable mineral phases, and the release of the U contained within these phases.

The linear exchange between ^{236}U and accessible ^{238}U in these experiments implies that the adsorption/ desorption reaction involving aqueous and adsorbed U(VI) is reversible. However, this isotopic exchange does not extend to the remainder of the U content of the samples

Table 9-6. Estimates of accessible natural ^{238}U in Koongarra substrates by isotope exchange compared with estimates from TAO-extraction.

	Accessible ^{238}U (μg/g)		
Sample	Isotope exchange in air[a]	Isotope exchange in 1% CO_2[b]	TAO extraction[c]
W1	37	42	42.6
W2	230	235	225
W2c	89	-	97.3

[a] from Figure 9-9 [b] from Figure 9-10 [c] from Table 9-1

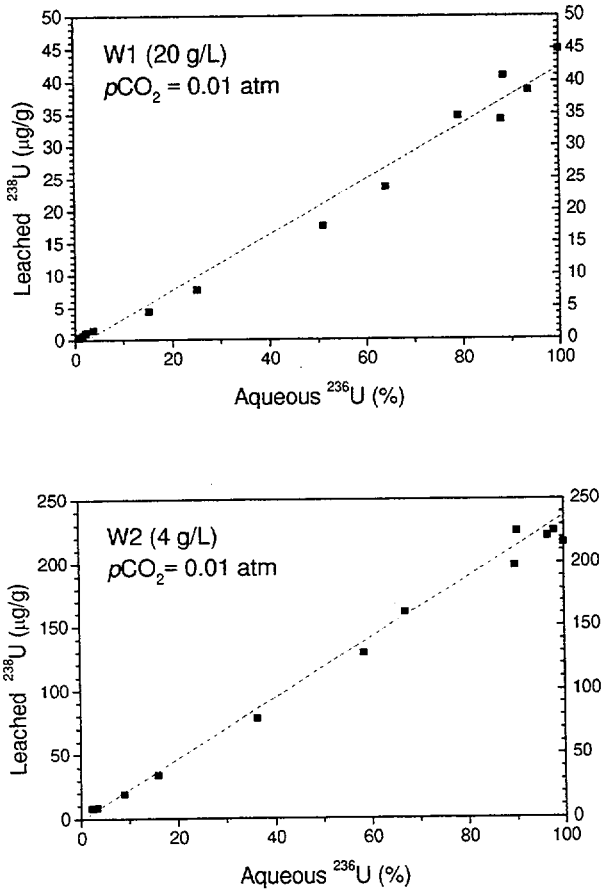

Figure 9-10. Summary isotope exchange plots for adsorption/desorption experiments. Koongarra sediments in systems equilibrated with 1% CO_2.

over the timescales of the experiments. Simiarly, the $^{234}U/^{238}U$ data in Table 9-4 show that some fraction of the U(VI) content of the samples is accessible, and that the remainder, having a significantly different ratio from the groundwater, remains isolated from the aqueous phase over much longer timescales.

9.3.9 COMPARISON OF NATURAL SAMPLES WITH FERRIHYDRITE AND KAOLINITE

As noted above, the experimental results obtained for the natural substrates are qualitatively similar to those obtained for model substrates. Data for the Koongarra W2 substrate are compared with data for ferrihydrite and kaolinite in Figure 9-11. The data sets have been chosen so that U_T and the surface area (in terms of m^2 per unit solution volume) are within a factor of 5 for all experiments compared. The experimental conditions are summarized in Table 9-7.

This comparison shows that, although results in the different systems are similar, there are significant differences between the natural substrate and the reference mineral phases. For example, the low pH edge on the natural materials commences at a lower pH value and also has a different slope from some of the model systems. These differences may be attributed to the effects of differing mineralogy or surface chemistry, and to complexing ligands (e.g., phosphate or humic acid) which may be present in the natural materials. These ligands may have a significant effect on the pH edge (see Sections 4 and 7). These results are considered in more detail and modeled in Section 16 of this report.

Table 9-7. Summary of experimental conditions for the data sets compared in Figure 9-11

Sample	Solid/ Liquid Ratio	Surface area		U_T
W2	4 g/L	52.3 m^2/g	209.2 m^2/L	3.9 μM (Table 9-5)
Kaolinite (KGa-1b)	4 g/L 40 g/L	11.7 m^2/g	46.8 m^2/L 468 m^2/L	1.0 μM 1.0 μM
Ferrihydrite	89 mg/L	600 m^2/g	53.4 m^2/L	1.0 μM

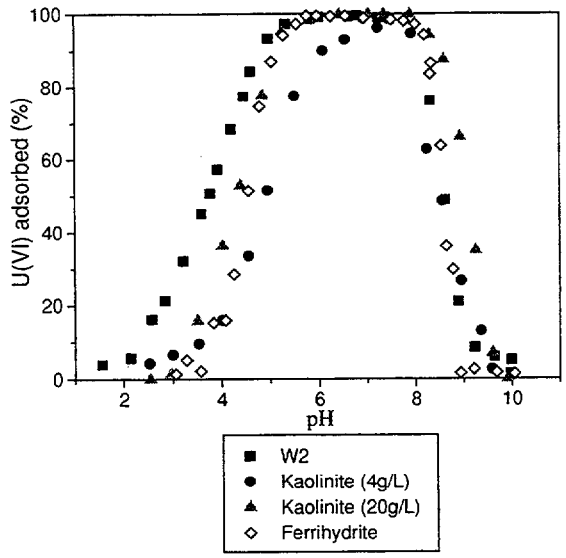

Figure 9-11. Comparison of U(VI) adsorption data on Koongarra sediments with data for reference minerals (kaolinite and ferrihydrite). The experimental conditions of the various experimental systems are summarized in Table 9-7.

9.4 Summary

The experimental studies undertaken in this project and in the previous ARAP study have provided a large amount of U(VI) adsorption data on the Koongarra natural substrates. The mineralogy of the samples is broadly similar, and the differences in adsorption behaviour (in experiments with low concentrations of ^{236}U added as spike) are attributed to the lower accessible U(VI) content in the W7 sample. In addition other species contained in the samples (e.g. humic acid, phosphate) may affect the outcome of the experiments.

The accessible U(VI) content, which contributes to the total U(VI) concentration (U_T) in experiments with the natural substrates, must be taken into account when interpreting the adsorption data. Several methods of estimating this quantity were considered. A sequential extraction of the substrates, together with associated $^{234}U/^{238}U$ ratios, provided valuable insights into the amount of accessible U(VI) in the Koongarra samples. The isotope exchange results obtained in adsorption experiments were consistent with the extraction results, and indicated the proportion of the natural U(VI) content which participated in adsorption/ desorption reactions. The isotope exchange results have the advantage that they do not involve chemical extractants and assumptions about their effects.

When compared with the reference mineral phases, U(VI) adsorption on the natural materials was broadly similar, including the effects of

- pH
- solid/liquid ratio

- ionic strength (affects the high pH edge but has little or no effect on the low pH edge)
- pCO_2
- U_T (indicating the presence of various site types)

Mg^{2+} had no effect on U(VI) adsorption, and was itself only weakly adsorbed. The effect of the CDB extraction was to decrease U(VI) adsorption. This may be attributed to the removal of strongly sorbing Fe oxides (and other oxides) with an associated reduction in surface area.

Further characterization of the natural substrate (with adsorbed U(VI)) is discussed in Section 10, and the adsorption data are modeled in Section 16 of this report.

10 PHYSICAL AND CHEMICAL CHARACTERIZATION OF SUBSURFACE MATERIAL FROM THE KOONGARRA WEATHERED SOIL ZONE

10.1 Overview & Introduction

In this section we report on investigations into the characteristics of the Koongarra sediments that might be expected to influence U(VI) adsorption. The sediments used in this study were from the W2c sample, which is described in Section 9. It has long been recognized that the dominant factor in the retardation of U(VI) migration at low concentrations in the subsurface environment is adsorption. It is only when a clearer understanding of the nature of the adsorbing phases and the type of U(VI) surface bonding has been attained that component additivity SCM can be developed (see Section 1). Sediments used in the chemical and physical characterization experiments reported here consisted of a weathered quartz/mica schist collected from the locale of the Koongarra uranium ore body, Alligator Rivers Uranium Province, Northern Territory, Australia. The bulk sediment was gravity separated into four size fractions, with attention focused on the nominally <25μm and 250-1000μm fractions of the bulk sample in order to assess effects of increasing particle size, and hence, decreasing particle specific surface area on U(VI) adsorption.

The characterization of the sediments was approached using two dissimilar but complementary methodologies. The first approach was to utilize conventional wet chemical methods which attempt to remove single mineral phases and then studying the kinetics and characteristics of U(VI) released in association with dissolution these mineral phases as described in Section 10.2. The second approach involved direct observation of the nature of the surface, including U(VI) bound to this surface, using *in situ* physical methods such as analytical transmission electron microscopy (AEM) and secondary ion mass spectroscopy (SIMS). These methods are described in Sections 10.3 and 10.4, respectively.

10.2 Cation Release from the Koongarra Sediments: Implications for Uranium(VI) Adsorption

10.2.1 INTRODUCTION

Early studies (*e.g.* Oades, 1963) concluded that iron oxides play an important role in the chemical reactivity of soils and sediments commonly found under oxic conditions in weathered environments. The mineralogical forms of iron range from poorly crystalline or amorphous species such as hydrous ferric oxide and ferrihydrite to cryptocrystalline and crystalline species such as goethite (FeOOH) and hematite (Fe_2O_3) (Schwertmann, 1973). As crystallinity of the species increases, the chemical reactivity per unit mass will tend to decrease, due to the decrease of surface area associated with the more crystalline phases, and therefore, a reduction in the number of reactive surface sites. Thus, high surface area phases such as ferrihydrite play a critical role in natural systems by adsorbing metals from permeating groundwaters. Other studies (Payne & Waite, 1991) have assumed that adsorption in a complex mineral assemblage is dominanted by single mineral phases such as those of the iron oxides and oxyhydroxides.

In this section, a determination of the major phases responsible for U(VI) binding in a complex natural mineralogical assemblage is sought. To achieve this, a series of wet chemical experiments have been utilized. That is, natural sediments have been leached using extracting agents which induce the release of U from specific mineral phases by desorption or dissolution, or by surface exchange by cation (including proton) exchange. The methodologies of these experiments have been extensively developed and refined over the past 80 years. While selective extractants have been used widely to assess the bulk content of particular

sediment fractions, most studies have been performed for a set time, only recording data once equilibrium or steady state conditions have been achieved. However, in this study, the temporal dependence of elemental release has been examined, thus enabling an assessment of the nature of the association of U with mineralogical phases of varying bulk chemical composition, both initially (near time zero) and during the dissolution of secondary minerals found as surface coatings.

10.2.2 SAMPLE TREATMENT

Sediment samples used in this study were collected using a cable tool rig from an area approximately 50 m south of the primary Koongarra uranium ore body in the direction of groundwater flow. The core samples were separated by gravity sedimentation, relying on Stokes law relating particle diameter to settling velocity, to give particle size fractions of nominally <25μm, 25-250μm, 250-1000μm and 1000-2000μm in diameter (ϕ). The fractions were stored wet in polypropylene or polycarbonate vessels at a temperature of <4°C until required for extraction (Moody & Lindstrom, 1977).

10.2.3 EXTRACTION METHODS

Numerous extraction methods have been documented in the literature for dissolution of iron and aluminium oxides and oxyhydroxides (Tessier *et al.*, 1979; Chao & Zhou, 1983). In this study, five different extraction methodologies were used. These were:

1. Hydrochloric acid (HCl)
2. Hydroxylamine hydrochloride - hydrochloric acid (HH)
3. Sodium citrate - sodium dithionite - sodium bicarbonate (DCB)
4. Ammonium oxalate - oxalic acid (TAO)
5. Sodium acetate - acetic acid (MOR)

Extractions were performed in teflon centrifuge tubes at 30±1°C with agitation of 120 oscillations per minute. Solid/liquid ratio was difficult to keep constant and changed slightly between experiments, with all experiments close to 1:25 (i.e., 1 g dry weight of the sediment in 25mL of extractant). Batch extractions using a wide range of solid/liquid ratios showed that there was very little effect if any attributed to the solid/liquid ratio over several orders of magnitude. Samples were drawn from the extraction mixture after the required time interval by micropipette. The aliquot was then driven through a 0.2μm microfilter by a polypropylene syringe to separate the solid from the solution. An aliquot of the filtrate was removed and prepared to volume with 2% HNO_3 for ICP-AES analysis. At the termination of the extraction (after 60 min) the supernatant was removed by pipette after centrifugation and the remaining sediment washed four times with Milli-Q water. These samples were then stored as a slurry at 4°C.

Each extraction was performed in triplicate to ensure reproducibility of the results. The results presented in this study are averages of the three replicates, with error bars representing the standard deviation from the average. It should be emphasized that extractions presented in this study have been undertaken in a parallel rather than sequential fashion. That is, the same source material was used in each extraction study and the effect of the extractant on the kinetics of release of U from the sediments was examined. This approach differs significantly from a sequential extraction approach, where an extractant is typically applied to the solid phases remaining from a previous extraction (see Section 9).

10.2.4 METAL ANALYSES & STATISTICAL INTERPRETATION

Trace metals, including U, were determined by inductively coupled plasma - atomic emission spectroscopy, ICP-AES (Perkin Elmer Optima 3000) with direct aspiration of the aqueous solution into the argon (Ar^+) plasma torch. All elements were determined using a multi-element technique and suitably matrix matched multi-element standards. Interferences were identified on the primary analytical wavelength of U at 409.014nm. Further testing attributed this to the presence of Mg and Fe in the matrix at

concentrations typically several orders of magnitude greater than those observed for U. This problem was countered by analyzing for U at the 367.007nm line. Other elements analyzed in this study were Fe(238.204nm), Si (251.611nm), Mn(257.610nm), Mg(279.079nm), Al(309.271nm), Ca(317.933nm) and K (766.491nm). All analyses were performed in triplicate and relative standard deviation (RSD) between replicates was significantly less than 1%.

The concentrations of metals leached by the various extractants for both the <25μm and 250-1000μm fractions were calculated from the measured dilute sample concentrations and normalized to the solid/liquid ratio of the experiment at the sampling point to a concentration per unit mass. The methods used for this calculation are described below:

Normalized conc. (mg/kg) = Measured conc. (mg/L) x Dil. Factor x Extractant volume (L) / dry sediment weight (kg)

During the experimental procedure, sampling reduced the extractant volume with time. The method of sampling involved the removal of a precise volume of solution from the reaction vessel with a micropipette. In the case of the agitated <25μm fraction, a small mass of the sediment was also removed, which was accounted for in the calculation. The sampling of the reaction vessel utilizing the 250-1000 μm fraction of the Koongarra sediments did not reduce the sediment weight in the reaction vessel. This artificially increased the solid/liquid ratio of the extractions performed on the material of this size fraction. This was also accounted for in the normalization calculation.

After normalized metal concentrations were calculated, the bivariate correlation of U to proposed components of surface coatings, such as Fe, Al & Mn, was examined. This correlation could be statistically described using a linear regression analysis, which plots the metal concentration of interest against the concentration of U released at the same data point. The linear fit of the resulting curve is described by the R parameter, which describes a perfect fit at a value of 1. The inter-correlation between the eight metals analyzed was significantly more complex and required multivariate data analysis. This was achieved by cluster analysis of the datasets, which transformed the data to points in n-dimensional space by extracting the eigenvectors and eigenvalues from the variance-covariance matrix, with extraction, by the method of principal components. The method yields plots of the elements where the proximity of the plotted datapoints in multi-dimensional space is proportional to the inter-element correlation.

10.2.5 RESULTS & DISCUSSION

The selection of reagents for the extractions was based specifically on either the ability to preferentially solubilize a required mineral fraction within the sediment or to exchange with U(VI) occupying ion exchange sites. This was then to be used to identify the release of U in conjunction with specific mineral fractions. The results of the sediment extractions using the described reagents are presented and discussed below.

10.2.5.1 Total Leachable Fraction

The total extractable fraction was evaluated using 4M HCl. This extraction is designed such that in the 60 min extraction period, bulk mineral dissolution is small, while most of the surface coatings are removed (Carpenter *et al.* 1978). As a check of this hypothesis, the concentrations of alkali metals associated with clay matrices (such as K in the crystal lattice of illite) were monitored. These concentrations increased slightly throughout the extraction, indicating a probable degree of clay mineral dissolution. This method has been used for the dissolution of metal oxides found in soils as both coatings and detrital minerals (Canney & Hawkins, 1968; Yanase *et al.* 1991). The dissolution of iron oxide minerals using the HCl extraction method is likely due to the formation of Fe-Cl complexes at the oxide surface. Formation of these complexes decreases the surface charge, increasing the affinity of protons for the surface, resulting in increased proton-

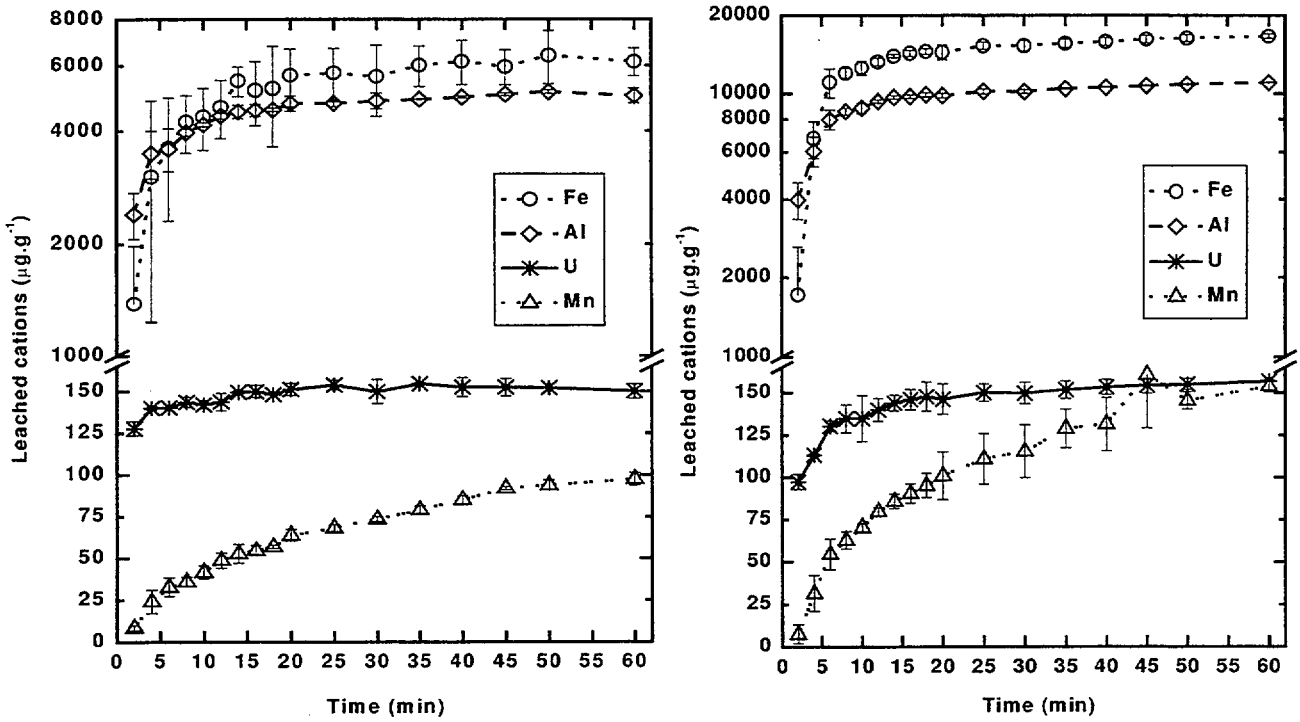

Figure 10-1. Mass normalized concentrations of U, Fe, Al & Mn released from the Koongarra weathered zone (composite sediment sample W2-C) on treatment with 4M HCl. Part A, left) leaching from the <25µm sediment fraction; part B, right) leaching from the 250-1000µm sediment fraction.

induced dissolution (Sidhu *et al.* 1981). In addition to oxide dissolution, the extraction also dissolves carbonate minerals and exchanges ions bound to both inorganic and organic phases (Chaundry & Bose, 1971; Maynard & Fletcher, 1973).

The concentrations of trace metals leached by 4M HCl were greater than any other method of extraction, with the exception of Fe dissolution from the fine fraction using the DCB method. At the end of the extraction, dissolution of Fe from the <25µm fraction was approximately 6100 mg per kg of sediment (Fig. 10-1a). This compares to approximately 12400 mg/kg at steady state using the DCB method on the fine fraction. The amount of Fe and Al dissolved per unit mass from the 250-1000 µm sediment fraction was approximately double that removed from the <25µm fraction. This would suggest that concentrations of these elements in secondary mineralizations increase as particle size increases. This result contrasts sharply with the amount of U leached, which was similar in both samples. Release of U from the fine fraction showed leached concentrations of 128 mg/kg at t=2min. and 145 mg/kg at steady-state at the end of the extraction. This can be compared with release of 98 mg/kg and 150 mg/kg (Fig. 10-1) at the same respective sampling times from the 250-1000µm size fraction. Concentrations of the alkaline elements continued to increase over the course of the extraction, indicating partial dissolution of clay minerals present in the sample. Results presented in Section 10.3 of this section show that a large proportion of clay minerals found in the sediment consists of illites. Typically, these are derived from weathering of potassium micas, such as muscovite ($KAl_2(AlSi_3O_{10})(OH)_2$). Chemically, they can be generally described as $K_xAl_4(Si,Al)_8O_{20}(OH)_4$, where x has a value between 1 and 1.5. By monitoring the release of K over the course of the extraction, the extent of primary mineral dissolution can be evaluated. Release of K from the fine fraction increased from 140 mg/kg

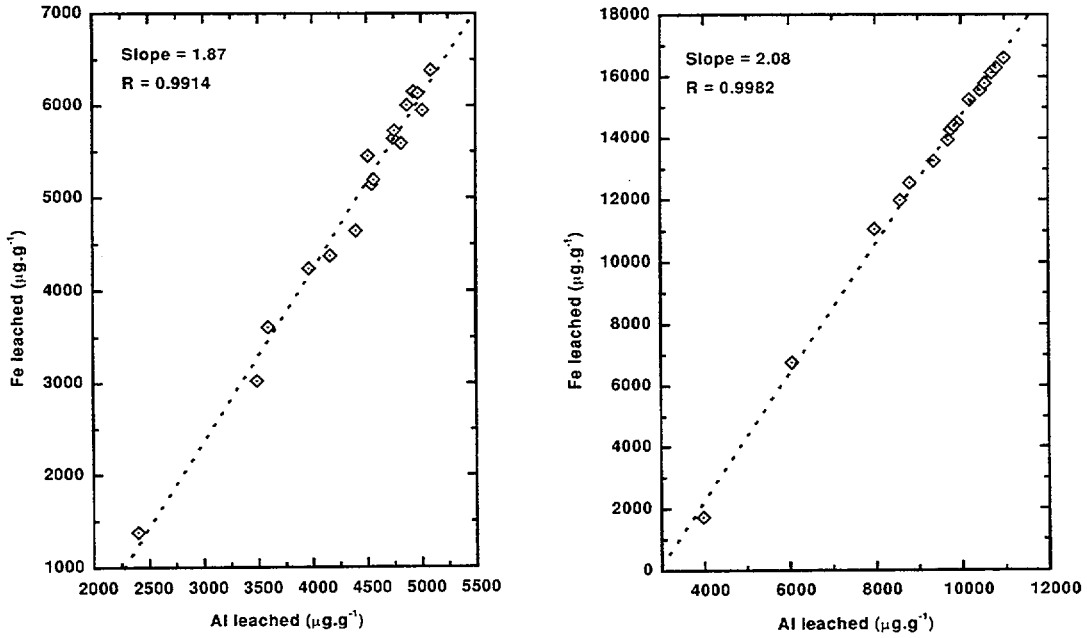

Figure 10-2. Linear regression analysis of Fe dissolution (ppm) versus Al dissolution (ppm) from the <25µm (part A, left) and 250-1000µm (part B, right) fractions of the Koongarra sediments using the 4M HCl extraction method.

initially to 180 mg/kg at steady-state at the end of the extraction, while the coarse fraction showed concentrations of 85 mg/kg increasing to 123 mg/kg. In comparison, the "mild" extractant TAO only mobilized approximately 70 mg/kg from both size fractions, with little increase over the extraction period. Clearly this indicates that, at least in the fine fraction, some degree of illite dissolution is occurring. The extraction results concur with the XRD analyses of the samples, which show that the clay minerals dominate the mineralogy of the fine fraction whilst the coarse fraction consists largely of quartz.

The 4M HCl extraction was performed to evaluate the total amount of coating material which may be removed and to ascertain the identity of contaminants associated with this fraction. However, as dissolution of the clay matrix occurred at least to some extent, it is difficult to properly distinguish metals derived from the bulk matrix and those adsorbed to surface sites. Further analysis of the data shows that the ratio of Fe to Al released is linear throughout the course of the extractions (Fig. 10-2) and that similarly, U release is linearly related to both Fe & Al dissolution (Fig. 10-3). Multivariate analysis of this data is statistically insignificant given the non-specific nature of the extractant. However, several broad trends can be defined. Figure 10-4 shows that there is some correlation (in both the fine and coarse fractions) in the release of U and the elements which have been identified in the composition of the surface coatings (Fe, Al & Mn). In addition, a reasonably strong negative correlation exists between Si and transition metal release, as represented in n-dimensional space.

10.2.5.2 U(VI) Bound with Iron and Aluminum Oxyhydroxides and Oxides

U associated with the iron/aluminium oxydrohydroxides in the sediments was evaluated using three extractants, TAO, DCB & HH.

A. 0.175M $(NH_4)C_2O_4$ - 0.100M $H_2C_2O_4$ (TAO)

McKeague & Day (1966) and Chao & Zhou (1983) have shown that extraction with Tamm's

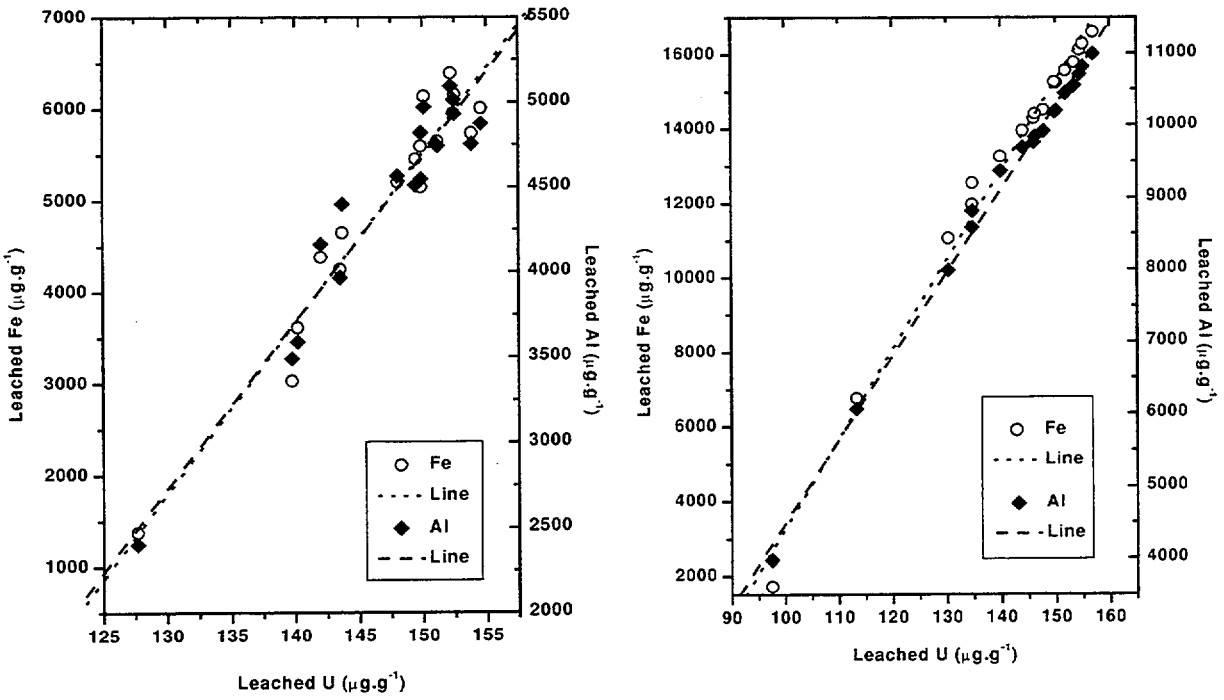

Figure 10-3. Dual linear regression plots. Fe vs. U & Al vs. U dissolved by the 4M HCl extraction method on the <25µm (part a, left) and 250-1000µm (part b, right) fractions of the Koongarra sediments.

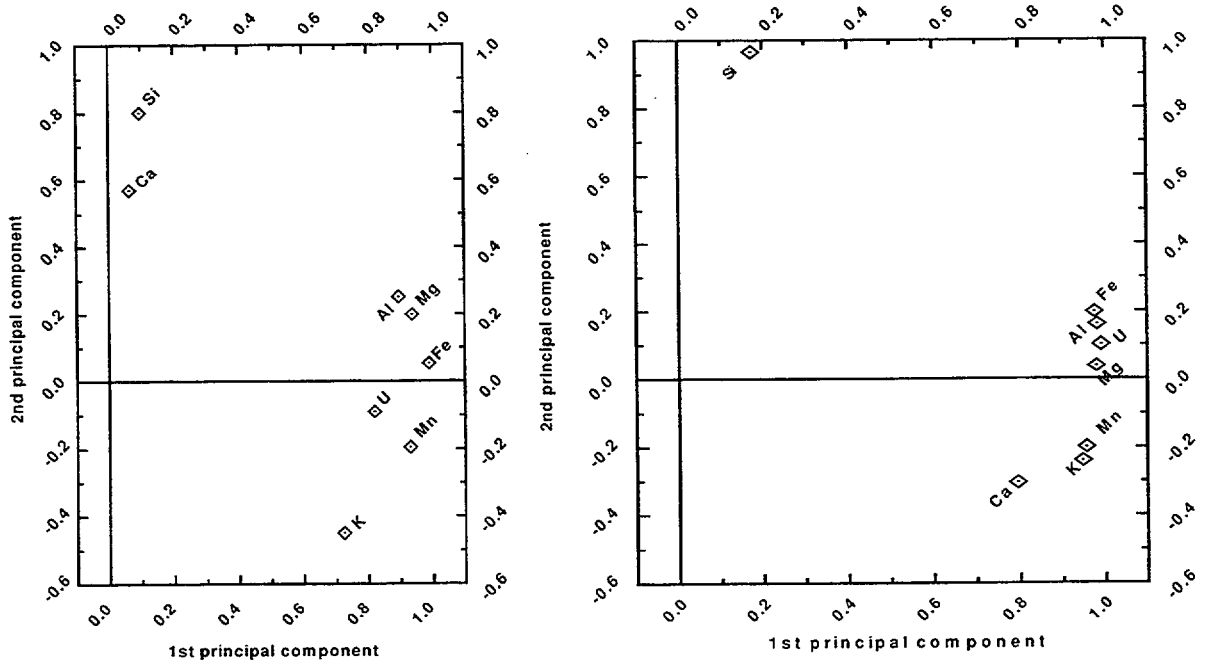

Figure 10-4. Multivariate principal component analysis of cation release from the Koongarra sediments on treatment with 4M HCl. Part A (left) shows results of the experiment on the <25µm fraction and part B (right) shows the same experiment performed on the 250-1000µm fraction.

reagent is very effective in the selective dissolution of amorphous phases, with crystalline oxides of iron such as hematite and goethite only sparingly soluble in the extract.

The success of this extraction as a selective reagent is dependent on the absence of organic chelates and magnetite, both of which can be solubilized by the reagent (McKeague, 1967). Chao & Zhou (1983) reported the solubility of hematites and goethites to be <1% after treatment of the minerals with TAO for 4 hours. Magnetites, in contrast, released significant amounts of Fe to solution, with approximately 17-20% dissolution in the same time period. The results of our study showed that, in the initial period of the extraction (t<20min.), the release of Al was significantly greater than that of Fe (Fig. 10-5). This release of Al was initially greater from the fine fraction (375 mg/kg) than from the coarse fraction (90 mg/kg). The greater concentrations of Al released continued throughout the course of the extraction, such that at equilibrium, [Al_{fine}] was 590 mg/kg and [Al_{coarse}] was 412 mg/kg (Fig. 10-5). The results show that the release of Al from the sediment is largely instantaneous, with >90% removed in the first 10 min. using TAO, for both the fineand coarse size fractions of the sediment. Associated with the fast release of Al was a similar rate of release of U, that is, >90% within the first 10 minutes of the extraction (Fig. 10-5). U released at steady state at the end of the TAO extraction accounted for approximately 70% of that removed by the 4M HCl extraction (see Section 10.2.5.1). Also, the concentrations of U released from each of the size fractions was quite similar (92 mg/kg and 91 mg/kg from the fine and coarse fractions, respectively), suggesting that the particle size had little effect on U(VI) adsorption. Given the selectivity of the extractant towards amorphous fractions, it may be inferred that a large proportion of the U(VI) adsorbed is associated with these amorphous mineral phases present as coatings. The release of Fe from the sediments during the TAO extraction showed a markedly different pattern of dissolution. At the first sampling point (t=2min), an insignificant concentration of Fe was released from the sediment (<1 mg/kg) for both size fractions. This accounted for <1% of the total Fe dissolved at steady state at the

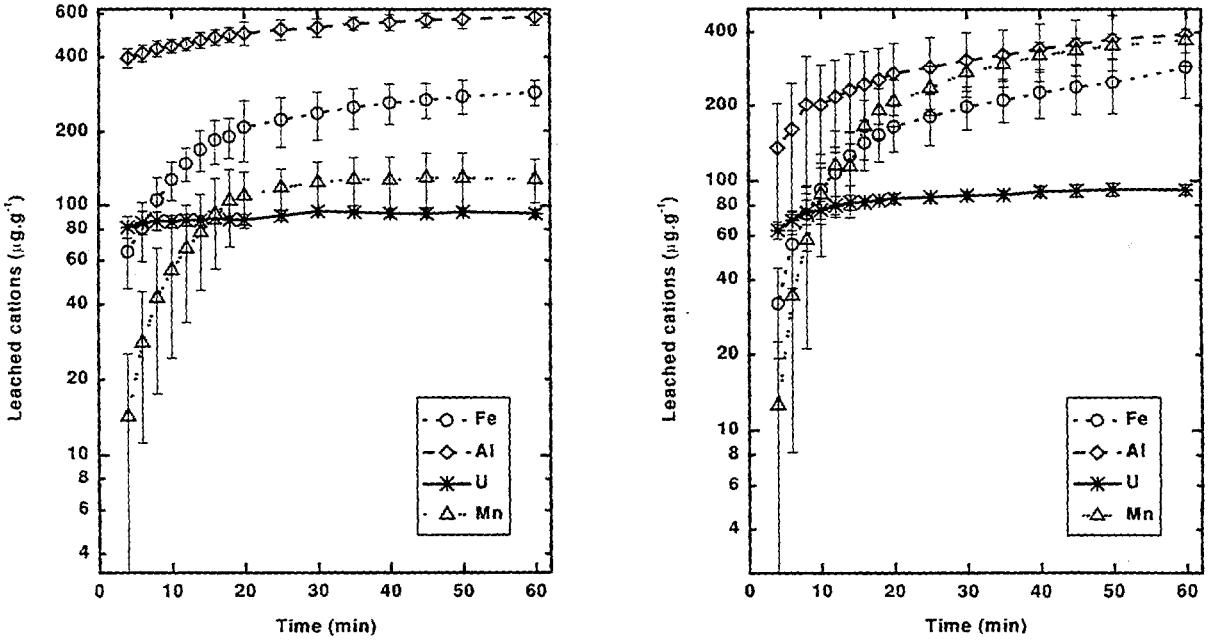

Figure 10-5. Mass normalized concentrations of U, Fe, Al & Mn dissolved and released from the Koongarra weathered zone (composite sediments) on treatment with TAO. Part A (left) shows leaching from the <25μm fraction and Part B (right) shows leaching from the 250-1000μm fraction.

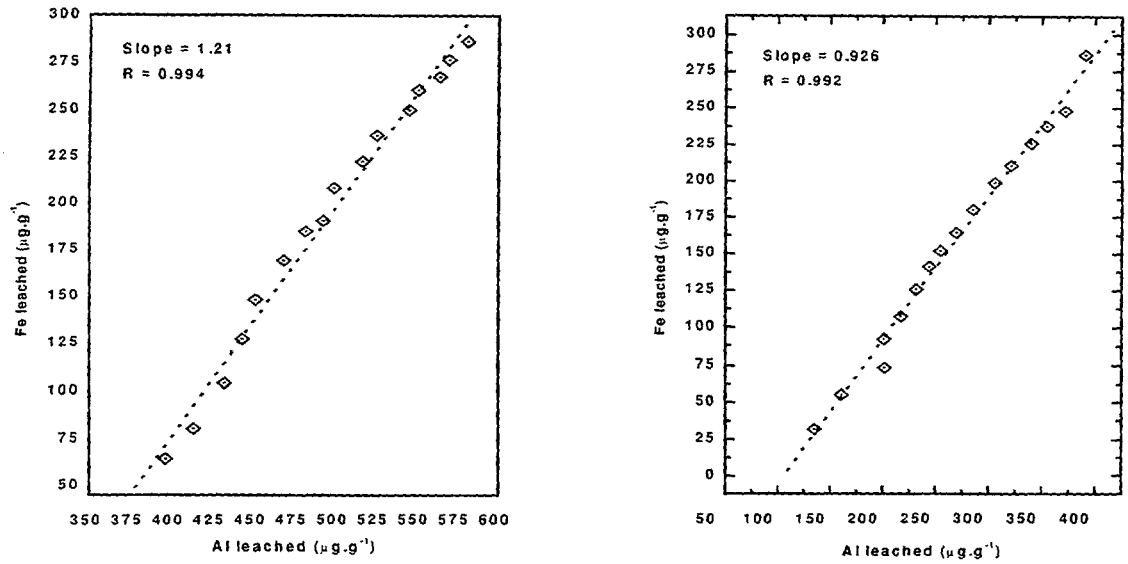

Figure 10-6. Linear regression analysis of Fe dissolution (ppm) versus Al dissolution (ppm) from the <25 µm (Part A, left) and 250-1000 µm (Part B, right) fractions of the Koongarra sediments, using the TAO extraction method. Fits of the regression are 0.994 and 0.992 for Parts A & B, respectively.

end of the extraction. This compares with Al concentrations at t=2 min equal to 65% and 23% of the final concentration (Figs. 10-5). The dissolution of Fe increased rapidly over the first 10 min. of the extraction, with 44% and 35% of the final concentrations dissolved from the fine and coarse fractions, respectively. The rate of Fe dissolution continued to rise until approximately t=30 min, when near steady-state conditions were achieved. At the end of the extraction the Fe:Al ratio was 1:2 and 2:3 for the fine and coarse fractions, respectively, compared with the early time ratios of 1:12 and 1:8 for the same size fractions (Fig. 10-6).

Statistically, the multivariate treatment of the extraction data (Figs. 10-7 and 10-8) show that the inter-element correlations between Al and U are quite good, especially in the datasets produced from the extraction of the <25µm fraction. Both datasets showed a strong relationship between Fe and Mn, and also a suite of the alkali metals. In addition, the results from the coarse fraction indicate that there is a good correlation between the Fe and Al dissolved. The small differences in the inter-element relationships between the extractions performed on the <25µm and 250-1000 µm fractions can be explained by the differences in bulk rock chemistry between the two size fractions.

B. 0.3M $Na_2S_2O_4$ - 0.175M Na-citrate buffered with 1M $NaHCO_3$ to pH 8.3 (DCB)

This method has been used extensively in the past for the specific dissolution of iron minerals (Makenzie, 1954; Mehra & Jackson, 1960 and Tessier *et al.* 1979). The original method after Makenzie used only dithionite for the reductive dissolution of Fe(III). Later modification introduced the citrate complexant, which forms stable, soluble Fe(II) complexes, thus keeping the reduced iron in solution. The relatively high pH of the system limits the dissolution of other oxide (e.g. Mn) and carbonate minerals. This extractant showed a high degree of selectivity towards the iron oxide phases, as shown in Figure 10-9.

In the initial stages of the extraction there was negligible release of Al from either the <25 or 250-1000 µm fractions. Dissolution of Al increased during the 60 min. extraction, to a maximum of 730 mg/kg and 200 mg/kg for the fine and coarse fractions. These values for Al dissolution at steady state account for only 14% and 2% of the total Al dissolved by the 4M HCl extraction.

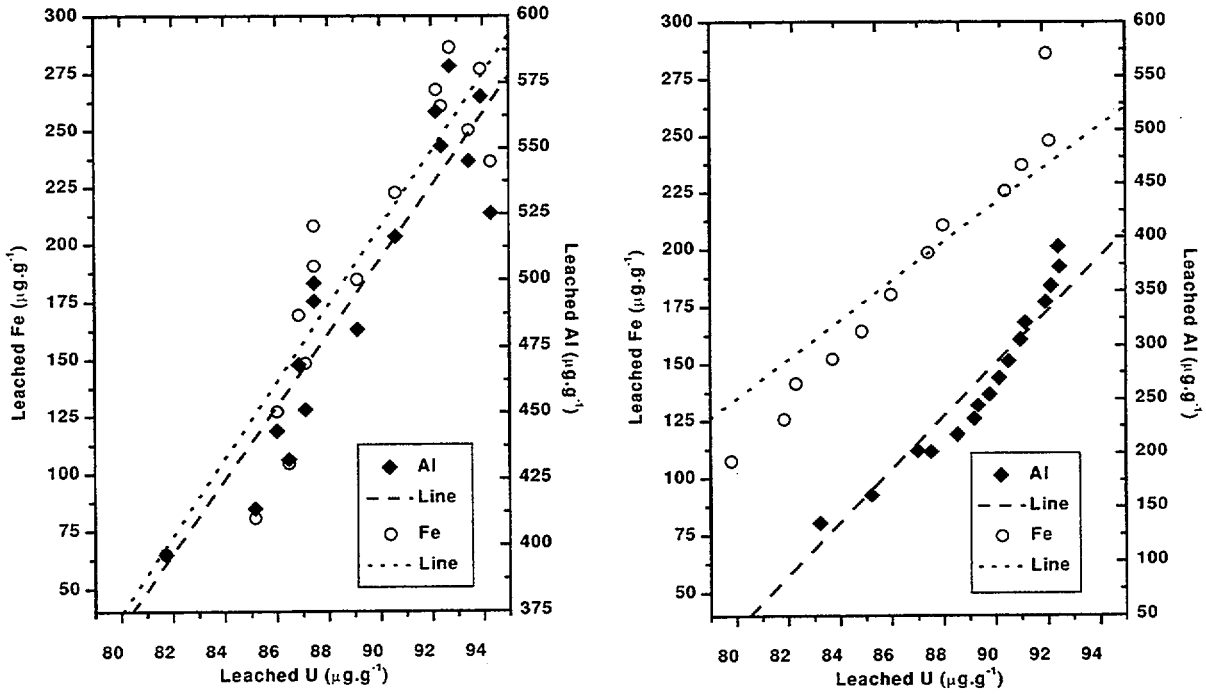

Figure 10-7. Dual linear regression plots. Fe vs. U and Al vs. U released during TAO extractions on the <25µm (Part A, left) and 250-1000µm (Part B, right) Koongarra sediment fractions.

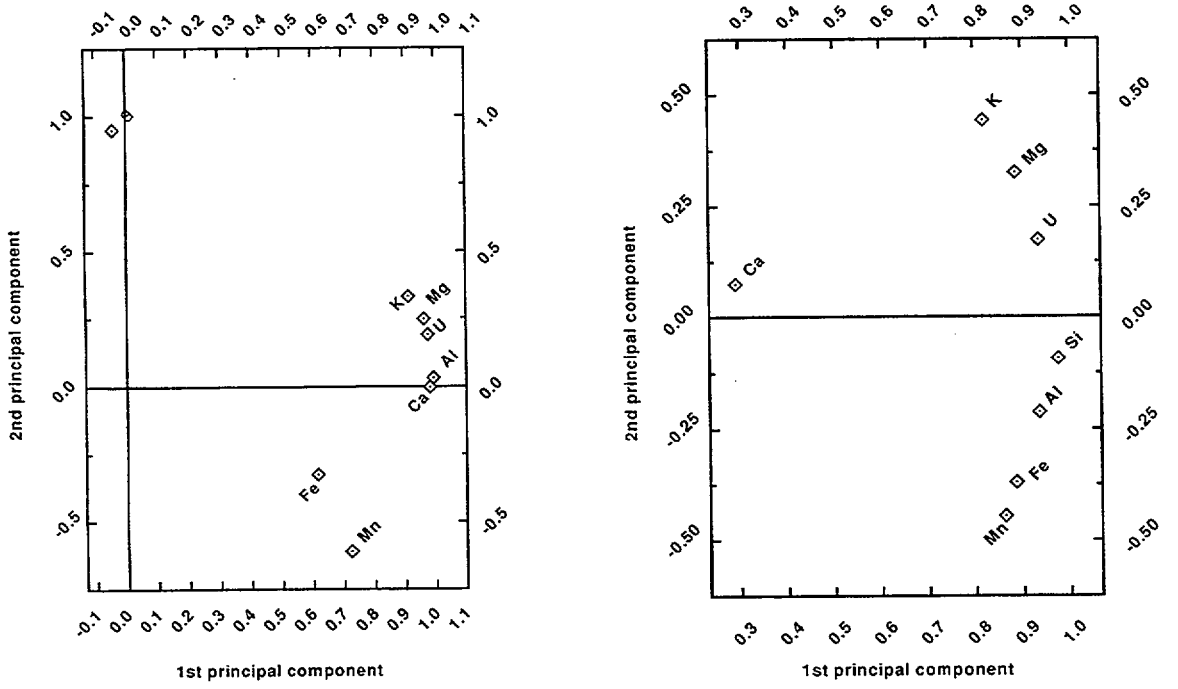

Figure 10-8. Multivariate principal component analysis of cation release from the Koongarra sediments, using the TAO extraction method. Part A (left) shows results of the experiment on the <25µm sediment fraction and Part B (right) shows the same experiment performed on the 250-1000µm fraction.

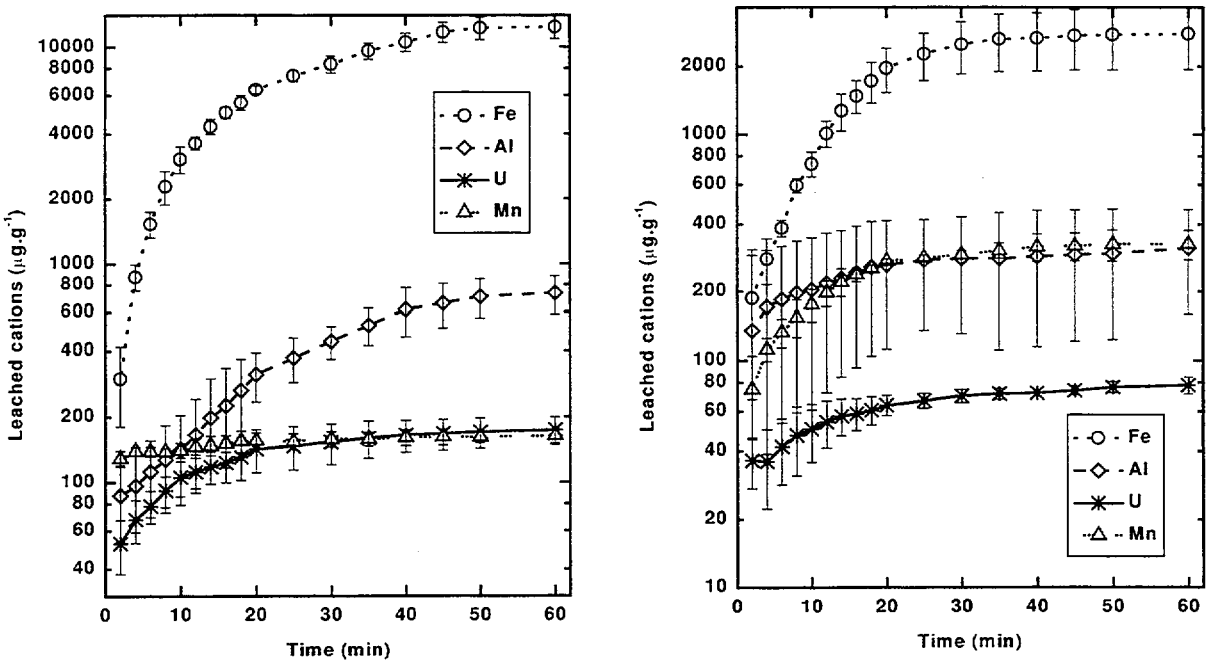

Figure 10-9. Mass normalized concentrations of U, Fe, Al & Mn extracted from the Koongarra sediments on treatment with DCB. Parts A and B (left and right) show leaching from the <25µm fraction and 250-1000µm sediment fractions, respectively.

These results for the dissolution of Al contrast sharply with those obtained for dissolution of Fe. The concentration of Fe initially was 298 mg/kg from extraction of the fine fraction and 49 mg/kg from the 250-1000 µm fraction. The rate of release increased rapidly over the first 20 minutes, with 50% and 61% of the total Fe dissolved by the 4M HCl extraction. The final concentrations of Fe dissolved by the DCB extraction were 12398 mg/kg from the <25 µm fraction and 3590 mg/kg from the 250-1000 µm fraction. The total Fe dissolved from the fine fraction by DCB was greater than the total Fe dissolved by treatment of the same size fraction with 4*M* HCl, which in comparison to the low total amount of Al dissolved, demonstrates that the extraction method was somewhat specific in the dissolution of Fe oxide phases. The correlation between Fe and Al dissolution for these fractions is shown in Figure 10-10.

The release of U from the fine fraction was fast over the first 20 minutes of the extraction, with slightly more than 80% of the final U concentration found in solution at that time. This rapid release of U between 2 and 20 min corresponds closely to the dissolution rate of Al from the sediment (Fig. 10-11). Similar results are seen in the leaching profile of the coarse fraction, where release was rapid during the first 20 min. Notably, while the U release kinetics were temporally similar in both size fractions, the total concentration of U released at steady state at the end of the extraction was approximately 130% greater from the <25µm fraction than that released from the coarse sediment fraction. This is potentially due to the high concentrations of Fe released from the <25µm fraction during the DCB extraction, which was not observed in the extraction of the 250-1000 µm fraction.

Inter-element relationships (Fig. 10-12) found during the course of this series of extractions were statistically determined to be strong between Fe, Al, Mn and U for both size fractions. Additionally, a very strong relationship between Fe and Si was observed in both datasets. Not shown here is the dissolution kinetics of K during the extractions. These

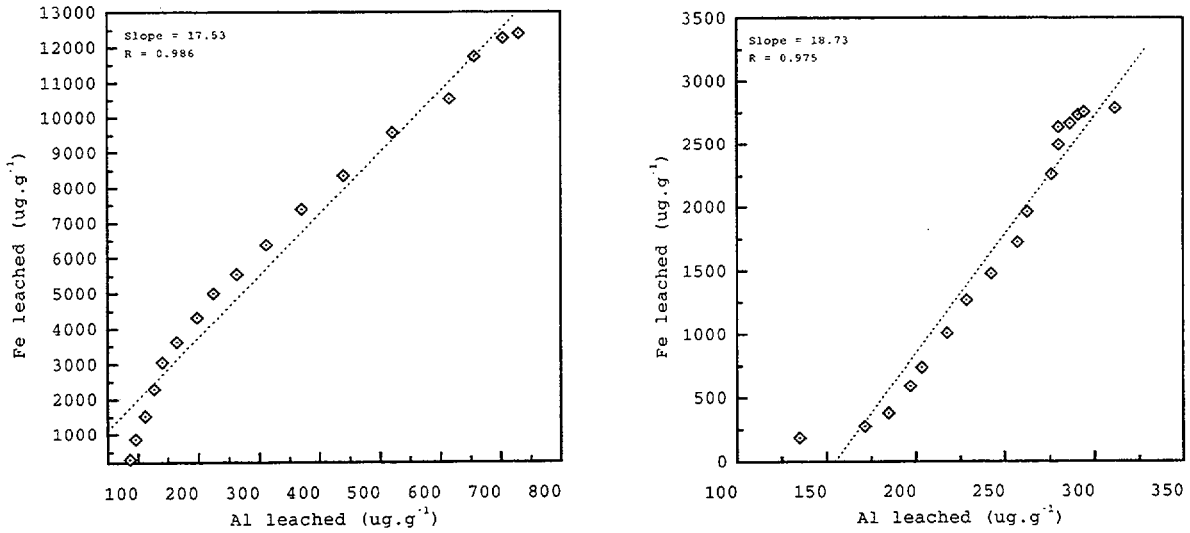

Figure 10-10. Linear regression analysis of Fe dissolution (ppm) versus Al dissolution (ppm) from the <25μm (Part A, left) and 250-1000μm (Part B, right) fractions of the Koongarra sediments using the DCB extraction method. Fit of the regression is 0.986 and 0.975 for Parts A and B, respectively.

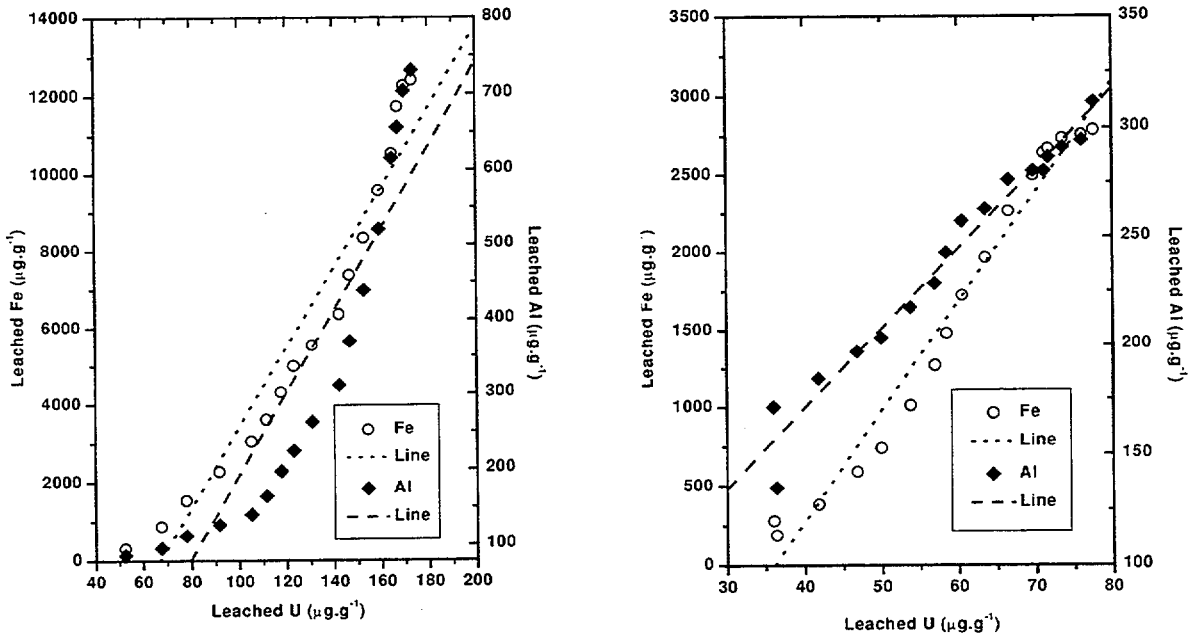

Figure 10-11. Dual linear regression plots. Fe vs. U & Al vs. U extracted by the DCB extraction method on the <25μm (part A, left) and 250-1000μm (part B, right) fractions of the Koongarra sediments.

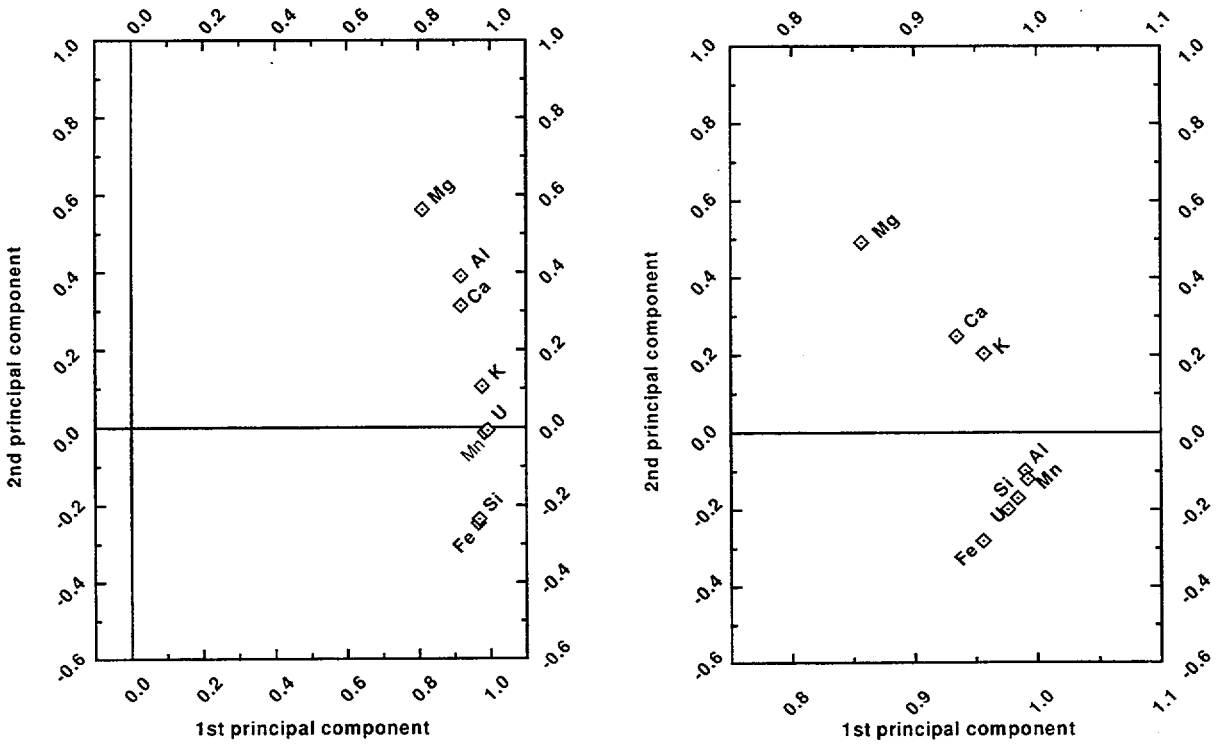

Figure 10-12. Multivariate principal component analysis of cation release from the Koongarra sediments in DCB extractions (part A, left: <25μm fraction; part B, right: 250-1000μm fraction).

results yielded similar profiles to those found in the 4M HCl extractions, indicating that possible dissolution of the unstable clay matrix was occurring, perhaps due to the formation of soluble Fe-citrate complexes at mineral solution interfaces.

C. 0.25M $NH_2OH.HCl$ - 0.25M HCl (Hydroxylaminehydrochloride - Hydrochloric acid) (HH)

This method was originally designed for the dissolution of crystalline iron/manganese oxides (Chao, 1972; Chao & Theobold, 1976). However, other studies have reported that the solubility of poorly crystalline aluminium oxides is also high (Coston *et al.* 1995; Fuller et al., 1996). Extraction of the Koongarra sediments using the HH reagent showed that relatively with large quantities of Al were solubilized initially (Fig. 10-13). For the fine fraction, the first sampling point recorded showed 734 mg/kg, a similar concentration of Al (807 mg/kg) dissolved from the 250-1000 μm fraction. For both fractions this large initial dissolution continued to increase steadily for about 20 min., at which time >95% of the final dissolution of Al had been achieved. The final concentration of Al released by HH extraction was far greater (4651 mg/kg) from the 250-1000 μm fraction than from the fine fraction (1944 mg/kg).

These results contrast somewhat with those observed for the dissolution of Fe from the sediment. The initial release of Fe during HH extractions was 35 mg/kg and 99 mg/kg for the fine and coarse fractions, respectively. As the extraction progressed, the concentrations of Fe in solution increased sharply during the first 30 min., by which time 58% and 45% of the final concentrations released during the 60 min. extraction had occurred. Only a small decrease in the rate of Fe dissolution occurred during the final 30 min of extraction, and dissolution was still incomplete at the end of the extraction. While the initial concentrations of Fe dissolved from the two fractions were similar, they were quite different by the termination of the extraction, with 1103 mg/kg leached from the fine fraction and 4106 mg/kg from the coarse

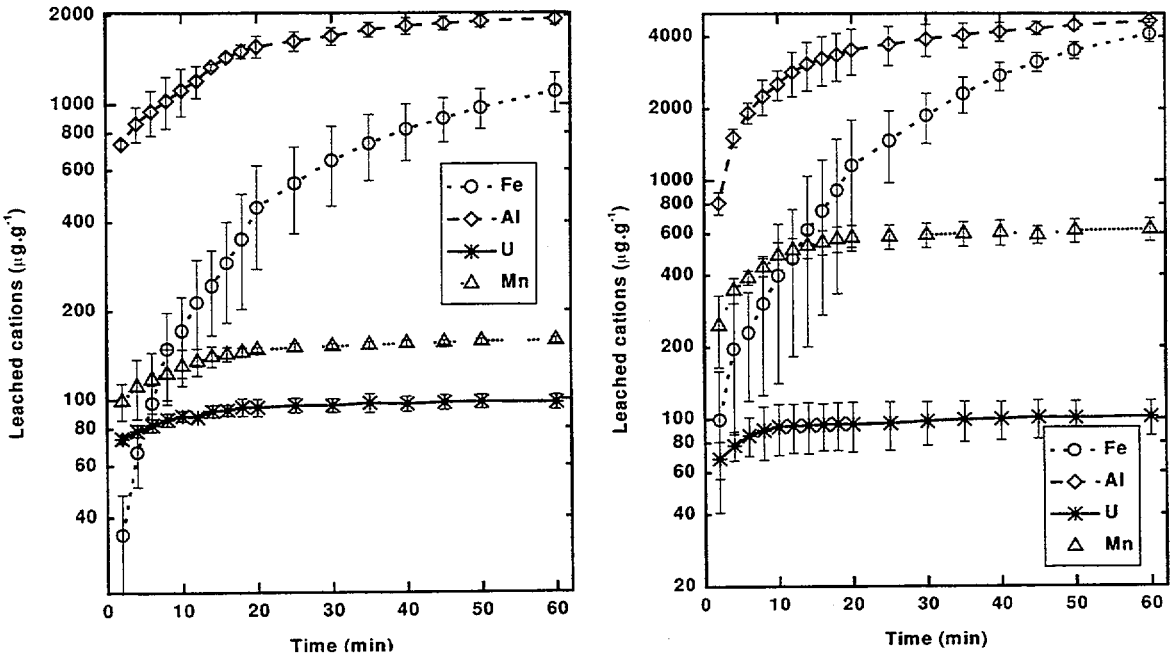

Figure 10-13. Mass normalized concentrations of U, Fe, Al & Mn extracted from the Koongarra sediments by the HH method (left, <25µm fraction; right, 250-1000µm fraction).

fraction. This represents approximately a fourfold increase in Fe dissolution from the 250-1000 µm fraction in comparison to the <25 µm fraction, whereas there was a 250% greater release of Al from the coarse fraction than from the fine fraction (Fig. 10-14). This would appear to indicate that the *crystallinity* of the secondary mineralizations found as surficial coatings on the 250-1000 µm fraction is greater than those associated with the fine fraction. This finding is supported by the results of the TAO extractions, designed to dissolve only poorly crystalline Fe oxides, which showed that dissolution of both Fe and Al from the <25 µm fraction was greater than that from the 250-1000 µm fraction.

The results for release of U from the sediment by HH extraction showed similar profiles for the fine and coarse fractions (Fig. 10-13). The rate of release for both size fractions exhibited a curve with approximately 75% of the total released at t=2min. The release reached a steady state concentration after 20 min. While the release of U was completed after 20 min., Fe dissolution continued steadily for the next 40 min. This suggests that the dissolution of some of the crystalline Fe material did not release additional U. Bivariate analysis (Fig. 10-15) of the Al and Fe dissolution against U release show that the linearity of the plots described by the R value is poor for both elements. In the case of the <25µm fraction $R_{Fe/U}$ and $R_{Al/U}$ were 0.84 and 0.96, respectively. Regression analysis of the coarse fraction yielded $R_{Fe/U}$ and $R_{Al/U}$ of 0.95 and 0.72, respectively (Fig. 10-15). Multivariate treatment of the data suggests that the correlation between Al and U is better than that between Fe and U, however, the correlations were not particularly strong (Fig. 10-16).

10.2.5.3 Extraction with Morgan's Reagent

U released by extraction with 1*M* NaOAc, buffered to pH 5 with *2M* HOAc (Morgan's reagent) was also determined. The results showed no detectable levels of Fe or Mn were released using this extractant during the 60 minute extraction. A small release of Al was observed (Fig. 10-17) from both the <25 µm and 250-1000 µm sediment fractions. Release of Al from both particle size fractions showed similar profiles and similar final concentrations

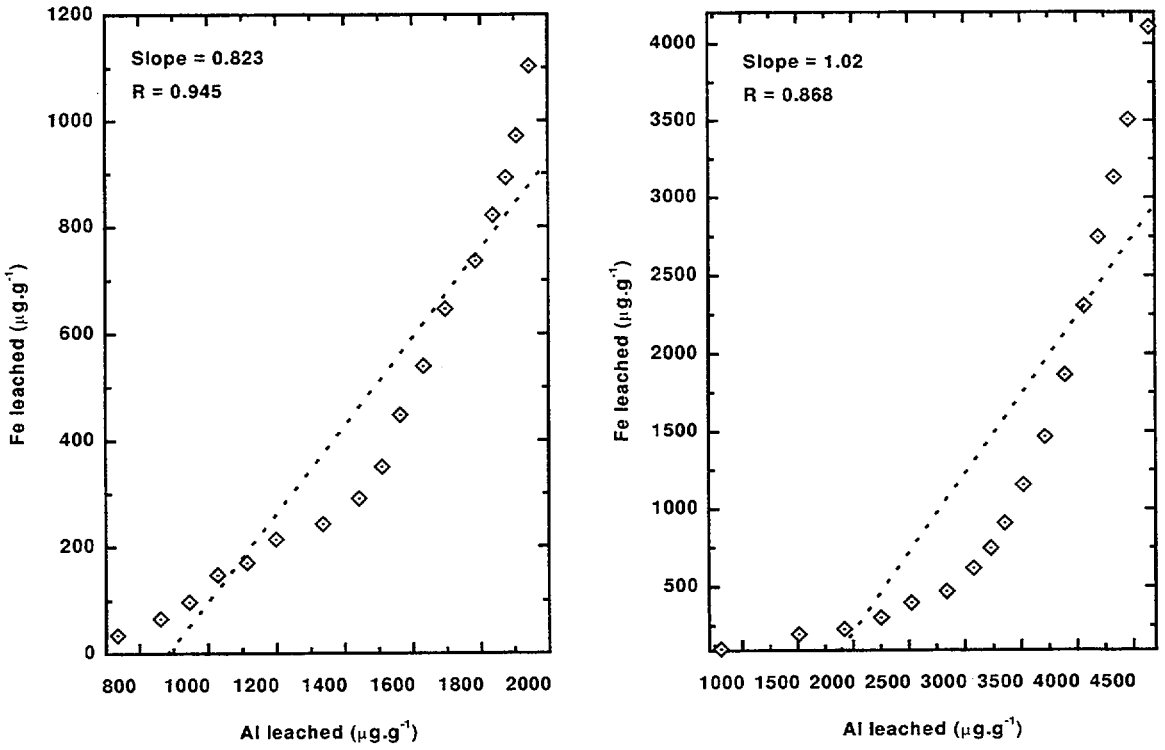

Figure 10-14. Linear regression analysis of Fe dissolution (ppm) versus Al dissolution (ppm) from the <25µm (Part A, left) and 250-1000µm (Part B, right) fractions of the Koongarra sediments by the HH extraction method.

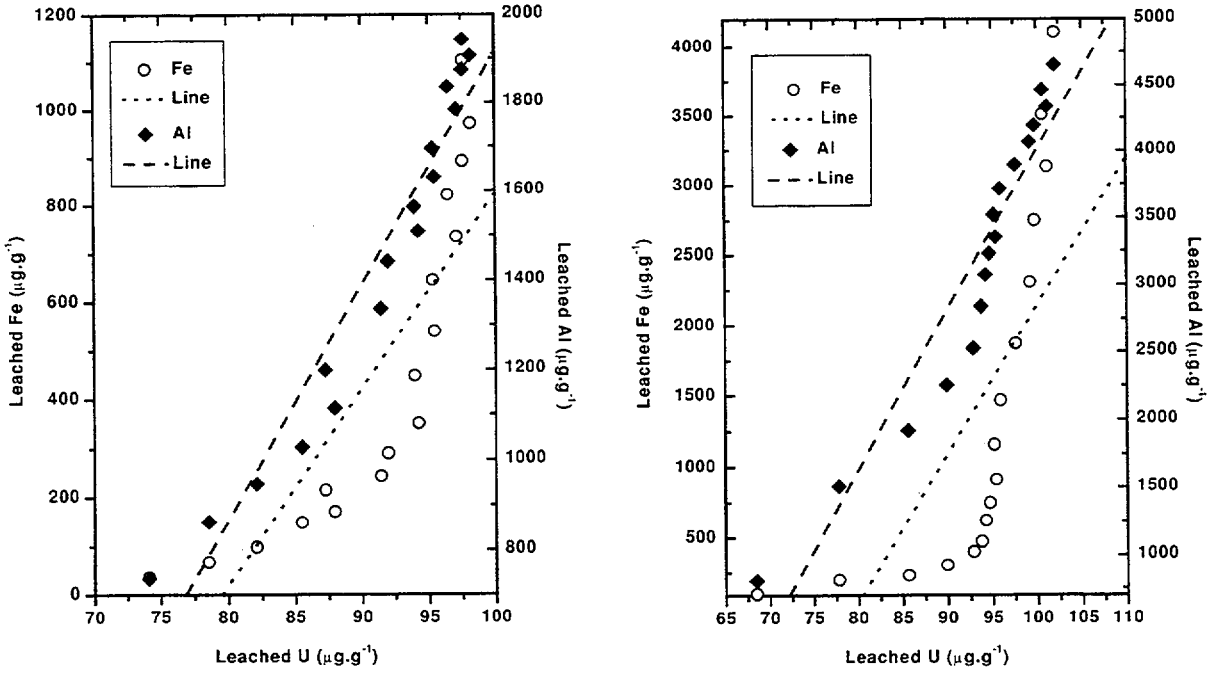

Figure 10-15. Dual linear regression plots of Fe vs. U & Al vs. U extracted by the HH extraction method on the <25µm (left) and 250-1000µm (right) fractions of the Koongarra sediments.

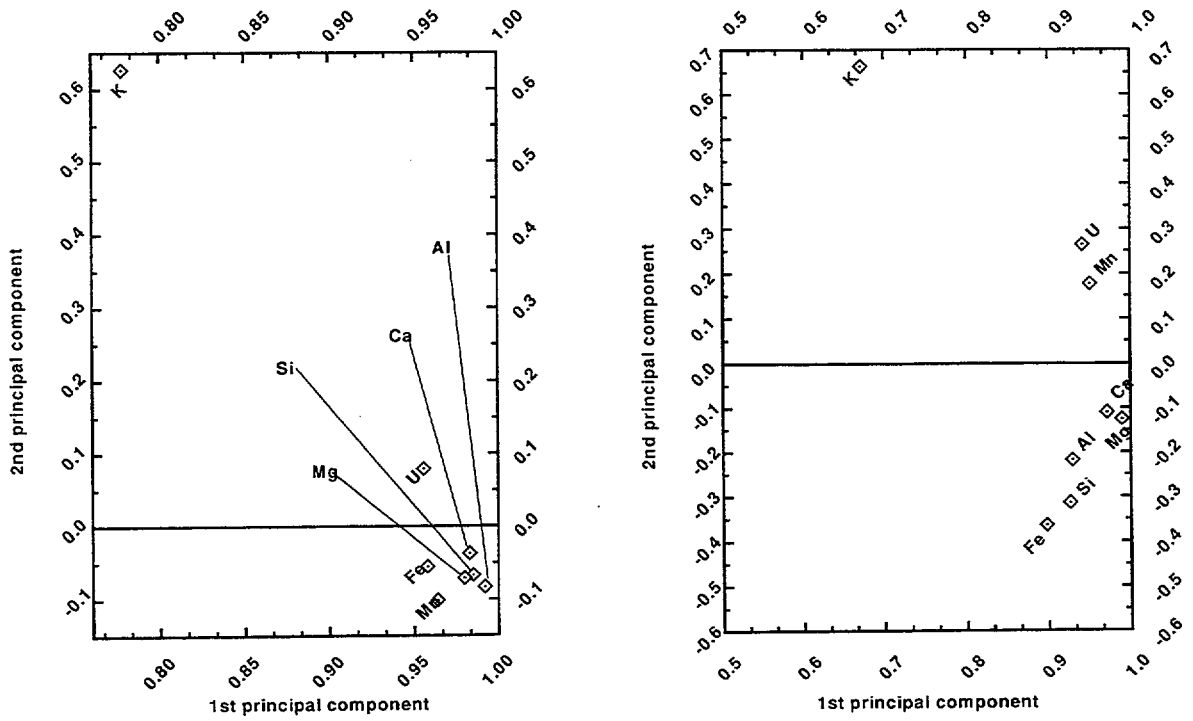

Figure 10-16. Multivariate principal component analysis of cation release from the Koongarra sediments in HH extractions (left, <25μm fraction; right, 250-1000μm fraction).

of Al dissolved, 60 mg/kg and 78 mg/kg from the fine and coarse fractions, respectively. >80% of the final Al concentration was dissolved at t=2 min. during extraction of both particle size fractions. Such a rapid release suggests that the Al is derived from exchange sites rather than dissolution of surface coatings. The total concentrations of Al released by Morgan's reagent was equal to approximately 1.5% and 0.5% of the total Al dissolved by the 4M HCl extraction of the fine and coarse fractions, respectively.

While insignificant amounts of Fe or Al were released during the extraction, 72 mg/kg and 60 mg/kg U were released from the <25 μm and 250-1000 μm fractions, respectively. These concentrations represent about 48% and 38% of the total U released by the 4M HCl extraction of the fine and coarse fractions, respectively. Although the classical interpretation of these results would suggest that the U released was bound either to ion exchange sites or associated with carbonate phases, it is highly likely that the U was released by partial desorption from Fe and Al oxide phases. U released during the first 8 min. of the extraction was 70% and 78% of the final U released by the extraction (from the <25 μm and 250-1000 μm fractions, respectively). U release was complete after 30 min. of extraction.

10.2.6 CONCLUSIONS FROM EXTRACTION STUDIES

Most studies of elements dissolved during selective extractions have been conducted for fixed periods of time. The kinetic approach used in this study enabled more incisive assessment of the extractants in terms of selectivity and elemental associations within the systems studied. The results show that U was strongly associated with both crystalline and amorphous Fe oxide phases. However, a significant relationship between U and Al was also identified, with a large fraction of the total U apparently bound in readily solubilized surface coatings rich in aluminium. U was released very quickly during the extractions with concomitant dissolution of Al.

It was also observed that U associated with the sediment (normalized per unit mass) was

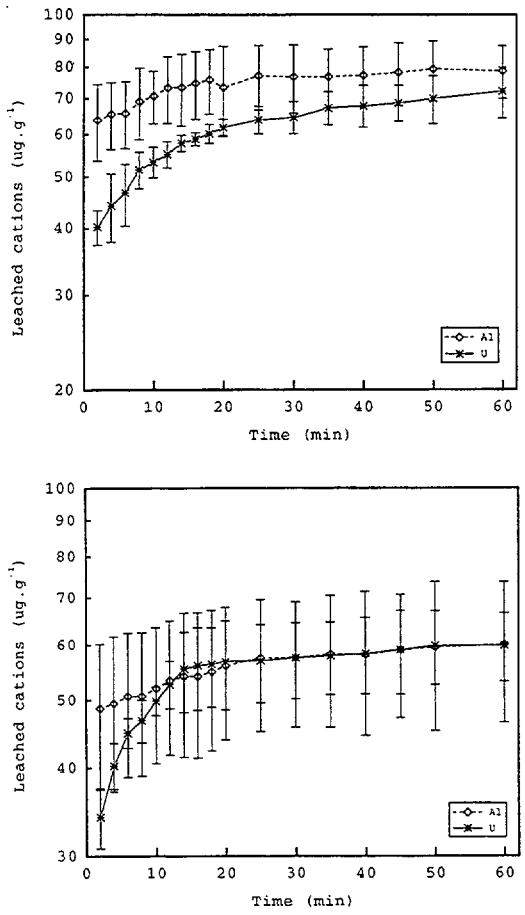

Figure 10-17. Mass normalized concentrations of U & Al released from the Koongarra sediments by MOR extractions (left, <25μm fraction; right, 250-1000μm fraction).

unrelated to particle size. This result suggests that porous surface coatings may be more important in U(VI) adsorption than the underlying bulk mineral phase.

Previous investigations have attempted to model the adsorption and transport of U(VI) using a single adsorbing phase, such as ferrihydrite. The results of this study suggest that other mineral phases may play an important role in the uptake of U(VI) and should be considered when developing an SCM to describe the adsorption and transport of radionuclides. An understanding of the nature and significance of (porous) surface layers is required to develop more accurate SCM models.

10.3 Surface Analysis

Two methods were used to investigate the surface chemistry of the Koongarra sediment material, Analytical Transmission Electron Microscopy (AEM), and Secondary Ion Mass Spectroscopy (SIMS). The objective of this work was to observe relationships between elements at or near the sediment surface.

10.3.1 ANALYTICAL TRANSMISSION ELECTRON MICROSCOPY

10.3.1.1 Experimental

Samples were prepared for AEM by collecting a drop of each liquid suspension and allowing them to dry on holey-carbon filmed, 3 mm copper grids. Individual particles of each sample were examined in a JEOL 2000FX transmission electron microscope operated at 200 keV using a low background, analytical sample holder. Spectra were collected using a hybrid Tracor-Northern Si(Li) EDS equipped with a standard 7.6 μm beryllium window interfaced to a Link ISIS microanalyzer. Analyses were acquired using spot size 5L in TEM mode (minimum probe size ~ 20nm) from thin regions of each particle for approximately 10-15 minutes. Variations in sample thickness were minimized by maintaining a current density of approximately 2-3 pA/cm^2 from point to point. Fluctuations in the energy resolution of the system were minimized by using a strict set of operating conditions, including beam current (120 μA), dead time (~ 20 %), and output count rate (500-700 cps). The system was calibrated using a spectrum collected from the edge of a Cu grid bar generally after every third or fourth analysis.

Peak counts, associated errors, and concentrations for up to 15 elements were calculated using the Link ISIS software package TEMQuant which employs a digital top hat filter to suppress background and a multiple least square fitting procedure for the determination of peak counts. Throughout this work, we used a library of reference spectra for peak fitting that were collected under conditions similar to those

used for the analyses. In this investigation, k-factors for Na, Mg, Al, Si, P, K, Ca, Ti, V, Cr, Mn, Fe, Zr, and U were determined experimentally from a collection of natural and synthetic reference samples. Due to the long counting times, use of low background sample holders, and relatively low mean atomic number of the samples (low backscattering cross-section), estimated detection limits range from ~ 0.1 wt% for Na, Zr, and U down to ~ 0.05 wt% for the transition metals.

Bright field images were taken at magnifications of 5,000-50,000X for routine work and up to 210,000X for detailed investigation of microstructures. Selected area diffraction patterns were taken to aid in phase identification. After setting the automatic exposure reading to 2.0 seconds at a magnification of 50,000X, the diffraction patterns were photographed at exposures of one and two seconds using a camera constant of 92 cm, calibrated using a Au standard.
A series of experiments was performed using this technique. Each experiment utilized the same <25μm fraction of Koongarra sediment, with varying concentrations of total U^{238} added. The equilibrium adsorption data relevant to each of the 6 experiments is shown in Table 10.1.

10.3.1.2 Results & Discussion

The results of the TEM analysis with the <25μm sediment fraction show the major elements present in the sample. By visually identifying some of the mineral phases present in the samples and then analyzing for the component ions, a clear indication of U(VI) partitioning between different minerals fractions could be established. However, by the nature of the analysis, that is, an electron beam passing through the sample, it is uncertain whether these mineral/uranium associations are surficial, incorporated into the crystal lattice of the mineral, or a combination of both processes.

The results of this work showed that in the fine fraction of the sediment, two disparate mineralogies were dominant; the clay minerals and the iron oxide minerals. Analytical TEM results for analyses performed on each of these components are presented and described below.

A. AEM analyses of the clay minerals present in the Koongarra sediments

Diffraction data obtained from analysis of a large number of clay samples show that the clays can be subdivided further into either Mg or K rich minerals, with the high Mg content defined as montmorillonites and the high K materials defined as illites. In producing spectra from these minerals, it was decided that in order to assess the adsorptive properties with respect to U(VI), only analyses in which Fe peaks were small (<5% by weight) would be included. Ten clay analyses were obtained from each sample of the sediment. The bulk mineralogy of each sample was similar, with the only difference being the concentration of U(VI) added to the samples.

The results show that the composition of the clay minerals are approximately 20% Al, 25% Si and 50% O by weight. The remainder of the composition was determined to be trace concentrations of the alkali metal ions and the transition metals, Fe and Ti. For the analyses of Sample 1, to which no U(VI) was added, the concentrations of U associated with the clay minerals was below the detection limit. Similarly, for Sample 2, to which 0.057% U(VI) by weight was added, most analyses showed U concentrations below the analytical detection limit. However, three of the analyses showed detectable concentrations of U within the sample. These correlated with higher concentrations of Fe also associated with the clay mineral, either as thin coatings at the clay surface which were not visually identifiable, or incorporated into the crystal lattice of the mineral. Analysis of Sample 3, which had 0.48% wt. of U(VI) added, identified significant concentrations of U associated with the clay minerals. The U measured in this sample ranged from 0% to 0.94%, with an average of 0.20%(±0.27%). Analysis of an illite particle showed 0.94% U by elemental weight, representing a two-fold increase in the measured U to the added U. This analysis also showed that

Table 10-1. Description of samples analyzed by AEM

	U^{238} present (wt. %)	U^{238} present (wt. % UO_2^{2+})
Sample 1	0.010	0.011
Sample 2	0.057	0.061
Sample 3	0.180	0.192
Sample 4	0.480	0.512
Sample 5	0.800	0.854
Sample 6	2.200	2.350

this clay particle had the highest concentration (of 10 analyses) of Fe measured (6.08%). The final two samples analyzed had 0.80 and 2.20% U(VI) added by weight respectively. These samples however, were found to have much smaller quantities of U associated with both the clay and iron mineral phases, than that of Sample 3 in which only 0.48% U(VI) had been added.

In the sequence of samples, the first three showed no evidence of U(VI) precipitation. Sample 4, to which 0.80% by weight U(VI) was added, was found to contain extensive quantities of an electron opaque uranium mineral. Analyses of this mineral around edges thin enough to permit the passing of the 200keV beam showed that its bulk chemical composition was that of a pure oxide phase. Diffraction patterns obtained from the uranium precipitate had d-spacings which correspond closely to a dehydrated form of schoepite (paraschoepite). It is thus suggested, that for Samples 5 & 6, the solubility product of the paraschoepite was likely exceeded, and thus precipitation became the dominant mechanism of U(VI) removal from the aqueous phase.

B. AEM analyses of the iron minerals present in the Koongarra sediments

Analysis of the <25μm sediment showed large quantities of iron minerals. The iron minerals present in the samples were found either as crystalline agglomerates with a radiating dendritic habit, or as coatings on the surface of clay minerals. These coatings were similar agglomerations of bladed or dendritic crystals. Diffraction data taken from these iron minerals, showed d-spacings corresponding with database d-spacings for both ferrihydrite and goethite. As goethite is an aging product of ferrihydrite, it is probable that the iron in the system had precipitated as ferrihydrite and then aged to the more crystalline form of the oxyhydroxide. Bulk chemical analyses of numerous iron mineral particles show that they contained greater than 50% Fe by weight, with most of the remaining composition comprised of O. Small quantities of Al and Si were also detected, representing small contaminations by clay minerals.

The concentrations of U associated with these iron oxide minerals were found to be significantly greater than those observed with the clay minerals from the same samples. In addition, the standard deviation from the average U concentration measured for the 10 replicates was calculated to be much lower than similar values derived for U concentrations found associated with clay particles, reflecting a greater degree of chemical purity in the iron minerals. For Sample 1, to which no U(VI) had been added in laboratory adsorption experiments, the average U detected in the iron minerals was found to be 0.11% by weight. This represents an accumulation of U on these minerals an order of magnitude above the concentration of U(VI) that was adsorbed to the <25μm fraction, as determined by acid extraction and ICP-AES analysis (≈0.01%). The AEM analysis of Sample 2, which had a total of 0.057% U(VI) by weight added, showed the sample to contain an average of 0.52 (± 0.19%) U associated with the iron minerals. This, like the results presented for Sample 1, shows an

increase in the U concentration found associated with the iron minerals of approximately an order of magnitude above the total concentration of U(VI) added to the sample. This trend continued with samples 3&4, which were found to have average concentrations of 1.33 and 2.74% by weight U associated with analyzed iron oxide mineral particles. These results compare with 0.18% wt. U(VI) added to Sample 3 and 0.48% U(VI) added to Sample 4.

The final two samples analyzed (5&6), showed low concentrations of U associated with the iron minerals present, 0.53 and 0.89% wt. respectively, even though they had 0.80 and 2.20% by weight U(VI) added to them in the batch adsorption experiments. This coincides with the detection of uranium oxide minerals in the samples as described above. The increasing trend of U concentration measured for the iron oxide minerals present in the samples against the concentration of U(VI) added to the system for samples 1-4 are shown in Figure 10-18.

10.3.1.3 Conclusions from AEM Analysis

The results obtained from the AEM analysis show that the Koongarra sediments are comprised of two major mineral groups, clays and iron oxide minerals. The analysis identified both the bulk chemical compositions of these minerals by TEM-EDS analysis of the samples and their crystal structures from diffraction patterns produced by the TEM electron beam interacting with the crystal matrix of individual minerals. The sediment was found to contain the clay minerals, illite and montmorillonite, and the iron oxide minerals, goethite and ferrihydrite. The clay minerals were predominantly found as individual particles, with occasional thick cohesive agglomerations of particles. The occurrence of the iron minerals was as individual particles, thick (electron opaque at 200keV) coatings on the surfaces of clay minerals, and although not visually observed, thin coatings of secondary iron oxide minerals. The presence of thin coatings of iron oxyhydroxide coatings is supported by analyses

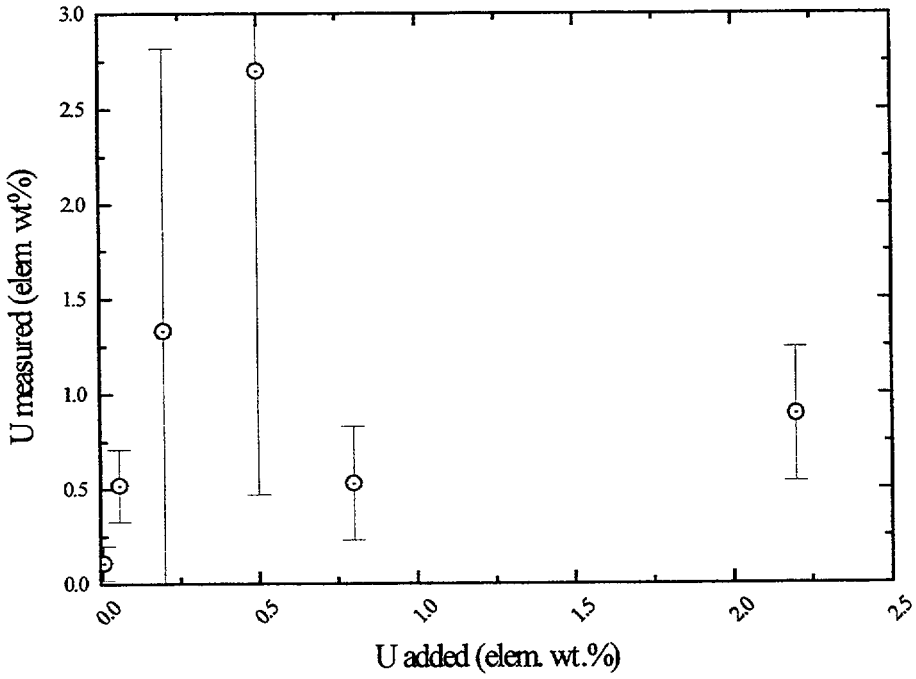

Figure 10-18. The mean concentration of U (element weight %) detected in iron minerals from the <25μm fraction of the Koongarra sediments, to which variable concentrations of U(VI) had been added in batch adsorption experiments. Error bars represent the range of U(VI) concentrations measured in the analysis of each sample.

of the clay minerals, which were typically found to contain traces of Fe in the spectra.

4*M* HCl extractions performed on the <25 μm fraction of the Koongarra sediment (as described in Section 10.2) showed that 6000 mg of Fe could be dissolved per kg of sediment. Assuming that a majority of the Fe is present in the amorphous form of the hydrous oxide (ferrihydrite: $Fe_2O_3.3H_2O$), this represents a total iron mineral content of about 11.48 g/kg, equating to a total of 1.15% of the sediment by weight, with the rest composed primarily of clay minerals.

The TEM-EDS analyses of the clay and iron minerals show that U was associated with both mineral phases. The concentration of U associated with the iron oxide minerals was found to average approximately an order of magnitude greater than that from added U(VI), until the addition was greater than approximately 0.50% U by weight.

On the other hand, the concentration of U associated with the clay minerals was below detection until a U(VI) concentration of 0.18% had been added. For the two samples measured in the range above the detection limit and below the precipitation threshold for paraschoepite, the concentration of U associated with the clay minerals averaged less than half the total of the U(VI) added to the system. Additionally, this average may be weighted by several anomalously high measurements taken from samples which contained high concentrations of Fe. This suggests that in these analyses, the U associated with the particles may have been adsorbed to a thin surface coating containing iron oxide.

It is thus apparent that a majority of the U(VI) added to the sediment binds to the several mineralogical phases of iron oxyhydroxides present. It is these phases which control the adsorption of U(VI) in the <25 μm fraction of the Koongarra sediment. Thus, in the context of modeling U(VI) adsorption, it is recommended that the total surface site concentration should be estimated from the total amount of Fe dissolved in TAO and DCB extractions.

10.3.2 SIMS CHARACTERIZATION

10.3.2.1 Experimental

SIMS, which analyzes only the first few atomic layers of a surface, was not able to directly observe U in the sediments, due to the poor detection limit for this element. The use of this technique however, proved invaluable in determining the nature of the surface environment of the Koongarra sediment.

Individual sediment grains were analyzed using a Kratos secondary ion mass spectrometer. A pulsed Ga^+ primary ion beam was used to sputter secondary ions into the mass spectrometer. Samples were mounted onto indium foil to reduce surface charging of the sample. Before mounting the samples were washed four times with milli-Q water and then particles were selected for analysis under 40x magnification using a reflected light optical microscope on the basis of the presence of visible iron stained surface coatings. The selected and mounted particles were typically 500-750μm in diameter and in cross section were found to have coatings of thicknesses up to 15μm. The samples were mounted onto the foil wet and loaded into the instrument where they were freeze dried before analysis. The samples were mapped over an area of between 1-4 μm^2 and analysis is constrained to only the near surface environment, *i.e.* 10-20 atomic layers. The elemental detection limit for analysis was generally less than 100 ppm, although this value was dependent on the ionization potential and molecular environment of each particular ion.

10.3.2.2 Results & Discussion

Surface analysis by SIMS on an untreated sample from the 250-1000μm fraction identified the major ions present (under vacuum conditions) in the surface environment of an accessory coating phase. Evident were quantities of Mg^{2+}, Al^{3+}, Si^{4+} and Fe^{3+}. Also resolved in

the spectra are a cluster of peaks in the 43-45 amu region (Figure 10-19). These were identified as the $Al(OH)^{2+}$ and $Si(OH)^{3+}$ species at 43.98 and 44.97 amu, respectively. While Fe was identified in the analysis, it would appear from the results that Al was more abundant and present in numerous mineralogical phases, at least in the near surface environment. The presence of significant amounts of Al in surface coatings supports the contention that phases other than those dominated by Fe may also be important in adsorption of U(VI). Analysis of the spectra in the region associated with the U^{238} ion revealed no peaks, presumably due to the relatively low concentration of U present and the relatively high detection limit for the element.

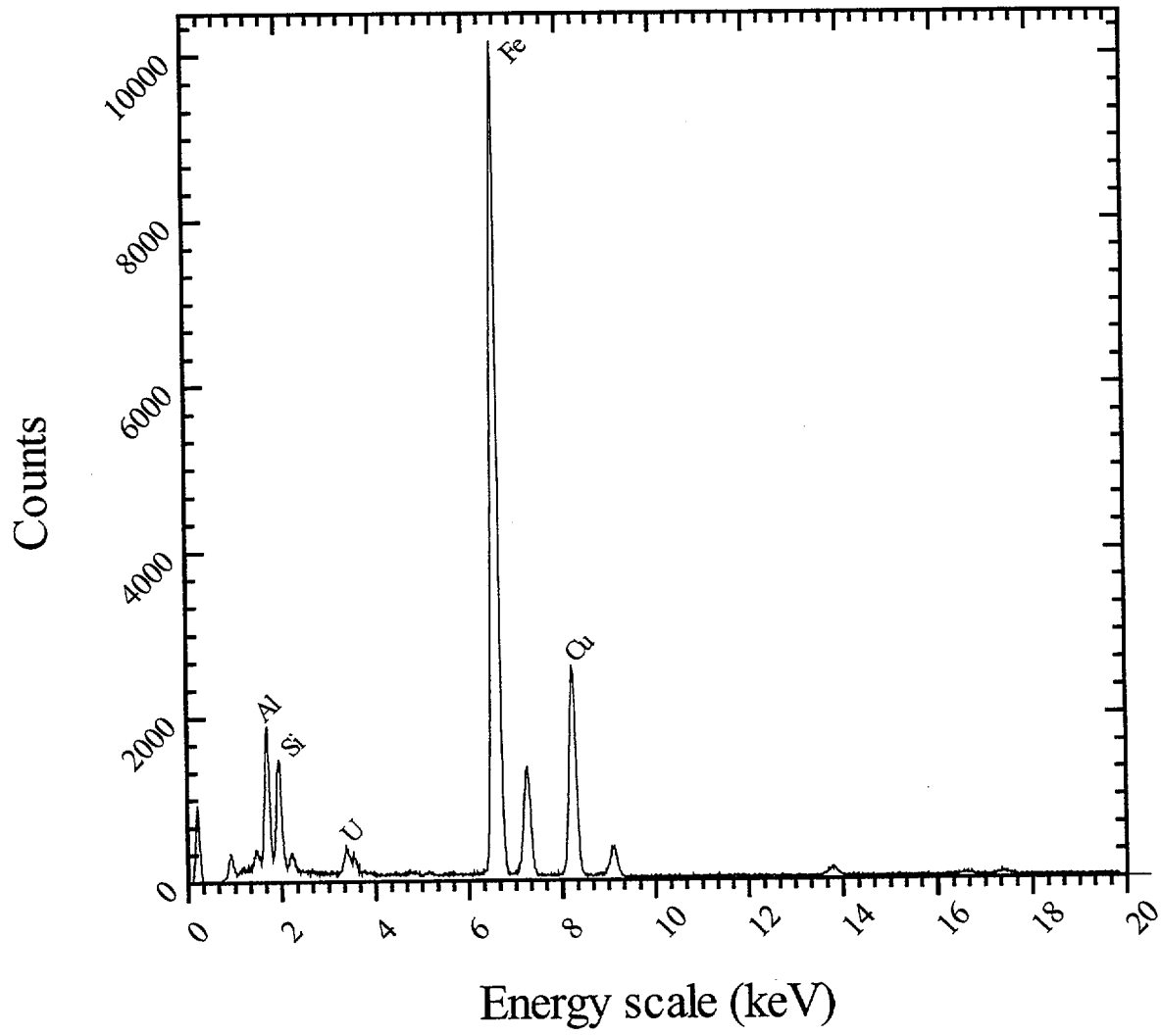

Figure 10-19. EDS spectra obtained from TEM analysis of a thin area of an Fe-O-H mineral phase from the <25μm fraction of the Koongarra sediments, showing a well resolved U-M series profile. U(VI) added to the sediments was 0.48% by weight.

11 COMPARISON OF "IN-SITU DISTRIBUTION COEFFICIENTS" WITH EXPERIMENTAL R_D VALUES FOR URANIUM(VI) IN THE KOONGARRA WEATHERED ZONE

11.1 Introduction

In Sections 12 through 16 of this report, the surface complexation approach is used to model U(VI) adsorption on various mineral phases. This permits quantitative modeling of U(VI) adsorption under a wide range of conditions, and the inclusion of multiple adsorption sites enables the simulation of non-linear adsorption isotherms. Thus, the surface complexation model allows complex adsorption phenomena to be modeled in a mechanistic fashion. However, in transport simulations, simpler models employing distribution coefficients ('K_d values') are often used to describe the partitioning of radionuclides between solid and liquid phases. These use the simple linear isotherm to describe adsorption. That is, the adsorption density of a solute (Γ) is assumed to be proportional to its dissolved concentration ([J]):

$$\Gamma = K_d[J] \qquad (11\text{-}1)$$

K_d values may be estimated from the results of adsorption experiments, which should preferably be carried out under conditions that closely simulate the natural environment. However, there are usually substantial differences between laboratory and field conditions, and the timescales, spatial extent, and complexity of environmental phenomena cannot be replicated in the laboratory. Thus, the applicability of laboratory data has been questioned, and it has been suggested that field measurements ('in-situ distribution coefficients') may provide a more accurate indication of 'true' partitioning coefficients [Ivanovich, 1991].

The subject of this section is the relationship between estimates of the numerical value of K_d for U(VI) obtained from experimental and field data at Koongarra. We therefore examine U(VI) partitioning data from laboratory experiments, and compare these with 'in-situ' measurements of U(VI) partitioning.

11.2 Terminology

The term K_d implies adsorption equilibrium, which may not be achieved in laboratory experiments [Erdal et al., 1980]. Therefore, we express the results of laboratory adsorption experiments by the term R_d, which is calculated:

$$R_d = \frac{\text{radionuclide adsorbed on solid phase (μmol/g)}}{\text{radionuclide concentration in aqueous phase (μmol/mL)}} \qquad (11\text{-}2)$$

The units of R_d are mL/g. Precipitates should be absent in the determination of R_d.

A similar expression has been used to calculate radionuclide partitioning in the field, with the resulting quantity being described by the term 'in-situ distribution coefficient' (in-situ K_d). It is preferable to use the term partition ratio (P), because K_d implies fast, reversible, linear adsorption [McKinley and Alexander, 1992], which is typically not the only process controlling field partitioning. In this section we consider two possible P values. The first of these (P_{tot}) relates the total radionuclide contents of solid and liquid phases:

$$P_{tot} = \frac{\text{total radionuclide on solid phase (μmol/g)}}{\text{total radionuclide concentration in aqueous phase (μmol/mL)}} \qquad (11\text{-}3)$$

The numerical value of P_{tot} may be quite different to K_d , because the solid phase may include precipitates, as well as occluded or 'inaccessible' radionuclides. In addition, the aqueous phase may include colloids. Consequently we define an 'accessible' partitioning term:

$$P_{acc} = \frac{\text{radionuclide adsorbed in accessible phases of solid (μmol/g)}}{\text{radionuclide dissolved in aqueous phase (μmol/mL)}} \qquad (11\text{-}4)$$

The term 'accessible' implies adsorbed phases which are available for adsorption interactions with the groundwater. Note that Equation 11-4 contains only dissolved radionuclide in the denominator (i.e. colloids are excluded).

A large number of laboratory and field techniques have been used to measure partitioning coefficients. It is therefore of value to investigate the relationship between R_d, P_{tot} and P_{acc} values. In interpreting the data presented in this section, it must be remembered that the adsorption isotherm may not be linear (i.e. K_d may vary with concentration). This may lead to inconsistencies between partitioning data obtained from different techniques, even if adsorption is the only process involved.

11.3 Methods

11.3.1 SOLID PHASE BULK SAMPLES AND GROUNDWATER ANALYSES

The data analysis in this section is based on analytical and experimental data which were collated and summarised during the Alligator Rivers Analogue Project [Waite et al., 1994a]. The solid phase samples were collected during the exploration of the Koongarra deposit, and in subsequent scientific studies of the site. The total U content of Koongarra sediments (U_{tot}) was measured either by solid phase analyses (such as proton induced x-ray and gamma-ray emission), or chemical dissolution followed by solution phase analysis (α-spectrometry and inductively coupled plasma mass-spectrometry) [Edis et al., 1994].

The Koongarra groundwater U(VI) data were obtained by α-spectrometry, kinetic phosphorescence analysis and inductively coupled plasma mass-spectrometry [Payne et al., 1994]. Generally these data were obtained after filtration through a 1 μm or 0.45 μm membrane. It has been established that colloidal transport of U(VI) associated with particles between 10 nm and 1 μm is not significant in the Koongarra system [Payne et al., 1994]. Thus, we are able to exclude the presence of colloids when calculating P values.

11.3.2 SIZE-FRACTIONATED SOLID SAMPLES

Cores were obtained from the Koongarra weathered zone using a cable-tool rig, which produces intact samples. Samples were from borehole W2 (14.0-14.2 m depth) and W1 (13.0-13.2 m). These materials are highly weathered schists with a mineralogy dominated by clay minerals (predominantly kaolinite) and Fe-oxides including goethite, hematite, and ferrihydrite [Waite et al., 1994a].

For the partitioning estimates and adsorption experiments with these samples, the size fraction below 10 μm was separated by wet-sieving followed by sedimentation [Waite et al., 1994a]. The resulting slurry contained a suspension of fine particles which could be reproducibly sub-sampled by vigorous agitation, followed by removal of an aliquot of known volume.

11.3.3 LABORATORY U(VI) ADSORPTION/ISOTOPE EXCHANGE EXPERIMENTS

The experimental techniques for adsorption experiments were similar to those described elsewhere in this volume for other mineral phases. Aliquots of slurry were transferred to 25 mL polypropylene centrifuge tubes, which had a 2mm hole in the lid to permit equilibration with air. Experiments were carried out in 0.1 M $NaNO_3$. For studies at pH > 7.0, $NaHCO_3$ was added, to ensure equilibrium with the CO_2 in air at the experimental pH. The pH of the slurry was adjusted to the experimental value, and the tube was shaken for 24 hours in a water bath at 25°C. At this stage, ^{236}U (10^{-7} M) was added to the aqueous phase and the pH readjusted. After 48 hours of equilibration, the solid and liquid phases were separated by centrifugation at >6500 g. ^{232}U tracer was added to the supernatant and the activities of ^{238}U, ^{236}U and ^{234}U were measured by α-spectrometry. The solid / liquid ratios were 500 mg / 25 mL for W1 and 100 mg / 25 mL for the W2 sample. The higher ratio for W1 sample (which had a lower accessible ^{238}U content) ensured that accurate information on ^{238}U desorption could be obtained. This enabled the estimation of

accessible U(VI) content by isotope exchange techniques.

Some experiments were performed in a glove box with an elevated partial pressure of carbon dioxide. This simulated the pCO_2 in Koongarra groundwaters, which is about 10^{-2} atm [Payne et al., 1994], whereas that of air is $10^{-3.5}$ atm. A mixture of 2% CO_2 and 98% N_2 was obtained, and the gas used in the glovebox was a 50:50 mixture of this gas with ordinary air. The gas composition was approximately 1% CO_2:10% O_2:89% N_2.

11.3.4 ESTIMATION OF P_{ACC}

As noted above, P_{acc} (unlike P_{tot}) requires an estimate of accessible U(VI) (U_{acc}). One way to provide this estimate is to use a chemical extraction with Tamm's acid oxalate (TAO) [Yanase et al., 1991]. TAO is a mild leaching agent which extracts U(VI) which is adsorbed or incorporated in relatively soluble phases such as amorphous iron oxides. The $^{234}U/^{238}U$ ratio in the TAO extract was generally the same as the ratio in Koongarra groundwater within experimental error [Yanase et al., 1991; Lowson et al., 1986]. This is a necessary, but not sufficient, condition to establish that the extracted U(VI) is in adsorption equilibrium with the groundwater [McKinley and Alexander, 1992].

The isotope exchange data from the adsorption experiments were used to determine the validity of the TAO estimate of U_{acc}. During the experiments, isotope exchange occurs between ^{238}U in accessible phases of the solid and ^{236}U in the aqueous phase. It has been previously shown that the labile pool of adsorbed U(VI) in Koongarra samples estimated by this means is similar to the TAO-extractable U [Payne and Waite, 1991].

11.4 Results and Discussion

11.4.1 BULK *IN-SITU* P VALUES (P_{TOT})

A plot of total ^{238}U concentrations in Koongarra cores against groundwater data from the same borehole at similar depths (Fig. 11-1) indicates a general relationship. However, the scatter indicates that there will be a range of P_{tot} values arising from the inhomogeneous distribution of U in the solid phase and the variability of dissolved U(VI) concentrations.

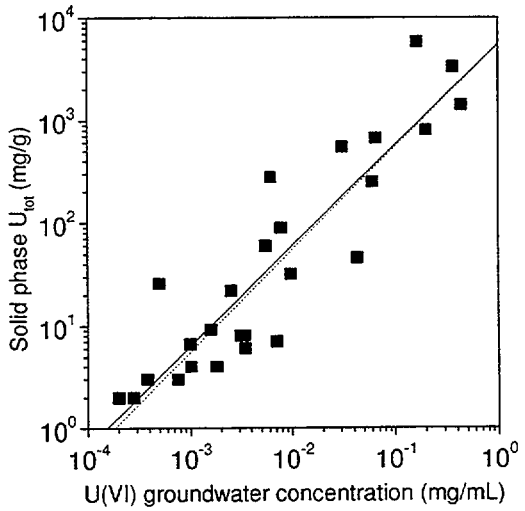

Figure 11-1. Relationship between U concentrations in Koongarra sediments and contacting groundwaters. The solid line is the least squares best fit of the data points. The dotted line is calculated for P_{tot} = 5500 mL/g, assuming a linear relationship with $U_{tot} = P_{tot}$ $(U(VI)_{gwater})$.

The dataset used to calculate values of P_{tot} for the bulk rock samples and associated groundwaters is given in Table 11-1. These values range from about 1000 to 60,000 mL/g. If a P_{tot} of 5500 mL/g and a linear relationship between U_{tot} and the concentration of U(VI) in the groundwater is assumed, a reasonable description of the data can be obtained (Figure 11-1). This does not imply, however, that the U(VI) distribution is a consequence of linear adsorption processes. In general, the considerable scatter of the data prevents the description of the data with a linear adsorption isotherm or any other mathematical model.

The concentration of ^{238}U in the fine particle fractions of the Koongarra W1 and W2 samples was then compared with concentrations in corresponding water samples. The water sampling points were sampled on several occasions, and a range of U(VI) concentrations

Table 11-1. Calculation of P_{tot} from the ratio of total U concentration in bulk rock samples to the U(VI) concentration in groundwater

Borehole (depth)	Bulk Rock U_{tot} (μg/g)	Groundwater $U(VI)_{gwater}$ (μg/L)	P_{tot} (mL/g)
PH14 (20-26 m)	548	30.8	1.8×10^4
PH14 (20-22 m)	670	65.2	1.0×10^4
PH49 (28-30 m)	5865	165.6	3.5×10^4
PH49 (44-46 m)	809	199.6	4.0×10^3
PH55 (26-28 m)	26	0.50	5.8×10^4
PH55 (40-42 m)	4	1.02	3.9×10^3
PH56 (26-28 m)	32	9.69	3.3×10^3
PH56 (43-45 m)	7	7.09	9.9×10^2
PH58 (25-27 m)	4	1.82	2.2×10^3
PH58 (38-40 m)	3	0.76	3.9×10^3
PH61 (26-28 m)	8	3.44	2.3×10^3
PH61 (43-45 m)	6	3.47	1.7×10^3
PH80 (17-20 m)	69	7.8	1.1×10^4
PH88 (28-30 m)	22	2.52	8.7×10^3
PH88 (38-40 m)	8	3.14	2.5×10^3
PH94 (26-28 m)	2	0.20	1.0×10^4
PH94 (40-42 m)	3	0.38	7.9×10^3
PH96 (16-26 m)	2	0.28	7.1×10^3
W1 (13 m)	278	6.2	4.5×10^4
W1 (24 m)	250	60.4	4.1×10^3
W2 (14 m)	426	43.3	9.8×10^3
W3 (14 m)	60	5.5	1.1×10^4
W3 (24 m)	9.2	1.60	5.8×10^3
W4 (14m)	1418	441	3.2×10^3
W4 (24 m)	3330	367	9.0×10^3
W7 (13 m)	6.6	1.0	6.7×10^3

have been measured [Payne et al., 1994]. This variation leads to a range of calculated P_{tot} (Table 11-2). In general, P_{tot} values for the fine fractions (5100 - 110,000 mL/g) are slightly higher than the bulk rock values (Table 11-1). Although there is only a small amount of data, this would be consistent with the higher specific surface area of the smaller particles.

11.4.2 DETERMINATION OF P_{ACC}

As noted above, U_{tot} includes inaccessible U, which means that P_{tot} is a poor indicator of partitioning by adsorption processes. Thus, P_{acc} (Equation 11-4) should be more relevant to U(VI) adsorption in the system. Values of P_{acc} were calculated using the estimate of U_{acc} from the TAO extraction of samples W1 and W2 (Table 11-2). (It was shown in Section 9 that the TAO extraction provides a similar estimate of labile U(VI) to that obtained from analysis of the isotope exchange data. This is discussed further below).

As expected, the value of P_{acc} tends to be somewhat lower than P_{tot}, and P_{acc} probably more closely represents the partitioning of adsorbed U(VI). The value of P_{tot} is certainly higher than the 'real' adsorption K_d. Clearly, the inappropriate substitution of P_{tot} for K_d in a transport code will lead to underpredictions of radionuclide mobility.

The use of an extraction to estimate U_{acc} is questionable, due to the operationally-defined nature of chemical extraction techniques. Therefore, we used isotope exchange data from the adsorption experiments to assess the extraction estimate of U_{acc}. This approach is based on the observation that added tracer (^{236}U) in the aqueous phase reached isotopic exchange equilibrium with U_{acc} (rather than U_{tot}) during adsorption experiments [Payne and Waite, 1991].

The amounts of both ^{238}U and ^{236}U in the aqueous phase in the adsorption experiments varied depending on the chemical conditions. A plot of natural ^{238}U leached from the solid against the percentage of added ^{236}U in solution at equilibrium (Figure 11-2) gives an indication of the amount of ^{238}U taking part in adsorption processes. The results can be compared with curves calculated on the basis that ^{236}U exchanges with U_{acc}, or alternatively, with U_{tot} (Figure 11-2). Clearly U_{acc} provides a better description of the data for the W1 and W2 samples. The estimation of U_{acc} by isotope exchange appears preferable to the extraction technique as no assumptions about the nature of extracted phases are required. The results of these studies confirm that P_{acc} is a better indicator of adsorption partitioning than P_{tot}, since U_{acc} is clearly significantly smaller than U_{tot}.

Table 11-2. Comparison of P_{tot} with P_{acc} (based on U_{acc} estimated by TAO extraction) for the fine particle fractions of samples from specified depths in boreholes W1 and W2

Borehole (depth)	U_{tot} (μg/g)	U_{acc} (μg/g)	$U(VI)_{gwater}$ (μg/L)	P_{tot} (mL/g)	P_{acc} (mL/g)
W1 (13.0-13.2 m)	356	43	3.2 - 8.8	4.0×10^4 to 1.1×10^5	4.9×10^3 to 1.4×10^4
W2 (14.0-14.2 m)	426	225	16.1 - 83.3	5.1×10^3 to 2.6×10^4	2.7×10^3 to 1.4×10^4

11.4.3 LABORATORY R_D VALUES

The R_d for U(VI) adsorption, calculated from the distribution of ^{236}U, varied over three orders of magnitude as a function of pH (Figure 11-3). The weak adsorption at high pH is due to the formation of strong aqueous uranyl carbonate complexes. The equilibrium K_d would have a similar pH dependence as R_d, and a single K_d value will therefore be insufficient to model the adsorption of radionuclides if they have strongly pH-dependent uptake curves. In general, the use of a constant K_d amounts to using a linear isotherm to describe adsorption, and ignores possible strong pH dependence as well as other chemical factors.

As noted above, the pCO_2 in Koongarra groundwaters is higher than that found in ordinary air. The computed R_d values for U(VI) adsorption experiments carried out with 1% pCO_2 are greatly reduced for pH values above 6.0, relative to experiments carried out in air (Figure 11-3). This is due to the greater dominance of uranyl carbonate complexes.

Figure 11-3 shows both the range of P_{tot} calculated for all Koongarra samples, and also the values of P_{acc} for the samples for which the U(VI) adsorption data were obtained. This allows a comparison of experimental and field distribution data. The hatched area in Figure 11-3 indicates the region in which experimental adsorption data obtained in the field pH range would be expected to fall if: a) U_{acc} accurately indicated the amount of U(VI) taking part in adsorption equilibria, and b) P_{acc} and R_d were the same in this pH range.

In general the agreement between P_{acc} and R_d is quite satisfactory in the field pH range of about 6.0 to 7.5.

Although the correspondence between experimental data and field data is not significantly improved in the experiments at higher pCO_2, the lower R_d values suggest that U(VI) adsorption experiments conducted at high pH in air-equilibrated conditions will tend to over-estimate R_d values for U. The results again

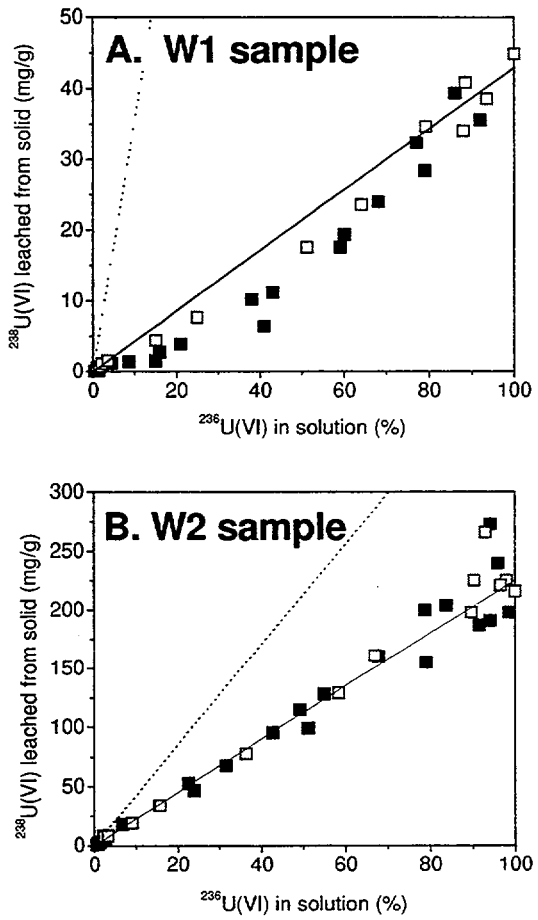

Figure 11-2. Isotope exchange data for W1 and W2 Koongarra sediment samples in laboratory adsorption experiments (μg ^{238}U(VI) leached/g sediment). Adsorption data obtained in air (filled squares) and 1% CO_2 (open squares). The solid line represents linear isotope exchange between ^{236}U(VI) in solution and U_{acc}, where U_{acc} is determined by TAO extraction. The dotted line represents linear isotope exchange between ^{236}U(VI) in solution and U_{tot}.

underline the importance of closely simulating field conditions in laboratory experiments.

While the correspondence between laboratory data and in-situ data (Figure 11-3) provides some support for both techniques, this is partly due to the use of the natural Koongarra samples in the laboratory experiments. Thus, the U(VI) content (and state of saturation of adsorption sites) in the experimental work may be similar to that in the field. Thus, some sources of

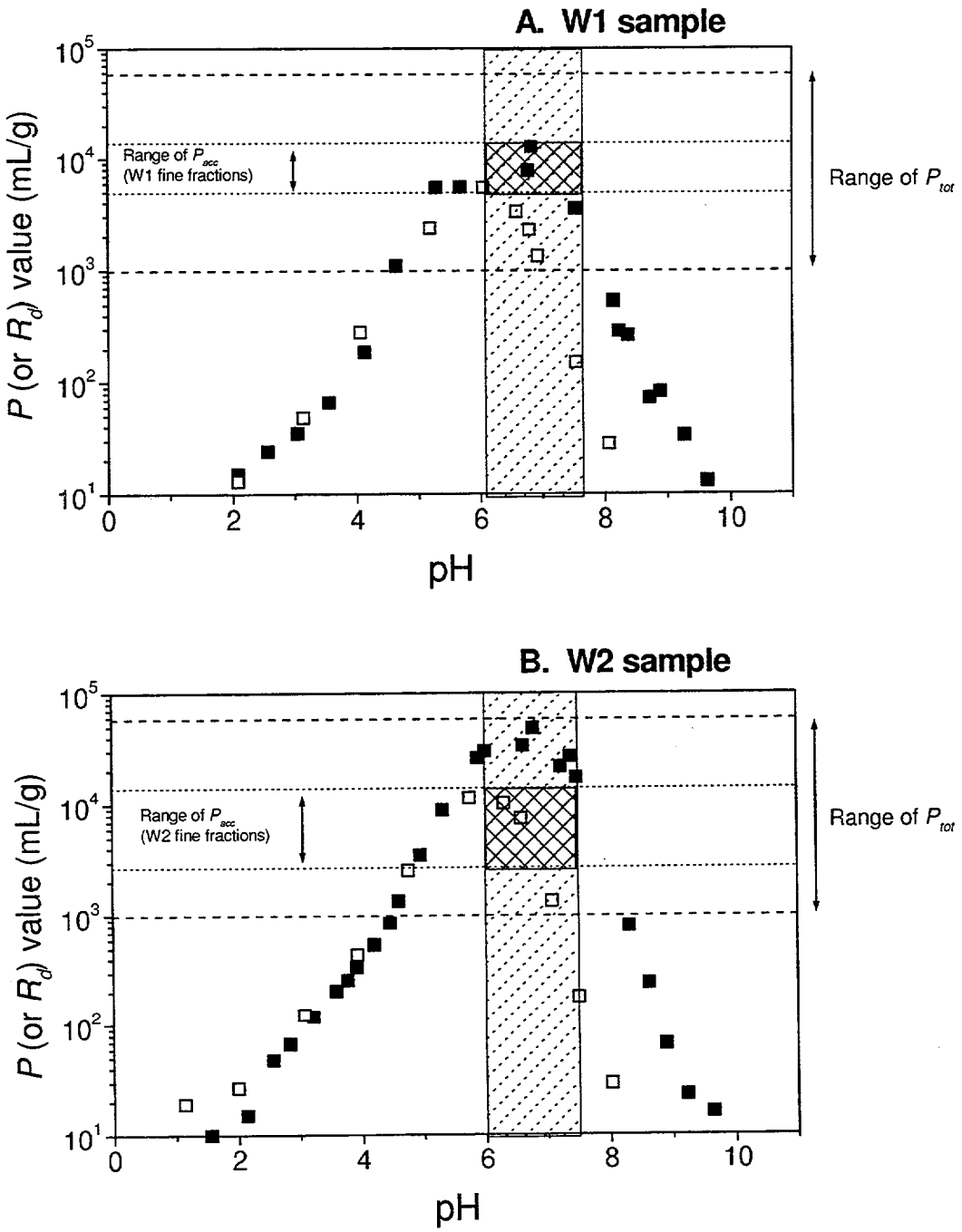

Figure 11-3. Comparison between field (P) and laboratory (R_d) partitioning of uranium. P_{tot} is calculated from the total uranium concentrations of Koongarra sediment and water samples. P_{acc} is constrained to the sample used in the adsorption experiments with W1 or W2 Koongarra sediment samples, and only considers U_{acc} in the calculation. Adsorption data obtained in air (filled squares) and 1% CO_2 (open squares). Note the lower R_d values at elevated pCO_2 for pH > 6. Shaded area indicates the Koongarra field site pH range. Hatched area indicates the region in which experimental adsorption data obtained in the field pH range would be expected to fall if U_{acc} accurately indicated the amount of U(VI) taking part in adsorption equilibria and P_{acc} and R_d were the same in this pH range.

variability have been reduced. However, many substantial differences exist between the field and laboratory conditions, including the background electrolyte and solid / liquid ratios.

As noted above, the similarity between field and laboratory data may be partly attributed to the similar occupancy of high and low-affinity sites in both cases. We carried out additional experiments in which U_T of 10^{-4} M was added to the system. This increased the labile U(VI) in the system by a factor of approximately 30, and probably resulted in saturation of the higher affinity sites. Consequently, the percentage of U(VI) adsorbed in this case was greatly decreased (Figure 11-4) resulting in lower R_d values. The maximum R_d value decreased by about an order of magnitude. This is consistent with the behaviour of reference mineral phases studied in the present work, where the percentage U(VI) adsorption was generally much lower when U(VI) present in the system is higher. For the purposes of performance assessment, it should be noted that this type of behaviour may invalidate the extrapolation of data obtained at tracer levels to higher concentrations, since in the latter cases much lower K_d values may occur, as has been demonstrated in this case for U.

11.5 Conclusions

Laboratory and field measurements may play a useful role in constraining the ranges of K_d values used to describe the partitioning of radionuclides between solid and liquid phases. A valid comparison between the two types of data can only be made when attention is restricted to adsorbed U(VI) (i.e. excluding precipitates or occluded phases) and species in true solution (i.e. excluding colloids). The correspondence between field and laboratory data improves when the pH values and partial pressures of CO_2 in laboratory experiments are similar to those found in the field. The non-linearity of the adsorption isotherm results in lower measured R_d values in systems containing greater amounts of U.

From the viewpoint of repository assessment it is encouraging that the field techniques and the laboratory measurements agree reasonably well in this case. However, the distinctions between P_{acc}, P_{tot}, R_d and the 'true' adsorption K_d must be clearly emphasized. None of the estimates of partitioning considered in this section yields quantities which can be uncritically substituted into transport equations as a K_d value. In particular, the inappropriate substitution of P_{tot} in transport equations in place of K_d could lead to results that are non-conservative (underestimate mobility). For the purpose of describing adsorption, P_{acc} is certainly preferable to P_{tot}, although the accessible radionuclide content may be difficult to estimate. In this study, isotope exchange data provided support for using a TAO extraction to estimate P_{acc}.

The results of this study suggest that with appropriate control of laboratory conditions and careful interpretation of field data, useful information about partitioning can be obtained from the techniques described herein. No matter how partitioning is estimated, it is clearly a function of many variables. Therefore, realistic partitioning information based on understanding of adsorption and its response to aqueous chemistry and geochemical considerations is required.

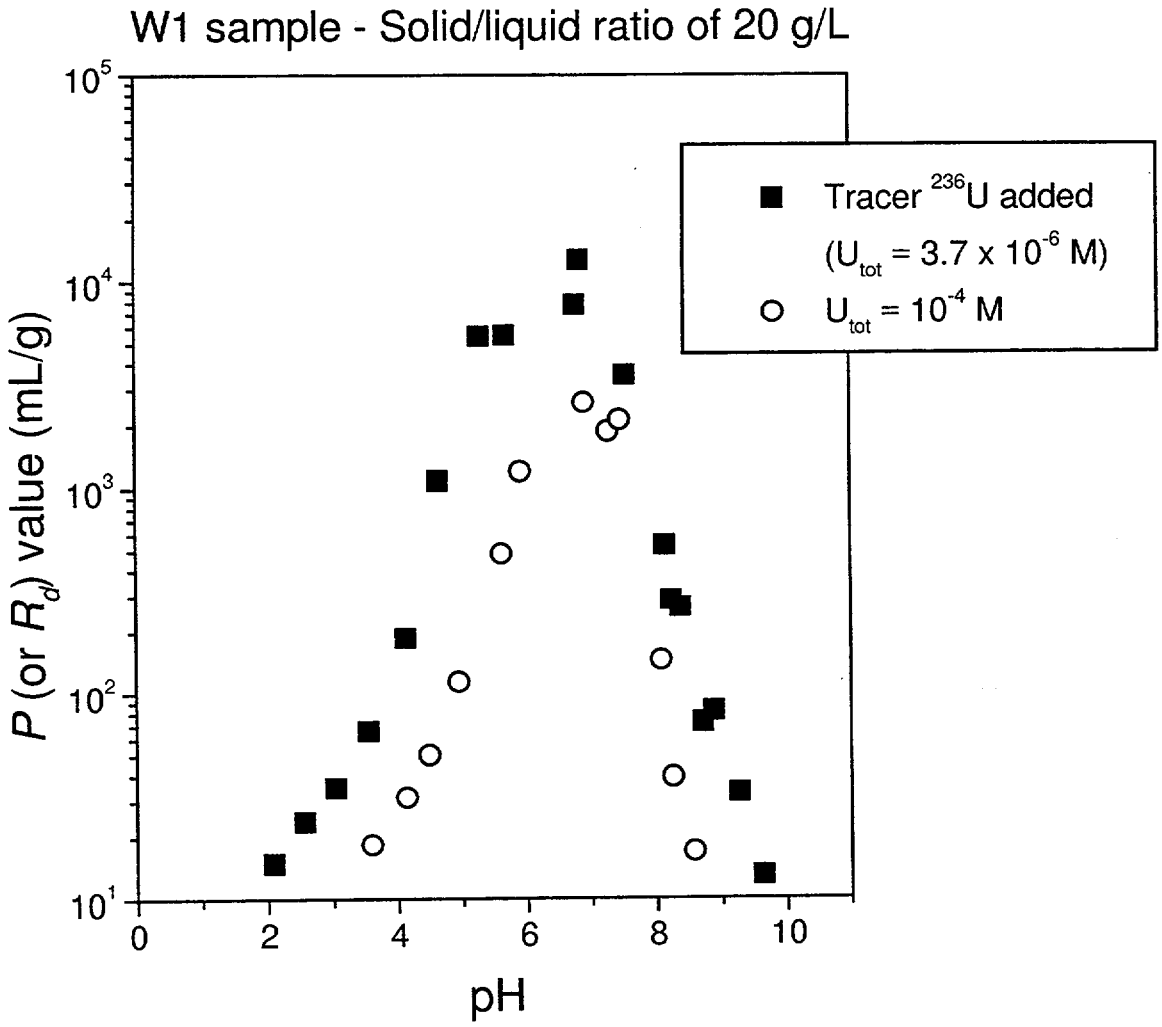

Figure 11-4. Experimental U(VI) adsorption data for systems with tracer U(VI) added (U_T of 3.7 μmol/L) and with U(VI) added to a total of 100 μM in the aqueous phase. Note the lower R_d values in the system with higher U_T.

12 SURFACE COMPLEXATION MODELING OF URANIUM(VI) ADSORPTION ON FERRIHYDRITE

In this section we present minor revisions in the surface complexation model previously developed for ferrihydrite by Waite et al. (1994b) and some testing of the sensitivity of the results to various parameters. Since the publication of Waite et al. (1994b), new thermodynamic constants have become available for certain aqueous U(VI) species. The thermodynamic constants used in this report (Table 2-1) that differ from that used by Waite et al. (1994b) are given in Table 12-1. In addition, some new U(VI) adsorption data were collected during the project, and these data were added to the entire dataset to better constrain the stability constants of U(VI) adsorption reactions in the surface complexation model.

First, the experimental data given in Waite el. (1994b) were refit using the current values for aqueous thermodynamic constants (Table 2-1) with the computer program FITEQL 3.1 (Herbelin and Westall, 1994). The results showed that the changes in thermodynamic constants for aqueous phase reactions shown in Table 12-1 had very little effect on the stability constants determined for U(VI) surface reactions or the fit to the experimental data.

Since publication of the Waite et al. (1994b) paper, additional U(VI) adsorption data were collected for the system with 10^{-3}M Fe as ferrihydrite, U_T of 10^{-5}M, and within the pH range 7-9.5. These data are reported in Section 4 and the additional data were added to the original dataset of Waite et al. (1994b). These data were expected to affect the values of the formation constants for the ternary uranyl-carbonate complexes.

The model parameters were reoptimized with the new data included and the new parameter values are given in Table 12-2. The fit of the model to the experimental data in the pH range 6.5-9 is given in Figure 12-1. Note that the fit to the data is relatively poor for the data with a U_T of 10^{-4}M. This was also the case for the model of Waite et al. (1994b). The data in the pH range 6.5-8 for the 10^{-4}M U_T system are very close to the solubility of schoepite, and any precipitation that occurred could create problems in fitting the data as an adsorption process only.

Table 12-1. Formation Constants for U(VI) Aqueous Phase Reactions

Reaction	log ß* (I = 0)[a)]	log ß* (I = 0)[b)]
$UO_2^{2+} + 2H_2O \Leftrightarrow UO_2(OH)_{2,aq} + 2H^+$	-11.50	-12.00
$2UO_2^{2+} + H_2O \Leftrightarrow (UO_2)_2OH^{3+} + H^+$	-2.70	-2.80
$UO_2^{2+} + CO_3^{2-} \Leftrightarrow UO_2CO_{3,aq}$	9.67	9.70
$UO_2^{2+} + 2CO_3^{2-} \Leftrightarrow UO_2(CO_3)_2^{2-}$	16.94	17.00
$UO_2^{2+} + 3CO_3^{2-} \Leftrightarrow UO_2(CO_3)_3^{4-}$	21.60	21.63
$2UO_2^{2+} + CO_3^{2-} + 3H_2O \Leftrightarrow (UO_2)_2CO_3(OH)_3^- + 3H^+$	-0.86	-1.18
$UO_2^{2+} + NO_3^- \Leftrightarrow UO_2NO_3^+$	0.3	Not considered

Footnotes:

a) Current thermodynamic constants, taken from Table 2-1.

b) Thermodynamic data used by Waite et al. (1994b).

Table 12.2 Formation Constants for U(VI) Surface Reactions on Ferrihydrite

Reaction	Log K (I=0.1)[a] Waite et al. (1994b)	Log K (I=0)[a] Waite et al. (1994b)	Log K (I=0)[b] This report
$(\equiv Fe_s(OH)_2) + UO_2^{2+} = (\equiv Fe_sO_2)UO_2 + 2H^+$	-2.57	-2.356	-2.341
$(\equiv Fe_w(OH)_2) + UO_2^{2+} = (\equiv Fe_wO_2)UO_2 + 2H^+$	-6.28	-6.066	-6.135
$(\equiv Fe_s(OH)_2) + UO_2^{2+} + CO_3^{2-} = (\equiv Fe_sO_2)UO_2CO_3^{2-} + 2H^+$	3.67	4.31	4.37
$(\equiv Fe_w(OH)_2) + UO_2^{2+} + CO_3^{2-} = (\equiv Fe_wO_2)UO_2CO_3^{2-} + 2H^+$	-0.42	0.22	-0.56

Footnotes:
a) Thermodynamic data for aqueous species from Waite et al. (1994b).
b) Current thermodynamic constants for aqueous species from Table 2-1.

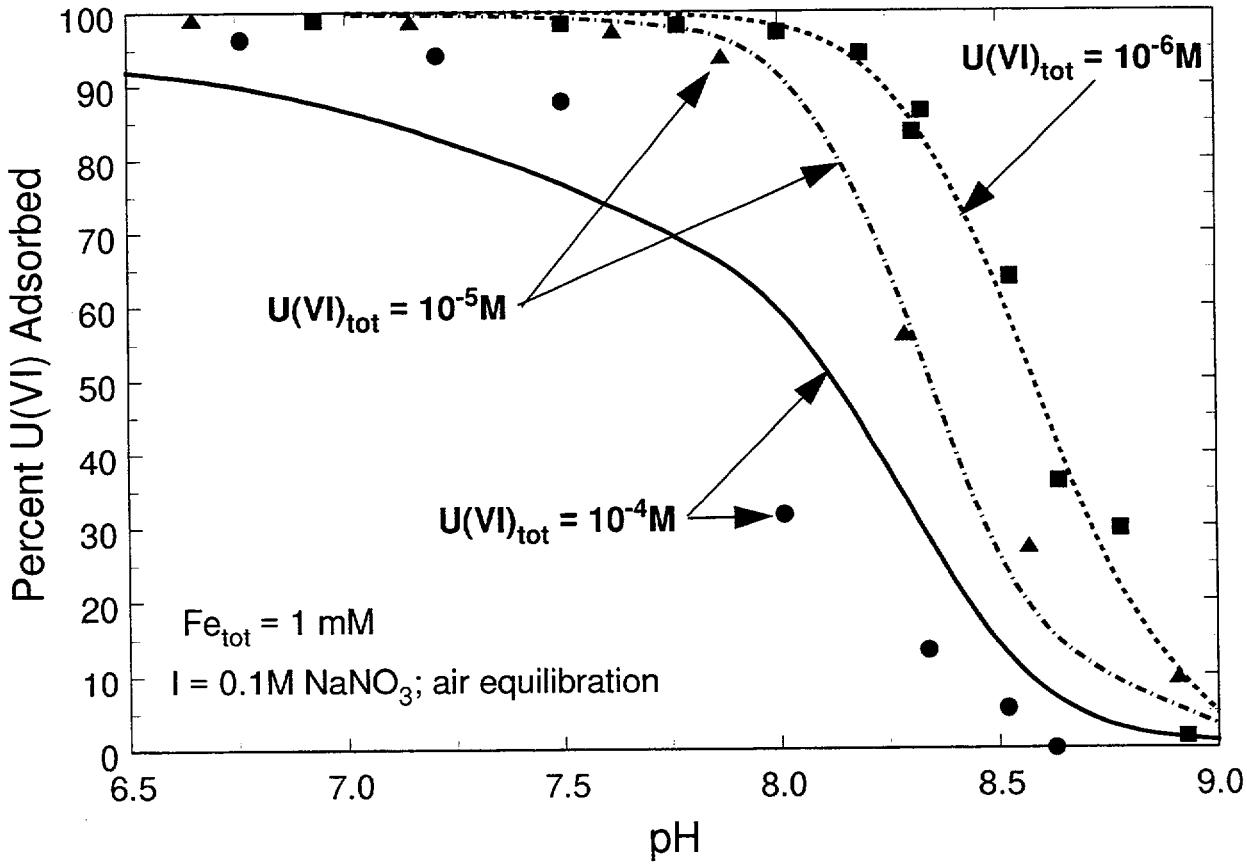

Figure 12-1. U(VI) adsorption by ferrihydrite as a function of pH and U_T concentration in 0.1M $NaNO_3$ solutions equilibrated with air. Curves are model simulations.

13 SURFACE COMPLEXATION MODELING OF URANIUM(VI) ADSORPTION ON QUARTZ

13.1 Introduction

In this section, a non-electrostatic (NE) surface complexation model is developed to describe the U(VI) adsorption data on quartz collected under the various conditions investigated, as described in Sections 5 and 8. The first step in the model development was to fit the data for U(VI) adsorption in the pH range 4 to 6 in the absence of added complexing ligands. The hypothesis is that the adsorption equilibria under these conditions are relatively simple and that the adsorption can be described by the reaction of the uranyl cation, UO_2^{2+}, with the surface hydroxyl groups on the quartz surface (Davis and Kent, 1990). After these data were fit, these equilibria were used to test whether simulations of the effects of ionic strength changes, higher pH values, and the presence of complexing ligands agree with experimental data. If significant disagreement occurred, modifications to the model were made to improve the goodness-of-fit with experimental data.

A goal of the model development was to keep the number of fit parameters to the minimum necessary to describe the main features of the U(VI) adsorption data. Included in this strategy was the objective of examining the performance of a model without electrical double layer correction to the adsorption equilibria. This type of model has been used with success in the generalized composite surface complexation modeling approach (see Section 1) when applied to aquifer sediments (Davis et al., 1998). If successful, the NE model simplifies the coupling of chemical reactions with transport, thus simplifying reactive transport modeling (Kohler et al., 1996). In addition, for the U(VI) adsorption data on quartz in the pH range 4 to 6, this approach is justified by the fact that quartz accumulates almost no surface charge under these conditions (Davis and Kent, 1990). For example, Schindler and Kamber (1968) reported that the acidity constant of silanol groups was approximately $10^{-6.8}$.

13.2 Model development

13.2.1 SITE DENSITY

Parameters for the NE surface complexation modeling approach are the surface site density, the site distribution (in case of a multisite model), and stoichiometries for the adsorption reactions and their formation constants. The adsorption equilibria are then included in the chemical equilibrium calculations with the formation constants of the aqueous complexes of all species involved (see Table 2-1).

The total surface site density was first estimated based on the batch adsorption data at the highest U_T concentrations of 10^{-4}M (for 100g/L) and 10^{-5}M (for 10g/L) as shown in Figure 5-8. These curves indicate a saturation corresponding to a surface site concentration near $3 \cdot 10^{-7}$ moles/g quartz. When normalized to surface area, this value is 0.54 sites/nm^2, which is considerably smaller than the "universal" recommended value of Davis and Kent (1990) of 2.31 sites/nm^2 and experimental measurements of site density, e.g. 5 sites/nm^2 (MacNaughton, 1973).

13.2.2 SURFACE REACTIONS

One-site and two-site NE models were tested for their ability to describe the U(VI) adsorption data on quartz as a function of pH and U(VI) concentration. A good fit to the data in the pH range 4-6 was obtained with a two-site model with only one reaction stoichiometry for each site, i.e.,

$$\equiv S_jOH + UO_2^{2+} + H_2O = \equiv S_jOUO_2OH + 2H^+ \quad (13\text{-}1)$$

where S_jOH represents a surface hydroxyl functional group, and the subscript j denotes the site type, each with a different binding affinity and surface site density. Note that the surface complexes are uncharged, which further justifies the use of the NE model in this case. The surface complexation formation constant is defined as,

$$K_j = (\equiv S_jOUO_2OH)(H^+)^2/(\equiv S_jOH)(UO_2^{2+}) \quad (13\text{-}2)$$

where the quantities in parenthesis denote the activity of each species. The activity coefficients of the surface species are assumed to be equal to one. The surface complexation formation constants for the one-site and two-site models were estimated with the nonlinear least squares optimization program, FITEQL [Herbelin and Westall, 1994], using the thermodynamic data for U(VI) given in Table 2-1, except that U(VI)-carbonate species were not included because of the pH range considered in the analysis of the adsorption data. (A few datapoints at low fractional uptake were omitted in the analysis because of large relative errors associated with these data points). Optimal site densities for each model formulation (Table 13-1) were determined from plots of site density vs. the goodness-of-fit of the model calculations to the U(VI) batch adsorption data. Note that these site densities corresponded well with the experimental measurements of highest U(VI) adsorption (Fig. 5-8).

13.2.3 MODELING RESULTS

Both the one-site (B1) and two-site (B2) models gave good fits to the adsorption data for systems containing 1 μM U_T, as shown in Figure 13-1. However, the two-site model produced a better fit to the data at variable U(VI) concentrations (Fig. 13-2). The one site model (B1) was not capable of reproducing the characteristic adsorption edges for different total U(VI) concentrations (Figure 13-3). This is not surprising since the isotherms were nonlinear (Figure 5-9). Model (B2) produced a good fit to the experimental data and captured all the main features and general trends of the adsorption edges, such as decreased adsorption with increasing total U(VI) concentration, flattening of the edges with increasing U(VI) concentration and saturation at a U_T of 10^{-4}M.

As will be described in detail in Section 18, model B2 was used to predict U(VI) transport through columns packed with quartz in eluants with pH ranging from 3.9 to 4.8. The

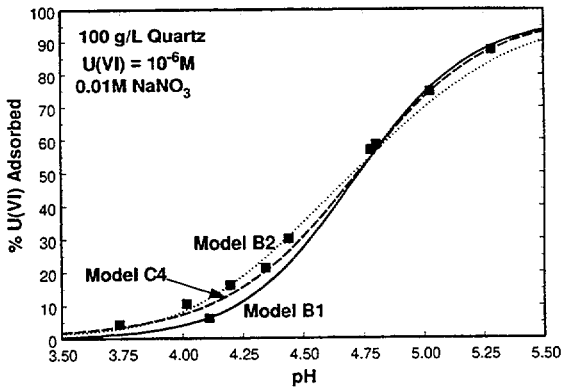

Figure 13-1. Calculated and experimental U(VI) adsorption on quartz as a function of pH in 0.01M $NaNO_3$ solution. Quartz = 100 g/L; U_T = 1 μM.

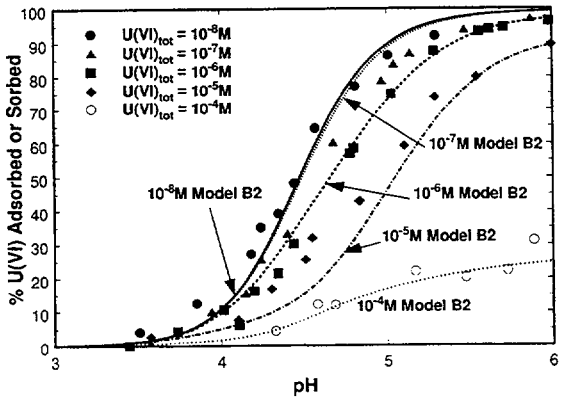

Figure 13-2. Calculated (two-site model B2) and experimental U(VI) adsorption on quartz as a function of pH and U_T concentration in 0.01M $NaNO_3$ solution. Quartz = 100 g/l.

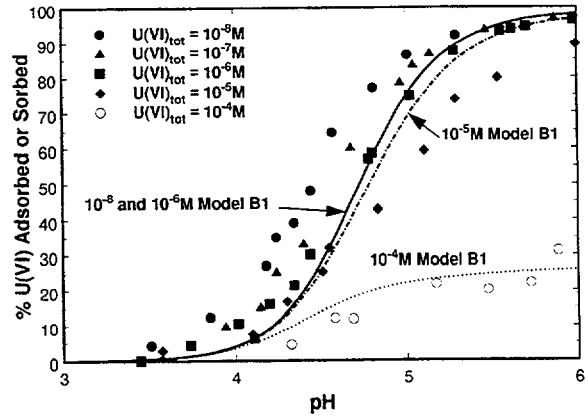

Figure 13-3. Calculated (one-site model B1) and experimental U(VI) adsorption on quartz as a function of pH and U_T concentration in 0.01M $NaNO_3$ solution. Quartz = 100 g/l.

Table 13-1: Surface Complexation Reactions and Model Parameters from Batch Adsorption Data

Model	Reactions	Log K[a]	f_i[b]
B1[c]	$S_1OH + UO_2^{2+} + H_2O = S_1OUO_2OH + 2H^+$	-4.64	1.00
B2[d]	$S_1OH + UO_2^{2+} + H_2O = S_1OUO_2OH + 2H^+$	-5.23	0.982
	$S_2OH + UO_2^{2+} + H_2O = S_2OUO_2OH + 2H^+$	-2.56	0.018
B3[e]	$S_1OH + UO_2^{2+} + H_2O = S_1OUO_2OH + 2H^+$	-4.95	0.988
	$S_2OH + UO_2^{2+} + H_2O = S_2OUO_2OH + 2H^+$	-3.19	0.012
	$S_1OH + UO_2^{2+} = S_1OUO_2^+ + H^+$	-0.03	0.988
	$S_2OH + UO_2^{2+} = S_2OUO_2^+ + H^+$	1.20	0.012
B4[f]	$S_1OH + UO_2^{2+} + H_2O = S_1OUO_2OH + 2H^+$	-5.28	0.982
	$S_2OH + UO_2^{2+} + H_2O = S_2OUO_2OH + 2H^+$	-2.56	0.018
	$S_1OH + UO_2^{2+} + H_2CO_3 = S_1OUO_2CO_3^- + 3H^+$	-6.50	0.982

Footnotes:

a) Apparent stability constant at I=0. For conversion to other ionic strengths, activity coefficients of all surface species are assumed equal to one. No electrical double layer correction to the mass laws for charged surface species.

b) Fraction of this surface site type compared to the total surface site density.

c) Total site density of 0.29 μmoles sites/g of quartz (0.88 μmoles sites/m^2). Fit with U(VI) adsorption data for pH values less than 6.0 and the aqueous thermodynamic data set in Kohler et al. (1996).

d) Total site density of 0.356 μmoles sites/g of quartz (1.08 μmoles sites/m^2). Fit with U(VI) adsorption data for pH values less than 6.0 and the aqueous thermodynamic data set in Kohler et al. (1996).

e) Total site density of 0.356 μmoles sites/g of quartz (1.08 μmoles sites/m^2). Fit with U(VI) adsorption data for pH values less than 6.0 and the aqueous thermodynamic data set in Table 2-1 of this report.

f) Total site density of 0.356 μmoles sites/g of quartz (1.08 μmoles sites/m^2). Fit with U(VI) adsorption data over the entire pH range and the aqueous thermodynamic data set in Table 2-1 of this report.

quartz/water ratio in the column was 3.7 kg/L. Although model B2 provides a good description of the batch U(VI) adsorption data, its prediction of U(VI) transport was less accurate. As described in Section 18 and in Kohler et al. (1996), the likely reason for the relatively poor transport prediction was that Model B2 was being extrapolated to consider a range of conditions (solid/water ratio, surface adsorption density, pH range) that were not well considered in the batch experiments. Accordingly, the NE approach for modeling U(VI) adsorption on quartz was also calibrated to the transport data set for a variety of different multisite models (see Table 13-2 and Section 18). These models also are quite successful in describing the U(VI) batch adsorption data. For example, the fit of Model C4 to the adsorption data for the system containing 100 g/L quartz and 1 μM U_T is shown in Figure 13-1.

Model C4 has one more surface reaction than Model B2, and thus it has one additional fitting parameter (the U(VI) binding constant for the additional reaction). As mentioned previously, the number of fitting parameters should be kept to a minimum. However, the need for an additional reaction became apparent when considering the U(VI) transport data at pH 3.9 (see Section 18). Very few batch data were collected at this low pH value, and thus the possibility of poor predictions of U(VI) transport

Table 13-2. Surface Complexation Reactions and Model Parameters from U(VI) Transport Data[a]

Model	Reactions	log K[b]	f_i[c]	χ^2[d]
C1	$S_1OH + UO_2^{2+} + H_2O = S_1OUO_2OH + 2H^+$	-4.96	1.0	3.810
C2	$S_1OH + UO_2^{2+} + H_2O = S_1OUO_2OH + 2H^+$	-4.94	0.9972	1.145
	$S_2OH + UO_2^{2+} + H_2O = S_2OUO_2OH + 2H^+$	-1.97	0.0028	
C3	$S_1OH + UO_2^{2+} + H_2O = S_1OUO_2OH + 2H^+$	-4.95	0.988	1.385
	$S_2OH + UO_2^{2+} = S_2OUO_2^+ + H^+$	1.23	0.012	
C4	$S_1OH + UO_2^{2+} + H_2O = S_1OUO_2OH + 2H^+$	-4.98	0.988	0.702
	$S_2OH + UO_2^{2+} + H_2O = S_2OUO_2OH + 2H^+$	-3.28	0.012	
	$S_2OH + UO_2^{2+} = S_2OUO_2^+ + H^+$	1.06		
C5	$S_1OH + UO_2^{2+} + H_2O = S_1OUO_2OH + 2H^+$	-5.04	0.9748	0.464
	$S_2OH + UO_2^{2+} + H_2O = S_2OUO_2OH + 2H^+$	-3.56	0.0250	
	$S_2OH + UO_2^{2+} = S_2OUO_2^+ + H^+$	0.642		
	$S_3OH + UO_2^{2+} + H_2O = S_3OUO_2OH + 2H^+$	-1.15	0.0002	
C6	$S_1OH + UO_2^{2+} + H_2O = S_1OUO_2OH + 2H^+$	-5.04	0.9756	0.511
	$S_2OH + UO_2^{2+} + H_2O = S_2OUO_2OH + 2H^+$	-3.55	0.0252	
	$S_2OH + UO_2^{2+} = S_2OUO_2^+ + H^+$	0.630		
	$S_3OH + UO_2^{2+} = S_3OUO_2^+ + H^+$	2.82	0.0002	
C7	$S_1OH + UO_2^{2+} + H_2O = S_1OUO_2OH + 2H^+$	-5.08	0.9627	0.999
	$S_2OH + UO_2^{2+} + H_2O = S_2OUO_2OH + 2H^+$	-3.58	0.0360	
	$S_3OH + UO_2^{2+} + H_2O = S_3OUO_2OH + 2H^+$	-1.62	0.0013	

a) Total site density used in all model calculations was 0.35 μmoles sites/g of quartz (1.06 μmoles sites/m^2). U(VI) transport data that were fit are given in Section 18 and in Kohler et al. (1996).
b) Apparent stability constant at I=0.01.
c) f_i is the fraction of the total surface site density for each site type.
d) χ^2 is the square of the weighted sum of the residuals as defined in Equation 18-1 (see Section 18).

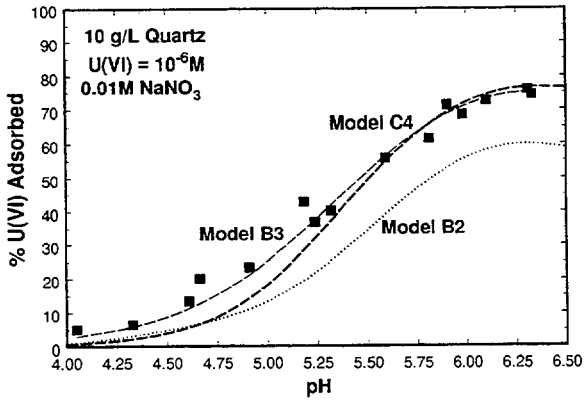

Figure 13-4. Calculated and experimental U(VI) adsorption on quartz as a function of pH in 0.01M $NaNO_3$ solution. Quartz = 10 g/l; U_T = 1 μM.

at pH 3.9 with Model B2 is not that surprising. The extra reaction in Model C4 is a one proton release reaction of the strong site, i.e.,

$$\equiv S_sOH + UO_2^{2+} = \equiv S_sOUO_2^+ + H^+ \quad (13\text{-}3)$$

Although the agreement between Models B2 and C4 and the experimental data does not seem that different in Figure 13-1, the discrepancy is more obvious in Figure 13-4 in the system with 10 g/L quartz. The agreement with the 10 g/L data can be further improved by adding an analogous reaction as in Equation 13-3 for the weak site. This is shown in Figure 13-4 as Model B3 and the parameters are given in Table 13-1. Model B3 obviously has more fitting parameters than Model B2, and the modeling application may determine when the larger number of parameters is acceptable. For this report, Model B3 was needed for modeling the systems with mixtures of quartz and ferrihdyrite (see Section 15).

Model B2 predictions of the effects of ionic strength (I) and the presence of the complexing

ligands fluoride (F) and carbonate are shown in Figures 13-5 through 13-7, respectively. Model B2 predicts almost no effect for a change of ionic strength from 0.005M to 0.01M, and only a slight decrease in adsorption from I = 0.01M to I = 0.1M. The magnitude of the predicted changes are within the experimental error of the data. In the presence of 100μM or 500μM F, the effect of F complexation on U(VI) adsorption was predicted very well by Model B2 or C4 (Fig. 13-6). The model predictions were made simply by adding the formation constants for F aqueous species to the calculations, including the U(VI)-F aqueous complexes (Table 2-1). The excellent agreement between the predictions and the experimental data suggests that it is very unlikely that U(VI)-F complexes adsorb on the quartz surface in appreciable amounts.

13.2.4 APPLICATION TO THE ALKALINE pH RANGE

At equilibrium with the atmospheric partial pressure of CO_2, model B2 predicted the U(VI) adsorption data reasonably well for pH values less than 7 (Fig. 13-7). For pH values greater than 7, however, the general trend in predicted U(VI) adsorption was similar to that observed, but the prediction underestimated the actual adsorption. The dependence of U(VI) adsorption on pH was very high in the pH range 7.5-9, and the predicted U(VI) adsorption was

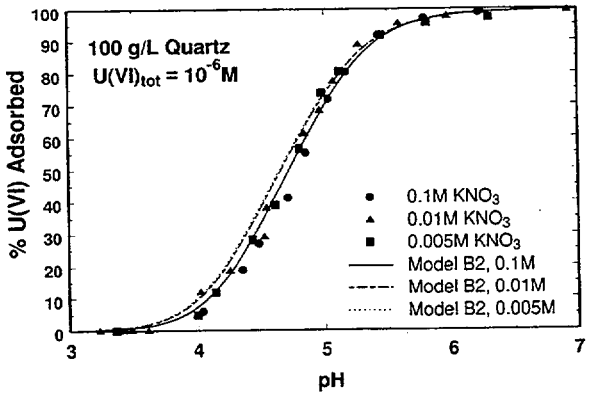

Figure 13-5. Calculated (model B2) and experimental U(VI) adsorption on quartz as a function of pH and ionic strength in KNO_3 solutions. Quartz = 100 g/l; U_T = 1 μM.

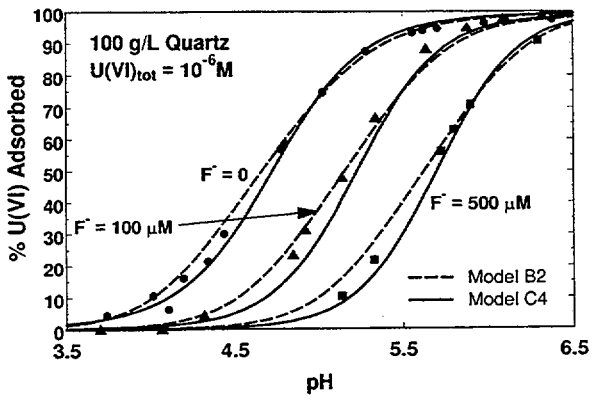

Figure 13-6. Calculated and experimental U(VI) adsorption on quartz as a function of pH and fluoride concentration. Quartz = 100 g/l; U_T = 1 μM.

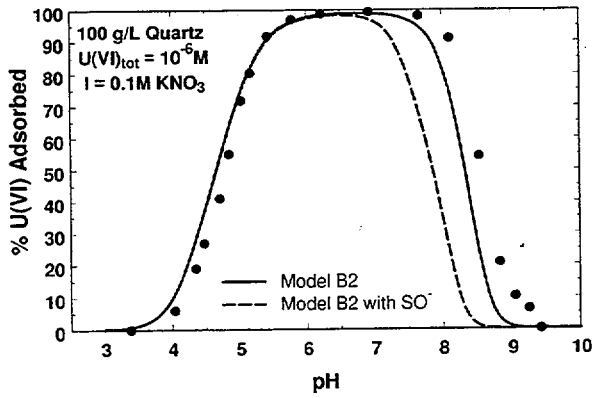

Figure 13-7. Calculated (model B2) and experimental U(VI) adsorption on quartz as a function of pH in 0.1M KNO_3 solution. Quartz = 100 g/l; U_T = 1 μM.

less than half of that measured at some pH values. Errors of this magnitude can have a very large influence on U(VI) transport predictions (see Section 18). If the acidity of surface silanol groups is included in the model, the disagreement between the predicted and observed U(VI) adsorption becomes larger for the pH range >7 (see dashed line in Fig.13-7). Deprotonation of $\equiv S_jOH$ to $\equiv S_jO^-$ reduces the activity of the sorbing species $\equiv S_jOH$ in Equation 13-1, and therefore decreases calculated U(VI) adsorption.

A likely explanation for the underestimation of U(VI) adsorption in the pH range 7.5-9 is the formation of ternary uranyl-carbonato surface complexes, which were not included in model B2. Although not confirmed spectroscopically for the quartz surface, such complexes have been identified by FTIR and EXAFS spectroscopy on the ferrihydrite and hematite surfaces (Section 3) and were included in the model of Waite et al. (1994b) for U(VI) adsorption on ferrihydrite (Section 12). To determine whether a similar ternary complex on the quartz surface would provide better agreement between calculated and observed U(VI) adsorption in the pH range 7.5-9, Model B4 was tested. Model B4 is the same as Model B2 except that it includes a ternary surface complex involving the uranyl cation, carbonate anion, and strong-site surface functional group. Because the only data available in the pH range 7.5-9 were for the system with 1 μM U(VI), only a weak site ternary complex was considered. Figure 13-8 shows the better agreement between the U(VI) adsorption data at high pH and Model B4, suggesting that uranyl-carbonato complexes may also exist on the quartz surface.

13.3 Summary

A two-site, nonelectrostatic surface complexation model (B2) with only one surface reaction stoichiometry (Eq. 13-1) was capable of describing U(VI) adsorption data on quartz over a wide range of U(VI) concentrations and pH. At high adsorption densities, a second reaction stoichiometry was needed to model U(VI) adsorption at low pH (Eq. 13-3, written for both strong and weak sites). Model B2 was able to predict the effect of fluoride complexation on U(VI) adsorption quite accurately simply by consideration of aqueous U(VI)-F complex formation. However, Model B2 underestimated U(VI) adsorption at pH values greater than 7.5 in the presence of carbonate, probably due to the formation of ternary uranyl-carbonato surface complexes. U(VI) adsorption data in the pH range 7.5-9 were well described by the addition of this surface reaction (Model B4).

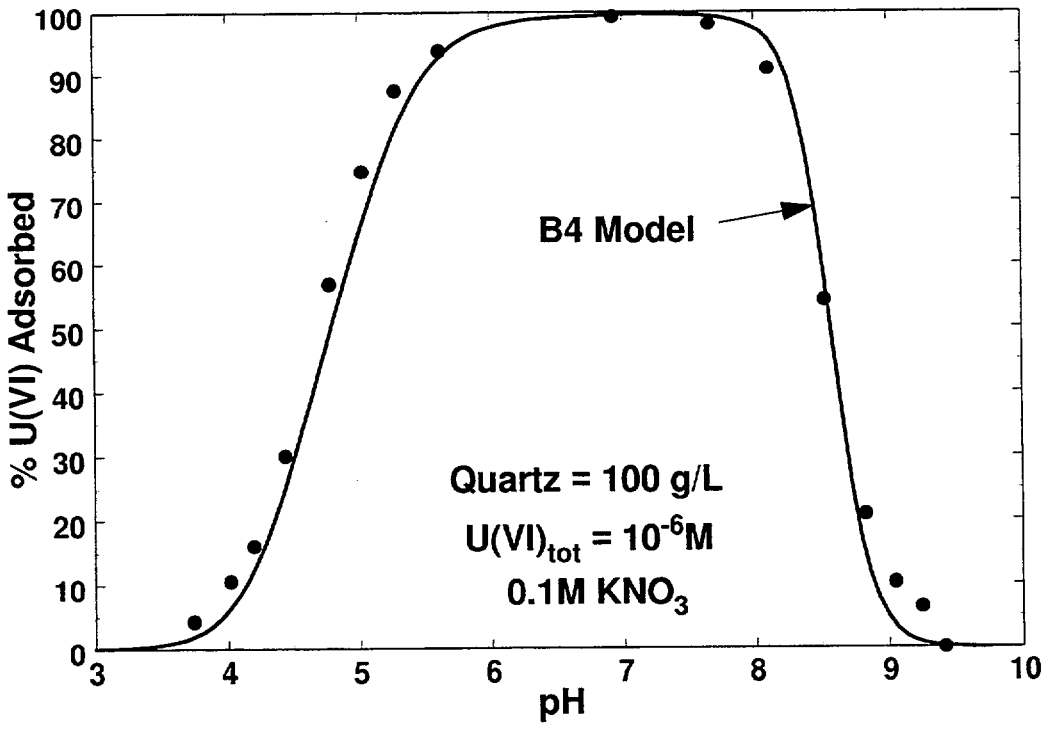

Figure 13-8. Calculated (model B4) and experimental U(VI) adsorption on quartz as a function of pH in 0.1M KNO_3 solution. Quartz = 100 g/L; U_T = 1 μM.

14 SURFACE COMPLEXATION MODELING OF URANIUM(VI) ADSORPTION ON IMOGOLITE

14.1 Model Development

In this section, a two-site diffuse double layer (DDL) model is developed to describe the U(VI) adsorption data for imogolite collected under various conditions, as described in Section 6. The first step in the model development was to fit the data for U(VI) adsorption in the pH range 4 to 6 in the absence of added complexing ligands. The initial modeling strategy was similar to that described in Section 13 and in Waite et al. (1994b), i.e., that U(VI) adsorption could be described by the reaction of the uranyl cation, UO_2^{2+}, with surface hydroxyl groups on the imogolite surface.

14.1.1 SITE DENSITY AND ELECTRICAL DOUBLE LAYER PARAMETERS

The total surface site density was estimated from the surface area (800 m^2/g, Section 6) and the tritium exchange data (9.51 sites/nm^2, Section 6), and was equivalent to a site concentration of 15.8 μmoles/m^2 of surface area. For the experimental conditions of 400 mg/L imogolite, this implies a surface site concentration of 5.06 mmoles sites/L. Acidity constants for the surface used in the model were pK_1=6.09 and pK_2=8.71 (at I=0), consistent with the experimental pH_{PZC} of 7.4 and an assumed ΔpK_a equivalent to that used in ferrihydrite modeling (Waite et al., 1994b). A molar ratio of strong sites to weak sites of 0.000148 was used in the model, based on a preliminary sensitivity test of the model fit to experimental adsorption data as a function of pH and total U(VI) concentration. Waite et al. (1994b) reported a ratio of 0.00206 for ferrihydrite. The surface complexation formation constants for the two-site model were estimated with the nonlinear least squares optimization program, FITEQL [Herbelin and Westall, 1994], using the thermodynamic data for U(VI) given in Table 2-1.

14.1.2 SURFACE REACTIONS

A good fit to the data in the pH range 4-6 (Figure 14-1) was obtained with the two-site model with only one reaction stoichiometry for each site, i.e.,

$$2{\equiv}S_jOH + UO_2^{2+} = ({\equiv}S_jO)_2UO_2 + 2H^+ \quad (14\text{-}1)$$

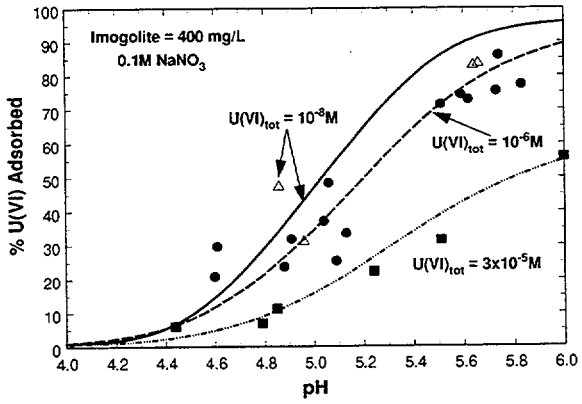

Figure 14-1. Calculated (two-site DDL model) and experimental U(VI) adsorption on imogolite as a function of pH and U_T concentration in 0.1M $NaNO_3$ solution. Imogolite = 400 mg/L.

where S_jOH represents a surface hydroxyl functional group, and the subscript j denotes the site type each with a different binding affinity and surface site density. Following the approach of Waite et al. (1994b), the surface complexation formation constant was defined as,

$$K_j = (({\equiv}S_jO)_2UO_2)(H^+)^2/({\equiv}S_jOH)(UO_2^{2+}) \quad (14\text{-}2)$$

where the quantities in parenthesis denote the activity of each species. The activity coefficients of the surface species are assumed to be equal to one. Following the approximation of Davis and Leckie (1980) and Waite et al. (1994b), the mass action equations involving bidentate U(VI) complexes with the surface site, $\equiv S_jOH$, are defined with an exponent of one for $\equiv S_jOH$, but the mass balance equation for the

surface site concentration assumes a stoichiometric coefficient of two for $\equiv S_jOH$ (i.e. each mole of bidentate complex occupies two moles of $\equiv S_jOH$ sites; this difference can be specified in the B matrix of FITEQL).

14.1.3 MODELING RESULTS

Figure 14-2 shows the predicted adsorption of U(VI) on the imogolite surface over the pH range 4-10 assuming that only the $\equiv S_sOUO_2OH$ and $\equiv S_wOUO_2OH$ surface species form (Eq. 14-1; s and w subscripts denote strong- and weak-binding, respectively). As was the case for

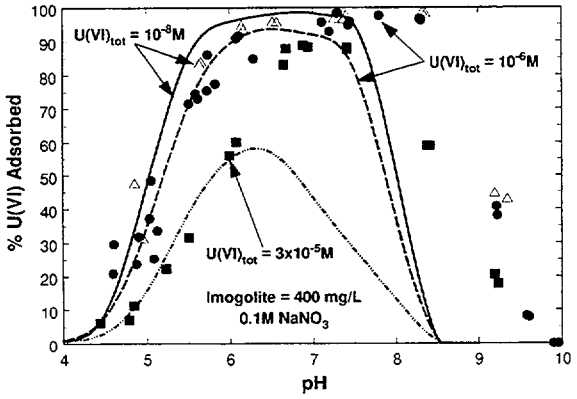

Figure 14-2. Calculated (two-site DDL model) and experimental U(VI) adsorption on imogolite as a function of pH and U_T concentration in 0.1M $NaNO_3$ solution. Imogolite = 400 mg/l.

ferrihydrite (Waite et al., 1994b), the model underestimates U(VI) adsorption in the alkaline pH range where the aqueous speciation is dominated by uranyl-carbonato complexes. However, in contrast to ferrihydrite, the underestimation of U(VI) adsorption by the model was large, e.g., adsorption in the system with a U_T concentration of 10^{-6}M was measured to be greater than 95% at pH 8.3, but the model predicted <5% U(VI) adsorbed.

Following the approach used in Waite et al. (1994b) for ferrihydrite and in Section 13 for quartz, a ternary uranyl carbonato surface complex was assumed to form and to account for the underestimation of U(VI) adsorption in the alkaline pH range. The reaction to form the ternary complex was written as follows:

$$2\equiv S_jOH + UO_2^{2+} + H_2CO_3 = (\equiv S_jO)_2UO_2CO_3^{2-} + 4H^+ \quad (14\text{-}3)$$

Because of the strong U(VI) adsorption on imogolite in the pH range 9-10, the stability constants for the strong- and weak-site ternary complexes (Eq. 14-3) were determined by fitting U(VI) adsorption data in this pH range. The two-site model predicted that bidentate uranyl complexes (Eq. 14-1) were insignificant at pH >8.5 (Fig. 14-2).

In the diffuse double layer (DDL) model, the net charge on the surface complex is assumed to be located within the same plane as the potential-determining ions (the σ_o plane, Davis and Kent, 1990). Following the usual convention, Waite et al. (1994b) used a charge of –2 for the strong- and weak-site ternary complexes (Eq. 14-3) in the equations that define surface charge and potential in the DDL model. However, this modeling approach was not as successful for imogolite as it had been for ferrihydrite. Using the U(VI) adsorption data in the alkaline pH range to determine the stability constants for the ternary complexes yielded a significant model overprediction of U(VI) adsorption in the pH range 3-6 (see the modeling result for σ_o= -2 in Figure 14-3). The overprediction was due to the large stability range of the proposed ternary complexes.

It was found that if the charge of the surface species is assumed to be zero, the model prediction passed through the data quite accurately (σ_o= 0 curve in Fig. 14-3). A thorough investigation of this effect will require the use of a triple layer model (Sahai and Sverjensky, 1997) to describe the electrical double layer properties. However, it would appear that a plausible explanation for the result in Figure 14-3 is that the charge of –2 of the ternary complexes is localized on the carbonate oxygen atoms, which are at a relatively large distance from the σ_o plane in the electrical double layer (Fig. 3-9). In this case, the

electrical potential at the σ_β or σ_d plane of the triple layer model may turn out to be a better approximation of the electrical potential term in the mass law for formation of the ternary complexes, rather than the σ_o plane of the DDL model. Triple layer model calculations with the electrostatic term defined in this way are expected to be close to that shown for σ_o= 0 in Figure 14-3, but these calculations are beyond the scope of the current report. In any case, these modeling results are consistent with the large pH range over which ≡FeOH-U(VI)-carbonato complexes were observed to be stable by FTIR aand EXAFS spectroscopy (Section 3).

Figure 14-4 and 14-5 show the results of two different models used to describe the U(VI) adsorption data with the DDL modeling approach, assuming that the effective charge of the ternary species is zero. Figure 14-4 shows the results as a function of the U_T concentration; the model describes the data well except for the pH range 6 to 7.5 in the system with a 30 μM U_T concentration. These particular experimental data may indicate that precipitation has occurred, because the dissolved U(VI) concentrations suggest saturation with respect to schoepite (Fig. 2-1).

Figure 14-5 shows the fit to the model if a different proton stoichiometry is assumed for formation of the ternary complex,

$$2{\equiv}S_jOH + UO_2^{2+} + H_2CO_3 = ({\equiv}S_jO)_2HUO_2CO_3^- + 3H^+ \quad (14\text{-}4)$$

In this case, one proton from one of the $\equiv S_jOH$ groups is not displaced by the uranyl cation. As in Figure 14-4, the charge of the ternary species in the model was set to zero. The addition of the proton to the complex increases its stability at low pH, and the overall pH dependence of the model calculations matches the experimental data better in the approach shown in Figure. 14-4.

14.2 Summary

Adsorption and modeling results suggest that uranyl-carbonato ternary complexes may exist on the imogolite surface, as has been confirmed for iron oxide surfaces in Section 3. Triple layer modeling may be required to describe U(VI) adsorption on imogolite because of the possible distribution of charge within the ternary surface species.

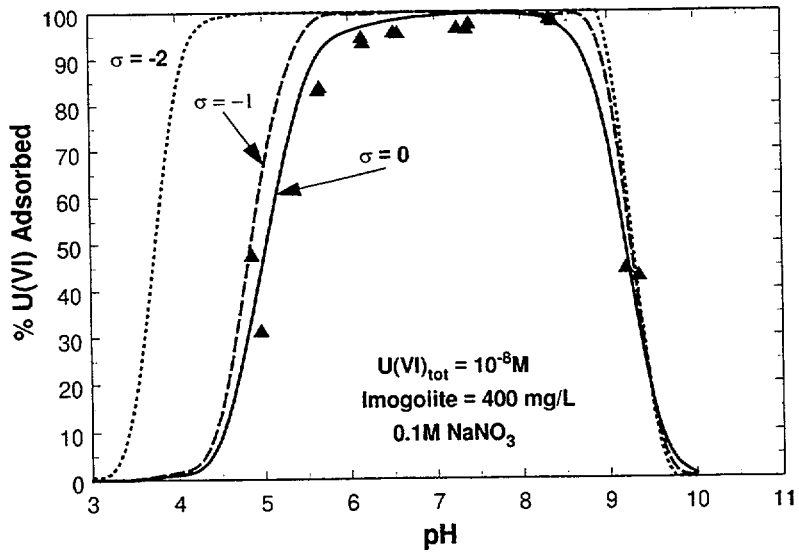

Figure 14-3. Comparison of DDL model simulations and experimental U(VI) adsorption on imogolite as a function of pH in 0.1M $NaNO_3$ solution. Imogolite = 400 mg/L; $U_T = 10^{-8}$M. Only U(VI) surface species in the model calculations was the ternary uranyl carbonato complex (Eq. 14-3). Simulations are shown for three values of the electrostatic correction term with charge, σ_o, of the ternary uranyl carbonato complex assumed to be –2, -1, or zero.

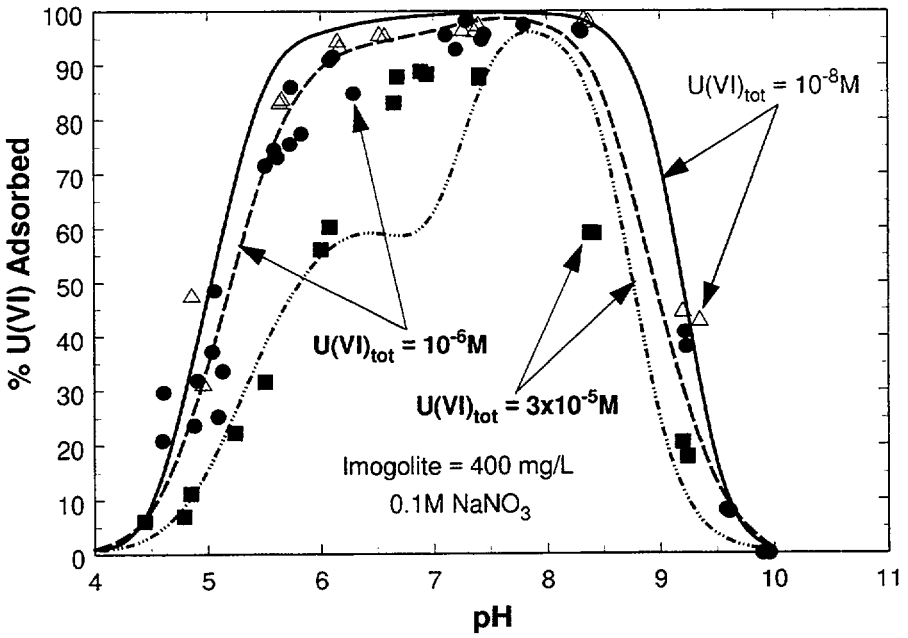

Figure 14-4. Calculated (two-site DDL model) and experimental U(VI) adsorption on imogolite as a function of pH and U_T concentration in 0.1M $NaNO_3$ solution. Imogolite = 400 mg/L. Only U(VI) surface species in the model calculations was the ternary uranyl carbonato complex (Eq. 14-3). Simulations are shown for the assumption that the charge, σ_o, of the complex was equal to zero.

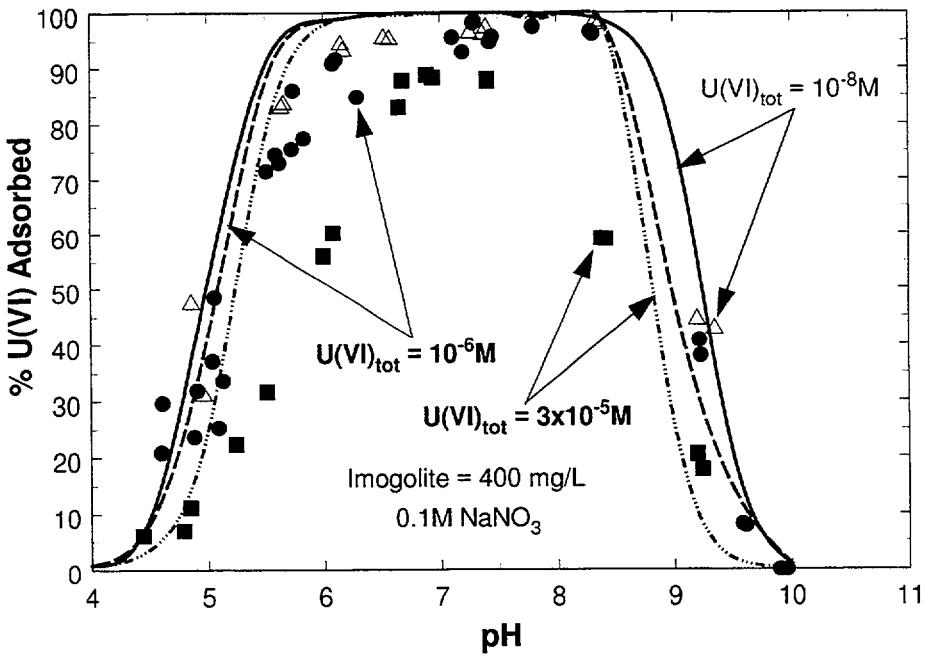

Figure 14-5. Calculated (two-site DDL model) and experimental U(VI) adsorption on imogolite as a function of pH and U_T concentration in 0.1M $NaNO_3$ solution. Imogolite = 400 mg/L. Only U(VI) surface species in the model calculations was a ternary uranyl carbonato complex (Eq. 14-4), with different proton stoichiometry for the reaction than in Figure 14-4. Simulations are shown for the assumption that the charge, σ_o, of the complex was equal to zero.

15 SURFACE COMPLEXATION MODELING OF URANIUM(VI) ADSORPTION ON QUARTZ WITH SYNTHETIC IRON OXYHYDROXIDE COATINGS

15.1 Introduction

In this section, surface complexation modeling is used to test whether U(VI) adsorption by quartz with iron oxyhydroxide coatings can be predicted from the SCM developed for quartz and ferrihydrite as separate phases. The model predictions are compared with the experimental data collected for various preparations of iron oxyhydroxide coatings, as described in Section 8.

15.2 Modeling U(VI) Adsorption by the Pure Phases

The experiments with coatings were all conducted with a quartz concentration of 10 g/L and a U_T concentration of 1 μM. In order to test whether U(VI) adsorption by quartz with iron oxyhydroxide coatings can be predicted from SCM developed for quartz and ferrihydrite as separate phases, one must have excellent agreement between the calculated and observed adsorption for the individual phases. The agreement is shown for quartz Model B3 in Figure 13-4. Model B3 was an extension of Model C4 (see Sections 13 and 18) with one extra reaction for the weak site. The extra reaction was added specifically to achieve an excellent agreement between the model and data for U(VI) adsorption on quartz considered in this Section.

The U(VI) adsorption experiments with quartz and iron oxyhydroxide coatings were all conducted with an Fe(III) concentration of 3 μmoles/g quartz (or 30 μM Fe_T) and a U_T concentration of 1 μM. The agreement between calculated and observed U(VI) adsorption for these conditions (in the absence of quartz) is shown in Figure 15-1 (dashed curve) using the ferrihydrite model described in Section 12. U(VI) adsorption under these conditions was significantly underpredicted with the model parameters given in Section 12. There are at least two potential reasons for the underprediction. First, the U(VI) adsorption density under these conditions is relatively high (approaching 20% of the maximum observed by Waite et al., 1994b), with all the strong sites occupied by adsorbed uranyl and the adsorption "edge" representing increased occupancy of weak sites only. At similar adsorption densities, the model of Waite et al. (1994b) also significantly underpredicted U(VI) adsorption on ferrihydrite (see the curve for a U_T concentration of 10^{-5}M in Fig. 11c by these authors). Achieving better agreement at these adsorption densities may require adding a third site type to the model, but Waite et al. (1994b) chose not to do so in order to keep the number of fitting parameters smaller. Another potential reason for the underprediction is that the properties of the ferrihydrite (e.g., surface area) are different when the ferrihydrite is precipitated at an Fe_T concentration of 30 μM instead of the 10^{-3}M concentration used by Waite et al. (1994b).

For the purpose of this Section, the ferrihydrite model of Section 12 was modified to achieve excellent agreement between the model and dataset for U(VI) adsorption by ferrihydrite shown in Figure 15-1. The only modification of the model was to recalibrate the stability constant for the weak site uranyl complexation reaction, i.e.,

$$\equiv Fe_w(OH)_2 + UO_2^{2+} = (\equiv Fe_wO_2)UO_2 + 2H^+ \quad (15\text{-}1)$$

which had a value of log K = -6.135 when the model was calibrated with the U(VI) adsorption dataset for 10^{-3}M ferrihydrite (Table 12-2). The solid curve in Figure 15-1 shows the best fit to the 30 μM dataset that can be achieved by recalibrating the constant for the reaction in Eq. 15-1. The new value of the constant was log K = -5.505. The dependence of U(VI) adsorption on pH is somewhat different between the model and the experimental data, but no further

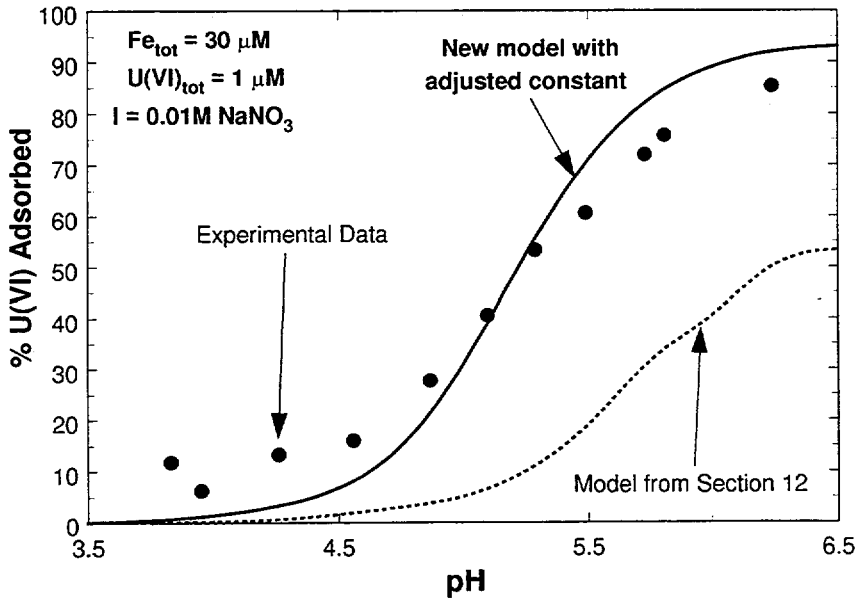

Figure 15-1. Calculated (two-site DDL model) and experimental U(VI) adsorption on ferrihydrite as a function of pH in 0.01M $NaNO_3$ solution. Ferrihydrite = 30 μM (as Fe_T); U_T = 1 μM. Model simulations shown are the model for ferrihydrite developed in Section 12 and a model with the stability constant adjusted for the binary uranyl complex with weak-binding sites (Eq. 15-1).

refinements were made to the model to compensate for that effect.

15.3 Modeling U(VI) Adsorption on Mixed Phases

With models calibrated for both the quartz and pure ferrihydrite phases under the appropriate conditions, it is now possible to compare predicted and observed U(VI) adsorption for the physical mixture of 10 g/L quartz and 30 μM Fe_T (as ferrihydrite; Method I, see Section 8). Figure 15-2 shows the agreement between the model prediction (solid curve) and the observed U(VI) adsorption by the mixture and the model-predicted distribution of adsorbed U(VI) between the quartz and ferrihydrite surfaces (dashed curves). It is important to remember that the model calculations presented here are not fit to the data collected for the quartz/ferrihydrite mixture; the models were calibrated to the data for each of the separate phases (Figs. 15-1 and 13-4, Model B3). The model prediction for the mixture slightly underpredicted the observed U(VI) adsorption (Fig. 15-2), but because of the small difference it can be argued that the result supports the concept of adsorptive additivity (Honeyman, 1984) for this system. The concept of adsorptive additivity simply states that the adsorption equilibria of mixtures of adsorbent phases can be simply determined by considering the equilibria of each of the individual phases as determined in monomineralic experiments (see Section 1). If the concept applies, no enhancement or diminution of adsorption by the mixture should be observed. This would imply that surface complexation models derived for individual mineral phases could be applied directly when such phases were present as mineral coatings in soils and sediments. In many laboratory studies of mixed mineral assemblages, however, the concept of adsorptive additivity has not been applicable.

Figure 15-3 compares the model for the physical mixture of the phases with the U(VI) adsorption observed for the titration-precipitation method of producing iron oxyhydroxide coatings (Method III – see Section 8). In this case, the model underprediction of U(VI) adsorption is greater than in Fig. 15-2, and as discussed in Section 8,

this may result from the formation of iron oxyhydroxide coatings of greater surface area. In this case, the results suggest that coatings formed in this manner are not as well described by the concept of adsorptive additivity, since they appear to be more reactive with U(VI) than when studied by precipitation of pure ferrihydrite.

Figure 15-4 compares the recalibrated model (solid curve) for U(VI) adsorption with 30 μM Fe_T (as ferrihydrite, Fig. 15-1) with experimental data for U(VI) adsorption by ferrihydrite precipitated in the presence of orthosilicate. As discussed in Section 8, adsorption of orthosilicate during the formation of ferrihydrite particles increases the adsorptive reactivity of U(VI) with the precipitate. Following the same procedure used to recalibrate the ferrihydrite model for the 30 μM pure ferrihydrite system, the constant for the reaction in Eq. 15-1 was redetermined to achieve the best fit to the U(VI) adsorption data for the ferrihydrite-silicate co-precipitate. The recalibration yielded the dashed model curve shown in Figure 15-4, and the constant was increased in value by roughly one order of magnitude. The modeling result illustrates that the adsorption constant determined with the pure phase ferrihydrite could be up to one order of magnitude in error when applied to mineral coatings. The co-adsorption of solutes like silicate and organic acids in nature during the precipitation of ferrihydrite and the formation of coatings hinders the growth of particles during precipitation, increases the surface reactivity (or area) of the particles, and thus causes problems in applying the concept of adsorptive additivity.

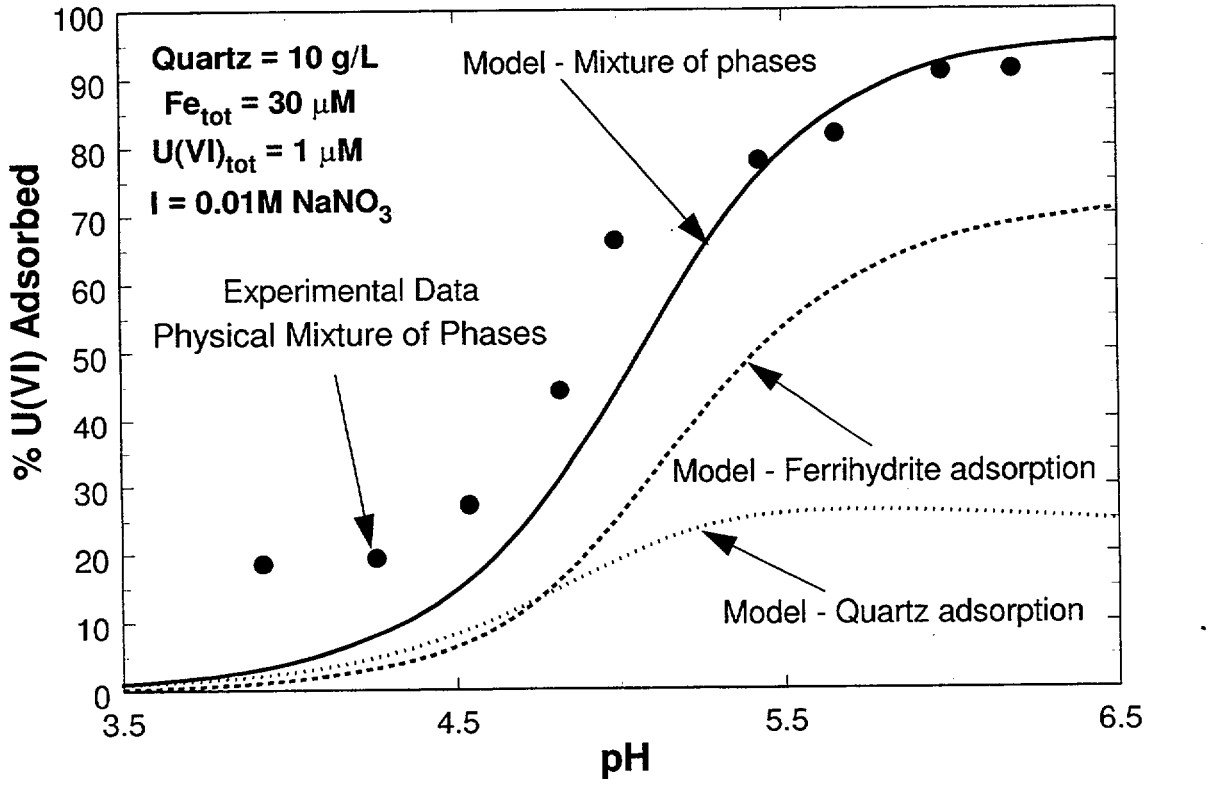

Figure 15-2. Calculated and experimental U(VI) adsorption on ferrihydrite, quartz, and a physical mixture of the two phases as a function of pH in 0.01M $NaNO_3$ solution. Quartz = 10 g/L; ferrihydrite = 30 μM (as Fe_T); U_T = 1 μM. Model simulations shown are for quartz alone (nonelectrostatic Model B3, see Fig. 13-4), for ferrihydrite alone (DDL model, see Fig. 15-1), and a prediction of U(VI) adsorption by a mixture of the two phases.

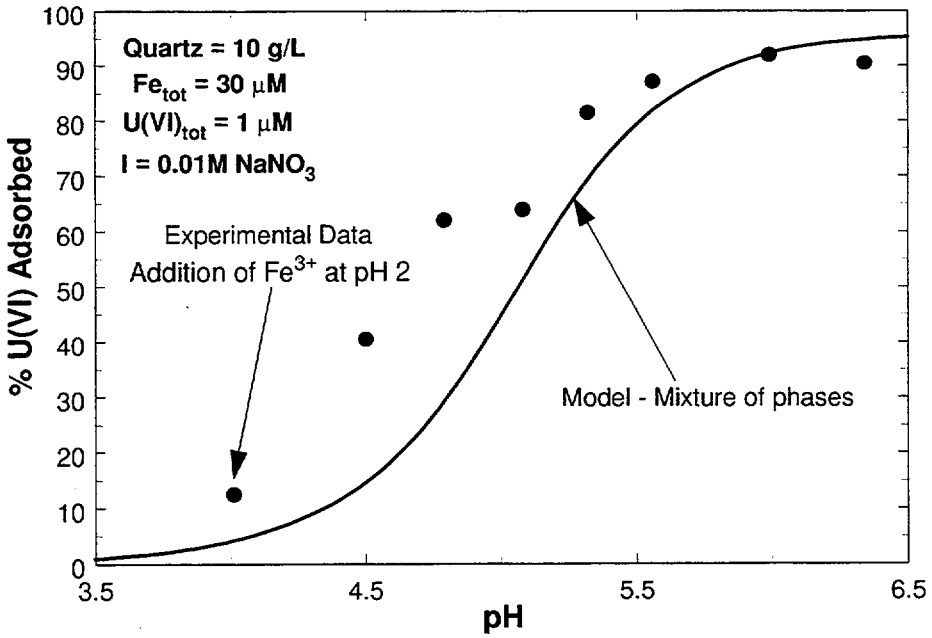

Figure 15-3. Experimental data for U(VI) adsorption on quartz with iron oxyhydroxide coatings produced by titration-precipitation method (Method III – see Section 8) compared to the model simulation of U(VI) adsorption by a physical mixture of the two phases. Quartz = 10 g/L; Fe_T = 30 μM; U_T = 1 μM. Model simulation is the same as that shown in Figure 15-2.

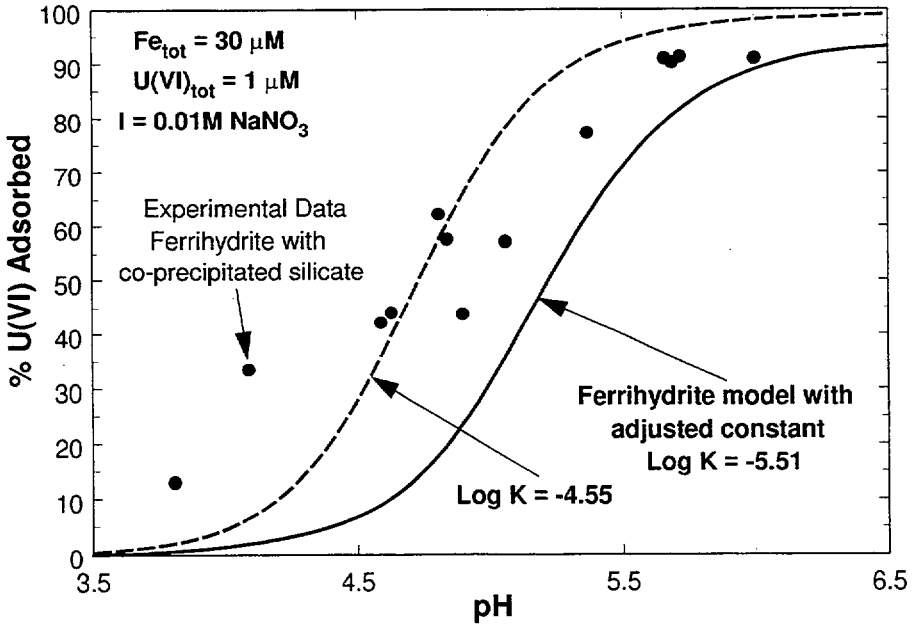

Figure 15-4. Calculated (two-site DDL model) and experimental U(VI) adsorption on ferrihydrite with and without co-precipitated silicate as a function of pH in 0.01M $NaNO_3$ solution. Ferrihydrite = 30 μM (as Fe_T); U_T = 1 μM. Model simulations shown are the DDL model with adjusted constant in Figure 15-1 and a fit to the data with co-precipitated silicate. In the latter simulation, the stability constant was adjusted again for the binary uranyl complex with weak-binding sites (Eq. 15-1).

16 SURFACE COMPLEXATION MODELING OF U(VI) ADSORPTION TO SUBSURFACE MATERIAL FROM THE KOONGARRA WEATHERED SOIL ZONE

16.1 Introduction

This chapter investigates the development and application of models suitable for the description of the partitioning of U(VI) between aqueous solutions and the surfaces of complex mineral assemblages.

Considerable progress has been made in recent years in developing models capable of describing the adsorption of trace ions to single mineral phases over a range of solution conditions. For example, Waite *et al.* (1994) used the surface complexation approach (Davis and Kent, 1990) to describe U(VI) adsorption to the amorphous iron oxide, ferrihydrite over a range of pH, uranium concentrations and CO_2 partial pressures and were able to reliably describe most of the experimental results obtained. The adopted model used information obtained from EXAFS studies to assign a bidentate stoichiometry to surface-located uranyl species and account was taken of both surface acidity reactions and variable electrostatic effects (using a diffuse layer description of the electrical double layer). This model has been refined slightly in Section 12 of this report with the revision of some of the uranyl solution complexes.

Similar success in applying the surface complexation modeling approach for trace ion adsorption to well-defined minerals has been reported by Kohler *et al.* (1996) in describing uranium(VI) sorption to quartz and by Kohler *et al.* (1999) in describing neptunium(V) sorption on hematite over a wide range of system conditions in both cases. Other examples of the successful application of the surface complexation modeling approach to description of the adsorption of uranium(VI) to single mineral phases are given in Sections 13 (quartz) and 14 (imogolite) of this report.

These experimental and computational investigations of trace ion adsorption to single mineral surfaces have been invaluable in demonstrating the relative ease with which the highly variable effects of solution conditions on solid-solution partitioning of trace species may be accounted for. Natural substrates however would appear to be significantly more complex than single minerals with a variety of constituents typically present each with particular site densities, acid-base chemistry and coordinative properties for solution species. In light of the need for sound prediction of trace ion partitioning to solid phases for purposes such as mineral exploration, contaminated site assessment and waste repository performance assessment, application of mechanistically-oriented models such as the surface complexation approach is attractive but non-trivial.

Davis *et al.* (1998) have suggested that the surface complexation approach to modeling trace ion adsorption to natural substrates can be subdivided into two major types: (a) the *component additivity* (CA) approach in which the modeler attempts to *predict* adsorption on a complex mineral assemblage using the results of a surface characterization of the assemblage and collected data for adsorption by pure, reference minerals or organic phases, and (b) the *generalized composite* (GC) approach in which it is assumed that the surface composition of the mineral assemblage is inherently too complex to be quantified in terms of the contributions of individual phases to adsorption. Instead, it is assumed that the adsorptive reactivity of the surface can be described by surface complexation equilibria written with "generic" surface functional groups, with the stoichiometry and formation constants for each surface complex equilibria determined by fitting experimental data.

In this section, we briefly examine application of the component additivity and generalized composite approaches to modeling the adsorption of uranium(VI) to natural substrates

obtained in the vicinity of the Koongarra uranium ore deposit in the northern region of Australia. Conclusions concerning appropriate methods of modeling trace ion adsorption to complex mineral assemblages are drawn from the results of these modeling studies.

16.2 The Koongarra Sediments and Experimental Datasets

The experimental data used for modeling purposes are selected sets from W1, W2 and W7 cores as described in Section 9 of this report. The datasets used are given in Table 16-1 and key information on these samples presented in Tables 16-2 and 16-3. This latter information is a re-presentation of information previously given in Section 9. Recall that the samples were gravity separated into 4 fractions based on settling velocity, which is directly related to particle diameter (ϕ). The laboratory adsorption experiments considered only the fine fraction delineated by particles with ϕ nominally <25μm. Further information on the procurement of these datasets can be found in Section 9.

It should be noted that analytical transmission electron microscopy, carried out as part of this study and described in Section 10, clearly showed that in experiments having more than approximately $1x10^{-5}$ mol/.L of added U(VI), precipitation was a significant process in the removal of U(VI) from the aqueous phase. For the purpose of surface complexation modeling, in which precipitation reactions are not being considered, datasets 3, 5 and 8, were not included in the models here as they had an added U(VI) concentration ≥ $1x10^{-4}$ M. The five sets

Table 16-1. Description of the W1, W2 and W7 datasets

W1 DATASET	pH range		Solid/liquid ratio	U_{tot}
	Low	High	(g/L)	(M)
SET 1	1.57	9.93	20.0	3.70E-06
SET 2	1.19	7.05	4.0	7.30e-07
SET 3	1.56	10.09	20.0	1.04E-04

W2 DATASET	pH range		Solid/liquid ratio	U_{tot}
	Low	High	(g/L)	(M)
SET 4	1.56	9.98	4.0	3.90E-06
SET 5	1.69	6.37	4.0	1.05E-04

W7 DATASET	pH range		Solid/liquid ratio	U_{tot}
	Low	High	(g/L)	(M)
SET 6	1.61	5.42	4.0	3.00E-08
SET 7	1.64	6.44	4.0	1.00E-06
SET 8	1.68	6.58	4.0	1.00E-04

Table 16-2. Summary of Koongarra samples used in adsorption experiments (data for separated fine fractions).

Sample name	Depth (m)	Total U content (μg/g)	Accessible U (μg/g)	BET surface area (m^2/g)
W1	13.0 – 13.2	356	42.6	24.6
W2	14.0 – 14.2	426	225.0	52.3
W7	13.0 – 13.2	10.4	1.0	51.9

[a]As determined by selective leaching using Morgan's and Tamm's acid oxalate reagents

Table 16-3. Calculations of total U(VI) concentrations in experimental systems.

Solid	Accessible U (μg/g)	Solid/liquid ratio (g/L)	Natural U(VI) in experiments[a]		Added U(VI) (μM)	Total U(VI) (μM)
			(μg/L)	(μM)		
W1	42.6	20	852	3.6	0.1	3.7
W1	42.6	4	170.4	0.72	0.01	0.73
W2	225	4	900	3.8	0.1	3.9
W7	1.0	4	4	0.017	0.01	0.03
W7	1.0	4	4	0.017	1.0 (as ^{238}U)	1.0

[a]Assumed to equal the U extracted by Morgan's and TAO reagents

of data used for modeling purposes in this section are shown in Figure 16-1 where data are presented both as percentage of accessible uranium adsorbed and as partition coefficients K_d where K_d = (U adsorbed on solid phase (μmol/g))/(U concentration in aqueous phase (μmol/mL)).

In qualitative terms, the data are similar to those of ferrihydrite (Waite *et al.*, 1994). In particular, sorption is greatest in the near-neutral pH range, with a "low pH edge" of increasing uptake from pH of about 2.5 to 6.5, and a steeper "high pH edge" (desorption edge) between pH 8 and 9. This is due to the effect of complexation between UO_2^{2+} and carbonate in the aqueous phase at high pH values (Waite *et al.*, 1994). The only marked difference to the ferrihydrite data is an apparently greater tendency for uranium to partition to the solid phase under highly acidic conditions (pH < 3) than was observed in the case of ferrihydrite (Waite *et al.*, 1994).

The sorption data for the W7 (0.03 μM U) sample are significantly different to the other samples. Since the data for W7 (1 μM U) are similar to W1 and W2, the stronger sorption observed in the low total uranium case is attributed to the presence of a small number of high U affinity binding sites on the surfaces of the natural substrates. These "strong" sites would be expected to dominate sorption phenomena when ΣU is small.

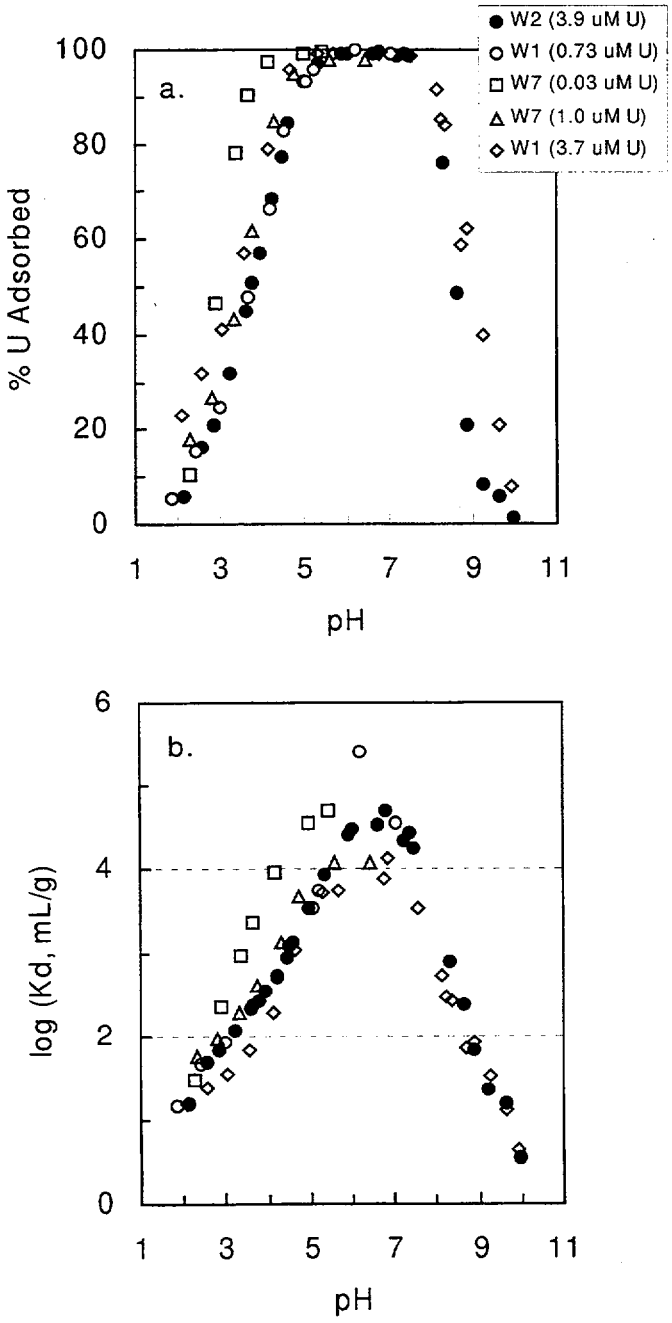

Figure 16-1. Part A, top) Percent uptake of accessible uranium (natural plus spike) and Part B, bottom) distribution coefficients K_d as a function of pH in experiments with Koongarra sediment. A solid/liquid ratio of 4 g/L was used for all samples except W1 (3.7 μM U) where 20 g/L was used. Background electrolyte is 0.1 M $NaNO_3$ in equilibrium with air.

16.3 Results of Surface Complexation Modelling

16.3.1 COMPONENT ADDITIVITY APPROACH

As indicated earlier, this approach is based on identification of the various mineral phases likely to be involved in adsorptive processes and summing their various contributions to overall adsorption from data obtained in single phase studies. While selective extraction studies on these samples suggest that both ferrinol and aluminol groups could be important in binding uranium (Fenton and Waite, 1996), extensive high resolution TEM studies indicate that surface-located uranium is principally associated with iron oxides present in these samples (Lumpkin *et al.*, 1999). Davis *et al.* (1998) found that surface coatings on natural substrates appear to exhibit site densities per unit mass similar to amorphous materials. In light of this, we shall first assume that all surface sites (measured as those accessible to N_2 in BET surface area analyses) can be attributed to amorphous minerals identical in properties to the hydrous ferric oxide ferrihydrite.

In comprehensive studies of U(VI) adsorption to ferrihydrite, Waite *et al.* (1994) found that a site concentration of 0.875 moles of sites per mole of Fe best described the sorption results obtained. Assigning a surface area of 600 m^2/g for this amorphous material (to which we ascribe the formula FeOOH), this corresponds to a site density of 16.38 μmoles sites/m^2. Using this site density and the measured BET surface areas for the Koongarra fine samples, we can calculate the total site concentrations of the various samples available for uranium uptake. Assuming the presence of weak (WOH) and strong (SOH) U(VI) binding sites as previously described by Waite *et al.* (1994) in the ratio [SOH] = 0.21% [WOH] and with stability constants for solution and surface equilibria as shown in Tables 16-4 and 16-5 respectively, we are able to predict the extent of U(VI) uptake attributable to these sites.

We have used the FITEQL Version 3.1 code (Herbelin and Westall, 1994) (in "equilibrium" mode) for these calculations with a diffuse double layer description of the double layer of "ferrihydrite-like" surfaces and Davies equation for ionic strength correction of solution phase species. An important feature of FITEQL is the facility for assigning different stoichiometries to mass law and mole balance equations. This is necessary for bidentate surface complexes where we have assumed that one uranyl species occupies two surface sites but exhibits a mass law dependency on the concentration of only one site (Waite *et al.*, 1994).

Selected results of this modeling approach are shown in Figure 16-2 and yield surprisingly good agreement with experimental data at pH values greater than approximately 4. While the % U sorbed results provide little definition at high proportions of U sorbed, the K_d results in Figures 16-2b and c (for samples W2 and W1 respectively) show that an assumption of ferrihydrite-like sites (with site concentration based on surface area) yield reasonable estimates of solid-liquid partitioning over the pH 4– 8 range. Underestimates in K_d values by up to one order of magnitude are observed at maximum adsorption capacity though some of this discrepancy may be related to errors in experimental data as a result of difficulty in separating very low concentrations of fine particulate matter from solution. Alternatively, we could justifiably conclude that the concentration of ferrihydrite-like U(VI) binding sites is overestimated and assign a lower surface site density to a portion of the measured surface area. Such sites could be associated with more crystalline iron oxide phases or with aluminum oxides. As indicated earlier, selective extraction studies suggest that metal oxides other than iron may be involved in U uptake but the extraction results provide no clear indication (or assist particularly in quantifying) the nature of sorbing phases.

At [SOH] = 0.21% [WOH], the strong site concentration is in all cases significantly greater than the total accessible uranium present in the

Table 16-4. Aqueous species used in surface complexation modeling. The thermodynamic constants are similar to those used in Section 12.

Reaction	*Log K (I=0)*
$UO_2^{2+} + H_2O \Leftrightarrow UO_2OH^+ + H^+$	-5.20
$UO_2^{2+} + 2H_2O \Leftrightarrow UO_2(OH)_2^0 + 2H^+$	-11.50
$UO_2^{2+} + 3H_2O \Leftrightarrow UO_2(OH)_3^- + 3H^+$	-20.00
$UO_2^{2+} + 4H_2O \Leftrightarrow UO_2(OH)_4^{-2} + 4H^+$	-33.00
$2UO_2^{2+} + H_2O \Leftrightarrow (UO_2)_2OH^{+3} + H^+$	-2.70
$2UO_2^{2+} + 2H_2O \Leftrightarrow (UO_2)_2(OH)_2^{+2} + 2H^+$	-5.62
$3UO_2^{2+} + 4H_2O \Leftrightarrow (UO_2)_3(OH)_4^{+2} + 4H^+$	-11.90
$3UO_2^{2+} + 5H_2O \Leftrightarrow (UO_2)_3(OH)_5^+ + 5H^+$	-15.55
$3UO_2^{2+} + 7H_2O \Leftrightarrow (UO_2)_3(OH)_7^- + 7H^+$	-31.00
$4UO_2^{2+} + 7H_2O \Leftrightarrow (UO_2)_4(OH)_7^+ + 7H^+$	-21.90
$2UO_2^{2+} + 3H_2O + H_2CO_3 \Leftrightarrow (UO_2)_2CO_3(OH)_3^- + 5H^+$	-17.543
$UO_2^{2+} + H_2CO_3 \Leftrightarrow UO_2CO_3^0 + 2H^+$	-7.013
$UO_2^{2+} + 2H_2CO_3 \Leftrightarrow UO_2(CO_3)_2^{-2} + 4H^+$	-16.426
$UO_2^{2+} + 3H_2CO_3 \Leftrightarrow UO_2(CO_3)_3^{-4} + 6H^+$	-28.449
$UO_2^{2+} + NO_3^- \Leftrightarrow UO_2NO_3^+$	0.30
$H^+ + CO_3^{2-} \Leftrightarrow HCO_3^-$	-6.354
$2H^+ + CO_3^{2-} \Leftrightarrow H_2CO_3^0$	-16.683

studies reported here. It is thus not surprising that the strong site surface complex $SO_2UO_2^0$ is predicted to dominate U(VI) adsorption over most of the pH region (Figure 16-2a). Ternary uranyl carbonate surface complexes are included in the model (Table 16-5) but are only important at pH > 7.5. It would also appear that a relatively acidic additional sorbing phase is required to account for uranyl uptake at low pH. Natural organic matter, bacterial cells or a surface-located anionic inorganic entity (such as phosphate) could account for this strong adsorption at low pH but, without further investigation, must remain the subject of speculation.

16.3.2 GENERALIZED COMPOSITE APPROACH

An assumption that little is known of the nature of the specific surface chemistry of the adsorbent or its interactions with U(VI) species underpins the generalized composite approach to surface complexation modeling. Generic surface sites are assumed with the chosen stoichiometry of U(VI) interaction with these sites based on a) the simplicity of the model and b) its goodness of fit.

In order to develop the most appropriate model, a number of "common sense" strategies were adopted: a) conditional surface equilibria were considered since no information on the acid-base

Table 16-5. Stability constants for surface equilibria used in component additivity modeling approach*

Reaction	*Log K (I=0.1)*
$SOH + H^+ \Leftrightarrow SOH_2^+$	6.51
$WOH + H^+ \Leftrightarrow WOH_2^+$	6.51
$SOH \Leftrightarrow SO^- + H^+$	-9.13
$WOH \Leftrightarrow WO^- + H^+$	-9.13
$S(OH)_2 + UO_2^{2+} \Leftrightarrow SO_2.UO_2^0 + 2H^+$	-2.57
$W(OH)_2 + UO_2^{2+} \Leftrightarrow WO_2.UO_2^0 + 2H^+$	-6.28
$S(OH)_2 + UO_2^{2+} + H_2CO_3 \Leftrightarrow SO_2.UO_2CO_3^{2-} + 4H^+$	-13.031
$W(OH)_2 + UO_2^{2+} + H_2CO_3 \Leftrightarrow WO_2.UO_2CO_3^{2-} + 4H^+$	-17.103

*A site density of 16.38 μmoles/m^2 and relative concentrations of strong to weak sites of 0.21% was assumed. Constants are identical to those derived for U(VI) adsorption to ferrihydrite by Waite *et al.* (1994).

behavior of the generic surface sites was available, b) a non-electrostatic model was used since little information of Coulombic effects at the surface was available, c) adsorption data for pH < 4 were not considered because of potential problems associated with sample dissolution under acidic conditions, d) best fit models for 4 < pH < 6 adsorption data were first investigated because of the likelihood of added complexity at higher pH due to ternary uranyl carbonate surface complex formation, and e) a model appropriate to description of all five data sets was initially sought though with the recognition that certain sets may need to be excluded if there were obvious outliers. In addition to these guidelines, a site density identical to that deduced for ferrihydrite by Waite *et al.* (1994) (i.e. 16.38 μmoles/m^2) was used in calculating site concentrations.

Using the above approach, the conditional constants for UO_2^{2+} binding at generic strong and weak sites were first obtained by fitting the five sets of adsorption data for 4 < pH < 6 using the chemical equilibrium code FITEQL Version 3.1 (Herbelin and Westall, 1994). Three simple options of binding stoichiometry were considered in this preliminary fitting process as shown below for strong site (SOH) complexation:

1. Monodentate single proton release:

$$SOH^\circ + UO_2^{2+} = SOUO_2^+ + H^+$$

2. Monodentate dual proton release:

$$SOH^\circ + UO_2^{2+} + H_2O = SOUO_2OH^\circ + 2H^+$$

3. Bidentate dual proton release:

$$S(OH)_2^\circ + UO_2^{2+} = SO_2UO_2^\circ + 2H^+$$

A relative error of 2% in adsorbed uranium measurements and an absolute error of ±0.05 in pH measurement was used in the FITEQL optimisation process. Relative concentrations of strong and weak sites were initially assumed to be the same as previously found by Waite *et al.* (1994) for ferrihydrite (i.e. [SOH] = 0.21% [WOH]) but this ratio was found to be unsatisfactory with the number of strong sites significantly in excess of that required. As can be seen from Figure 16-3, variation of the relative concentrations of strong and weak sites whilst maintaining total site concentrations

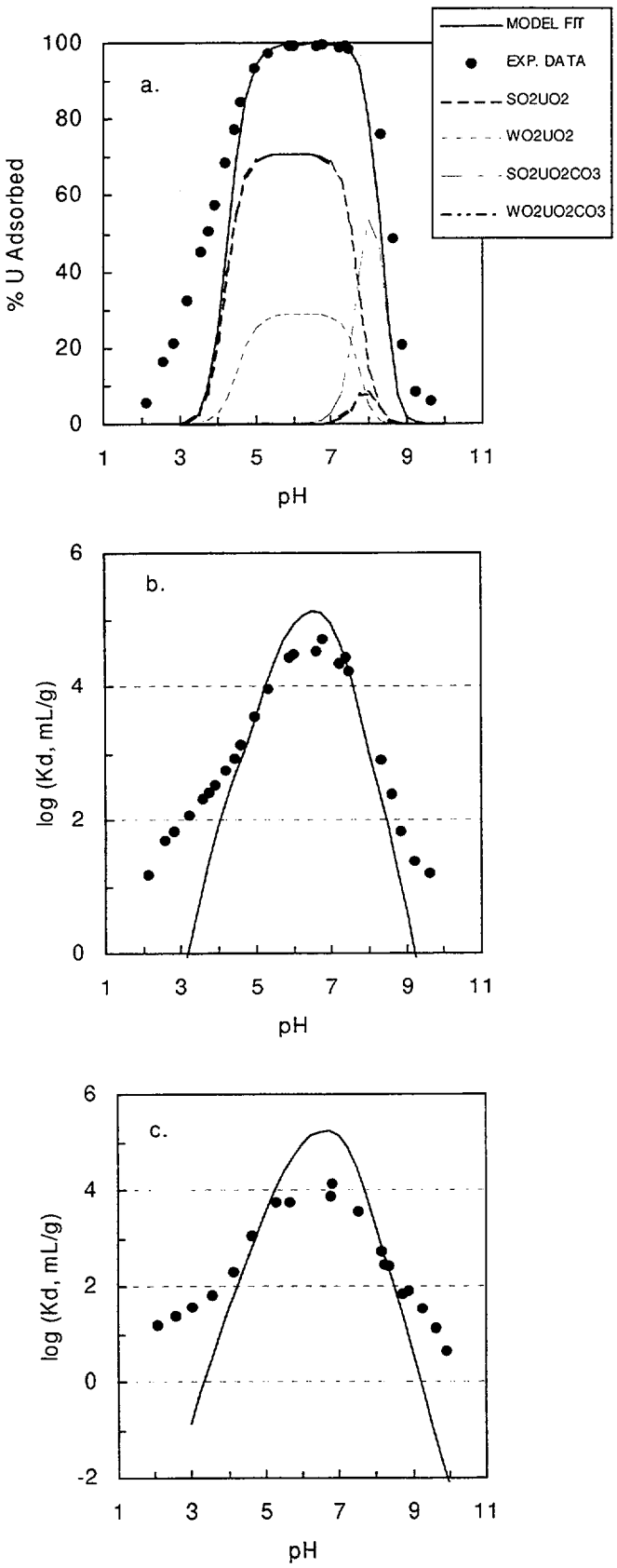

Figure 16-2. Results of component additivity (CA) modeling approach assuming adsorption attributable to ferrihydrite-like surface sites. Part A, top) Percent U(VI) adsorbed to W2 substrate with total uranium concentration of 3.9 μM (distribution of individual uranyl surface species also shown); Part B, middle) U(VI) distribution coefficient (K_d) for W2 substrate with total uranium concentration of 3.9 μM; Part C, bottom) U(VI) distribution coefficient (K_d) for W1 substrate with total uranium concentration of 3.7 μM.

constant led to significant improvement in fits (as indicated by the goodness-of-fit parameter, WSOS/DF, the weighted sum of squares of the difference in value between model calculations and experimental data points divided by the degrees of freedom) with a ratio of strong to weak sites of 0.05% found to give the most satisfactory results.

Using site concentrations for the various solids consistent with this ratio, fits for each of the three reaction stoichiometries described above rapidly converged with values of the goodness of fit parameter (WSOS/DF) equal to 3.807, 2.489 and 1.468 for options 1, 2 and 3 respectively. In light of these results, a bidentate stoichiometry for the uranyl surface complexes at strong and weak sites was assumed in further computations.

Best-fit formation constants obtained for these bidentate surface complexes are shown in Table 16-6. Note that while the possibility of ignoring certain data sets if they proved to be "outliers" was flagged earlier, this was unnecessary given the goodness of fit achieved to the complete set of data.

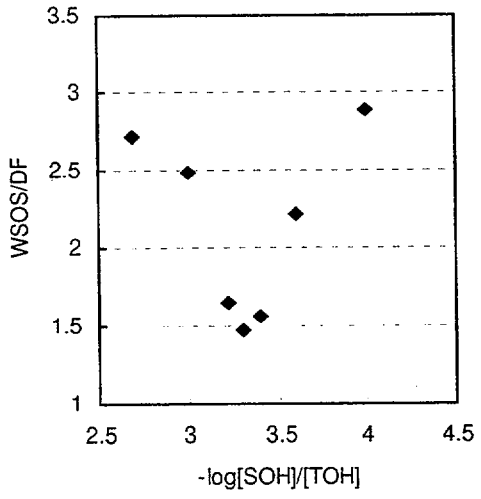

Figure 16-3. Goodness of fit (as judged by WSOS/DF FITEQL parameter) as a function of strong site concentration (as a proportion of total site concentration).

Given the clear spectroscopic evidence that has now been provided for the formation of uranyl carbonato complexes at mineral surfaces (Bargar *et al.*, Section 3), the complete set of adsorption data (i.e. all data for pH > 4) was then used to obtain the best fit conditional constants for bidentate ternary uranyl carbonate surface complexes at the generic strong and weak sites. For this fitting process, the conditional constants for the $SO_2UO_2^\circ$ and $WO_2UO_2^\circ$ surface complexes were fixed at their previously determined values. Optimal constants for the uranyl carbonato surface complexes are given in Table 16-6. The presence of these ternary complexes was found to have minimal effect on the optimal conditional constants for the $SO_2UO_2^\circ$ and $WO_2UO_2^\circ$ surface complexes which dominated at lower pH.

The predicted adsorption of U(VI) to W1 and W2 samples (based on the best fit constants to the five data sets combined) are shown in Figure 16-4 above. As can be seen from the species distribution data for W2 shown in Figure 16-4a, weak site binding dominates the uptake of uranium at this uranium concentration (3.9 μM) and for the relatively low strong site concentration (0.05% of weak site concentration) deduced to be optimal for adsorption of uranium to this set of substrates.

Uranyl carbonato species are observed to contribute to a minor extent to overall uranium adsorption and then only at pH > approx. 8. Of course, the relative importance of these carbonato surface species would increase at higher partial pressures of CO_2. Apart from the expected deviation between observed and predicted values at low pH (i.e. pH < 4 data for which fitting was not attempted), the agreement between the experimental and predicted percentage U(VI) sorbed is very good. Similarly, agreement between observed and predicted partition coefficient data is excellent for data at pH > 4 in the "pH edge" regions.

While agreement between observed and predicted partition coefficients appears to be less satisfactory at pH's where strong adsorption

Table 16-6. Fitted conditional stability constants for uranyl surface equilibria to generic strong (SOH) and weak (WOH) surface sites*

Reaction	*log K (I = 0.1)*
$S(OH)_2 + UO_2^{2+} = SO_2.UO_2^0 + 2H^+$	-0.56
$W(OH)_2 + UO_2^{2+} = WO_2.UO_2^0 + 2H^+$	-5.46
$S(OH)_2 + UO_2^{2+} + H_2CO_3 = SO_2.UO_2CO_3^{2-} + 4H^+$	-12.48
$W(OH)_2 + UO_2^{2+} + H_2CO_3 = WO_2.UO_2CO_3^{2-} + 4H^+$	-17.45

*A site density of 16.38 μmoles sites/m^2 and relative concentrations of strong to weak sites of 0.05% were assumed.

occurs (i.e. where the K_d values are large), it should be remembered that the concentration of U(VI) in solution is very low under these conditions and the error between observed and predicted concentrations of uranium adsorbed is correspondingly low.

16.4 Conclusions

Two approaches to modeling uranium(VI) adsorption to natural substrates, the component additivity and generalized component approaches, have been examined in this section. In applying the component additivity approach, the assumption that sorbing sites were ferrihydrite-like with site concentration based on BET surface area gave estimates of U(VI) adsorbed that were in reasonable agreement with the experimental data for pH > 4. An additional strongly acidic site would appear to be needed to describe the less than pH 4 data.

According to the generalized composite approach (with total site concentration based on surface area and a site density equal to that of ferrihydrite), a four bidentate surface species ($SO_2UO_2^\circ$, $WO_2UO_2^\circ$, $SO_2UO_2CO_3^{2-}$, $WO_2UO_2CO_3^{2-}$) model gave a very good fit (as adjudged by the WSOS/DF) to the available, combined experimental data set. Acid-base chemistry and electrostatic effects were not considered explicitly in this model.

These results suggest that while a component additivity approach is one means of obtaining a reasonable estimate of solid-liquid partitioning of trace ions as a function of system conditions, a generalized composite approach to sorption modeling is a workable, pragmatic approach provided it is implemented in a careful manner with simplicity and goodness of fit as the major criteria of acceptance.

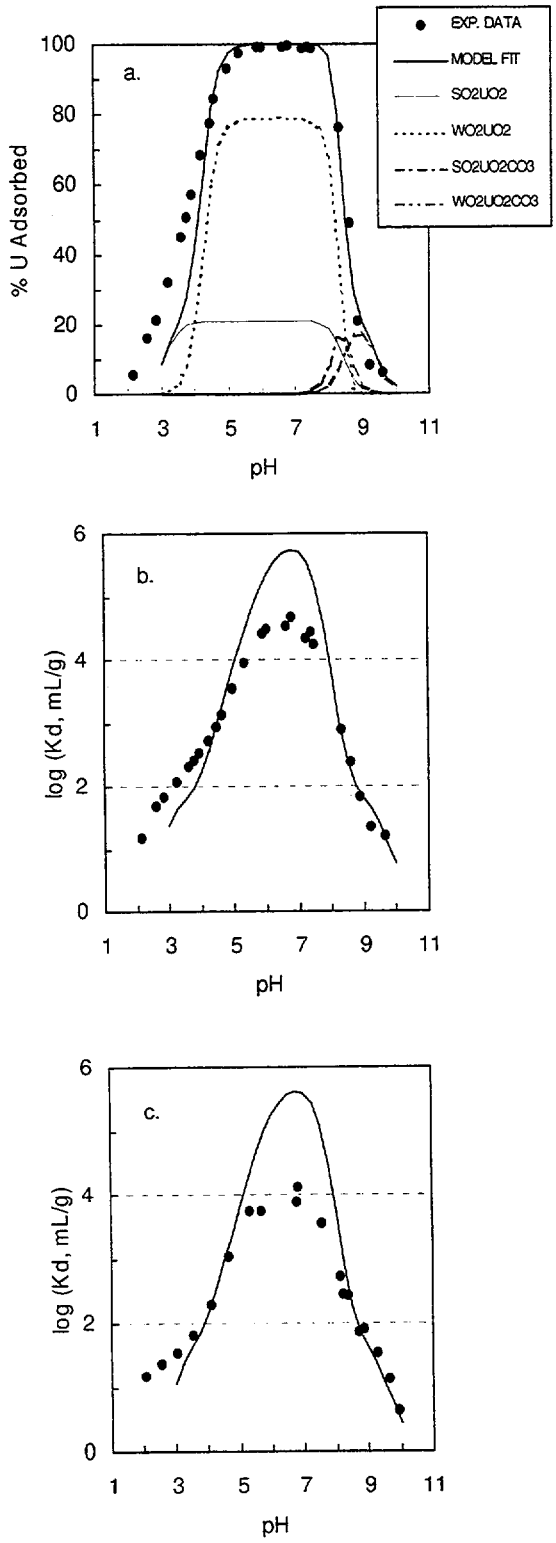

Figure 16-4. Results of generalized composite (GC) modeling approach assuming formation of bidentate uranyl and uranyl carbonato complexes and generic strong and weak surface sites. Part A, top) Percent U(VI) adsorbed to W2 substrate with total uranium concentration of 3.9 μM (distribution of individual uranyl surface species also shown); Part B, middle) U(VI) distribution coefficient (K_d) for W2 substrate with total U(VI) concentration of 3.9 μM, and c) U(VI) distribution coefficient (K_d) for W1 substrate with total uranium concentration of 3.7 μM.

17 EXPERIMENTAL INVESTIGATION OF URANIUM(VI) TRANSPORT THROUGH QUARTZ POROUS MEDIA UNDER VARIABLE CHEMICAL CONDITIONS

This section presents the results of transport experiments through columns packed with the same cleaned quartz powder that was used in the batch experiments described in Sections 5 and 13. The experiments examine the effect of U(VI) aqueous speciation on its transport. A majority of the results are also presented in Kohler et al. (1996).

17.1 Methods

17.1.1 THE COLUMN AND PUMP SYSTEM

Figure 17-1 depicts the experimental setup. The assembly consists of two stainless steel cylindrical piston pumps (ISCO Model #314), each with a volume of 375 mL and a flow rate adjustable up to 200 mL/hr. Experiments were conducted at flow rates of 5 and 20 mL/hour (corresponding to average linear pore velocities of $0.87 \cdot 10^{-3}$ and $3.50 \cdot 10^{-3}$ cm/s, Table 17-1). A pressure gauge was put in line at the outlet of each pump (range 0-15 psi). The chromatography column (inner diameter 2.2 cm, adjustable length 9-30 cm) could be fed from either of two pump-reservoir systems. System 1 was used during the pretreatment and elution

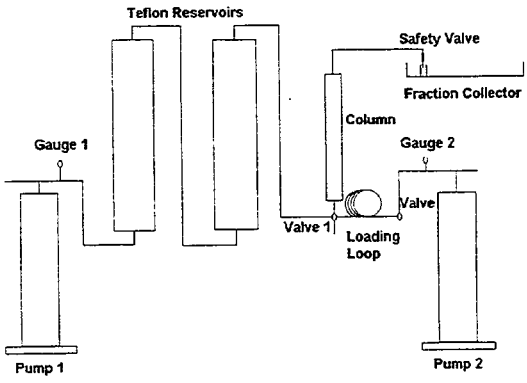

Figure 17-1. Experimental setup for column experiments.

phases of an experiment. To avoid contact between low pH electrolyte and the stainless steel pump, pump 1 was filled with a sucrose solution of density 1.2 g/mL, which was pumped into the first of two 650 mL Teflon reservoirs containing the electrolyte solution. The sucrose-electrolyte transition zone never reached the second reservoir during any experiment. System 2 was used to feed the column with a pulse of solution containing tritiated water and dissolved U(VI). Pump 2 was filled with water from a Nanopure water purification system (hereafter referred to as deionized water) that had a resistivity of 17.6 to 18.1 MOhm/cm. The pulse solution was displaced from the loading loop into the column. All tubing and fittings between the electrolyte reservoirs and the column and between the loading loop and the column were made of either 1/8" or 1/16" outer diameter (OD) Teflon, and the valves were 4-way Hamilton valves (Alltech Associates). A 1/16" OD Teflon tube was placed between the column outlet and the fraction collector.

Uniform packing in the column was obtained by pouring a suspension of 122 g of the treated quartz sample in 110 mL of deionized water into the column. Excess water was displaced by quickly immersing a plunger into the column. The length of the quartz bed was (21.1±0.1) cm.

17.1.2 FLUORIDE (F) ANALYSIS

F concentrations were determined with an Orion-Ross fluoride selective combination electrode (Model 96-09). Solutions were buffered with acetate buffer (0.5M total acetate) to pH 5.4. Equal volumes of sample or NaF standards and buffer were mixed and the electrode potential measured. A Nernstian relationship between the electrode potential and log [F] was found between $5 \cdot 10^{-6}$ M and $5 \cdot 10^{-4}$ M F with a slope equal to 60.25±0.26 mV/pF. Nitrate at the level of the background electrolyte concentration had no effect on the electrode potential.

Table 17-1. Average linear pore velocity and coefficient of hydrodynamic dispersion

Q [cm^3/hr]	pore velocity [cm/s]	dispersion coefficient, D_h [cm^2/s]
5	$8.70\pm0.05\cdot10^{-4}$	$1.65\pm0.6\cdot10^{-5}$
20	$3.501\pm0.005\cdot10^{-3}$	$3.62\pm0.13\cdot10^{-5}$

17.1.3 EXPERIMENTAL PROTOCOL FOR COLUMN EXPERIMENTS AT ACIDIC pH VALUES

The Teflon reservoirs (Fig. 17-1) were first filled with electrolyte adjusted to the appropriate pH. Standard electrolyte was 0.01M $NaNO_3$ at the experimental pH, but also contained F or acetate buffer if these solutes were being used in the experiment. To precondition the column, approximately 10 pore volumes of electrolyte were pumped through at the experimental flow rate. pH and F concentrations were measured at the outflow of the column. The column was considered as pretreated when pH differences between inflow and outflow were smaller than 0.02 pH units. The pulse solution was spiked with tritiated water, ^3HHO (hereafter referred to as HTO) and U(VI) stock solutions, and its pH was adjusted with 0.01N NaOH or HNO_3 to within 0.02 pH units of the pH of the electrolyte solution in the Teflon reservoirs. HTO (New England Nuclear) was diluted with deionized water to a stock solution containing 1 μCi/mL. A quench correction curve was recorded for ^3H using a standard quench set (Code #NBS 181340). Both the Beckman quench parameter ("H-number") and the quench correction curve were used to convert count rates into activities for ^3H. An aliquot of the pulse solution was then taken for activity references, and then the solution was loaded into the loading loop. An aliquot (about 10 mL) of U(VI) solution in the loading loop was discarded, and then another activity reference sample was pumped out of the loading loop through the valve below the column. While the column was still being pretreated with electrolyte from system 1, system 2 was activated to build up pressure to 5 psig, which was the pressure required to sustain a flow rate of 20 mL/hr through the column (a pressure of approximately 1.3 psi was required for the 5 mL/hr experiment). The U(VI) solution was pumped into the column to start the experiment by switching valve 1, starting pump 2 and stopping pump 1. Putting system 2 under pressure before actually displacing the U(VI) solution out of the loading loop ensured a smooth transition from one system to the other. In all cases, the U(VI) solution pulse injected into the column had a volume of 40 mL. Approximately 300 μL per fraction was collected during breakthrough and complete elution of HTO, and then the column outlet tubing was connected to the fraction collector. Four mL samples were collected by the fraction collector during U(VI) breakthrough. All fractions were weighed. Since vials on the fraction collector were left open overnight, some evaporation did occur. A curve of weight loss versus time was recorded and the weights of the fractions were corrected accordingly. At the end of an experiment the loading loop was emptied and a measurement of the activity of the last aliquot indicated that no significant adsorption occurred in the loading loop. The loading loop was then filled and rinsed with 0.01N HNO_3 and flushed with deionized water. The column was either flushed with $NaNO_3$ solution adjusted to pH = 3 (about 10 pore volumes) or pretreated with electrolyte for the next experiment. At the end of the series of experiments the column material was extruded, dried and weighed.

17.1.4 EXPERIMENTAL PROTOCOL FOR COLUMN EXPERIMENT AT pH 8.6

This experiment was conducted by injecting a four hour pulse of a solution containing 10^{-6}M dissolved U(VI). The supporting electrolyte was made up so that the total ionic strength was 0.01M. In comparison to the previous experiments at low pH, a relatively large fraction of the ionic strength came from the

contribution of $NaHCO_3$. A batch of five liters of electrolyte was made by adding four liters of deionized water to a jar. This water was purged with compressed air with an analyzed partial pressure of pCO_2 of 373 ppm, which is slightly higher than the often reported $10^{-3.5}$ atm (= 316 ppm). This was followed by dissolving 2.655g ($3.12 \cdot 10^{-2}$ mol) $NaNO_3$, 1.517g ($1.81 \cdot 10^{-2}$ mol) $NaHCO_3$ and 7.22 mL 0.1M NaOH, and the addition of sufficient deionized water to achieve a volume of one liter. This solution was mixed with the 4 liters of aerated deionized water, and the electrolyte was equilibrated again with the compressed air. The calculated pH of this water was 8.75 (HYDRAQL, Papelis et al., 1988); however, the electrolyte solution was slightly diluted by the addition of HTO and U(VI) stock solutions, lowering the pH of the pulse to 8.67±0.03.

17.1.5 EXPERIMENTAL PROTOCOL FOR COLUMN EXPERIMENT WITH A MIXTURE OF QUARTZ AND FERRIHYDRITE

Ferrihydrite was precipitated in the presence of dissolved silicate following the procedure of Method II described in Section 8. An acidic ferric nitrate solution containing 200 µM Fe(III) and 100 µM $Si(OH)_4$ was titrated to a pH of 6.8 during which precipitation occurred. (At low pH and at concentrations below 10^{-3}M, silicic acid should be present as a monomeric species). The precipitated ferrihydrite (Fe = $3.66 \cdot 10^{-4}$ moles) was mixed with 122g of quartz and packed into a column. The iron concentration was 3 µmoles Fe(III)/g quartz, which was the same as used in U(VI) batch adsorption experiments described in Section 8. The transport experiment was conducted in 0.01M $NaNO_3$ at pH 4.27±0.03 using a two hour pulse with 10^{-6}M dissolved U(VI) at a flow rate of 20 mL/h.

17.2 Results and Discussion

17.2.1 COEFFICIENTS OF HYDRODYNAMIC DISPERSION

Breakthrough curves of tritiated water (HTO) injected as a pulse at a flow rate of 20 mL/hr were reproducible and symmetrical in 10 experiments. All breakthrough curves were analyzed with CXTFIT [Parker and van Genuchten, 1984], a non-linear least squares fitting program, in order to estimate the linear pore velocity, v, and the hydrodynamic dispersion coefficient, D_h. Two HTO breakthrough curves for flow rates of 20 and 5mL/h, respectively are shown in Figure 17-2. The results are summarized in Table 17-1. From a plot of D_h vs. v, a value of $1.0 \cdot 10^{-5}$ cm^2/s was estimated for the diffusion coefficient of HTO in the porous medium (D_m^*) and the dispersivity, α, was estimated as $7.5 \cdot 10^{-3}$ cm. As expected, D_m^* was smaller than reported values for D_m, the diffusion coefficient of HTO in water, e.g., Nakayama and Jackson [1963] have reported a value of D_m of $2.4 \cdot 10^{-5}$ cm^2/s. The fact that D_m^* and D_h are of the same order of magnitude indicates that mixing in the column was in a range where molecular diffusion is comparable to mechanical dispersion. The Péclet number, defined as $Pe = L \cdot v/D_h$, where L is the column length [Schweich and Sardin, 1981; Bürgisser et al., 1993], was equal to approximately 2000, indicating that the overall transport was strongly advection dominated. The pore volume, V_p, calculated from HTO breakthrough curves was 32.67±0.10 mL after correcting for the volume of the tubing (0.97 mL), which was determined geometrically. This value of the pore volume agreed well with that determined by the weight of water in the saturated packed column determined by weight differences (32.71±0.30

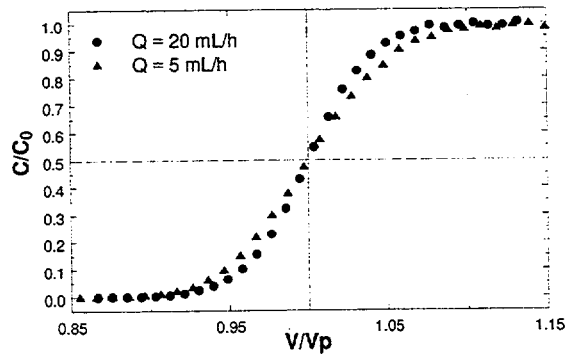

Figure 17-2. Breakthrough curves of tritiated water through quartz-packed columns at flow rates of 5 and 20 mL/hr.

mL). The porosity of the quartz bed, *n*, was 0.42.

17.2.2 FLUORIDE TRANSPORT

F breakthrough in the absence of U(VI) was investigated by injecting a pulse containing 1mM NaF at pH 5.6 (see Fig. 17-3 and Expt. 6 in Table 17-2). This concentration, which is an order of magnitude higher than that used in experiments with U(VI), was necessary because of the low sensitivity of the F electrode. Alternate fractions of the eluant were analyzed for HTO or F. No retardation of F relative to HTO was measured, indicating that F did not adsorb significantly on the quartz at this pH value.

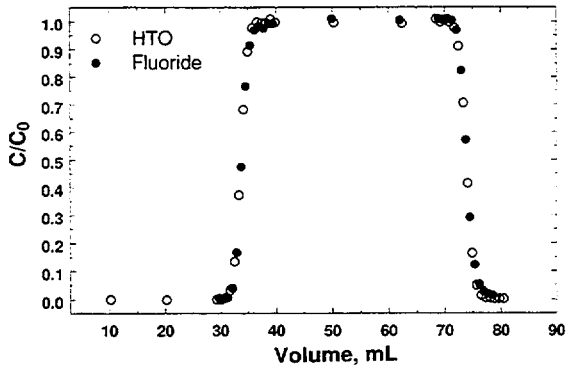

Figure 17-3. Comparison of the breakthrough and elution of tritiated water for a pulse of 1mM NaF solution at pH 5.6 at a flow rate of 20 mL/hr.

17.2.3 URANIUM (VI) TRANSPORT

Adsorption caused the breakthrough of U(VI) to be retarded relative to the nonreactive tracer, HTO. The extent of retardation depended on the solution chemistry. Table 17-2 lists the chemical concentrations used in the column studies. Breakthrough curves for each U(VI) transport experiment are presented in Figure 17-4. In all cases, the pH of the influent and the pulse solutions remained at a constant value (within 0.02 pH units). In the 50 μM dissolved U(VI) pulse experiments, the dissolved U(VI) concentration was comparable to the concentration of H^+ (approximately 56 μM) at pH 4.22. Because protons are released from surface hydroxyl groups as U(VI) is adsorbed (see Section 13), adsorption of U(VI) in the 50 μM dissolved U(VI) pulse experiment may

Table 17-2: Chemical conditions for column experiments

Experiment	pH	[U(VI)] [μM]	[F] [μM]	% U(VI) Recovered	Retardation Factor
1	4.26±0.02	1.0	0	96.9	8.9
2	3.90±0.02	1.0	0	98.6	3.2
3	4.79±0.02	1.0	100	94.8	8.7
4	4.39±0.02	1.0	100	97.1	2.5
5[1]	3.89±0.02	1.0	0	96.0	2.9
6	5.6±0.1	0	1000	N/A[2]	N/A
7	4.26±0.02	50.0	0	99.4	6.5
8[3]	4.22±0.02	50.0	0	99.5	3.7

Footnotes:

[1]*Flow rate was 5.0 mL/hr*

[2]*N/A means not applicable*

[3]*Contained 2mM Acetate Buffer*

cause a decrease in pH. To minimize pH changes, so that the effect of U(VI) concentration alone could be examined, a 2 mM acetate buffer was utilized in Experiment (Expt) 8. All other experiments were conducted in unbuffered media. Table 17-2 gives R_f, the retardation factor, for each breakthrough curve. R_f was calculated from the normalized first temporal moment of the U(VI) breakthrough [Roberts et al., 1986].

17.2.4 INFLUENCE OF pH AND FLOW RATE ON U(VI) BREAKTHROUGH

At a pulse input concentration of 1 μM U(VI), breakthrough curves at pH 4.26 and 3.90 show that the retardation factor, R_f, decreased from 8.9 to 3.2 (Figure 17-4a and Table 17-2). A decrease in retardation was expected because of

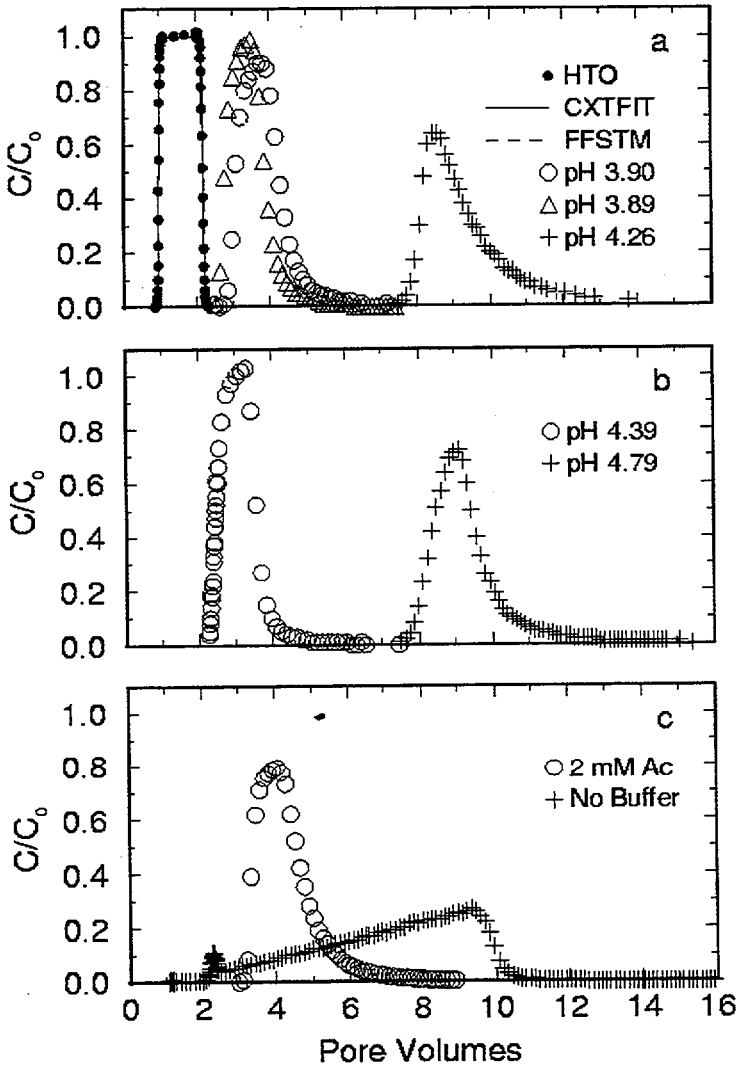

Figure 17-4. Breakthrough curves of U(VI) through quartz-packed columns under variable chemical conditions. a) Breakthrough of pulses of 1 μM U(VI) solution in 0.01M $NaNO_3$ eluant at pH 3.9 and 4.26 at a flow rate of 20 mL/hr, and at pH 3.89 at 5 mL/hr; breakthrough of HTO shown for comparison, b) Breakthrough of pulses of 1 μM U(VI) solution in 0.01M $NaNO_3$ eluant containing 100 μM fluoride at pH 4.39 and 4.79 at a flow rate of 20 mL/hr, c) Breakthrough of pulses of 50 μM U(VI) solution in buffered and unbuffered 0.01M $NaNO_3$ eluant at a flow rate of 20 mL/hr. Eluant was buffered at pH 4.22 with 2 mM acetate buffer in the former case. In the unbuffered experiment, the initial pH of the pulse and the eluant was 4.26.

the pH dependence of U(VI) adsorption on quartz (see Sections 5 and 13).

U(VI) breakthrough at flow rates of 5 and 20 mL/hr at pH = 3.89±0.02 and pH = 3.90±0.02, respectively, had retardation factors that differed by approximately 10% (Table 17-2). If the rate of U(VI) adsorption was rate-limiting during transport, then the initial arrival of the U(VI) pulse at 20 mL/hr would be expected to occur before that observed at 5 mL/hr, rather than slightly later (Fig. 17-4a). This is because the residence time for U(VI) in the column was four times longer at the slower flow rate, and therefore more time was available to reach equilibrium. Similarly, if desorption of U(VI) was rate-limiting, the trailing edge should be longer at 20 mL/hr than at 5 mL/hr, whereas the observations showed similar shapes for the two breakthrough curves. This suggests that the transport of U(VI) was not rate-controlled at either of these flow rates.

17.2.5 U(VI) TRANSPORT IN THE PRESENCE OF FLUORIDE

Uranium breakthrough in the presence of 100 μM F is shown in Figure 17-4b. If F had no effect, then the breakthrough of U(VI) at pH 4.39 (Expt 4) would be expected to be later than that observed at pH 4.26 in the absence of F (Expt 1), because retardation should increase with increasing pH (Fig. 17-4a). However, the R_f in Expt 4 was only 2.5 (Table 17-2). In the presence of 100 μM F, it is necessary to increase the pH considerably to achieve an R_f similar to that observed in Expt. 1. At a pH of 4.79 (Expt. 3), the retardation was nearly the same as in Expt. 1. These results illustrate that the formation of aqueous U(VI)-F complexes increased U(VI) mobility, which is consistent with the observation that F decreased U(VI) adsorption (Sections 5 and 13). A comparison of Expts. 1 and 3 (Figs. 17-4a and b) shows that the effects of increasing pH and fluoride complexation can cancel each other. The increased pH of Expt. 3 should cause a larger retardation factor, whereas the increase in F concentration should decrease the retardation. The result in this particular case was that the two retardation factors are nearly the same (Table 17-2).

17.2.6 THE EFFECT OF U(VI) CONCENTRATION ON TRANSPORT

Results for U(VI) breakthrough at a pulse concentration of 50 μM total U(VI) at pH = 4.26±0.02 are shown in Figure 17-4c. In the buffered system, the breakthrough curve exhibited a steep rising limb and long tail, as was observed for the previous experiments (Figs.17-4a and b). A comparison of the R_f for Expts. 1 and 8, which were conducted at nearly identical pH values, shows that the increase in the inlet U(VI) concentration from 1 to 50 μM U(VI) decreased the R_f from 8.9 to 3.7. This trend in retardation can be explained in terms of the fraction of the total U(VI) that is adsorbed (referred to below as fractional adsorption). The Freundlich isotherms observed for U(VI) (Fig. 5-9) had a slope less than one, which means that fractional adsorption decreases with increasing U(VI) concentration, as was observed in batch studies (Fig. 5-8). The decrease in fractional adsorption at the higher U(VI) concentration results in greater U(VI) mobility (Fig 17-4c).

The breakthrough curve for the unbuffered experiment at 50 μM U(VI) was significantly less symmetric than all others observed in this study (Fig. 17-4c). A small peak eluted at 2.4 pore volumes, followed by a long increase in C/C_0 up to approximately 9.3 pore volumes, and this was followed by a sharp drop in C/C_0. As mentioned above, the dissolved U(VI) concentration of 50 μM at the inlet was comparable to the initial H^+ concentration of approximately 56 μM. The unusual shape of the breakthrough curve likely resulted from spatial and temporal changes in pH within the column caused by U(VI) adsorption. These results are discussed further in Section 18.

17.2.7 COMPARISON OF ADSORPTION IN BATCH AND COLUMN EXPERIMENTS

The extent of adsorption in the batch and column studies can be compared by plotting adsorption isotherms from the observed

breakthrough curves. These isotherms can be determined from the trailing edge of breakthrough curves, assuming that dispersion is negligible and that U(VI) is the only solute with a changing concentration. The method of deriving these isotherms is explained in detail by Bürgisser et al. [1993] and Schweich and Sardin [1981]. Bürgisser et al. [1993] stated that dispersion can be ignored if the Peclet number exceeds 100, and since the Peclet number in our studies was approximately 2000, this assumption should create negligible errors. Given the assumptions above, the following equation quantifies the slope of the adsorption isotherm at the outlet of the column, i.e.,

$$\left(\frac{\partial q}{\partial c}\right)_{x=L} = \frac{n}{\rho_s(1-n)}\left(\frac{t_L(c)}{t_o} - 1\right) \qquad (17-1)$$

where q is the concentration of the adsorbed solute on the solid in moles/g, c is the solute concentration in solution in mol/cm^3, L is the column length in cm, n is the porosity, ρ_s the mineral density in g/cm^3, $t_L(c)$ is the travel time of concentration c, and t_0 is the travel time of a conservative tracer. Equation 17-1 indicates that the slope of the isotherm at a given concentration, c', is proportional to the retention time of a parcel of fluid exiting the column at concentration c'. Integration of Equation 17-1 from c = 0 to c = c' leads to the isotherm, q = q(c'). Since the trailing edge of the breakthrough curve is used, the computed isotherm corresponds to a desorption isotherm.

Figure 17-5 shows isotherms determined from the breakthrough curves at pH values of 3.90 and 4.26. At those two pH values, isotherms derived from the transport data (open symbols) are essentially coincident with the isotherms obtained from batch adsorption data (filled symbols). The isotherm for the buffered case at 50 μM U(VI) (triangles) has the same slope, but is shifted slightly to lower adsorption compared to the 1 μM U(VI) data. The decrease in adsorption can be attributed to the formation of aqueous U(VI)-acetate complexes (see Table 2-1). Speciation calculations show that 26% of

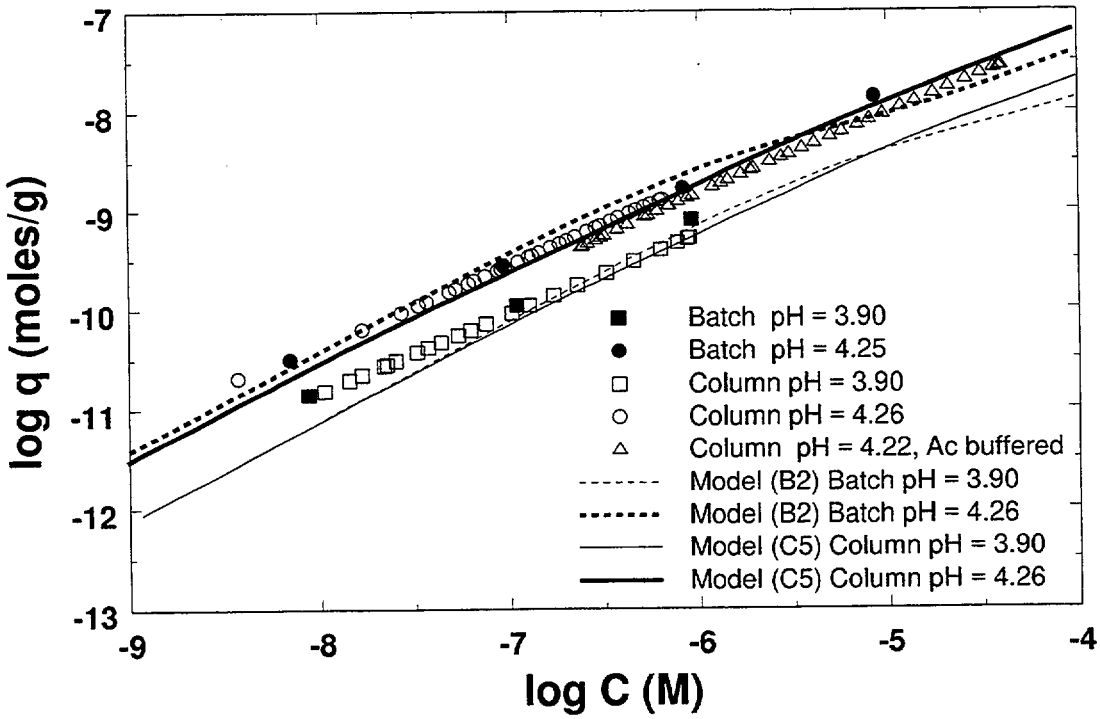

Figure 17-5. Adsorption isotherms for U(VI) adsorption on quartz determined from batch and column experiments. Model curves are discussed in Section 18.

total dissolved U(VI) should be complexed with acetate under the chosen conditions. If it is assumed that U(VI)-acetate complexes do not adsorb, like U(VI)-F complexes (see Section 13), then the dissolved U(VI) which is not complexed with acetate in the buffered experiment is decreased by 0.13 log units compared to the same system without acetate. A shift in the abscissa of 0.13 log units would essentially eliminate the difference between the two isotherms at pH 4.26 (Fig. 17-5, open circles and triangles).

Adsorption isotherms at pH values of 3.9 and 4.25 were derived from the batch adsorption data (as described above) and are shown in Figure 17-5. The isotherms are non-linear and each can be described by a Freundlich isotherm, $q = K_f c^{1/n}$. The slopes (= 1/n) of both isotherms were equal to 0.85±0.02, and were independent of pH over a wide U(VI) concentration range (Table 17-3). The Freundlich constant, K_f (q in mol/g; c in mol/mL), increased with increasing pH.

The close agreement between the Freundlich isotherm parameters derived from breakthrough curves and batch experiments (Table 17-3) suggests that the same adsorption equilibria occur in the batch and transport experiments, despite the greater solid/water ratio in the column. This conclusion is independent of any particular adsorption model, since it is based only on the relation between c and q determined experimentally. The agreement between the batch adsorption isotherms and column-derived desorption isotherms, and the lack of a kinetic effect with varying flow rate (Fig. 17-4a), support the validity of the local equilbrium assumption used in the multicomponent transport simulations discussed in Section 18.

The characteristic features of the breakthrough curves, a steep rising limb and a long trailing edge, are consistent with adherence to the Freundlich isotherm, with 1/n values less than 1 [Schweich and Sardin, 1981]. Although these breakthrough curve shapes could theoretically be caused by rate-limiting adsorption or desorption processes, the results suggest that local equilibrium applies.

17.3 Preliminary Studies of Uranium(VI) Transport in Other Systems

17.3.1 TRANSPORT EXPERIMENT AT pH 8.6 WITH CARBONATE COMPLEXES

In natural systems, U(VI)-carbonate aqueous complexes are important species above pH 7 (see Section 2). Concentrations of these species can become important at even lower pH values if the partial pressure of CO_2 increases above atmospheric levels, as is common in many aquifers. In batch experiments, U(VI) adsorption decreased at alkaline pH values in a system open to the atmosphere (Fig. 5-6a). It was therefore interesting to study U(VI) transport in an experiment with carbonate as a complexing ligand. A preliminary experiment was tried at a pH value of 8.6, in equilibrium with compressed air containing 373 ppm CO_2.

Table 17-3. Freundlich Isotherm Parameters Obtained from Batch and Column Experiments

	pH = 3.9		pH = 4.25	
	Log K_f	1/n	log K_f	1/n
Batch	-1.32±0.06	0.86±0.04	-1.01±0.03	0.85±0.01
Column	-2.11±0.005	0.79±0.002	-1.20±0.003	0.84±0.001
Column with 2mM Acetate			-1.48±0.02	0.82±0.004

The results of this experiment are shown in Figure 17-6. Clearly, U(VI) breakthrough is retarded with respect to the conservative HTO tracer. A retardation factor of approximately 7.7 was observed which is equivalent to a fractional uptake of 86.96% at the column conditions of 3.74 kg quartz/L.

17.3.2 TRANSPORT EXPERIMENT WITH A MIXTURE OF QUARTZ AND FERRIHYDRITE AS THE SOLID PHASE

There is evidence that solid mineral grains in the Koongarra system have coatings that contain ferrihydrite (see Section 9). The surface chemical features controlling adsorption and retardation may thus be strongly influenced by the properties of the coatings rather than the underlying mineral grains (see Section 8). A physical mixture of quartz and ferrihydrite, co-precipitated with silicate (Method II, Section 8) was chosen as a starting point for transport experiments involving more complicated solid phases.

The breakthrough curves for HTO and U(VI) in the column packed with the quartz/ferrihydrite mixture are shown in Figure 17-7. As opposed to the system with quartz only, a very flat breakthrough curve was obtained which had a very long tail. For comparison, data from the experiment that was conducted under the same conditions with quartz only are indicated in Figure 17-7 as open triangles. The peak shapes are very different. The ferrihydrite/quartz mixture seems to have a number of strong sites that delay the breakthrough of U(VI). Notice also that the HTO breakthrough curve does not show the steep rising and falling limbs as was the case in the systems with quartz only (see Figures 17-2 and 17-4a).

17.4 Summary and Conclusions

Transport of U(VI) through a porous medium of cleaned quartz was strongly influenced by the competing effects of adsorption and complexation reactions with ligands, such as F and carbonate. Retardation of U(VI) was very sensitive to pH, with retardation increasing threefold with an increase in pH from 3.9 to 4.26. At constant pH, a fifty fold increase in U(VI) concentration resulted in earlier breakthrough, with retardation decreasing by a factor of 2.5, because of the nonlinearity of the adsorption isotherm. The presence of 100 μM F greatly increased the mobility of U(VI), due to the formation of U(VI)-F complexes that did not adsorb on the quartz surface. Local chemical equilibrium was achieved within the range of conditions studied, as demonstrated by a negligible effect of flow rate on U(VI) breakthrough and the excellent agreement between desorption isotherms derived from the trailing edge of breakthrough curves and adsorption isotherms from batch adsorption data. The system studied is a conceptual representation of reaction types that may govern U(VI) mobility in oxidized natural waters, where competition between adsorption and complexation with the carbonate ligand control U(VI) transport.

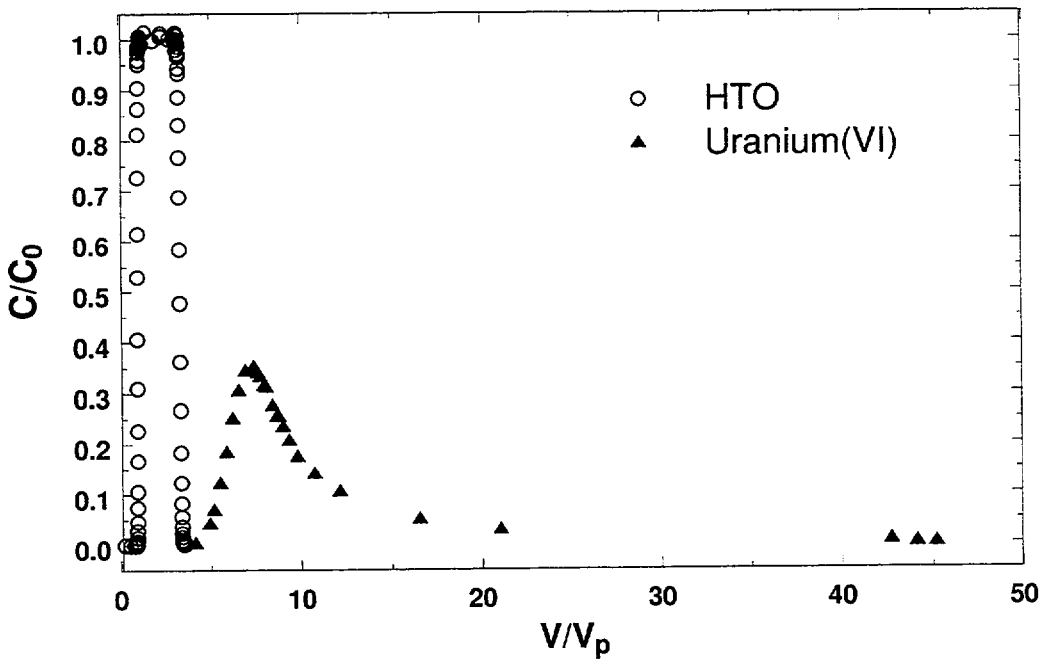

Figure 17-6. Breakthrough of a pulse of HTO and 1 μM U(VI) solution in 0.01M $NaNO_3/NaHCO_3$ eluant equilibrated with a partial pressure of 373 ppm CO_2 at pH 8.6 through a quartz-packed column at a flow rate of 20 mL/hr.

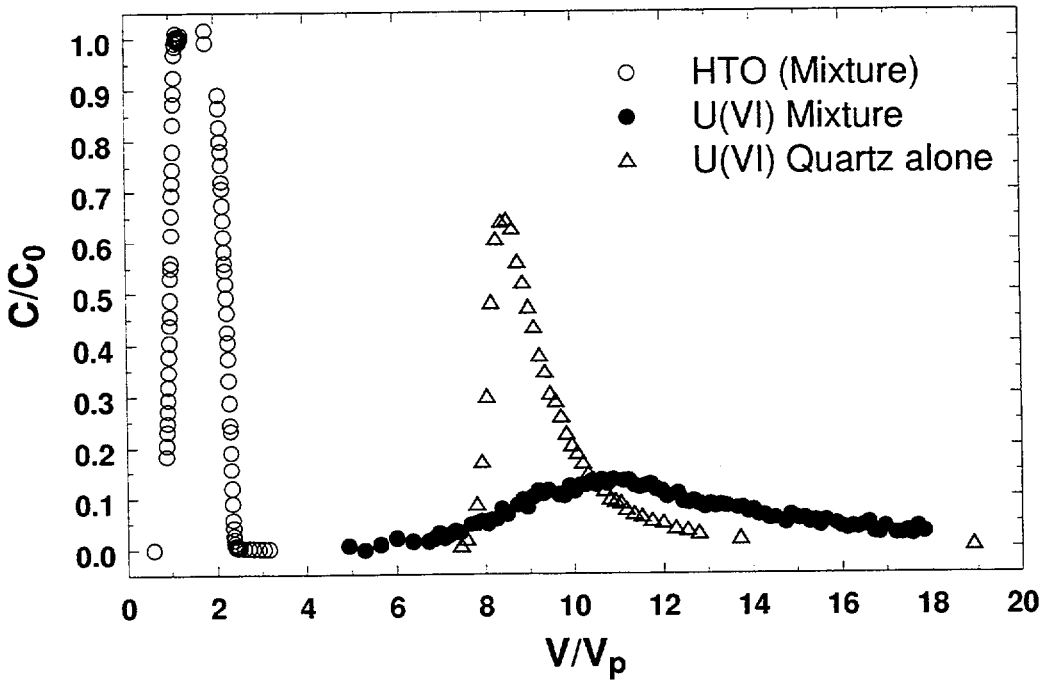

Figure 17-7. Breakthrough of a pulse of HTO and 1 μM U(VI) solution in 0.01M $NaNO_3$ eluant at pH 4.26 through a column packed with a mixture of quartz and ferrihydrite (3 μmoles Fe(III)/g quartz) at a flow rate of 20 mL/hr. Breakthrough of a pulse of U(VI) through quartz only under identical conditions shown for comparison.

18 REACTIVE TRANSPORT MODELING OF URANIUM (VI) MIGRATION THROUGH QUARTZ POROUS MEDIA UNDER VARIABLE CHEMICAL CONDITIONS

In this section, multispecies reactive solute transport simulations are described that: 1) evaluate the applicability of using a nonelectrostatic surface complexation modeling approach to simulate U(VI) transport under variable chemical conditions, and 2) compare the use of batch adsorption and transport data for estimation of parameters of the surface complexation model. The reactive transport simulations are also described in Kohler et al. (1996). First, transport simulations were performed to assess the ability of Models B1 and B2 (from batch data, Section 13) and their associated model parameter values to describe the U(VI) transport data. Next, a transport code was coupled with a non-linear least squares routine and applied to a subset of the transport data. Surface complexation model parameters were estimated to maximize the agreement between the transport data and the reactive transport simulations. The remaining transport data were predicted with the previously obtained parameters. Finally, the transport simulations with surface complexation parameters derived from batch adsorption and transport data were compared, and the differences between parameter values are discussed.

18.1 Modeling Approach

There are several approaches to modeling multicomponent solute transport. In one such approach, the chemistry is posed separately of the mass transport equations, which are written for each chemical component. Then, the numerical solution is obtained sequentially by iterating between a mass transport module and a chemical equilibrium module [Cederberg et al, 1985, Yeh and Tripathi, 1991]. Alternatively, a numerical solution can be obtained by directly inserting all of the chemical equilibrium equations into the transport equations [Jennings et al., 1982]. This yields a coupled nonlinear transport equation for each species. The equilibrium-controlled, multispecies transport simulations presented here were obtained using the Feed Forward Solute Transport Model (FFSTM) which was an early version of RATEQ Curtis (in preparation). FFSTM is based on the Feed Forward (FF) numerical method [Rubin, 1990]. The FF method effectively combines features of the two approaches mentioned above, such that the number of transport equations solved is the same as in the sequential approach, but the chemical equilibrium equations are differentiated and substituted into the transport equations to express the surface concentrations in terms of the primary dependent variables of the transport equations. For this study, the advection-dominated transport equations were solved using a flux-corrected transport algorithm [Boris et al., 1993], which gives oscillation-free results for grids that are significantly coarser than those required by standard finite difference methods or finite element methods based on linear basis functions. Simulations of HTO breakthrough (see Figure 17-4a) with FFSTM were of equal quality to the analytical solution from CXTFIT. FFSTM can accommodate all of the solution equilibria listed in Table 2-1, as well as multiple surface complexation reactions (without corrections for electrostatic energy). Short simulation times were important in this study, because FFSTM was also coupled to a nonlinear least squares fitting routine to enable the estimation of parameter values for various surface complex model formulations.

Several surface complexation models are commonly used that include correction for electrostatic interactions between charged surfaces and adsorbing ions [Davis and Kent, 1990]. If one includes an electrical double layer (EDL) model, such as the diffuse double layer model [Dzombak and Morel, 1990; Waite et al., 1994b] or the triple layer model [Davis et al., 1978], additional reactions and adjustable parameters must be included in the coupled transport model. Davis and Kent [1990] and Kohler et al. [1996] have argued that there is considerable uncertainty in determining the

values of EDL parameters in natural systems, and thus, a nonelectrostatic surface complexation approach may be a useful simplification for developing reactive transport models for practical applications. Davis et al. [1999] compared the various surface complexation models and found that the nonelectrostatic model performed as well as those with EDL correction in describing U(VI) batch adsorption data on quartz. For these reasons, a nonelectrostatic surface complexation model was used in this study. This approach simplifies the transport model and renders it easier to apply in studies of contaminated aquifers.

18.2 Transport Predictions with a Surface Complexation Model Derived from Batch Adsorption Data

The first transport simulations with FFSTM were performed to predict the breakthrough of U(VI) in the column experiments using the surface complexation model parameters derived from batch adsorption data (models B1 and B2; Section 13). As was the case in modeling the batch adsorption data, the one-site model (B1) did not fit the breakthrough curves well (simulations not shown). This is not surprising, since the non-linearity of the isotherms (Figs. 5-9 and 17-5) implies that a multi-site model is needed to describe U(VI) adsorption at variable U(VI) concentrations. Model B2 overpredicted retardation in the transport experiments with an initial U(VI) pulse concentration of 10^{-6}M (Fig. 18-1). The overprediction is large at pH 4.26 and relatively small at pH 3.9. However, Model B2 underpredicted retardation at pH 4.26 with an initial U(VI) pulse concentration of 50 μM (Expt 8). Although retardation was only estimated to within 30% in these simulations, the peakshapes were described fairly well in each case.

The discrepancy between the transport data and simulations with Model B2 (Fig. 18-1) likely occurs because of the extrapolation to conditions that were not considered in the batch adsorption studies. Figure 18-2 illustrates a Model B2 prediction of U(VI) adsorption as a function of pH under the column conditions of 3.7 kg/L quartz. Under these conditions, high U(VI) fractional adsorption is predicted in the pH range 3.9-4.3. The surface complexation model parameters of Model B2 were derived from FITEQL fits of batch adsorption data in 100 g/L quartz suspensions in the pH range 3.5-6.0 at various U(VI) concentrations (Section 13). Thus, the column experiments were conducted within the lower end of the pH range considered in the batch experiments, but at a much higher quartz/water ratio. The batch adsorption data collected in the pH range 3.5-4.2 showed very low fractional adsorption, and as a result, these points had a relatively high experimental error. Moreover, Model B2 did not fit the batch adsorption isotherm well at low U(VI) concentration at pH 3.9 (Fig. 17-5). Thus, the poor agreement between the transport data and Model B2 simulations illustrate the uncertainties inherent in such extrapolations (Kohler et al., 1996).

18.3 Surface Complexation Model Calibration with Transport Data

Because the predictions of U(VI) retardation with Model B2 were in error by as much as 30%, transport simulations were performed to estimate the surface complexation model parameters directly from the transport data. The objective was to evaluate various surface complexation reaction sets, including variable reaction stoichiometries and surface site types, to determine the simplest reaction set necessary to describe the observed breakthrough data. Each reaction set is referred to as a different surface complexation model. A total site density of 0.35 μmoles sites/g quartz was used in all the transport simulations. Parameters for each model were obtained by fitting both the effects of pH and U(VI) concentration simultaneously. Initial simulations showed that the effects of pH and U(VI) concentration could not be reproduced by fitting only two breakthrough curves. Consequently, data from three experiments (Expts 1, 2 and 8) were used as the calibration data set, which had different pH values at 1μM U(VI) and different U(VI) concentrations at pH 4.26. These data were used

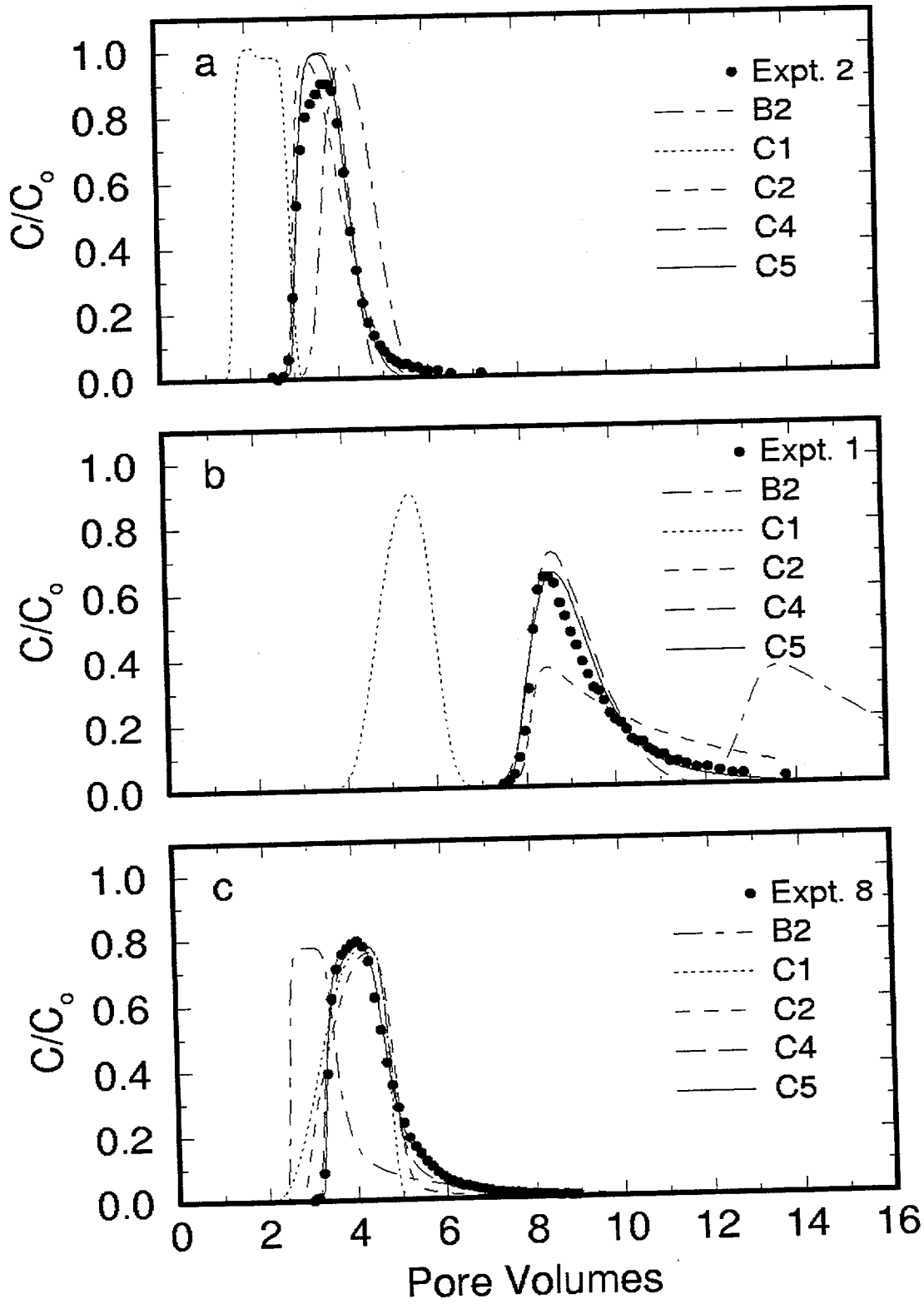

Figure 18-1. Comparison of U(VI) breakthrough curve data and transport model calibration simulations. Experimental conditions are described in Table 17-2. Reaction sets included in each model simulation are given in Tables 13-1 or 18-1.

Table 18-1. Surface Complexation Reactions and Parameter Estimation for Transport Modeling[a]

Model	Reactions	log K_i	f_i[b]	χ^2[c]
C1	$S_1OH + UO_2^{2+} + H_2O = S_1OUO_2OH + 2H^+$	-4.96	1.0	3.810
C2	$S_1OH + UO_2^{2+} + H_2O = S_1OUO_2OH + 2H^+$	-4.94	0.9972	1.145
	$S_2OH + UO_2^{2+} + H_2O = S_2OUO_2OH + 2H^+$	-1.97	0.0028	
C3	$S_1OH + UO_2^{2+} + H_2O = S_1OUO_2OH + 2H^+$	-4.95	0.988	1.385
	$S_2OH + UO_2^{2+} = S_2OUO_2^+ + H^+$	1.23	0.012	
C4	$S_1OH + UO_2^{2+} + H_2O = S_1OUO_2OH + 2H^+$	-4.98	0.988	0.702
	$S_2OH + UO_2^{2+} + H_2O = S_2OUO_2OH + 2H^+$	-3.28	0.012	
	$S_2OH + UO_2^{2+} = S_2OUO_2^+ + H^+$	1.06		
C5	$S_1OH + UO_2^{2+} + H_2O = S_1OUO_2OH + 2H^+$	-5.04	0.9748	0.464
	$S_2OH + UO_2^{2+} + H_2O = S_2OUO_2OH + 2H^+$	-3.56	0.0250	
	$S_2OH + UO_2^{2+} = S_2OUO_2^+ + H^+$	0.642		
	$S_3OH + UO_2^{2+} + H_2O = S_3OUO_2OH + 2H^+$	-1.15	0.0002	
C6	$S_1OH + UO_2^{2+} + H_2O = S_1OUO_2OH + 2H^+$	-5.04	0.9756	0.511
	$S_2OH + UO_2^{2+} + H_2O = S_2OUO_2OH + 2H^+$	-3.55	0.0252	
	$S_2OH + UO_2^{2+} = S_2OUO_2^+ + H^+$	0.630		
	$S_3OH + UO_2^{2+} = S_3OUO_2^+ + H^+$	2.82	0.0002	
C7	$S_1OH + UO_2^{2+} + H_2O = S_1OUO_2OH + 2H^+$	-5.08	0.9627	0.999
	$S_2OH + UO_2^{2+} + H_2O = S_2OUO_2OH + 2H^+$	-3.58	0.0360	
	$S_3OH + UO_2^{2+} + H_2O = S_3OUO_2OH + 2H^+$	-1.62	0.0013	

[a] *Total site density used in all model calculations was 0.35 μmoles sites/g of quartz (1.06 μmoles sites/m^2)*

[b] *f_i is the fraction of the total surface site density for each site type.*

[c] *χ^2 is the square of the weighted sum of the residuals as defined in Equation 18-1 (see text).*

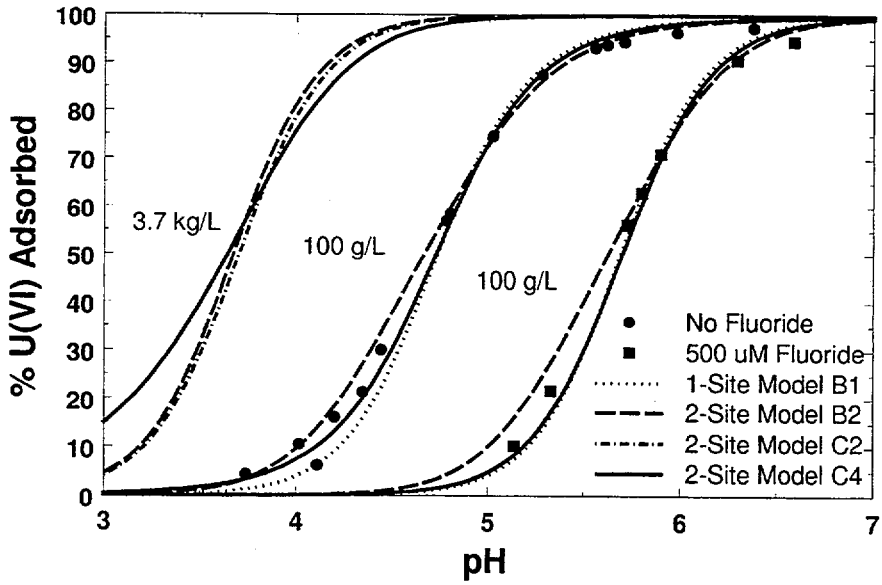

Figure 18-2. Comparison of U(VI) batch adsorption data and equilibrium chemistry model simulations for either column conditions (3.7 kg quartz/L) or batch experimental conditions (100 g/L). Curves and data on the righthand side of figure are for a system with 500 μM fluoride. Reaction sets included in each model simulation are given in Tables 13-1 or 18-1.

to obtain parameters (surface complexation formation constants and site densities) for each model. Aqueous U(VI)-acetate complexes (Table 2-1) were accounted for in modeling Expt 8, and it was assumed that these complexes did not adsorb on quartz. The assumption that acetate and U(VI)-acetate complexes do not adsorb is supported by the results of Davis [1982], who showed that adsorption of organic acids on quartz was only measurable at pH values less than 3. The different models considered, and their U(VI) surface reaction sets, are listed in Table 18-1. The first two models (C1 and C2) have the same reactions as Models B1 and B2 discussed in Section 13. The third and fourth model formulations (C3 and C4) introduce a second surface species, with the strong site releasing only one proton. The remaining model formulations (C5 - C7) consider a third type of surface site.

Once the best fit for a particular reaction set was obtained, the model was used to predict the effects of fluoride complexation and transport of 50 μM U(VI) in an unbuffered solution. Thus, the performance of a particular model (i.e., a reaction set) could be judged by the goodness-of-fit to the calibration data set and by its predictive capability.

The distribution of the fractional site densities and the surface complexation formation constants were estimated by a nonlinear least squares fit of the transport predictions to the breakthrough data. This fit was obtained by minimizing χ^2, the weighted sum of the residuals defined by:

$$\chi^2 = \sum_{j=1}^{N_S} \sum_{i=1}^{N_{d(j)}} (y_{i,j}^s - y_{i,j})^2 \qquad 18\text{-}1$$

where y^s is the simulated C/C_o, y is the observed C/C_o, N_d is the number of data points for each experiment, and $N_s = 3$ is the number of experimental data sets. χ^2 was minimized by the Levenberg-Marquardt method as implemented in MINPACK [Moré et al., 1980].

The one-site surface complexation model (Model C1) gave an inadequate fit to the observed data (Fig. 18-1). The model did fit the 50 μM data fairly well (Fig. 18-1c), but there was very little overlap of the computed breakthrough with either data set at 1 μM. The poor fit obtained with the one-site model is analogous to the difficulties in fitting batch adsorption data as a function of U(VI) concentration (see Section 13 and Waite et al., 1994b). At low U(VI) concentrations, a small population of surface sites is capable of adsorbing U(VI) more strongly, giving rise to greater fractional adsorption than observed for higher U(VI) concentrations. This results in greater retardation of U(VI) at lower concentrations at the same pH value (Figs. 17-4a and 17-4c). The values of log K and χ^2 for the best fit of Model C1 are given in Table 18-1. Attempts to manually fit the data with Model C1 indicated that it was not possible to fit both 1 μM data sets simultaneously, and that only one breakthrough curve could be matched well for a given log K. The tailing behavior was not reproduced by a one-site model. The fit to the 50 μM data gave the smallest χ^2 because this set had the most data points, and the data exhibited less tailing.

Introducing a second surface site type improved the fit of the transport simulations significantly to the observed data (Fig. 18-1, Model C2). However, in examining the fits to the three breakthrough curves, systematic deviations still remained. In Model C2, one surface reaction for each site type was used with the same reaction stoichiometry (two protons released, see Table 18-1), as was suggested from the two-site Model (B2) for batch adsorption data (Section 13). Model C2 fit the data of Expts 2 and 8 fairly well, but the prediction for Expt 1 showed a long tail beyond the data. The simulated long tail was caused by a combination of a very small fraction of strong sites (only 0.0028) with a log K that was three orders of magnitude larger than the weak site log K. That the tailing in Model C2 was less of a problem at lower pH (compare Figs. 18-1a and b) suggested that an additional surface reaction with different proton stoichiometry should be considered. Changing the stoichiometry of the strong site reaction so that only one proton was released by U(VI)

adsorption (Model C3) decreased the quality of the fit (a slightly larger value of χ^2). These simulations (not shown) fit the 50 μM data well, but slightly underestimated and overestimated retardation in Expts 1 and 2, respectively. However, when both the one proton and two proton release reactions were considered for the strong site (Model C4), the fit improved significantly (Fig. 18-1). The two-site Models C3 and C4 improved the fit to the tailing observed in the 50 μM U(VI) experiment (Fig. 18-1c), but did not reproduce the tailing for the experiments at 1 μM U(VI).

Three different three-site models (C5, C6 and C7) were considered. The purpose of introducing a third site was to evaluate if the tailing observed in the experiments could be simulated for all three breakthrough curves. To avoid introducing two additional fitting parameters for this new site type, the site density of the third site was held constant at 0.02% of the total site density in Models C5 and C6. The fit for Model C5, which had the smallest χ^2 of all models tested, is illustrated in Figure 18-1. These simulations capture all of the main features for each of the observed breakthrough curves, including the location of the center of the mass, the steep rising limbs, and especially in the cases of Expts 1 and 8, the long tails. For Model C6, the χ^2 was approximately 10 percent larger. For Model C7, the site density of the third site was allowed to vary, since this resulted in the same number of fitting parameters as in Models C5 and C6. Interestingly, the two-site Model C4 gave a better overall fit to the data than C7. This occurred because the model capability to fit the variation with pH was limited in Model C7, as all 3 proposed surface reactions released two protons.

18.4 Comparison of Batch- and Column-Derived Models

It is interesting to compare the breakthrough simulations for Models B2 and C2, which had identical model formulations. Model B2 simulations for both 1 μM breakthrough curves fell to the right of the observed data, and the simulation for the 50 μM curve fell to the left of the observed data (Fig. 18-1). The results suggest that the strong site contribution to the calculated U(VI) adsorption density was too large in Model B2. In the 1 μM U(VI) Model B2 simulations, adsorbed U(VI) at the peak of the breakthrough curve was bound approximately 85% to strong and 15% to weak sites, whereas at 50 μM U(VI) the contribution from the strong sites was essentially negligible. For Model C2, which was calibrated with the transport data, the distribution of adsorbed U(VI) at the peak of breakthrough was 40% bound to strong sites and 60% to weak sites in the 1 μM U(VI) simulations. The difference between the two models occurred primarily because of the values obtained for the strong site density, which was smaller by a factor of 6.4 in Model C2 compared to B2 (Tables 5-1 and 18-1). Although the parameters of the B and C models appear quite different, the C models generally produced a good fit to batch adsorption data, as shown for Model C4 in Figure 18-2.

Figure 18-2 also illustrates a comparison of predicted U(VI) adsorption as a function of pH under column conditions (quartz = 3.7 kg/L) for Models B2, C2 and C4. Fractional adsorption computed from the three models generally agreed to within six percent or less in the pH range of 3.9 to 4.26. The Model C4 adsorption edge is somewhat flatter than Models B2 and C2 due to the contribution of the adsorption reaction with one proton released (Table 18-1). Although the differences among these model simulations appears relatively small when plotted as adsorption edges (Fig. 18-2), the differences appear much greater when compared as simulated breakthrough curves (Fig. 18-1a,b). An R_f can be roughly estimated from the mean fraction of adsorption, f, using the relation, $R_f = 1/(1-f)$. At pH 4.26, values of f equal to 0.88 and 0.93 for models C4 and B2, respectively, correspond to R_f values of 8.6 and 14.4. For this case, a 5% increase in fractional adsorption increases R_f by over 60%. Thus, even a small error in estimated fractional uptake that results from the extrapolation of Model B2 to column conditions (high surface site concentrations, low pH) will seem greater when viewed as an error in predicted retardation.

The surface complexation model formulations can also be compared by calculating model isotherms and evaluating how well these agree with experimental data. Figure 17-5 shows calculated isotherms using the two-site Model B2 and the three site Model C5. The isotherm calculated with Model B2 underestimates adsorption at U(VI) concentrations in the range 10-50 μM. The disparity is consistent with the transport simulations for Model B2, which showed too little retardation for a pulse concentration of 50 μM U(VI) (Fig. 18-1c). The isotherm calculated from Model C5, however, agrees well with the data at pH 4.25 over a wide U(VI) concentration range.

The comparison of optimized surface complexation model parameters derived from batch and transport experiments is important, because batch adsorption data are easier to collect at a variety of chemical conditions. The results suggest that transport data could be preferable for model calibration, due to the highly sensitive relationship between fractional adsorption and retardation. However, this hypothesis should be viewed with considerable caution, as the batch-derived model parameters may have been affected by the extrapolation to column conditions. The results illustrate that batch experiments should be conducted under conditions as close as possible to those needed in modeling applications; high solid-water ratios should be studied in order to develop models for aquifers. Batch experiments may be preferable in cases where adsorption-desorption processes are rate-limiting and local equilibrium cannot be achieved in a column study. Furthermore, batch experiments will often be more convenient for calibrating models in systems where retardation values are expected to be extremely large.

18.5 Multicomponent Transport Predictions

Breakthrough curves for the remaining four data sets were simulated for all of the different model formulations in Table 18-1 without additional fitting. Predicted breakthrough curves based on Models C2, C4 and C5 are presented in Figure 18-3. Figure 18-3a shows the predictions at pH 3.89 and a flow rate of 5mL/hr (Expt 5). The agreement between the predictions and the data is good, but not as good as the fitted case with similar chemical conditions but a faster flow rate (Expt. 2, Fig. 18-1a). The difference between the predictions and data in Figure 18-3a may be partly due to small errors in the measurement of pH. For example, at a pH value of 3.85, model simulations (not shown) match the experimental data (measured pH of 3.89) in Fig. 18-3a very well. This result emphasizes the sensitivity of the simulations to variations in pH.

Predicted breakthrough curves in the presence of 100 μM F are shown in Figures 18-3b and c. At pH 4.39, all of the models shown reproduce the steep rising limb of the data and the significant decrease in retardation caused by complexation with F (Fig. 18-3b). The observed tailing is most accurately reproduced by the three site Model C5. The simulations at pH 4.79 (Fig. 18-3c) exhibited greater differences among the various model formulations. Model C2, which has only one reaction (two proton release) for each site type, showed significant deviations between the simulations and the data. Model C4, which is also a two-site model but includes two reactions on the strong site, reproduced the observed breakthrough reasonably well. The predicted rising limb occurred slightly before the data and the tail was not reproduced, but the center of mass was quite close. Model C5, which adds a third site to C4, yielded similar results except that the long tail was better simulated.

Figure 18-3d shows that the results of Expt. 7 (50 μM U(VI), unbuffered) were predicted very well despite the unusual shape of the breakthrough curve. All of the models reproduced the flat rising limb from 2.4 to 9.3 pore volumes, which was followed by a steep decrease in U(VI) concentration. However, only Model C2, which produced the most asymmetric breakthrough curves in all of the other cases, had a small peak at 2.4 pore volumes similar to the observed data.

Insight into the processes governing the unusual peak shape for the unbuffered 50 μM case can be gained by considering simulated

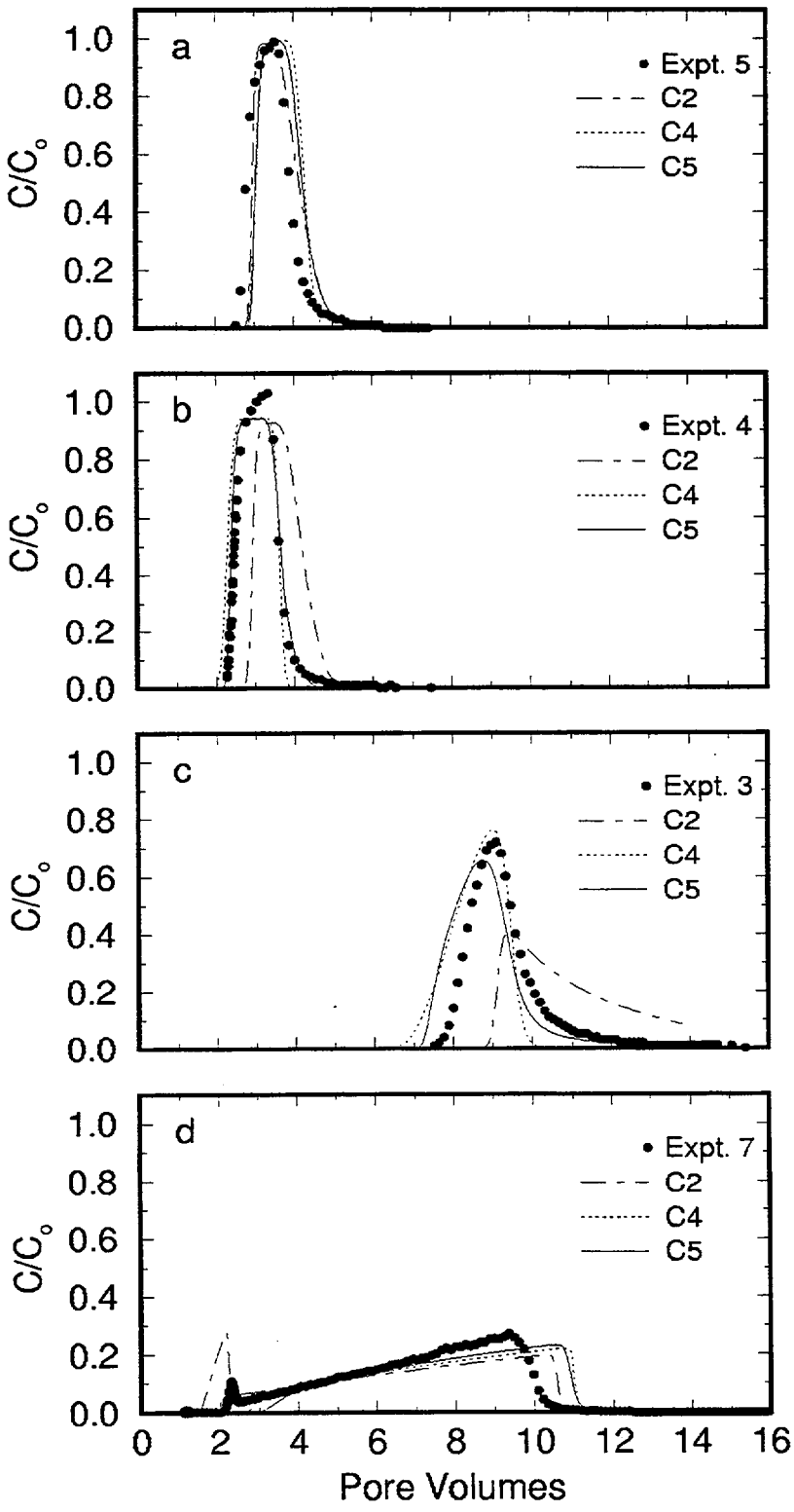

Figure 18-3. Comparison of U(VI) breakthrough curve data and transport model predictions with surface complexation model parameters derived from the transport calibration dataset. Experimental conditions are described in Table 17-2. Reaction sets included in each model simulation are given in Table 18-1.

concentration profiles in the column at various times. Model C5 was used to calculate total dissolved U(VI) and pH after 1.5, 2.5 and 12.5 hours (Fig. 18-4). One pore volume is transported in 1.63 hours, so at 1.5 hours, HTO would be nearing the peak of breakthrough. After 1.5 hours, total dissolved U(VI) and pH near the inlet of the column are predicted to stabilize at the concentration in the boundary condition. Proceeding downstream, pH decreases because H^+ is released as U(VI) adsorbs (Table 18-1). The U(VI) concentration also decreases, because the pulse has not completely filled the column. Note that dissolved U(VI) near the leading edge of the pulse is being transported at a pH of approximately 3.8. Experiments at pH 3.9 suggest that breakthrough at a low concentration should occur at approximately 2.2 pore volumes, which agrees well with the observed initial breakthrough at 2.1 pore volumes. After 2.5 hours, the U(VI) pulse has been completely contained within the column for a period of 30 minutes. At this time, U(VI) at the inlet of the column is desorbing and H^+ is adsorbing, causing the pH to increase. A steep concentration gradient in the upstream edge of the dissolved U(VI) front develops as U(VI) desorbs and H^+ adsorbs. On the downstream front, dissolved U(VI) concentrations remain

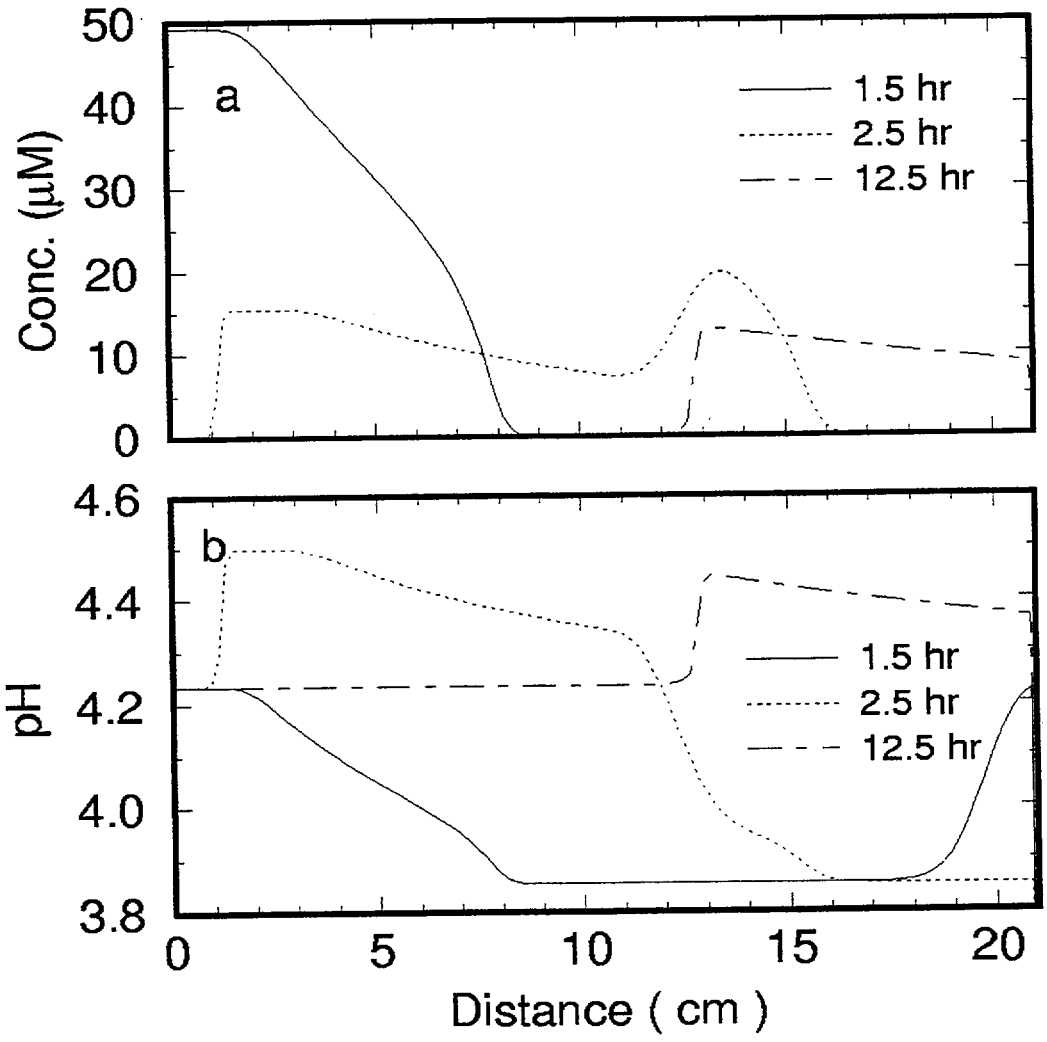

Figure 18-4. Evolution of pH and dissolved U(VI) concentrations simulated within the column using Model C5 at 1.5, 2.5 and 12.5 hours after the pulse injection in Experiment 7 (see Table 17-2).

high, as the higher pH region has not yet reached the downstream limits of the U(VI) containing solution. In simulations based on Model C2, this peak reaches the end of the column before the high pH front and causes the small peak in the computed breakthrough curve that is qualitatively similar to the observed data (Fig. 18-3d). The profile at 12.5 hr shows that the peak in U(VI) concentration near the end of the column is being transported at a pH of about 4.4, and the pH in the tailing edge of the breakthrough curve decreases to a value of 4.22 as the U(VI) concentration drops to zero.

Not surprisingly, the goodness-of-fit of model simulations to the transport data generally increased as additional fitting parameters were added to the model (Table 18-1). At least two site types were needed to obtain an adequate fit to the calibration data set used for parameter estimation. In addition, to account for pH effects, it was necessary to postulate that at least one of the surface reactions released only one proton. This approach was more successful than adding a third surface reaction site alone (Model C4 vs. Model C7). Model C4, which included three surface reactions and two site types (five fitting parameters) fit all of the data well and gave good predictions of the steep rising limbs and center of mass of the breakthrough. Adding a third site type (Model C5, seven fitting parameters) gave improved simulations that also reproduced the long tails in the breakthrough curves. Model C4 may give adequate results for estimating arrival times or for describing mean breakthrough behavior. However, this model would likely under predict the time required for a contaminated site to reach some minimum dissolved U(VI) concentration. Thus, the number of surface reactions and site types needed in a model formulation could vary with the application of the model.

It can be argued that the number of fitting parameters used in the surface complexation model is too large for reactive transport modeling. However, the general applicability of the model must be taken into account in this regard. Model C4 (with five fitting parameters) did a good job of simulating the results of all seven U(VI) transport experiments. A K_d modeling approach would have had only one fitting parameter to account for retardation; however, a different value of K_d would have to be determined separately for each experiment and the asymmetric shape of the breakthrough curves would not have been simulated. The asymmetric shape can be simulated in a transport model that is coupled with a Freundlich isotherm, but such a model would only be valid at one pH value and would not account for the effects of aqueous complexation under variable chemical conditions.

Chemical conditions were held constant in the column in all of the experiments of this study except Expt 7 (50 μM U(VI), unbuffered). In that case, pH varied spatially and temporally in the column. For that experiment, neither a K_d or Freundlich isotherm modeling approach could account for the variable chemical conditions in the column and the resultant effects on transport, whereas the surface complexation model could. In addition, the surface complexation model can account for the effects of any number of F concentrations or for a F concentration gradient in time or space, whereas the K_d or Freundlich isotherm modeling approaches require new parameter values for each F concentration and cannot be easily applied to a system with an F concentration gradient. The surface complexation model can also be used to calculate K_d values under variable chemical conditions as an input to larger modeling exercises, such as waste repository performance assessment models.

The general applicability of the surface complexation model under variable chemical conditions illustrates the utility of this approach in reactive transport modeling. This is particularly true for modeling the transport of inorganic solutes that undergo significant changes in solution speciation as chemical conditions vary. For example, aqueous U(VI) speciation in natural waters is highly complex, with both carbonate and organic acids forming very strong bonds with UO_2^{2+} [Waite and Payne, 1993; Waite et al., 1994b; Pompe et al., 1996]. These species may strongly influence the migration of U(VI) in many aquifers and soil solutions [Lienert et al., 1994; Waite and Payne,

1993], and any chemical variations or gradients in these systems can best be accounted for with reactive transport modeling that includes the surface complexation concept.

18.6 Concluding Remarks

Multispecies reactive transport modeling examined the tradeoff between minimizing the number of surface complexation model parameters and maximizing the goodness-of-fit to observed U(VI) breakthrough data. A nonelectrostatic, one-site surface complexation model, which required only two fitting parameters (surface site density and an equilibrium constant for one adsorption reaction), gave poor fits to the breakthrough data. A two-site model (strong- and weak-binding sites) with three adsorption reactions (five fitting parameters) produced good fits to the three breakthrough curves used for model calibration. In addition, without additional fitting, this model was able to predict the effects of F complexation on U(VI) transport and the unusual breakthrough of U(VI) that resulted from temporal and spatial variations in pH in one experiment. Reasonable simulation of the tails of breakthrough curves required the addition of a third site type to the model, increasing the number of fitting parameters to seven. A two-site model (four fitting parameters) calibrated by optimization of the fit of a U(VI) batch adsorption data set gave good qualitative predictions of U(VI) transport (retardation within 30%) in the quartz column. The discrepancy between these model simulations and the breakthrough curve data was probably caused by extrapolation to conditions in the column that were not studied in the batch experiments.

The results demonstrate the general applicability of coupled reactive transport and chemical speciation models that include the surface complexation concept to describe adsorption. Such models calculate the activities of the aqueous components involved in the formation of surface complexes (adsorbed species). Therefore, this modeling approach can better account for variations in aquifer chemistry on the fate and transport of reactive metal ions in groundwater.

19 STATUS OF SURFACE COMPLEXATION MODELING WITH NATURAL MINERAL ASSEMBLAGES AND APPLICATION TO PERFORMANCE ASSESSMENT MODELING

19.1 Introduction

Applications of the surface complexation concept to adsorption of ions by soils and sediments are relatively rare due to the complexity of natural systems. Some notable examples include Turner et al. (1996), Zachara et al. (1995a), Zachara et al. (1995b), Stollenwerk (1995), and Davis et al. (1998). One of the complexities of soils and sediments is identifying the mineralogical composition in the near-surface region of sediment grains (Coston et al., 1995). In addition, the composition of aqueous solutions is not easily controlled in experiments with soils and sediments. This makes it more difficult to determine condition-independent stability constants of molecular scale reactions than is the case for single, insoluble mineral phases bathed in simple electrolyte solutions.

The surface properties of mineral phases in soil and subsurface environments are greatly altered by the accumulation of poorly crystalline phases of iron(III) and aluminum oxyhydroxides and silicates (Padmanabhan and Mermut, 1996). Diagenesis and interactions with bacteria may cause leaching of surface layers of minerals (Hiebert and Bennett, 1992), formation of various mixed layer clays, and the deposition of extremely fine-grained, high surface area precipitates (Parfitt et al., 1992). For surface complexation modeling (SCM), the principal difficulties posed by these materials are that the identity, structure, composition, and electrical double layer properties of the wetted surface are usually not well known. As will be discussed below, this fact has important ramifications for the approach to SCM, as some of the *a priori* assumptions and experimental techniques that are used in developing an SCM for a pure, single mineral phase may not be valid for developing an SCM for a complex mineral assemblage.

In many cases, the surface chemical properties of sediments may be completely dominated by secondary minerals or grain coatings, which usually constitute only a minor fraction of the sediment mass (Coston et al., 1995; Jackson and Inch, 1989; Davis, 1984). It has been shown that the surfaces of silica, rutile, ferrihydrite, and goethite become enriched with Al when they are mixed with poorly crystalline alumina phases or solutions containing dissolved Al (e.g., Lovgren et al., 1990). These types of surface enrichment can greatly alter the chemical and adsorptive properties of mineral surfaces (Ainsworth et al., 1989). Coston et al. (1995) showed that metal ion adsorption by an aquifer sediment was far more reactive than pure quartz surfaces because of the extensive Al- and Fe-rich surface coatings present on the quartz grains of the sediment. This scenario of surface reactivity being significantly altered by the presence of grain coatings is expected to be typical for natural mineral assemblages.

19.2 General SCM Development Methodology

The methodology used for developing an SCM to describe radionuclide adsorption for natural mineral assemblages in an aquifer can be considered as consisting of two major parts: 1) a field characterization phase, and 2) an SCM development phase. Characterization of the field site is required to: 1) determine the porosity of an unconsolidated aquifer (in the case of fractured rock, the wetted mineral surface area per unit volume of groundwater), 2) determine the reactive surface area of aquifer sediments, 3) identify the bulk *and surficial* composition of solid phases present in the aquifer sediments, including both chemical and mineralogical data, and 4) determine the chemical composition and aqueous speciation of groundwater solutes. It is important that the spatial variability of each of these properties of the aquifer be considered in the field characterization. The porosity value and reactive surface area is used to scale the SCM

(calibrated with laboratory data) to the field conditions.

The mineral and solution phase composition data are used to develop a geochemical model of the aquifer. The initial objective of geochemical model development is to obtain coherence between groundwater chemical and aquifer mineralogical data, and values calculated using thermodynamic relations for mineral phase solubility and aqueous speciation equilibria (Altmann and Bruno, 1999). Among the difficulties frequently encountered at this stage are large uncertainties in the solubilities of complex, heterogeneous solid phases, such as clay minerals.

The mineral and solution phase composition data and the geochemical model are used to propose hypotheses about which solid phases are likely to govern radionuclide transport and the range of system compositions over which K_d values will be needed. Generally, one or more minerals known to be capable of undergoing adsorption reactions with the radionuclides can be identified (Altmann and Bruno, 1999). In this case, experimental results and existing data bases for adsorption on reference solid phases can be used as the basis for formulating initial hypotheses regarding the stoichiometry of radionuclide adsorption reactions and the effects of the temporal or spatial variability of other solutes on radionuclide K_d values.

In the SCM development phase, the experimental and modeling approach to be used for each radionuclide of interest is defined based on the above information. The experimental approach typically commences with measurements designed to provide an initial estimate of the number and total concentration of adsorptive components (Altmann and Bruno, 1999; Davis et al., 1998; Coston et al., 1995). This is followed by a stepwise, iterative modeling process of testing surface complexation reaction equations for the various adsorbing components, wherein potential stoichiometries and adsorbed radionuclide species formation constants are compared in their capability to accurately represent experimental data (Davis et al., 1998; Turner, 1995).

As mentioned in Section 1, there are two major approaches for applying the SCM concept to radionuclide adsorption in soils and sediments (Davis et al., 1998): 1) the component additivity (CA) approach, and 2) the generalized composite (GC) approach. In the CA approach, the modeler attempts to *predict* adsorption on a complex mineral assemblage, using the results of a surface characterization of the assemblage and collected data for adsorption by pure, reference minerals and organic phases. It is assumed in this approach that the wetted surface of the complex mineral assemblage is composed of a mixture of one or more mineral (or organic) phases, whose surface properties are known from independent studies of the individual phases. Once the relative abundance and identity of the major adsorptive phases have been determined and the appropriate databases for reference mineral phases have been assembled, a system of mass law equations can be written to describe the SCM equilibria of each radionuclide with each solid phase in the mixture. Radionuclide adsorption by the mixture can then be calculated by summing the adsorptive contributions of each phase, weighted according to its relative abundance in the mixture.

In the *generalized composite* (GC) approach, it is assumed that the surface composition of the mineral assemblage is inherently too complex to be quantified in terms of the contributions of individual phases to adsorption. Instead, it is assumed that the adsorptive reactivity of the surface can be described by SCM equilibria for each radionuclide written with "generic" surface functional groups, with the stoichiometry and formation constants for each equilibria determined by fitting experimental measurements of radionuclide adsorption by the mineral assemblage.

19.2.1 DETERMINATION OF TOTAL SURFACE SITE DENSITY FOR NATURAL MINERAL ASSEMBLAGES

For a complex mineral assemblage, the most expedient approach for determining the total surface site density for SCM is to carefully measure the "reactive" specific surface area of the assemblage. The reactive surface area of a sample depends on its composition and the nature of the adsorption reactions under consideration. For example, the basal planes of 2:1 layered aluminosilicate minerals are considered unreactive for strongly sorbing ions (Zachara et al., 1994; McKinley et al, 1995), and it is recommended that this surface area be excluded from the model, except in cases where the radionuclide participates in ion exchange reactions, e.g., ^{90}Sr. For radionuclides dominated by strong covalent bonding at the surface (e.g., the actinide elements), the BET surface area of the sample may be the best experimental determination of the reactive surface area (Davis and Kent, 1990). For certain poorly crystalline structures, e.g., ferrihydrite or imogolite, the reactive surface area may be larger than what is determined by the BET method, and the surface area may need to be assumed based on values found in the literature for these poorly crystalline phases.

Once the reactive surface area has been determined, one can quantify the concentration of functional groups that participate in SCM by multiplying the area by the surface site density (i.e., moles of sites/unit surface area). For the GC modeling approach, the recommended site density is 3.84 μmoles of surface sites per square meter of surface area (Davis et al., 1998). In the CA modeling approach, one must estimate the relative surface areas of each adsorbing phase that is present in the mineral assemblage, or assume that a particular phase or set of phases dominates radionuclide adsorption. Once this estimate or assumption is made, the concentration of functional groups for each phase in the model can be determined by multiplying its surface area by the site density for that phase. The site densities of many mineral phases per unit surface area are available in the literature (Davis and Kent, 1990).

19.2.2 ELECTROSTATIC CORRECTION TERMS FOR SURFACE COMPLEXATION EQUILIBRIA

Several SCM approaches for correcting mass action equations for coulombic effects have been proposed. In the diffuse double layer (DDL) model of Dzombak and Morel (1990), for example, the molecular scale reaction that describes the adsorption of divalent metal ions by iron oxides is:

$$Me^{2+} + \equiv FeOH \overset{K_{Me}}{\leftrightarrow} \equiv FeOMe^{+} + H^{+} \qquad (19\text{-}1)$$

where ≡FeOH refers to a structurally undefined, average ferrinol group on the surface (assumed to be an amphoteric hydroxyl group), and K_{Me} is the "intrinsic" stability constant for the mass action equation. The mass law for Eq. (19-1) is written as follows:

$$[\equiv FeOMe^{+}]\{H^{+}\} = [\equiv FeOH]\{Me^{2+}\}K_{Me}(\exp(-F\Psi/RT)) \qquad (19\text{-}2)$$

where { } denotes the activity of a dissolved solute, [ ] denotes the concentration of an adsorbed species, and the exponential term is the electrostatic energy for forming a surface species with a charge of +1, in which Ψ is the mean field potential at the surface (Dzombak and Morel, 1990).

Equation 19-1 suggests that one proton is released per Me^{2+} adsorbed at the surface; however, this considers only the stoichiometry of the reaction in Eq. (19-1). The charged species formed, $\equiv FeOMe^{+}$, increases the surface charge and mean field potential, and this promotes additional proton release through coulombic repulsion via the following reaction,

$$\equiv FeOH \leftrightarrow \equiv FeO^{-} + H^{+} \qquad (19\text{-}3)$$

Thus, with correction to Eq. (19-1) for coulombic effects, calculations with the DDL model suggest that a macroscopic release of 1.7 to 2.0 protons per Me^{2+} adsorbed should be observed

experimentally, depending on the pH and ionic strength of the solution (Dzombak and Morel, 1990). This point emphasizes the potential importance of the magnitude and accuracy of electrostatic correction terms in SCM.

Perhaps the simplest of all SCM is the non-electrostatic model (NEM), which considers surface equilibria strictly as chemical reactions, without explicit correction for electrostatic attraction or repulsion (Davis et al., 1998). In the NEM, the pH-dependent coulombic energy contribution to the mass action equation is simply included within the apparent binding constant. The apparent binding constants and the stoichiometry of the mass action equations are derived by fitting the *macroscopic* dependence of ion adsorption as a function of pH. As a consequence, the mass action equations that describe ion adsorption in an NEM are not expected to provide accurate representations of the stoichiometry of the reactions at the molecular scale.

While it has been applied in relatively few instances (Davis et al., 1998; Bradbury and Baeyens, 1997; Zachara et al., 1994, 1995a; Koss, 1988), the NEM may be the most appropriate for environmental applications because of its simplicity. Since it is difficult to assess the actual surface charge of mineral phases in complex mixtures of phases, it will usually not be possible to determine the appropriate electrostatic correction terms that are required in the more complex SCM (Davis et al., 1998), such as the DDL or the triple layer model (TLM). It is known that the surface charge of mineral phases in natural waters is very different from that observed in simple electrolyte solutions. For example, the adsorption of some major ions in natural waters (e.g., Mg^{2+}, Ca^{2+}, SO_4^{2-} and silicate) and the formation of organic coatings are known to cause large changes in measurements of the point-of-zero-charge (pH_{PZC}) and isoelectric point (pH_{IEP}) of mineral phases.

19.3 Scientific Contributions of this Report

In Sections 3 through 8 of this report we examined the nature of U(VI) adsorption to a variety of single minerals and, in so doing, developed an appreciation for the type of models that may be appropriate for description of U(VI) adsorption by a complex mineral assemblage, the Koongarra sediments. The studies increased our understanding of U(VI) adsorption to ferrihydrite, quartz, imogolite, kaolinite, hematite, and quartz with ferrihydrite coatings. This research is important since it forms a foundation upon which U(VI) adsorption by the Koongarra weathered soil and other mineral assemblages can be understood. Continued studies of radionuclide adsorption by pure mineral phases are also needed to continue the development of thermodynamic databases for adsorption (Turner, 1995). The SCM developed in Sections 12 through 15 also contribute to this goal, as well as serving as a starting point for modeling the Koongarra weathered soil (Section 16).

The study of U(VI) adsorption by the Koongarra sediments (Sections 9-11) is important because so few comprehensive studies of radionuclide adsorption by natural materials have been published. The research included methods for identifying and quantifying adsorbing mineral phases present in complex mineral assemblages. This is essential in order to be able to make use of the qualitative and quantitative information gained in studies of radionuclide adsorption by pure mineral phases. To use the CA modeling approach, it was assumed that the phases responsible for U(VI) adsorption by the weathered soil could be dissolved by Tamms' acid oxalate and dithionite-citrate-bicarbonate extractions. Using these data, it was found that the CA modeling approach provided a good description of U(VI) partitioning between solid and liquid phases in the mid-pH range (Section 16). The model was less successful in describing U(VI) adsorption at the pH extremes,

underpredicting the extent of adsorption at pH<6 and overpredicting adsorption at pH>8.

In comparison, the GC modeling approach provided a better description of the extent of U(VI) adsorption as a function of system conditions than did the CA approach. The GC approach enabled a reasonable prediction of the extent of U(VI) adsorption over a wider range of system conditions (Section 16). The research also showed that laboratory partitioning data, obtained from batch suspension studies, was representative of both partitioning observed in laboratory column studies over a wide range of system conditions (Sections 17 and 18) and of partitioning observed in the field (Section 11) over a much narrower range of conditions.

19.4 Implications to Performance Assessment Modeling

Advanced performance assessment (PA) modeling of nuclear waste repositories requires an estimation of the geochemical evolution of the entire repository system for various time-dependent scenarios. This is normally done by studying the variation of key chemical parameters (pH, Eh, major ion groundwater composition) in the various parts of the repository system with geochemical modeling. The variability in the geochemical composition of the system influences the adsorptive reactivity of radionuclides along a migration path. Thermodynamic models that include SCM can be integrated within a common framework, allowing simultaneous consideration of both the geochemical variability of the system and its influence on radionuclide adsorption, thereby providing support for the selection and uncertainty estimation of radionuclide K_d values (Altmann and Bruno, 1999).

From a practical standpoint, modeling with SCM offers advantages to the PA modeling effort: 1) the SCM approach is based on fundamental chemical principles, and therefore can be defended in terms of its scientific rationale, and 2) SCM modeling can be cost effective to the U. S. Nuclear Regulatory Commission and its licensees over the long term, in comparison to the large number of K_d values that should be required for advanced PA modeling. A great deal of effort has been invested in experimentally determining K_d values for a relatively small number of radionuclides on a wide variety of geological solids (Altmann and Bruno, 1999). It is now recognized that a K_d measured for a given radionuclide/solid phase combination under one set of conditions cannot generally be used to accurately predict a K_d for another set of conditions (Kohler et al., 1996). In contrast, an SCM modeling approach allows predictions of radionuclide partitioning over a wider range of system conditions because it quantifies the fundamental parameters responsible for radionuclide partitioning and couples adsorption calculations with aqueous speciation (Davis et al., 1998).

In addition, an SCM distinguishes between the chemical processes of adsorption and precipitation, each of which may contribute to radionuclide partitioning during a PA calculation. As a result, the PA modeler will have a better understanding of the nature and reactivity of the radionuclide, and predictions of its transport under hypothetical scenarios of changing chemical conditions, either spatially or temporally, will be more accurate. Thus, the long term fate of the radionuclide can be predicted with greater confidence.

Given the relative success of the SCM models in describing the adsorption of U(VI) to sediments in the laboratory (Section 16) and the apparent equivalence of partitioning of U(VI) to laboratory suspensions and sediments in the field (Section 11), the SCM modeling approach can provide a tool of considerable benefit to PA modeling.

It is necessary for PA transport and SCM modelers to work more closely together in order to build confidence and provide technical support for the efforts being pursued in each of these scientific communities. SCM modelers need to support PA transport modelers, by providing an understanding of the SCM modeling approach and an appreciation of the

importance of knowing how and why K_d values may vary with geochemical conditions. These collaborative efforts could reduce the uncertainties of quantifying adsorption in PA transport modeling and increase its scientific defensibility.

In summary, SCM can be of significant value to PA if it is used to determine the range of K_d values that need to be considered and provide a scientific basis for the range of values chosen. The uncertainties in SCM parameters are less than the uncertainties in K_d values (when considered over a range of chemical conditions), and the uncertainties are more easily quantified. If used properly, SCM for radionuclide adsorption has the potential to increase the confidence and scientific credibility of PA transport modeling by reducing the uncertainty in quantifying adsorption and by providing a means of better quantifying that uncertainty.

20 CONCLUSIONS AND RECOMMENDATION

20.1 Conclusions

a) Spectroscopic data showed that ternary ferrinol-uranyl-carbonato complexes exist at the surface of iron oxide mineral phases over a wide pH range. Analogous surface species may be the predominant form of adsorbed U(VI) on many oxide and aluminosilicate mineral phases.

b) Mineral coatings were more important than bulk mineralogy in controlling U(VI) adsorption by Koongarra subsurface weathered soils. The coatings were derived from the sorption of iron, aluminum, silica and other elements that result from chemical and physical weathering of primary mineral phases in the underlying geological formation. The sorption process is followed by polymerization, aging, and precipitation of secondary minerals that comprise the coatings.

c) K_d values for U(VI) adsorption at the Koongarra field site, measured in the laboratory, and predicted with the *Component Additivity* surface complexation modeling approach were within one order of magnitude of each other. Trends in K_d values with pH and pCO_2 were predicted well with the *Component Additivity* modeling approach, but the absolute values were generally only within a factor of five of the measured K_d. U(VI) adsorption by Koongarra sediments was very similar to U(VI) adsorption by ferrihydrite on an equal surface area basis. However, quantification of the amount of adsorptive material in mineral coatings was technically difficult to determine and contributed to the error in predicting K_d values with the *Component Additivity* surface complexation modeling approach. In addition, uncertainties in thermodynamic data for aqueous U(VI) speciation in the pH range 6-8.5 may have contributed significantly to the overall uncertainty in predicting K_d values.

d) The *Generalized Composite* surface complexation modeling approach yielded better results for prediction of K_d values at Koongarra as a function of variable chemical conditions. This modeling approach has the potential to reduce the uncertainty in K_d values chosen for advanced performance assessment modeling.

e) Any comparison of laboratory and field K_d values should be done at the appropriate (field) partial pressure of CO_2.

f) At chemical equilibrium, surface complexation models of adsorption processes can be used to predict changes in retardation that are due to variability in chemical conditions, with uncertainties similar in magnitude to the uncertainties of thermodynamic data.

g) Surface complexation model parameters can be determined for single reference mineral phases by fitting transport data in column studies, if the local equilibrium assumption applies. However, the model parameters determined are sensitive to the range of chemical variables considered in the calibration data sets. In this study, an *extrapolation* of K_d values determined in batch experiments to the chemical and solid/liquid ratio conditions used in column experiments resulted in errors on the order of 30% in predicting retardation. For certain performance assessment calculations, it is possible that this is a tolerable uncertainty, since many other factors contribute to the overall uncertainty in K_d values.

h) Expert judgement has a significant role to play in determining the values of surface complexation model parameters from experimental data. Surface complexation modeling offers a scientifically defensible means of linking the selection of K_d values within PA modeling to our existing knowledge of thermodynamic data for radionuclides and radionuclide speciation in aqueous systems.

20.2 Recommendation

The value of surface complexation modeling of adsorption in supporting the selection of K_d values should be given wider recognition within the performance assessment modeling process.

The selection of K_d values should be supported by modeling adsorption with the surface complexation concept, whenever possible. The choice of K_d values for performance assessment modeling should be documented and should include an evaluation of uncertainty in the values, especially the uncertainties caused by spatial or temporal variability in geochemical conditions.

21. REFERENCES

Ainsworth, C.C., D.C. Girvin, J.M. Zachara, and S.C. Smith, "Chromate Adsorption on Goethite: Effects of Aluminum Substitution," *Soil Science Soc. Amer. J.*, Vol. 53, 411-418, 1989.

Allard, B., U. Olofsson, and B. Torstenfelt, "Environmental actinide chemistry," *Inorganica Chimica Acta*, Vol. 94, 205-221, 1984.

Allison, L.E., "Organic Carbon," *Methods of Soil Analysis*, American Society of Agronomy, Madison, 1965.

Altmann, S.A., Ph.D. thesis, Stanford University, Stanford, CA, 1984.

Altmann, S.A. and J. Bruno, *Using Thermodynamic Sorption Models for Guiding Radioelement Distribution Coefficient (K_d) Investigations for Performance Assessment – A Status Report*, Nuclear Energy Agency, Paris, 2001.

American Public Health Association, *Standard Methods for the Examination of Water and Wastewater*, Sixteenth edition, 1985.

Anderson, P.R. and M.M. Benjamin, "Effects of Silicon on the Crystallization and Adsorption Properties of Ferric Oxides," *Environ. Sci. Technol.*, Vol. 19, No. 11, 104-1053, 1985.

Baes, C.F. and R.D. Sharp, "A Proposal for Estimation of Soil Leaching and Leaching Constants for Use in Assessment Models," *J. Environ. Quality*, Vol. 12, 17-28, 1983.

Barger, J.R., G.E. Brown, Jr., and G.A. Parks, "Surface Complexation of Pb(II) at Oxide-water Interfaces: I. XAFS and Bond-valence Determination of Mono- and polynuclear Pb(II) Sorption Products on Al-oxides," *Geochim. Cosmochim. Acta*, Vol. 61, 2617-2638, 1997a.

Barger, J.R., G.E. Brown, Jr., and G.A. Parks, "Surface Complexation of Pb(II) at Oxide-water Interfaces: II. XAFS and Bond-valence Determination of Mononuclear Pb(II) Sorption Products and Surface Function Groups on Fe-oxides," *Geochim. Cosmochim. Acta*, Vol. 61, 2639-2652, 1997b.

Benjamin, M.M. and N.S. Bloom, "Effects of Strong Binding of Anionic Adsorbates on Adsorption of Trace Metals on Amorphous Iron Oxyhydroxide," *Adsorption from Aqueous Solution*, Plenum Press, New York, 41-60, 1981.

Berry, J.A., "A Review of Sorption of Radionuclides under Near- and Far-Field Conditions of an Underground Radioactive Waste Repository: Parts I, II, and III," Oxfordshire, United Kingdom, Her Majesty's Inspectorate of Pollution/Department of the Environment, Harwell Laboratory, DOE/HMIP/RR/92/061, 1992.

Berube, Y.G., G.Y Onoda, Jr., and P.L. de Bruyn, "Proton Adsorption at the Ferric oxide/aqueous Solution Interface:II Analysis of Kinetic Data," *Surface Science*, Vol. 8, 448-461, 1967.

Blake, R. L. et al., "Refinement of the Hematite Structure," *Amer. Mineral.*, Vol. 51, 123-129, 1966.

Bolland, M.D.A., A.M. Posner, and J.P. Quirk, "Zinc Adsorption by Goethite in the Absence and Presence of Phosphate," *Aust. J. Soil Res.*, Vol. 15, 279-286, 1977.

Borgaard, O.K, "The Influence of Iron Oxides on the Surface Area of Soil," *Journal of Soil Science*, Vol. 33, 443-449, 1982.

Boris, J.P., A.M. Landsberg, E.S. Oran, and J.H. Gardner, "LCPFCT – A Flux-corrected Transport Algorithm for Solving Generalized Continuity Equations," *NRL Memo Rept.*, 6410-93-7192, 1993.

Borovec, Z., "The Adsorption of Uranyl Species by Fine Clay," *Chemical Geology*, Vol. 32, 45-58, 1981.

Borovec, Z., "Evaluation of the Concentrations of Trace Elements in Stream Sediments by Factor and Cluster Analysis and the Sequential Extraction Procedure," *Sci. Tot. Env.*, Vol. 177, 237-250, 1996.

Bourg, A.M.C., D. Darmendrail, and J. Ricour, "Geochemical Filtration of Riverbank and Migration of Heavy Metals Between the Deule River and the Ansereuilles Alluvion-chalk Aquifer (Nord, France)," *Geoderma*, Vol. 44, 229-244, 1989.

Bradbury, M.H. and B. Baeyens, "A Mechanistic Description of Ni and Zn Sorption on Na-Montmorillonite. Part II: Modelling," *J. Contam. Hydrol.*, Vol. 27, 223-248, 1997.

Brusilovskii, S. A., "Investigation of the precipitation of hexavalent uranium hydroxide,", *Proceedings of the USSR Academy of Science*, Vol. 120, 343-347, 1958.

Burgisser, C.A. et al., "Determination of Nonlinear Adsorption Isotherms from Column Experiments: An Alternative to Batch Studies," *Environ. Sci. Tech.*, Vol. 27, 943-948, 1993.

Canney, F.C. and D.B. Hawkins, "Cold Acid Extraction of Copper from Soils and Sediments - A Proposed Field Method," *Econ. Geol.*, Vol. 53, 877-886, 1968.

Carpenter, R.H., G.D. Robinson, and W.B. Hayes, "Partitioning of Manganese, Iron, Copper, Zinc, Lead, Cobalt & Nickel in Black Coatings on Stream Boulders in the Vicinity of the Magruder Mine, Lincoln Co., Georgia," *J. Geochem. Explor.*, Vol. 10, 75-89, 1978.

Cederberg, G.A., R.L. Street, and J.O. Leckie, "A Groundwater Mass Transport and Equilibrium Chemistry Model for Multicomponent Systems," *Water Resources Research*, Vol. 21, 1095-1104, 1985.

Chao, T.T., "Selective Dissolution of Manganese Oxides from Soils and Sediments with Acidified Hydroxylamine Hydrochloride," *Soil Sci. Soc. Am. Proc.*, Vol. 36, 704-768, 1972.

Chao, T.T. and P.K. Theobold, "The Significance of Secondary Iron and Manganese Oxides in Geochemical Exploration," *Econ. Geol.*, Vol. 71, 1560-1569, 1976.

Chao, T. T. and L. Zhou, "Extraction Techniques for Selective Dissolution of Amorphous Iron Oxides from Soils and Sediments," *Soil Sci. Soc. American Journal*, Vol. 47, 225-232, 1983.

Chaundry, A.N. and B.B. Bose, "Role of "Humus Matter" in the Formation of Geochemical Anomalies," *Geochemical Exploration. Canadian Institute of Mineralogy and Metallurgy*, Vol. 11, 410-415, 1971.

Chiou, C.T., D.W. Rutherford, and M. Manes, "Sorption of N_2 and EGME Vapors on Some Soils, Clays and Mineral Oxides and Determination of Sample Surface Areas by Use of Sorption Data," Environ. *Sci. and Tech.*, Vol. 27, 1587-1594, 1993.

Choppin, G.R., H.R. Erten, and Y-X Xia, "Variation of Stability Constants of Thorium Citrate Complexes with Ionic Strength," *Radiochimica Acta*, Vol. 74, 123-127, 1996.

Clark, C.J. and M.B. McBride, "Cation and Anion Retention by Natural and Synthetic Allophane and Imogolite," *Clays and Clay Minerals*, Vol. 32, 291-299, 1984a.

Clark, C.J. and M.B. McBride, "Chemisorption of Cu(II) and Co(II) on Allophane and Imogolite," *Clays and Clay Minerals*, Vol. 32, 300-310, 1984b.

Clark, D.L., D.E. Hobart, and M.P. Neu, "Actinide Carbonate Complexes and their Importance in Environmental Chemistry," *Chem. Rev.*, Vol. 95, 25-48, 1995.

Cleveland, J.M., and T.G. Rees, "Characterization of Plutonium in Maxey Flats Radioactive Trench Leachates," *Science*, Vol. 212, 1506-1509, 1981.

Coleman, P.B., *Practical Sampling Techniques for Infrared Analysis*, CRC Press, 1993

Coston, J. A., C.C. Fuller, and J.A. Davis, "Pb^{2+} and Zn^{2+} Adsorption by a Natural Al-and Fe-bearing Surface Coating on an Aquifer Sand," *Geochim. Cosmochim. Acta*, Vol. 59, 17, 3535-3547, 1995.

Cradwick, P.D.G. et al., "Imogolite, a Hydrated Aluminum Silicate of Tubular Structure," *Nature Physical Science*, Vol. 240, 187-189, 1972.

Crine, J.P., "Ionic Impurities in Water Contained in Plastic and Pyrex Bottles," *Polym. Eng. Sci.*, Vol. 27, 611-614, 1987.

Dahlgren, R.A. and F.C. Ugolini, "Formation and Stability of Imogolite in a Tephritic Spodosol, Cascade Range, Washington, U.S.A.," *Geochim. Cosmochim. Acta*, Vol. 53, 1897-1904, 1989.

Dahlgren, R.A., M. Nanzyo, and S. Shoji, "Mineralogical Characteristics of Volcanic Ash Soils," *Volcanic Ash Soils: Genesis, Properties and Utilization*, Vol. 5. Elsevier, 1993.

Davis, J.A., "Adsorption of Trace Metals and Complexing Ligands at the Oxide/Water Interface," Ph.D. Dissertation, Stanford University, U.S.A, 286, 1977.

Davis, J.A. and J.O. Leckie, "Surface Ionization and Complexation at the Oxide/ water Interface. II. Surface Properties of Amorphous Iron Oxyhydroxide and Adsorption of Metal Ions," *J. Colloid. Int. Sci.*, Vol. 67, 90-107, 1978.

Davis, J.A., and J.O. Leckie, "Effect of Adsorbed Complexing Ligands on Trace Metal Uptake by Hydrous Oxides," *Environ. Sci. Technol.*, Vol. 12, 1309-1315, 1978.

Davis, J.A. and J.O. Leckie, "Surface Ionization and Complexation at the Oxide/ water Interface. III. Adsorption of Anions," *J. Colloid. Int. Sci.*, Vol. 74, 32-43, 1980.

Davis, J.A., "Adsorption of Natural Dissolved Organic Matter at the Oxide/water Interface," *Geochim. Cosmochim. Acta*, Vol. 46, 2381-2393, 1982.

Davis, J.A., C.C. Fuller, and A.D. Cook, "A Model for Trace Metal Sorption Processes at the Calcite Surface: Adsorption of Cd and Subsequent Solid Solution Formation," *Geochim . Cosmochim. Acta*, Vol. 51, 1477-1490, 1987.

Davis, J.A., and D.B. Kent, "Surface Complexation Modeling in Aqueous Geochemistry, In Mineral-Water Interface Geochemistry," Mineralogical Society of America, Washington, DC, *Mineralogy*, Vol. 23, 177-260, 1990.

Davis, J.A. et al., "Application of the Surface Complexation Concept to Complex Mineral Assemblages," *Environ Sci. Tech.*, Vol. 32, 2820-2828, 1998.

Doner, H.E., "Chloride as a Factor in the Mobilities of Ni(II), Cu(II) and Cd(II) in Soil," *Soil Sci. Soc. Amer. Journal.*, Vol. 42, 882-885, 1978.

Dongarra, G. and D. Langmuir, "The Stability of UO_2OH^+ and $UO_2[HPO_4]_2^{2-}$ Complexesat 25°C," *Geochim. Cosmochim. Acta*, Vol. 44, 1747-1751, 1980.

Dousma, J. and P.L. De Bruyn, "Hydrolysis-precipitation Studies of Iron Solutions. I. Model for Hydrolysis and Precipitation from Fe(III) Nitrate Solutions," *J. Colloid Interface Sci.*, Vol. 56, 527-539, 1976.

Drits, V.A. et al., "Structural Model for Ferrihydrite," *Clay Mineral*, Vol. 28, 185-207, 1993.

Dzombak, D.A. and F.M.M. Morel, *Surface Complexation Modeling: Hydrous Ferric Oxide*, Wiley & Sons, New York, 393, 1990.

Dzombak, D.A. and M.A. Ali, "Hydrochemical Modeling of Metal Fate and Transport in Freshwater Environments," *Water Pollution Res. J. Canada*, Vol. 28, 7-50,1993.

Edis, R. et al., "Chemistry and Mineralogy of Rocks and Soils", *Alligator Rivers Analogue Project, ANSTO*, 8, 1992.

Edis, R. et al., "Chemistry and Mineralogy of Rocks and Soil," *Alligator Rivers Analogue Project, Final Report, ANSTO*, 8, 1994.

Egashira, K. and S. Aomine, "Effects of Drying and Heating on the Surface Area of Allophane and Imogolite," *Clay Science*, Vol. 4, 231-242, 1974.

Elliott, H.A., M.R. Liberati, and C.P. Huang, "Effect of Iron Oxide Removal on Heavy Metal Sorption by Acid Subsoils," *Water, Air and Soil Pollution*, Vol. 27, 379-389, 1986.

Erdal, B.R. et al., "Laboratory Studies of Radionuclide Transport in Geologic Media," *Underground Disposal of Radioactive Wastes*, IAEA, Vienna, 2, 1980.

Environmental Protection Agency, "Soil Screening Guidance: User's Guide" EPA/540/R-96/018, Washington, D. C., 1996.

Farmer, V.C., A.R. Fraser, and J.M. Tait, "Synthesis of Imogolite: a Tubular Aluminum Silicate Polymer," *J. Chem. Soc.*, Vol. 13, 462-463, 1977.

Farmer, V.C. and A.R. Fraser, "Synthetic Imogolite" (M. Mortland and V.C. Farmer, eds.), *Int. Clay Conf.*, Amsterdam, Elsevier, 547-553, 1979.

Farmer, V.C., "Significance of the Presence of Allophane and Imogolite in Podzol Bs Horizons for Podzolization Mechanisms: a Review," *Soil Sci. Plant Nutri.*, Vol. 28, No. 4, 571-578, 1982.

Farmer, V.C. et al., "Synthetic Imogolite: Properties, Synthesis, and Possible Applications," *Clay Minerals*, 18, 459-472, 1983.

Fenton, B.R. and T.D. Waite, "A Kinetic Study of Cation Release from a Mixed Mineral Assemblage: Implications for Determination of Uranium Uptake," *Radiochim. Acta,* Vol. 74, 251-256, 1996.

Fuller, C.C., J.A. Davis, and G.A. Waychunas, "Surface Chemistry of Ferrihydrite. II. Kinetics of Arsenate Adsorption and Coprecipitation," *Geochim. Cosmochim. Acta*, Vol. 57, 2271-2282, 1993.

Fuller C.C. et al., "Characterization of Metal Adsorption Variability in a Sand and Gravel Aquifer, Cape Cod Massachusetts, USA," *Journal of Contaminant Hydrology*, Vol. 22, 3-4, 165-187, 1996.

George, G.N., EXAFSPAK, Stanford Synchrotron Radiation Laboratory, 1993.

Giblin, A.M., "The Role of Clay Adsorption in Genesis of Uranium Ores," *Uranium in the Pine Creek Geosyncline*, (J. Ferguson and A.B Goleby, Eds.). IAEA, Vienna, 1980.

Gregg, S.J. and K.S.W. Sing, *Adsorption, Surface Area, and Porosity*, Academic Press, 1982.

Grenthe, I. et al., *Chemical Thermodynamics 1; Chemical Thermodynamics of Uranium*, NEA, OECD, Elsevier, Holland, 1992.

Grossman, R.B. and J.C. Millet, "Carbonate Removal from Soils by a Modification of the Acetate Buffer Method," *Soil Sci. Soc. Am. Proc.*, Vol. 25, 325-326, 1961.

Harsh, J.B. et al., "Adsorption of Cations on Imogolite and their Effect on Surface Charge Characteristics," *Clays and Clay Minerals*, Vol. 40, 700-706, 1992.

Hawke, D., P.D. Carpenter, and K.A. Hunter, "Competitive Adsorption of Phosphate on Goethite in Marine Electrolytes," *Environ. Sci. Technol.*, Vol. 23, 87-191, 1989.

Herbelin, A.L. and J.C. Westall, *FITEQL, A Computer Program for Determination of Chemical Equilibrium Constants from Experimental Data*, Ver. 3.1, Dept of Chemistry, Oregon State Univ., 1994.

Hester, R.E. and W.E.L. Grossman, "Vibrational Analysis of Bidentate Nitrate and Carbonate Complexes," *Inorg. Chem.*, Vol. 5, 1308-1312, 1966.

Hiebert, F.Z. and P.C. Bennett, *Science*, Vol. 258, 278-281, 1992.

Ho, C.H. and D.C. Doern, "The sorption of uranyl species on a hematite sol," *Canadian J. Chem.*, Vol. 63, 1100-1104, 1985.

Ho, C.H., and N.H. Miller, "Effect of Humic Acid on Uranium Uptake by Hematite Particles," *J. Colloid Interface Sci.*, Vol. 10, 281-288, 1985.

Ho, C.H. and N.H. Miller, "Adsorption of Uranyl Species from Bicarbonate Solution onto Hematite Particles," *J. Colloid Interf. Sci.*, Vol. 110, 165-171, 1986.

Hobart, D.E., "Actinides in the Environment," *Fifty years with Transuranium Elements*, 379-436, 1990.

Hohl, H., and W. Stumm, "Interaction of Pb^{2+} with hydrous γ-Al_2O_3", *J. Colloid Interf. Sci.*, Vol. 55, 281-288, 1976.

Honeyman, B.D., Ph.D. Thesis, Stanford University, Stanford, CA 1984.

Honeyman, B.D. and J.O. Leckie, "Macroscopic Partitioning Coefficients for Metal Ion Adsorption: Proton Stoichiometry at Variable pH and Adsorption Density," *Geochemical Processes at Mineral Surfaces*, J. A. Davis and K. F. Hayes (eds.), ACS Symp. Series 323, American Chemical Society, Washington, D. C., pp. 162-190, 1986.

Horikawa, Y., "Electrokinetic Phenomena of Aqueous Suspensions of Allophane and Imogolite," *Clay Science*, Vol. 4, 255-263, 1975.

Hsi, C-K.D. and D. Langmuir, "Adsorption of Uranyl onto Ferric Oxyhydroxides: Application of the Surface Complexation Site-Binding Model," *Geochim. Cosmochim. Acta*, Vol. 49, 1931-1941, 1985.

Huang, C.P. and W. Stumm, "Specific Adsorption of Cations on Hydrous α- Al_2O_3," *J. Colloid Int. Sci.*, Vol. 22, 231-259, 1973.

Inoue, T. and K. Wada,, "Reactions between Humified Clover Extract and Imogolite as a Model of Humus-clay Interaction: Part I," *Clay Science*, Vol. 4, 61-70, 1971.

Isherwood, D. "Geoscience Data Base Handbook for Modeling a Nuclear Waste Repository", U. S. Nuclear Regulatory Commission, NUREG/CR-0912, 1, 1981

Ivanovich, M., "Aspects of Uranium / Thorium Series Disequilibrium Applications to Radionuclide Migration Studies," *Radiochim. Acta*, Vol. 52/53, 257-268, 1991.

Jardine, P.M., G.K. Jacobs, and J.D. O'Dell, "Unsaturated Transport Processes in Undisturbed Heterogeneous Porous Media: II. Co-contaminants," *Soil Sci. Soc. Am. J.*, Vol. 57, 954-962, 1993.

Jennings, A.A., D.J. Kirkner, and T.L. Theis, "Multicomponent Equilibrium Chemistry in Groundwater Quality models," *Water Resources Research*, Vol. 18, 1089-1096, 1982.

Jensen, B.S., *Migration Phenomena of Radionuclides into the Geosphere*, Harwood Academic Publishers, Brussels, 1982.

Jongmans, A.G. et al., "Allophane, Imogolite, and Gibbsite in Coatings in a Costa Rican Andisol," *Geoderma*, Vol. 64, 327-342, 1995.

Karube, J. et al., "Electrophoretic Behavior of Imogolite under Alkaline Conditions," *Clay and Clay Minerals*, Vol. 40, 625-628, 1992.

Killey, D.R.W. et al., "Subsurface Cobalt-60 Migration from a Low-level Waste Disposal Site," *Environ. Sci. Tech.*, Vol. 18, 148-157, 1984.

Kinniburgh, D.G., J.L. Jackson, and J.K. Syers, "Adsorption of Alkaline Earth, Transition, and Heavy Metal Cations by Hydrous Oxide gels of Iron and Aluminum," *Soil Sci. Soc. Amer. J.*, Vol. 40, 796-799, 1976.

Kohler, M. et al., "Experimental Investigation and Modeling of Uranium(VI) Transport under Variable Chemical Conditions," *Water Resources Research*, Vol. 32, 3539-3551, 1996.

Kohler, M., Honeyman, B.D., Leckie, J.O.: Neptunium(V) Sorption on Hematite (α-Fe_2O_3) in Aqueous Suspension: The Effect of CO_2, Radiochim. Acta **85**, 33-48 (1999).

Koβ, V., Modeling of U(VI) Sorption and Speciation in a Natural Sediment-Groundwater System, *Radiochim. Acta*, Vol. 44/45, 403-406, 1988.

Krauskopf, K.B., *Radioactive Waste Disposal and Geology,* Chapman & Hall, 1991.

Krupka, K.M., and J.R. Serne, "Input Vault and Sorption Values for Use in the NRC Low-Level Radioactive Waste Performance Assessment Test Case," Richland, Washington, Pacific NW Laboratory/Water and Land Resource. Dept., Task Order 1 Letter Rept, October 1, 1996

Kung, K.S., and I.R. Triay, "Effect of Natural Organics on Cs and Np sorption," *Radiochim. Acta*, Vol. 66/67, 421-426, 1994.

Landa, E.R., and R.G. Gast, "Evaluation of Crystallinity in Hydrated Ferric Oxides," *Clays and Clay Minerals*, Vol. 21, 121-130, 1973.

Lienert C., S.A. Short, and H.R. von Gunten, "Uranium Infiltration from a River to Shallow Groundwater," *Geochim Cosmochim. Acta*, Vol. 58, 5455-5464, 1994.

Lieser, K.H., S. Quandt-Klenk, and B. Thybusch, "Sorption of Uranyl Ions on Hydrous Silicon Dioxide," *Radiochim. Acta*, Vol. 57, 45-50, 1992.

Looney, B.B. et al., "Estimation of Geochemical Parameters for Assessing Subsurface Transport at the Savannah River Plant", Aiken, S.C, Savannah River Lab., DPST-85-904, 1987.

Lovgren, L., S. Sjoberg, and P.W. Schindler, "Acid/base Reactions and Al(III) Complexation at the Surface of Goethite," *Geochim. Cosmochim. Acta*, Vol. 54, 1301-1306, 1990.

Lowson, R.T. et al., "$^{234}U/^{238}U$ and $^{230}Th/^{234}U$ Activity Ratios in Mineral Phases of a Lateritic Weathered Zone," *Geochim. Cosmochim. Acta*, Vol. 50, 1697-1702, 1986.

Lumpkin, G.R., Payne, T.E., Fenton, B.R., Waite, T.D.: Preferential Association of Adsorbed Uranium with Mineral Surfaces: A Study Using Analytical Electron Microscopy, Mater. Res. Soc. Proc. **556,** 1999.

MacNaughton, M.G., "Adsorption of Mercury(II) at the Solid-water Interface," Ph.D. Thesis, Department of Civil Engineering, Stanford University, 1973.

Makenzie, R.C., "Free Iron Oxide Removal from Soils," *J. Soil. Sci.*, Vol. 5, 167-172, 1954.

Malcolm, R.L. and P. MacCarthy, "Limitations in the Use of Commercial Humic Acids in Water and Soil Research," *Environ. Sci. Technol.*, Vol. 20, 904-911, 1986.

Matijevic, E. and P. Scheiner, "Ferrous Hydrous Oxide Sols III. Preparation of Uniform Particles by Hydrolysis of Fe(III)-chloride, -nitrate, and –perchlorate Solutions," *J. Coll. Inter. Sci.*, Vol. 63(3), 509-524, 1978.

Maynard, D.E. and W.K. Fletcher, "Comparison of Total and Partial Extractable Copper in Anomalous and Background Peat Samples," *J. Geochem. Explor.*, Vol. 2, 19-24, 1973.

McKeague, J.A. and J.H. Day, "Dithionite and Oxalate Extractable Fe and Al as Aids in Differentiating Various Cases of Soils," *Can. J. Soil Sci.*, Vol. 5, 167-172, 1966.

McKeague, J.A., "An Evaluation of 0.1M Pyrophosphate and Pyrophosphate-dithionite in Comparison with Oxalate as Extractants of the Accumulation Products in Podsols and Some Other Soils," *Can. J. Soil Sci.*, 47, 95-99, 1967.

McKeague, J.A. and H. Kodama, "Imogolite in Cemented Horizons of Some British Columbia Soils," *Geoderma*, Vol. 25, 189-197, 1981.

McKinley, I.G. and W.R. Alexander, "Constraints on Applicability of 'In-situ Distribution Coefficient' Values," *J. Environ. Radioactivity*, Vol. 15, 19-34, 1992.

McKinley, I.G. and A. Scholtis, "A Comparison of Sorption Databases Used in Recent Performance Assessments", in Radionuclide Sorption from the Safety Evaluation Perspective, NEA-OCDE, Paris, 1992.

McKinley, J.P., J.M. Zachara, S.C. Smith, and G.D. Turner, "The Influence of Hydrolysis and Multiple Site-Binding Reactions on the Adsorption of U(VI) to Montmorillonite," *Clays Clay Min.*, Vol. 43, 586-598, 1995.

Mehra, O.P. and M. Jackson, "Iron Oxide Removal from Soils and Clays by a Dithionite-citrate System Buffered with Sodium Bicarbonate," *Proc. 7th. Int. Conf. Clays Clay Min., 1958,* Washington D.C., 317-327, 1960.

Moll, H., "Zur Wechselwirkung von Uran mit Silicat in wässrigen Systemen," Ph.D. Thesis, Technische Universität Dresden, 1997.

Moody, J.R. and R.M. Lindstrom, "Selection and Cleaning of Plastic Containers for Storage of Trace Element Samples," *Anal. Chem.*, Vol. 49, 2664-2667, 1977.

Moré, J.J., B.S. Garbow, and K.E. Hillstrom, "User guide to MINPACK-1," *Argonne Natl. Lab. Rept.*, ANL-80-74, 1980.

Morrison, S.J. and L.S. Cahn, "Mineralogical Residence of Alpha-emitting Contamination and Implications for Mobilization from Uranium Mill Tailings," *J. Contam. Hydrol.*, Vol. 8, 1-21, 1991.

Moulin, V. and G. Ouzounian, "Role of Colloids and Humic Substances in the Transport of Radio-elements through the Geosphere," *Appl. Geochem. Suppl.*, Vol. 1, 179-186, 1992.

Murakami, T. et al., "Weathering and its Effects on Uranium Redistribution," *Alligator Rivers Analogue Project, Final Report*, ANSTO, Menai, 9, 1994.

Nakamoto, K., *Infrared and Raman Spectra of Inorganic and Coordination Compounds*, J. Wiley and Sons, 1986.

Nakayama, F.S. and R.D. Jackson, "Diffusion of Tritiated Water ($H^3H^1O^{16}$) in Agar Gel and Water," *J. Phys. Chem.*, Vol. 67, 932-933, 1963.

Nomizu, T. et al., "Determination of Humic and Fulvic Acids in River Waters by Concentration with Anion Exchanger followed by Centrifugation," *Analytical Sciences*, Vol. 5, 363-365, 1989.

Oades, J.M., "The Nature and Distribution of Iron Compounds in Soils," *Soil Fert.*, Vol. 26, 69-80, 1963.

Pabalan, R.T., D.R. Turner, and F.P. Bertetti, "Sorption Modelling for HLW Performance Assessment," *NRC High-level Radioactive Waste Research at CNWRA, January-June 1994*, Center for Nuclear Waste Regulatory Analyses, San Antonio, 77-96, 1994.

Pabalan, R.T. and D.R. Turner, "Uranium(6+) Sorption on Montmorillonite: Experimental and Surface Complexation Modeling Study," *Aquatic Geochemistry*, Vol. 2, 203-226, 1996.

Padmanabhan, E. and A. R. Mermut, *Clays and Clay Minerals*, Vol. 40, 675-681, 1996.

Papelis, C., K.F. Hayes, and J.O. Leckie, "HYDRAQL: A Program for the Computation of Chemical Equilibrium Composition of Aqueous Batch Systems Including Surface Complexation Modeling of Ion Adsorption at the Oxide/solution Interface," *Technical Report No. 306*, Department of Civil Engineering, Stanford University, Stanford, CA, 1988.

Parfitt, R.L., S.J. Van der Gaast, and C.W. Childs, *Clays and Clay Minerals*, Vol. 40, 675-681, 1992.

Parfitt, R.L. et al., "Adsorption of Phosphate on Imogolite," *Clays and Clay Minerals*, Vol. 22, 455-456, 1974.

Parker, J.C. and M.T. van Genuchten, "Determining Transport Parameters from Laboratory and Field Tracer Experiments," Bulletin *84-3*, Virginia Agricultural Experimental Station, Virginia Polytechnic Inst. and State Univ., Blacksburg, VA, 1984.

Payne, T.E. and T.D. Waite, "Surface Complexation Modelling of Uranium Sorption Data Obtained by Isotope Exchange Techniques," *Radiochim. Acta*, Vol. 52/53, 487-493, 1991.

Payne, T.E., R. Edis, and T. Seo, "Radionuclide Transport by Groundwater Colloids at the Koongarra Uranium Deposit," (C. G. Sombret, ed.) *Scientific Basis for Nuclear Waste Management XV*, Mat. Res. Soc. Symp. Proc. 257, 481-488, 1992.

Payne, T.E., J.A. Davis, and T.D. Waite, "Uranium Retention by Weathered Schists - The Role of Iron Minerals," *Radiochim. Acta*, Vol. 66/67, 297-303, 1994a.

Payne, T.E., et al., "Groundwater Chemistry," *Alligator Rivers Analogue Project, Final Report*, Australian Nuclear Science and Technology Organization, Menai, 7, 185, 1994b.

Payne, T.E., J.A. Davis, and T.D. Waite, "Uranium Adsorption on Ferrihydrite –Effects of Phosphate and Humic acid," *Radiochim. Acta*, Vol. 74, 239-243, 1996.

Persson, P., N. Nilsson, and S. Sjoberg, "Structure and Bonding of Orthophosphate Ions at the Iron Oxide-aqueous Interface," *J. Coll. Interf. Sci.*, Vol. 177, 263-275, 1996.

Pohle, W., M. Bohl, and H. Bohlig,, "Interpretation of the Influence of Hydrogen Bonding on the Stretching Vibrations of the PO_2- Moiety," *J. Mol. Struct.*, Vol. 242, 333-342, 1990.

Pohl, P.I., J.L. Faulon, and D.M. Smith, "Pore Structure of Imogolite Computer Models," *Langmuir*, 12, 4463-4468, 1996.

Pompe, S. et al., "A Comparison of Natural Humic Acids with Synthetic Humic acid Model Substances: Characterization and Interaction with Uranium(VI)," *Radiochim. Acta*, Vol. 74, 135-140, 1996.

Prikryl, J.D. et al., "Uranium Sorption on α-alumina: Effects of pH and Surface Area/solution-volume Ratio," *Radiochim. Acta*, Vol. 66/67, 291-296, 1994.

Pruett, R.J. and H.L. Webb, "Sampling and Analysis of KGa-1B Well Crystallized Kaolin Source Clay," *Clays Clay Mineral,* Vol. 41, 514-519, 1993.

Rea, B.A., J.A. Davis, and G.A. Waychunas, "Studies of the Reactivity of the Ferrihydrite Surface by Iron Isotopic Exchange and Mossbauer spectroscopy," *Clays Clay Mineral*, Vol. 42, 23-34, 1994.

Redden, G.D., J. Li, and J.O. Leckie, "Ternary Uranyl-citrate Surface Complex Formation on Goethite, Gibbsite and Phylosilicate Minerals," *Abstract GEOC114*, ACS National Meeting, New Orleans, 1996.

Rehr, J.J. and R.C. Albers, "Scattering-matrix Formulation of Curved-wave Multiple-scattering Calculations of X-ray Absorption Fine Structure," *Phys. Rev.*, Vol. B 41, 8131-8149, 1990.

Rehr, J.J. et al., "Theoretical x-ray Absorption Fine Structure Standards," *J. Amer. Chem. Soc.,* Vol. 113, 5135-5140, 1991.

Rehr, J.J., S.I. Zabinsky, and R.C. Albers, "High-order multiple-scattering calculations of x-ray absorption fine structure," *Phys. Rev. Lett.*, Vol. 69, 3397, 1992.

Roberts, P.V., M.N. Goltz, and D.M. Mackay, "A Natural Gradient Experiment on Solute Transport in a Sand Aquifer, 3. Retardation Estimates and Mass Balances for Organic Solutes," *Water Resources Research*, Vol. 22, 2047-2058, 1986.

Ross, S.D., *Inorganic Infrared and Raman Spectra*, McGraw Hill, 1972.

Rubin, J., "Solute Transport with Multisegment, Equilibrium-controlled Reactions: A Feed-forward Simulation Method," *Water Resources Research*, Vol. 26, 2029-2055, 1990.

Sagert, N.H., C.H. Ho, and N.H. Miller, "The Adsorption of Uranium(VI) onto a Magnetite sol," J. *Colloid Interface Sci.*, Vol. 130, 283-287, 1989.

Sahai, N. and D.A. Sverjensky, "Evaluation of internally consistent parameters for the triple-layer model by the systematic analysis of oxide surface titration data,", *Geochim. Cosmochim. Acta*, Vol. 61, 2801-2826, 1997.

Salbu, B. et al., "Size Fractionation Techniques in the Determination of Elements Associated with Particulate or Colloidal Material in Natural Fresh Waters," *Talanta*, Vol. 32, 907-913, 1985.

Sandino A. and J. Bruno, "The Solubility of $(UO_2)_3(PO_4)_2 \bullet 4H_2O_{(s)}$ and the Formation of U(VI) Phosphate Complexes: Their Influence in Uranium Speciation in Natural Waters," *Geochim. Cosmochim. Acta*, Vol. 56, 4135-4145, 1992.

Schindler, P.W. and H.R. Kamber, "Die aciditat von silanolgruppen," *Helv. Chim. Acta*, Vol. 51, 1781-1786, 1968.

Schindler, P.W. et al., "Ligand Properties of Surface Silanol Groups, I. Surface Complex Formation with Fe^{3+}, Cu^{2+}, Cd^{2+}, and Pb^{2+}," *J. Colloid Interface Sci.*, Vol. 55, 469-475, 1976.

Schneider, W. and B. Schwyn, "The Hydrolysis of Iron in Synthetic, Biological, and Aquatic Media," *Aquatic Surface Chemistry*, W. Stumm (ed.), Wiley-Interscience, New York, Chap. 7, 167-196, 1987.

Schweich, D. and M. Sardin, "Adsorption, Partition, Ion-exchange, and Chemical Reaction in Batch Reactors or in Columns – A Review," *J. Hydrology*, Vol. 50, 1-33, 1981.

Schwertmann, U., "Use of Oxalate for Fe Extraction from Soils," *Can. J. Soil. Sci.*, Vol. 53, 244-246, 1973.

Schwertmann U., and H. Thalmann, "The Influence of [Fe(II)], [Si], and pH in the Formation of Lepidocrocite and Ferrihydrite during Oxidation of Aqueous $FeCl_2$ Solutions," *Clay Minerals*, Vol. 11, No. 3, 189-200, 1976.

Schwertmann, U. and W.R. Fischer, "Natural Amorphous ferric hydroxide," *Geoderma,* Vol. 10, 237-247, 1973.

Sheppard, M.I. and D.H. Thibault, "Default Soil Solid/Liquid Partition Coefficients, K_ds, for Four Major Soil Types: A Compendium," *Health Physics*, Vol. 59, 471-482, 1990.

Sidhu, P.S. et al., "Dissolution of Iron Oxides and Oxyhydroxides in Hydrochloric and Perchloric Acids," *Clays Clay Min.*, Vol. 29, 269-276, 1981.

Silva, R.J., "Mechanisms for the Retardation of Uranium(VI) Migration," *Mat. Res. Soc. Symp. Proc.* 257, 323-330, 1992.

Silva, R.J. et al., "Thermodynamics 2; Chemical Thermodynamics of Americium; with an appendix on "Chemical Thermodynamics of Uranium"; *Nuclear Energy Agency*, OECD, North-Holland, Elsevier, 1995.

Smith, R.M. and A.E. Martell, *Critical Stability Constants,* Plenum, New York, 6, 2, 1989.

Snelling, A.A., "Geologic Setting," *Alligator Rivers Analogue Project Final Report,* ANSTO, Menai, Australia, 2, 1994.

Snelling, A.A., "Koongarra Uranium Deposits," In: The Geology of the Mineral Deposits of Australia and Papua New Guinea, F. E. Hughes, The Australasian Inst. of Mining and Metallurgy, Melbourne, Australia, 807-812, 1990.

Solomah, A.G., "Effects of Temperature on the Leaching Behavior of Sintered Modified Synroc-B Waste Form," *Nucl. Technol.*, Vol. 62, 311-316, 1983.

Sposito, G., "On the Use of the Langmuir Equation in the Interpretation of "Adsorption" Phenomena. II. The Two-surface Langmuir Equation," *Soil Sci. Soc. Am. J.,* Vol. 46, 1147-1152, 1982.

Sposito, G., "Distinguishing Adsorption from Surface Precipitation," *Geochemical Processes at Mineral Surfaces*, J. A. Davis and K. F. Hayes (eds.), ACS Symp. Series 323, American Chemical Society, Washington, D. C., pp. 217-229, 1986.

Sposito, G., *The Chemistry of Soils*, Oxford University Press, New York, 277, 1989.

Starik, I.E., F.E. Starik, and A.N. Appolonova, "Adsorption of Microquantities of Uranium by Iron Hydroxides and its Desorption by the Carbonate Method, " *J. Inorg. Chem.*, USSR, Vol. 3, 181-193, 1958.

Stollenwerk, K.G., "Modeling the Effects of Variable Groundwater Chemistry on Adsorption of Molybdate," *Water Resources Res.*, Vol. 31, 347-357, 1995.

Strickland, J.D.H. and T.R. Parsons, "A Manual for Seawater Analysis," Bull. *Fish. Res. Bd.,* Canada 167, 311, 1968.

Stumm, W., *Chemistry of the Solid-water Interface*, Wiley Interscience, New York, 428, 1992.

Stumm, W., C.P. Huang, and S.R. Jenkins, "Specific Chemical Interactions Affecting the Stability of Dispersed Systems," *Croat. Chem. Acta*, Vol. 42, 223-244, 1970.

Su, C., J.B. Harsh, and P.M. Bertsch, "Sodium and Chloride Sorption by Imogolite and Allophanes," *Clay and Clay Minerals*, Vol. 40, 280-286, 1992.

Su, C. and J.B. Harsh, "Electrophoretic Mobility of Imogolite and Allophane in the Presence of Inorganic Anions and Citrate," *Clay and Clay Minerals*, Vol. 41, 461-471, 1993.

Su, C., J.B. Harsh, and J.S. Boyle, "Solubility of Hydroxy-aluminum Interlayers and Imogolite in a Spodosol," *Soil Sci. Soc. Am. J.*, Vol. 59, 373-379, 1995.

Teo, B.K., EXAFS*: Basic Principles and Data Analysis*. Springer-Veriag, 1986.

Tessier, A., P.G.C. Campbell, and M. Bisson, "Sequential Extraction Procedure for the Speciation of Particulate Trace Metals," *Analytical Chemistry*, Vol. 51:844-850, 1979.

Thompson, H., G.E. Brown, Jr., and G.A. Parks, "XAFS Spectroscopic Study of Uranyl Coordination in Solids and Aqueous Solutions," *Amer. Mineral*, Vol. 82(5-6), 483-496, 1997.

Tipping, E., "Modelling the Binding of Europium and the Actinides by Humic Substances," *Radiochimica Acta*, Vol. 62, 141-152, 1993.

Tripathi, V.S.,"Uranium (VI) Transport Modelling: Geochemical Data and Sub-models." Ph.D. Thesis, Stanford University, 1983.

Turner, D., "A Uniform Approach to Surface Complexation Modeling of Radionuclide Sorption," CNWRA Rept. 95-001, Center for Nuclear Waste Regulatory Analyses, San Antonio, TX, 1995.

Turner, G.D. et al., "Surface-charge Properties and UO22+ Adsorption of a Subsurface Smectite," *Geochim. Cosmochim. Acta*, Vol. 60, 3399-3414, 1996.

Urbanec, Z. and J. Cejka, "Infrared Spectra of Liebigite, Andersonite, Voglite, and Schroeckingerite," *Collection Czechoslov. Chem. Commun.*, Vol. 44, 10-23, 1979a.

Urbanec, Z. and J. Cejka, "Infrared Spectra of Rutherfordine and Sharpite," *Collection Czechoslov. Chem. Commun.*, Vol. 44, 1-9, 1979b.

VanGeen, A., A.P. Robertson, and J.O. Leckie, "Complexation of Carbonate Species at the Goethite Surface: Implications for Adsorptions of Metal Ions in Natural Waters," *Geochim. Cosmochim. Acta*, Vol. 58, 2073-2086, 1994.

Van Olphen, H. and J.J. Fripiat, *Data Handbook for Clay Materials and Other Non-metallic Minerals*, Pergamon, Oxford, 1979.

Venkataramani, B. and A.R. Gupta, "Effect of Anions on the Sorption of Uranyl Ions on Hydrous Oxides: Application of the Surface Hydrolysis Model," *Colloids and Surfaces*, Vol. 53, 1-19, 1991.

Violante, P. and J.M. Tait, "Identification of Imogolite in Some Volcanic Soils from Italy," *Clay Minerals*, Vol. 14, 155-158, 1979.

Vuceta, J., "Adsorption of Pb(II) and Cu(II) on α-Quartz from Aqueous solutions: Influence of pH, Ionic Strength, and Complexing Ligands," Ph.D. Thesis, California Institute of Technology, Pasadena, California, 1976.

Wada, K. and T. Henmi, "Characterization of Micropores of Imogolite by Measuring Retention of Quaternary Ammonium Chlorides and Water," *Clay Science*, Vol. 4, 127-136, 1972.

Wada, S.I., A. Eto, and K. Wada, "Synthetic Allophane and Imogolite," *J. Soil Science*, Vol. 30, 347-355, 1979.

Wada, K., "Allophane and Imogolite," *Minerals in Soil Environments,* Second edition (J. B. Dixon and S. B. Weed, eds.), Soil Science Society of America, 1989.

Waite, T.D. et. al., "Uranium Sorption," *Alligator Rivers Analogue Project*, ANSTO, 13, 1992.

Waite, T.D. and T.E. Payne, "Uranium Transport in the Subsurface Environment: Koongarra – A Case Study, in Metals in Groundwater," (H. Allen, E.M. Perdue, and D.S. Brown, eds.), Lewis Pub., Ann Arbor, 349-410, 1993.

Waite, T.D. et al., "Uranium Sorption," *Alligator Rivers Analogue Project, Final Report*," ANSTO, Menai, 13, 106, 1994a.

Waite, T.D. et al, "Uranium(VI) Adsorption to Ferrihydrite: Application of a Surface Complexation Model," *Geochim. Cosmochim. Acta*, Vol. 58, 5465-5478, 1994b.

Waychunas, G.A. et al., "Surface Chemistry of Ferrihydrite. 1. EXAFS Studies of the Geometry of Coprecipitated and Adsorbed Arsenate," *Geochim. Cosmochim. Acta*, Vol. 57, 2251-2269, 1993.

Waychunas, G.A. et al., "Wide Angle X-ray Scattering (WAXS) Study of the "two-line" Ferrihydrite Structure: Effect of Arsenate Sorption and Counterion Variation and Comparison with EXAFS Results," *Geochim. Cosmochim. Acta,* Vol. 60(10), 1765-1782, 1996.

Waychunas, G.A., J.A. Davis, and R. Reitmeyer, "GIXAFS Analysis of Fe^{3+} Sorption on Natural Quartz r(101) and m(100) Surfaces," *Abstracts, Geochemistry Division, American Chemical Society National Meeting*, Las Vegas, NV, September 1997.

Weaver, C.E., "The Nature of TiO_2 in Kaolinite," *Clays Clay Miner.*, Vol. 24, 215-2, 1976.

Westall, J.A., "FITEQL: A Program for the Determination of Chemical Equilibrium Constants from Experimental Data," Chemistry Department, Oregon State University, Corvallis, Oregon, 1982.

Westall, J.C. et al., "Models for Association of Metal Ions with Heterogeneous Environmental Sorbents. 1. Complexation of Co(II) by Leonardite Humic Acid as a Function of pH and $NaClO_4$ Concentration", *Environ. Sci. Tech.*, Vol. 29, 951-959, 1995.

Wieland, E. and W. Stumm, "Dissolution Kinetics of Kaolinite in Acidic Aqueous Solutions at 25°C.," *Geochim. Cosmochim. Acta*, Vol. 56, 3339-3355, 1992.

Wilkins, R.W.T., "Infrared Spectroscopy in the Mineralogical Analysis of Uranium Ores," *Neues Jahrb. Mineral. Montash*, Vol. 1, 440-450, 1971.

Wirth, G.S. and J.M. Gieskes, "The Initial Kinetics of the Dissolution of Vitreous Silica in Aqueous Media," J. *Colloid Interf. Sci.*, Vol. 68, 492-500, 1979.

Yanase, N. et al., "Uranium Distribution in Mineral Phases of Rock Sequential Extraction Procedure," *Radiochim. Acta.*, Vol. 52/53, 387-393, 1991.

Yanase, N., T.E. Payne, and K. Sekine, "Groundwater Geochemistry in the Koongarra Ore Deposit, Australia (I): Implications for Uranium Migration," *Geochem. J.*, Vol. 29, 1-29, 1995.

Yates, D.E. and T.W. Healy, "Mechanism of Anion Adsorption at the Ferric and Chromic Oxide/Water Interfaces," *J. Colloid Int. Sci.*, Vol. 52, 222-228, 1975.

Yates, D.E. and T.W. Healy, "The Structure of the Silica/electrolyte Interface," *J. Colloid Interf. Science*, Vol. 55, 9-19, 1976.

Yeh, G.T. and V.S. Tripathi, "A Model for Simulating Transport of Reactive Multispecies Components: Model Development and Demonstration," *Water Resources Research*, Vol. 27, 3075-3094, 1991.

Zachara, J.M., P.L. Gassman, S.C. Smith, and D. Taylor, "Oxidation and Adsorption of Co(II)$EDTA^{2-}$ Complexes in Subsurface Materials with Iron and Manganese Oxide Grain Coatings," *Geochim. Cosmochim. Acta*, Vol. 59, 4449-4464, 1995a.

Zachara, J.M., C.T. Resch, and S.C. Smith, "Influence of Humic Substances on Co^{2+} Sorption by a Subsurface Mineral Separate and its Mineralogic Components," *Geochim. Cosmochim. Acta*, Vol. 58, 553-566, 1994.

Zachara, J.M. and S.C. Smith, "Edge Complexation Reactions of Cadmium on Specimen and Soil-Derived Smectite," *Soil Science Soc. Amer. J.*, Vol. 58, 762-769, 1994.

Zachara, J.M., S.C. Smith, and L.S. Kuzel, "Adsorption and Dissociation of Co-EDTA Complexes in Iron Oxide-Containing Subsurface Sands," *Geochim. Cosmochim. Acta*, Vol. 59, 4825-4844, 1995b.

NRC FORM 335 (2-89) NRCM 1102, 3201, 3202

U.S. NUCLEAR REGULATORY COMMISSION

BIBLIOGRAPHIC DATA SHEET

(See instructions on the reverse)

1. REPORT NUMBER (Assigned by NRC, Add Vol., Supp., Rev., and Addendum Numbers, if any.)

NUREG/CR-6708

2. TITLE AND SUBTITLE

Surface Complexation Modeling of Uranium (VI) Adsorption on Natural Mineral Assemblages

3. DATE REPORT PUBLISHED

MONTH	YEAR
March	2001

4. FIN OR GRANT NUMBER

W6054

5. AUTHOR(S)

J.A. Davis

6. TYPE OF REPORT

Technical

7. PERIOD COVERED *(Inclusive Dates)*

1993-1997

8. PERFORMING ORGANIZATION - NAME AND ADDRESS *(If NRC, provide Division, Office or Region, U.S. Nuclear Regulatory Commission, and mailing address; if contractor, provide name and mailing address.)*

U.S. Geological Survey
Menlo Park, CA 94025

9. SPONSORING ORGANIZATION - NAME AND ADDRESS *(If NRC, type "Same as above"; if contractor, provide NRC Division, Office or Region, U.S. Nuclear Regulatory Commission, and mailing address.)*

Division of Risk Analysis and Applications
Office of Nuclear Regulatory Research
U.S. Nuclear Regulatory Commission
Washington, DC 20555-0001

10. SUPPLEMENTARY NOTES

J.D. Randall, NRC Project Manager

11. ABSTRACT *(200 words or less)*

The value of surface complexation modeling of radionuclide adsorption in supporting the selection of Kd values should be given wider recognition in performance assessment modeling. Studies of uranium (VI) adsorption by a weathered schist and specimen mineral phases in the schist were conducted as a function of aqueous chemical conditions in laboratory experiments. The schist came from weathered, subsurface soil in the vicinity of the Koongarra uranium deposit in Australia. The variable aqueous chemical conditions in the experiments caused significant variations in the specification of dissolved uranium(VI) and the distribution coefficient Kd, that describes the partitioning of uranium(VI) between aqueous and solid phases. Laboratory-determined Kd values compared favorably with in-situ partitioning constants derived from analyses of dissolved uranium(VI) in groundwater and in the subsurface soils. Mineral coatings were more important than bulk mineralogy in controlling uranium(VI) adsorption by the schist. One of several surface complexation modeling approaches examined, the Generalized Composite approach, can reduce the uncertainty in Kd values chosen for performance assessment modeling. Surface complexation modeling offers a scientifically defensible means of linking the selection of Kd values for performance assessment to existing knowledge of thermodynamic data for radionuclides and radionuclide speciation in aqueous systems.

12. KEY WORDS/DESCRIPTORS *(List words or phrases that will assist researchers in locating the report.)*

Radionuclide transport, distribution coefficient, surface complexation modeling, performance assessment

13. AVAILABILITY STATEMENT

unlimited

14. SECURITY CLASSIFICATION

(This Page)

unclassified

(This Report)

unclassified

15. NUMBER OF PAGES

16. PRICE

NRC FORM 335 (2-89)

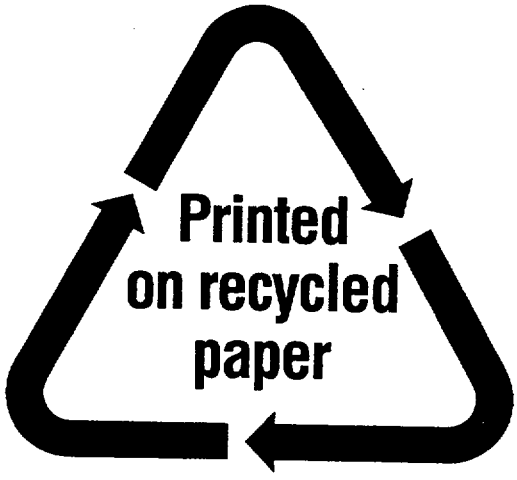

Federal Recycling Program

UNITED STATES
NUCLEAR REGULATORY COMMISSION
WASHINGTON, DC 20555-0001